Improved method for the characterisation of mechanical fatigue of rubber materials applied on a study to the lifetime-influence of dwell periods

Dissertation

zur Erlangung des akademischen Grades

Doktoringenieur
(Dr.-Ing.)

von: M. Sc. Oliver Gehrmann

geb. am: 04. November 1991 in Wismar, Deutschland

genehmigt durch die Fakultät: Maschinenbau der Otto-von-Guericke-Universität Magdeburg

Gutachter: Herr Prof. Dr.-Ing. Daniel Juhre

                Herr Prof. Yann Marco

                Herr Dr. Alan Muhr

Promotionskolloquium am: 15. März 2022

Zusammenfassung

Experimente bei denen Probekörper bis zum Ausfall mit einer oszillierenden Last beaufschlagt werden, sind ein etabliertes Vorgehen, um Erkenntnisse über das Ermüdungsverhalten von Elastomeren zu gewinnen. In der vorliegenden Arbeit werden Verbesserungen dieser Methode mit Fokus auf präzisere Lebensdauerergebnisse vorgeschlagen und in einer Studie zum Einfluss von Rastphasen im Lebensdauertest angewandt.

Zum Einstieg wird der starke Temperatureinfluss auf die Ermüdung von Elastomeren gezeigt. Eine Kühlung durch erzwungene Konvektion im Zusammenspiel mit einer amplitudenabhängigen Frequenzanpassung stellt sich als effektive Methodik heraus, um eine konstante Materialtemperatur über eine ganze Messreihe hinweg zu gewährleisten.

Daran anschließend, wird die häufig getroffene Annahme *weggesteuertes Oszillieren gleich dehnungsgesteuertes Oszillieren* auf den Prüfstand gestellt. Dafür wird die Dehnung bei maximaler Auslenkung innerhalb der oszillierenden Last optisch über die Dauer des Lebensdauerversuches aufgezeichnet. Als Ergebnis wird eine bemerkenswerte Zunahme der Dehnung über die Lastzyklen detektiert. Dieser Effekt stellt sich als geometrie-, last- und materialabhängig heraus. Lebensdauerergebnisse angewandt zur Betriebsfestigkeitsabschätzung werden meist in der Form *konstante Belastung in Abhängigkeit der Ausfallzyklen* (Stichwort: Wöhlerkonzept) verarbeitet. Daher wird ein Verfahren zur Umrechnung dieser über Lastzyklen inkonstanten Dehnungen zu Wöhler-konformen konstanten Vergleichsdehnungen vorgestellt.

Weiterhin wird eine neue Probekörpergeometrie entworfen. Denn in der Literatur fällt auf, dass die überwiegende Mehrheit der Lebensdaueruntersuchungen mit Probekörpern durchgeführt werden, welche durch oberflächliche Risse ausfallen. Folglich wird der neue Probekörper derart geformt, dass dessen Lebensdauer durch Anrisse im Vollmaterial dominiert wird. Eine Vergleichsstudie zwischen Probekörpergeometrien beweist die deutliche Lebensdauerzunahme bei oberflächenunabhängiger Rissinitiierung. Die Unregelmäßigkeiten an der Oberfläche führen zu abgeänderten Lebensdauerdaten. Eine solche Unregelmäßigkeit ist z.B. der Grat geformt durch die Formtrennnaht. Bruchbilduntersuchungen ergeben eine Konzentrierung der Initiierungen auf diese vulkanisationsformabhängige Schwachstelle. Auch innerhalb dieser Kategorie von oberflächlichen Unregelmäßigkeiten zeigen sich deutliche Lebensdauerabweichungen - Grat ist nicht gleich Grat.

Basierend auf den vorgestellten verbesserten Vorgehensweisen zur Ermüdungsmessung, wird der Einfluss von Rastphasen innerhalb von ansonsten kontinuierlich oszillierenden Lasten untersucht. Im Gegensatz zu Daten aus der Literatur, ermittelt durch Risswachstumsmessungen, ergibt sich keinerlei Einfluss dieser Rastphasen bei den Lebensdauertests der vorliegenden Arbeit. Einzig und allein für einen Styrol-Butadien-Kautschuk ohne Füllstoff stellt sich eine große Lebensdauerabnahme für Haltephasen unter Last ein. Dieser Effekt kann auf lastzeitabhängiges statisches Risswachstum zurückgeführt werden.

Abstract

Experiments with oscillating loads until failure applied on simple test pieces are often used for the characterisation of the fatigue behaviour of rubber materials. In this work, the method of fatigue testing is further optimised with the objective of increased precision in lifetime results. These improvements are applied on a study of dwell periods and their influence on durability.

At first, the strong dependency of the rubber lifetime on temperature is shown. Forced convection combined with an adaptation of frequency, with respect to the amplitude, is found to be an effective approach to obtain experimental data with similar material temperatures from different test piece geometries exposed to various loading conditions. Subsequently, the validity of the assumption *displacement-controlled testing is equivalent to strain-controlled testing* is examined. Therefore, fatigue tests on filled natural rubber and styrene butadiene rubber materials, using dumbbells die-cut from moulded sheet are performed. The strains in the narrow section at maximum deflection of the dumbells are measured with an optical method. A remarkable shift of this strain occurs over the length of oscillation, even though the displacement amplitude was constant. It turns out, that the effect of the strain shift over cycles dependents on the test piece (or engineering component) geometry, the amplitude as well as on the material. This geometry dependent evolution of the damaging propensity of the cyclic strain has influence on whatever lifetime prediction methodology is favoured. A method is introduced to transfer the continuously changing strains into a Wöhler curve-compliant constant equivalent strain.

In addition, a new fatigue test piece is designed. While the majority of the fatigue-data in literature originate of test pieces with locus of failure initiation at the free surface, motivates the design of the new test piece with failure initiation locus in the bulk material. This new test piece shows a strong lifetime-prolonging effect if benchmarked with test pieces that suffer from crack initiation at the surface. Inside the group of test pieces with surface initiations, significant lifetime differences are measured, even though the failures initiated nominally at the same locus, specifically at the flash.

In conclusion, based on all preceding suggestions for improvement, a presumably fatigue-influencing factor is investigated; dwell periods in otherwise commonly continuous sinusoidal load-signals. In disagreement with crack growth measurements from literature, no significant impact of dwell periods on the fatigue of rubber material is found. This is verified for a broad range of dwell conditions. Due to static crack growth, solely for unfilled styrene butadiene rubber, a lifetime-reducing effect for loaded dwell periods is found.

Declaration of Honor

I hereby declare that I produced this thesis without prohibited external assistance and that none other than the listed references and tools have been used. I did not make use of any commercial consultant concerning graduation. A third party did not receive any nonmonetary perquisites neither directly nor indirectly for activities which are connected with the contents of the presented thesis.
All sources of information are clearly marked, including my own publications. In particular

I have not consciously:

- Fabricated data or rejected undesired results

- Misused statistical methods with the aim of drawing other conclusions than those warranted by the available data

- Plagiarized data or publications

- Presented the results of other researchers in a distorted way

I do know that violations of copyright may lead to injunction and damage claims of the author and also to prosecution by the law enforcement authorities. I hereby agree that the thesis may need to be reviewed with an electronic data processing for plagiarism.
This work has not yet been submitted as a doctoral thesis in the same or a similar form in

Germany or in any other country. It has not yet been published as a whole.

Hanover, March 18, 2022

Contents

Acronyms

2D   two-dimensional

3D   three-dimensional

6PPD   N-(1,3-Dimethylbutyl)-N-phenyl-p-phenylendiamin

AE2   French: *Axisymétrique Entaillée* with a radius of $2\,\mathrm{mm}$

ASTM   American Society for Testing and Materials

B   Batch

c   cross-link - used in subscript only $(...)_c$

CBS   N-CyclohexylBenzothiazol-2-Sulphenamide

CDF   cumulative distribution function

cond   thermal conductivity - used in subscript only $(...)_{cond}$

const   constant - used in subscript only $(...)_{const}$

crit   critical - used in subscript only $(...)_{crit}$

CV   Controlled Viscosity

d   dwell - used in subscript only $(...)_d$

DIK   German: *Deutsches Institut für Kautschuktechnologie e.V.*

e   eigenvalue - used in subscript only $(...)_e$

eol   end-of-life - used in subscript only $(...)_{eol}$

EPDM   Ethylene Propylene Diene M-class rubber

f   filler - used in subscript only $(...)_f$

FE   Finite Element

FEA   Finite Element Analysis

glob   global - used in subscript only $(...)_{glob}$

GmbH   German: *Gesellschaft mit beschränkter Haftung*

H   Hencky strain concept - used in subscript only $(...)_H$

inv   inverse

ISO   International Organization for Standardization

iso   isochoric - used in subscript only $(...)_{iso}$

lgn   log-normal distribution - used in subscript only $(...)_{lgn}$

loc   local - used in subscript only $(...)_{loc}$

MS   Material Softening - used in subscript only $(...)_{MS}$

N   Normal curing

n   nominal strain concept - used in subscript only $(...)_n$

na   narrow - used in subscript only $(...)_{na}$

nor   normal distribution or Gaussian distribution - used in subscript only $(...)_{nor}$

NR   Natural Rubber

num   numerical - used in subscript only $(...)_{num}$

ovl   overall - used in subscript only $(...)_{ovl}$

p   polymer - used in subscript only $(...)_p$

p.   page

PDF   probability density function

phr   parts per hundred rubber

PK   Piola Kirchoff - used in subscript only $(...)_{PK}$

r   reduction - used in subscript only $(...)_r$

s   random sample - used in subscript only $(...)_s$

SBR   Styrene Butadiene Rubber

SD   Sudden-Death - used in subscript only $(...)_{SD}$

SMR   Standard Malaysian Rubber

stn	standard normal distribution - used in subscript only $(...)_{stn}$
TARRC	Tun Abdul Razak Research Centre
TBBS	N-$\underline{T}$ert-$\underline{B}$utyl-$\underline{B}$enzothiazole $\underline{S}$ulfonamide
TDS	TARRC-DIK-Specimen
TMTD	$\underline{T}$etra$\underline{m}$ethyl$\underline{t}$hiuram $\underline{D}$isulfide
tot	total - used in subscript only $(...)_{tot}$
V1	first Version
V2	second Version
ve	visco-elastic - used in subscript only $(...)_{ve}$
WB	Weibull distribution - used in subscript only $(...)_{WB}$
wi	wide - used in subscript only $(...)_{wi}$

1 Introduction

Rubber can not only be found in car tyres. Independent of where you are right now, have a thorough look in your environment. The probability of finding rubber components is very large. First hint, have a look on how the window is sealed. But what is actually rubber and why, as the title of this thesis suggest, is it worth of spend several years on the investigation of the mechanical fatigue of this flexible material.

1.1 What is Rubber?

Gent very well answers this question on the second page of his book [1]: "*Elastomers (natural and synthetic rubber) are amorphous polymers to which various ingredients are added* (see Figure 1.1)*, creating what the rubber chemist refers to as a compound. After heating and reaction (vulcanization), these materials become 'rubber'.*"
Here, an overview is given of polymers, ingredients and process of vulcanization, as applied in this work. This overview is reduced to the essential, starting with natural rubber as the oldest known gum rubber due to its origin in nature [2].

Figure 1.1: Example polymer with various example ingredients. Shown is the polymer, a resin, the curing-system (composed of sulphur, accelerators and retarder) and activators (zinc-oxide and stearic-acid) f.l.t.r.

Natural Rubber (NR)
The foundation for NR (see Figure 1.2), or named more chemically, natural cis-1,4-polyisoprene, is the latex of the Hevea brasiliensis tree [1]. Yet, it is the most important elastomer as measured by usage in weight [2]. As a result of the identical configuration (called stereoregular), the NR macromolecules are able to crystallise [1,2]. During crystallisation, caused by low temperatures (max. rate at $-25\,°C$) or large deformations, the

macromolecules bundle together leading to high resistance against e.g. severe deformations [1].

Styrene-Butadiene Rubber (SBR)

Similar to NR, SBR (see Figure 1.2) belongs to the general group of hydrocarbon polymers [1]. It has the highest use by volume among the many synthetic rubbers [1–3]. The base components Styrene and Butadiene originate from petroleum [2]. Cut growth and similar properties are significantly better for NR compared to SBR. However, SBR has greater resistance against high temperatures (up to 100 °C), ageing and substances like oils, fats, alcohol and water [2].

Figure 1.2: Natural rubber and oil extended Styrene-Butadiene rubber.

Vulcanisation / Curing

Vulcanisation is the process which transforms the elastomer, principally a very high viscosity liquid, to an elastic solid [1]. Within the vulcanisation process (aka. curing) the macromolecules obtain, additional to the pre-exciting weak physical links, strong chemical links. Many methods are used to create these chemical links (aka. cross-links). Only sulfur curing is applied in this study and is therefore briefly introduced.

Sulfur curing can only be performed for macromolecules with double bonds of allylic hydrogens [1, 2]. However, crosslinking with sulfur alone requires vulcanisation times of several hours [1]. For this reason, sulfur curing is applied in combination with curing accelerators to increase the efficiency and rate of cross-linking [1]. Accelerators used in the present study are labelled with the short-cuts CBS, TBBS and TMTD. Whereby the latter has a sulfur-donating function as well. Another class of ingredients are the so-called activators. They are used to activate the accelerators and therefore enable a more efficient accelerated sulfur curing. Examples from the applied recipes are zinc-oxide and stearic-acid.

Reinforcement

The term reinforcement originates from the ability of certain fillers (i.e. insoluble particulate materials) added to the rubber formulation to improve physical properties e.g. the

mechanical strength by more than 10 times [1, 4]. In this work only carbon black based reinforcing fillers are used. A filler particle (aka. primary particle) needs to be small ($\varnothing < 1\,\mu m$) to possess a high specific surface area, up to few hundreds m^2 per gram, to cause strong interactions with the polymer macromolecules and other filler particles [1]. Donnet et al. [4]: "*It is recognized that the main parameters of carbon blacks which govern their reinforcing ability in rubber are the following:*

- *The size and distribution of primary particles [...] which are joined by fusion into aggregates arranged at random. The particle size and its distribution directly determine the surface area of the carbon blacks.*

- *The size, shape and distribution of aggregates (aggregate complexity), i.e., the degree of irregularity of the carbon black units or the development of branchings due to the aggregation of primary particles and the asymmetry of the aggregates. These parameters are generally termed carbon black 'structure'.*

- *Surface activity which, in a chemical sense, is related to the reactivity of the chemical groups in the carbon black surface, and, in terms of physical chemistry, is referred to as adsorption capacity. This capacity is determined by carbon black surface energy, both its dispersive and specific components, and the energy distribution on the carbon black surface.*"

The two carbon blacks used in this study are labelled with N330 and N339. The first digit after the 'N' stands in correlation with the primary particle diameter [2], whereas the last two digits correlate with the structure of the carbon black aggregates. High structure, in simplified terms, describes the three-dimensional expansion of the aggregate divided by the actual aggregate volume [1].

Carbon black is very effective in reinforcing non-crystallising elastomers e.g. SBR [1]. Without carbon black, SBR and these kind of synthetic rubbers show inferior properties [2]. Due to the ability to significantly crystallise, NR already has a self-reinforcing mechanism. Actually, unfilled and black-filled NR exhibit the same tensile strength, nevertheless the latter has improved resistance to tearing and abrasion [1].

Process aids and Softener

As its name implies, process aids are added in order to lower the viscosity of the rubber compound and therefore to ease processing without much affecting vulcanisate properties [1]. The process oil labelled with Sunthene 410 is used in a NR compound in the present work. On the other hand, softeners reduce the viscosity of the rubber compound but also the stiffness of the vulcanisate [2]. Additionally, softeners e.g. support the absorption of fillers like carbon black [1].

Process oils are added in small amounts, whereas softeners are added in sufficient quantities, usually substantially higher than needed for processing.

Antioxidants

All organic rubbers succumb to degradation by light and oxidation. The NR and SBR rubber used in this study are especially sensitive to these processes due to their double bonds at the back bone [2]. Antioxidants interrupt the oxidative chemical reaction [2]. The antioxidant labelled with the shortcut 6PPD is added to the NR and SBR formulations in Section 4.2.

1.2 Fatigue and end-of-life prediction

In research, tests with oscillating loads using simple test pieces are conducted in order to quickly gather insights about the fatigue behaviour of rubber under the conditions of interest. In a more industrial environment, these kind of tests are often performed as a foundation for the lifetime prediction of components, using the procedure developed by August Wöhler [5]. The Wöhler concept is to express lifetimes (measured in cycles to failure) as a function of the amplitude of a repeated mechanical duty cycle. A plot of the amplitude against log(lifetime) - the Wöhler curve - may then be interpolated or extrapolated to estimate the maximum amplitude consistent with a desired lifetime (see Figure 1.3). The Wöhler curve is usually measured based on simple test pieces to save time and costs. One main advantage of the Wöhler approach is that physical experiments need to be performed only for simple test pieces but not for the *industrial* component. A virtual existence of the component, e.g. in form of a finite element model is sufficient. However, for rubber materials, there is a large list of fatigue-influencing factors (e.g. temperature) as will be shown in Chapter 3. The simple test piece and the component usually differ in these influencing factors. Therefore, one main challenge within the Wöhler concept is the choice of the so-called: fatigue criterion. This criterion is plotted at the ordinate of the Wöhler diagram. Prominent representatives of such criterion are strain and stress. The objective of the criterion is to correctly consider differences in fatigue-influencing factors between the component and the simple test pieces used to issue the Wöhler curve. For the unique case of:

$$\text{simple test piece geometry and load signal}$$
$$\hat{=}$$
$$\text{component geometry and component load signal,}$$

any criterion, even the global reaction force for a given displacement, leads to correctly predicted lifetimes since there is no difference in fatigue-influencing factors between these two. In a similar case in which the component is generally equal to the simple test piece, but larger or smaller (scaled) in all directions in space, the global reaction force fails as criterion for end-of-life prediction, and a local criterion like stress is necessary for a correct prediction. This insight will be of significant importance for the Chapters 4 to 6. In a more industrial environment there are often several fatigue-influencing factors that are

different between the component and the simple test piece. For research purposes the simple test pieces can also be compared among themselves. Within such an investigation, different kinds of load, e.g. for the same test piece geometry, or different test pieces with particular geometries exposed to the same kind of loading etc. can be considered (see later Chapter 6). Doing so, it is possible to isolate single fatigue-influencing factors and free of interference study their influence on the lifetime.
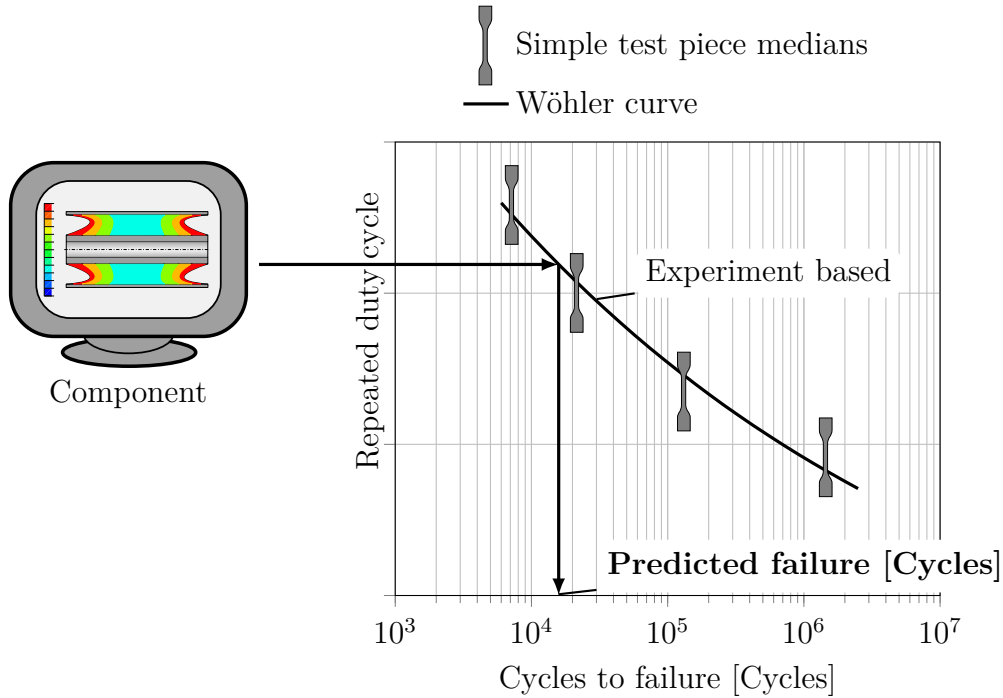
Figure 1.3: Wöhler's concept of end-of-life prediction.

Interest in the mechanical fatigue of rubber has continued unabated since one of the first methodical investigations by Cadwell et al. [6], in 1940. The identification of what mechanism within rubber exposed to a dynamic load results in a defined end-of-life, is fundamental for the design of rubber components (e.g. the car tyre, the window-seal of your room). However, after 80 years of research and far more than 400 articles (see introducing words of State of the Art Chapter 3) dealing with the fatigue of rubber, many major explanations for certain behaviour are still not given. In order to progress in rubber fatigue research, simple test piece geometries with defined conditions at the locus of the failure are used. A large number of publications present some fatigue results or extensive databases of lifetime data using such test pieces. These experimental databases are often further applied to develop or compare high-end end-of-life criteria, with the final goal to unite the many fatigue-influencing factors of rubber in one end-of-life prediction criterion. Within this study, no new fatigue criterion is proposed. Instead, it is focused on the measurement of accurate fatigue test data (see Chapter 4). In Section 4.1 the impact of temperature variations on the lifetime are shown and a straightforward procedure for

temperature-control is assessed. In addition, in Section 4.2 the strain evolution over the duration of displacement-controlled lifetime testing is investigated and its implication on the final fatigue results is shown. With the main objective to further improve the accuracy of fatigue results, a new fatigue test piece geometry, with *surface-effects independent* fatigue, is designed in Section 4.3 and is benchmarked with other entrenched test pieces in Chapter 5. Also partially using this new geometry, a possibly new factor influencing the lifetime of rubber is investigated in Chapter 6. There, the influence of dwell periods on the fatigue of rubber is measured.

2 Theoretical fundamentals

As foundation for the analytical and numerical analyses from Chapter 4 to 6, the principals of continuum mechanics are given in Section 2.1, followed by different continuum mechanical models of its mechanical response to deformation in Section 2.2. The last Section 2.3 of the present Chapter focuses on the statistical evaluation of experimental fatigue.

2.1 Continuum mechanics

All matter is naturally discontinuous [7]. The discontinuities start on the atomic level (different arrangements of molecules) and still exist on a larger scale in the form of inhomogeneities e.g. cracks, inclusions, interfaces (for rubber see [8]). In continuum mechanics these microscopic inhomogeneities are neglected. Instead, the material is assumed to be continuous (dense). The properties of the continuous material can be interpreted as statistical averages of the microscopic properties over a representative volume.

Continuum mechanics deals with the determination of interior forces and deformations of a body as a result of a given exterior load. These interior forces are locally described by so called stress-states and the local deformations by strain-states [9].

2.1.1 Tensor algebra

In order to describe loading/deformation states in a continuum body, the setting has to be described mathematically using vector/tensor algebra. Within the present work, only orthogonal coordinate systems are considered.

Definition of first- and second-order tensors

In a three-dimensional system, a first-order tensor may be depicted by a (3×1) vector $\vec{a}$. A second-order tensor $\underline{\underline{A}}$ is a linear operator that acts on a vector $\vec{a}_1$ generating another vector $\vec{a}_2$ [10]:

$$\vec{a}_2 = \underline{\underline{A}}\,\vec{a}_1 \tag{2.1}$$

Eigenvalues, Eigenvectors, Invariants

One can derive tensorial characteristic variables (e.g. eigenvalues and invariants) that are invariant of coordinate transformations. These characteristic variables originating from

deformation and stress tensors will turn out to be a unique describer of the deformation and stress states in Section 2.1.2 and 2.1.3.

To obtain the eigenvalues λ_{ei} and eigenvectors $\vec{n}_i$ of an arbitrary second-order tensor $\underline{\underline{A}}$ (so $i = 1, 2, 3$) the equation

$$\underline{\underline{A}}\, \vec{n}_i = \lambda_{ei}\, \vec{n}_i \tag{2.2}$$

is fundamental [10]. Rearranging gives the following eigenvalue problem [11]

$$(\underline{\underline{A}} - \lambda_{ei}\, \underline{I})\vec{n}_i = \vec{0} \tag{2.3}$$

with $\underline{I}$ as the identity tensor. For the eigenvalue problem a non-trivial solution for $\vec{n}_i$ exists only if [11]:

$$\det(\underline{\underline{A}} - \lambda_{ei}\, \underline{I}) = 0 \tag{2.4}$$

To determine the unknown eigenvalues, solving the cubic Equation 2.5 is required:

$$\lambda_{ei}^3 - I_1\lambda_{ei}^2 + I_2\lambda_{ei} + I_3 = 0 \tag{2.5}$$

This equation is the so called characteristic polynomial for (in this case) $\underline{\underline{A}}$ [9]. The polynomial contains the invariants $I_i(\underline{\underline{A}})$. As included in the name, the invariants are independent (invariant) on coordinate transformations. Same applies for the eigenvalues, although not for the eigenvectors. Therefore, the scalars $I_i(\underline{\underline{A}})$ and λ_{ei} are characteristic for $\underline{\underline{A}}$. The invariants are defined by [10]:

$$I_1(\underline{\underline{A}}) = \text{tr}\,\underline{\underline{A}} = \lambda_{e1} + \lambda_{e2} + \lambda_{e3} \tag{2.6}$$

$$I_2(\underline{\underline{A}}) = \frac{1}{2}[(\text{tr}\,\underline{\underline{A}})^2 - \text{tr}(\underline{\underline{A}}^2)] = \lambda_{e1}\lambda_{e2} + \lambda_{e1}\lambda_{e3} + \lambda_{e2}\lambda_{e3} \tag{2.7}$$

$$I_3(\underline{\underline{A}}) = \det\underline{\underline{A}} = \lambda_{e1}\lambda_{e2}\lambda_{e3} \tag{2.8}$$

With the known eigenvalues, the eigenvectors can be determined with Equation 2.3. The eigenvectors form an orthonormal system if the tensor $\underline{\underline{A}}$ is symmetric [10]. By normalising the eigenvectors $\vec{n}_i$ and arranging them in a matrix one obtains the orthogonal matrix $\boldsymbol{N}$. The spectral decomposition is given by [10]:

$$\underline{\underline{A}} = \boldsymbol{N}\boldsymbol{\Lambda}\boldsymbol{N}^T \tag{2.9}$$

The diagonal matrix $\mathbf{\Lambda}$ is obtained by diagonalization of $\underline{\underline{A}}$:

$$\boldsymbol{N}^T \underline{\underline{A}} \, \boldsymbol{N} = \mathbf{\Lambda} = \begin{bmatrix} \lambda_{e1} & & \\ & \lambda_{e2} & \\ & & \lambda_{e3} \end{bmatrix} \tag{2.10}$$

The spherical and deviatoric parts of a second-order tensor

In Section 2.1.2 and 2.1.3 is shown, using the example of strain and stress tensors, that the separation of a second-order tensor $\underline{\underline{A}}$, in its spherical and deviatoric part, is a useful operation:

$$\underline{\underline{A}} = a_{\text{spher}} \underline{\underline{I}} + \text{dev} \, \underline{\underline{A}} \tag{2.11}$$

$$\text{with: } a_{\text{spher}} = \frac{1}{3} \, \text{tr} \, \underline{\underline{A}} \tag{2.12}$$

2.1.2 Deformations and strains

Using the previous mathematical definition, the deformation of a solid can be described by two points (P_1, P_2) with a certain separation on a continuum body. Unless the deformation is homogeneous, this separation has to be infinitesimal. Moreover, it is necessary to define a reference configuration, since no deformation can be detected without any knowledge of the reference or *undeformed* configuration. Finally, the location of the points with respect to themselves, is stored in a vector. This vector begins at P_1 and ends at P_2 and is labelled $\mathrm{d}\vec{X}$ and $\mathrm{d}\vec{x}$ in the reference and deformed configuration, respectively (see Figure 2.1).
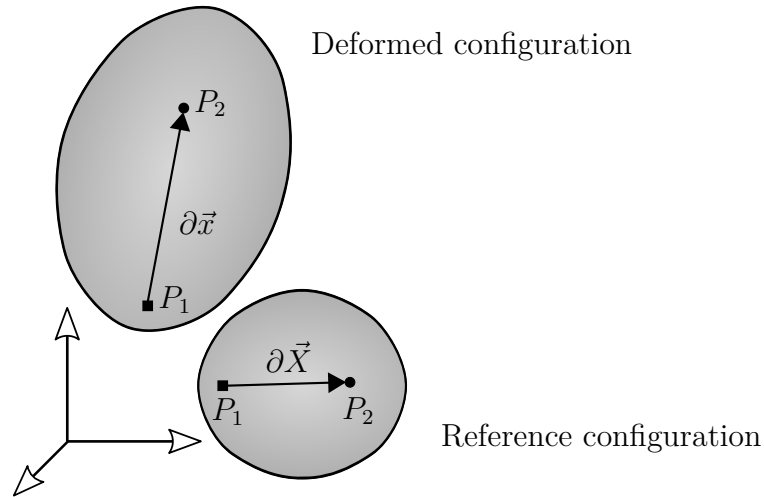
Figure 2.1: Reference and current (*deformed*) configurations of a continuum body.

The conversion from vector $\mathrm{d}\vec{X}$ to $\mathrm{d}\vec{x}$ may be described by the transformation matrix $\boldsymbol{F}$:

$$\boldsymbol{F} = \frac{\mathrm{d}\vec{x}}{\mathrm{d}\vec{X}} = \left[\frac{\mathrm{d}x_i}{\mathrm{d}X_j}\right] = \begin{bmatrix} \dfrac{\mathrm{d}x_1}{\mathrm{d}X_1} & \dfrac{\mathrm{d}x_1}{\mathrm{d}X_2} & \dfrac{\mathrm{d}x_1}{\mathrm{d}X_3} \\ \dfrac{\mathrm{d}x_2}{\mathrm{d}X_1} & \dfrac{\mathrm{d}x_2}{\mathrm{d}X_2} & \dfrac{\mathrm{d}x_2}{\mathrm{d}X_3} \\ \dfrac{\mathrm{d}x_3}{\mathrm{d}X_1} & \dfrac{\mathrm{d}x_3}{\mathrm{d}X_2} & \dfrac{\mathrm{d}x_3}{\mathrm{d}X_3} \end{bmatrix} \tag{2.13}$$

This matrix $\boldsymbol{F}$ expressed independently of a particular coordinate system yields a second-order tensor, namely, the deformation gradient $\underline{\underline{F}}$. This deformation gradient $\underline{\underline{F}}$ is a located tensor and measures deformations, but also pure rotations of a solid [12]. Deformation gradient $\underline{\underline{F}}$ may be split by use of polar decomposition:

$$\underline{\underline{F}} = \underline{\underline{R}}\,\underline{\underline{U}} \tag{2.14}$$

The tensor $\underline{\underline{U}}$ and tensor $\underline{\underline{R}}$ are known as right stretch tensor and rotation tensor, respectively.

For the definitions of strains, solid body rotations are not considered. Note that unlike displacements, that are measured in units of length, strains depend on the choice of definition, of which several are in common use [10].

Prior to the definition of strain concepts, the right Cauchy-Green tensor $\underline{\underline{C}}$ is introduced:

$$\underline{\underline{C}} = \underline{\underline{F}}^T\underline{\underline{F}} = \underline{\underline{U}}^T\underline{\underline{U}} \tag{2.15}$$

The square root of the eigenvalues $\lambda_{\mathrm{e}i}$ of $\underline{\underline{C}}$ are known as stretches λ_i with $i = 1, 2, 3$ (see Section 2.1.1). Note, that the principal directions of $\underline{\underline{C}}$ are defined by the directions of its eigenvectors.

Imagine three thin and short cylinders, cut out from a continuous body. These cylinders deform affinely with the material and are located at a material point. Moreover, they are oriented in the principal directions of $\underline{\underline{C}}$ at this material point. The eigenvalues of the symmetric second-order tensor $\underline{\underline{C}}$ in this material - the stretches - are the factors between initial cylinder length (blue) and deformed cylinder length (red).
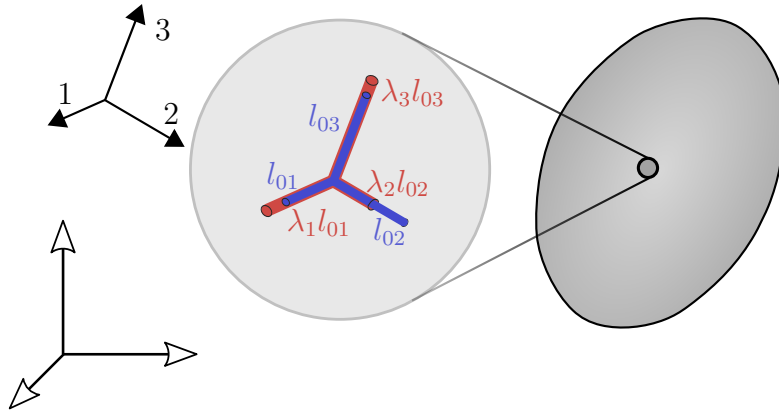
Figure 2.2: Schematic illustration of the change in vector length (l_{01}, l_{02}, l_{03}), measured by the stretches (λ_1, λ_2, λ_3).

Two strain concepts are introduced. Firstly the nominal strain concept, with the corresponding Biot strain tensor, defined as follows:

$$\underline{\underline{E}}_n = \sqrt{\underline{\underline{C}}} - \underline{\underline{I}} \tag{2.16}$$

Nominal strains will regularly be used throughout this work, since they are intuitively interpretable by humans. Only for the definition of strain-states, the Hencky strain concept is employed, with its tensor given by:

$$\underline{\underline{E}}_H = \frac{1}{2} \ln(\underline{\underline{C}}) \tag{2.17}$$

As an example, for a one-dimensional deformation, the two strain concepts are compared in Figure 2.3.
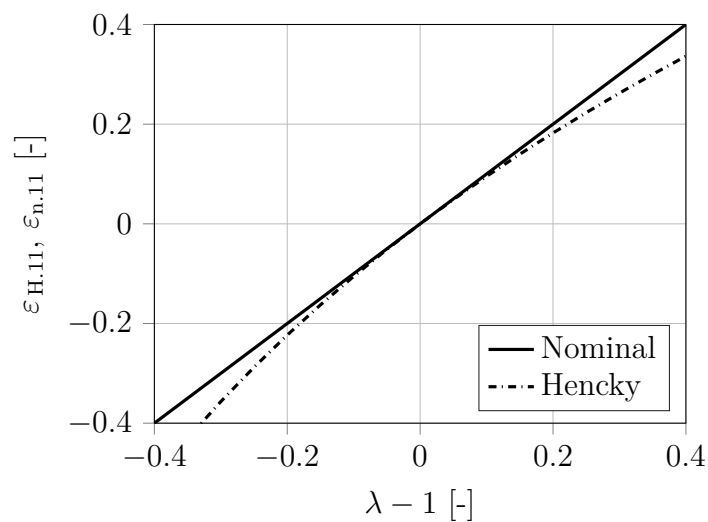
Figure 2.3: Strain concepts in comparison for one dimension.

The components of the nominal strain tensor $\underline{\underline{E}}_n$ are shown (see matrix representation in Equation 2.18). Further, a Cartesian coordinate system with the axes notation x, y, z is assumed.

$$\underline{\underline{E}}_n = \begin{bmatrix} \varepsilon_{n.11} & \varepsilon_{n.12} & \varepsilon_{n.13} \\ \varepsilon_{n.21} & \varepsilon_{n.22} & \varepsilon_{n.23} \\ \varepsilon_{n.31} & \varepsilon_{n.32} & \varepsilon_{n.33} \end{bmatrix} = \begin{bmatrix} \varepsilon_{n.x} & \frac{1}{2}\gamma_{xy} & \frac{1}{2}\gamma_{xz} \\ \frac{1}{2}\gamma_{yx} & \varepsilon_{n.y} & \frac{1}{2}\gamma_{yz} \\ \frac{1}{2}\gamma_{zx} & \frac{1}{2}\gamma_{zy} & \varepsilon_{n.z} \end{bmatrix} \tag{2.18}$$

The quantities $\varepsilon_{n.x}$, $\varepsilon_{n.y}$, $\varepsilon_{n.z}$ measure length changes, similar to the stretches λ_i. Whereas the non-diagonal matrix entries measure pure angle changes [9] (see Figure 2.4). Figure 2.4 shows the length change measured by $\varepsilon_{n.x}$ only.

(a)   (b)

$$\varepsilon_{n.x} = \frac{u_x}{l_x} \qquad\qquad \gamma_{xy} = \frac{u_x}{l_y} + \frac{u_y}{l_x}$$
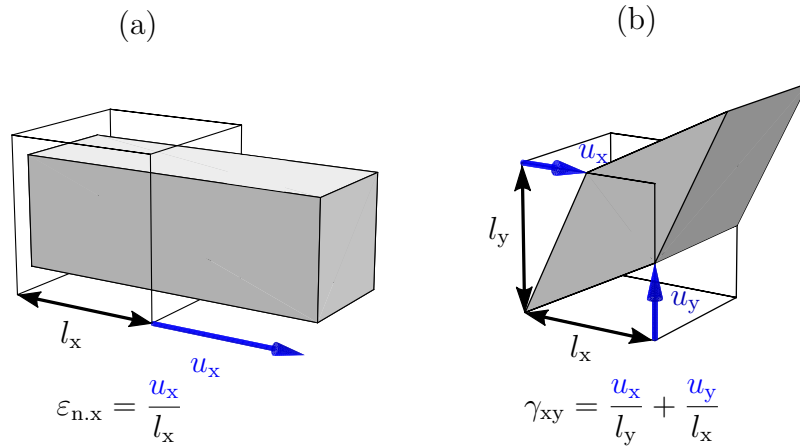
Figure 2.4: Implication of the the diagonal and non-diagonal elements of the nominal strain tensor $\underline{\underline{E}}_n$ on small deformations.

It is possible to rotate $\underline{\underline{E}}_n$ in a sense that the deformation can be only described by its diagonal elements $\varepsilon_{n.x}, \varepsilon_{n.y}, \varepsilon_{n.z}$. In order to obtain the diagonalised $\underline{\underline{E}}_n$, Equation 2.10 is applied:

$$N^T \underline{\underline{E}}_n N = \begin{bmatrix} \varepsilon_{n.1} & & \\ & \varepsilon_{n.2} & \\ & & \varepsilon_{n.3} \end{bmatrix} \tag{2.19}$$

Figure 2.5 illustrates the concept of eigen-directions. The body highlighted in blue represents a very small part of the enclosing body. This blue cuboid is always oriented in alignment with the principal axis system. Assuming that $\varepsilon_{n.1} > \varepsilon_{n.2} > \varepsilon_{n.3}$, they may be labelled with maximum, middle and minimum principal nominal strain ($\varepsilon_{n.max}$, $\varepsilon_{n.mid}$, $\varepsilon_{n.min}$). The local $\varepsilon_{n.max}$ is frequently applied within the present work in order to compare fatigue data from e.g. different test piece geometries. It is assumed that the gained knowledge from comparing the lifetime data is independent on the concept of strain.
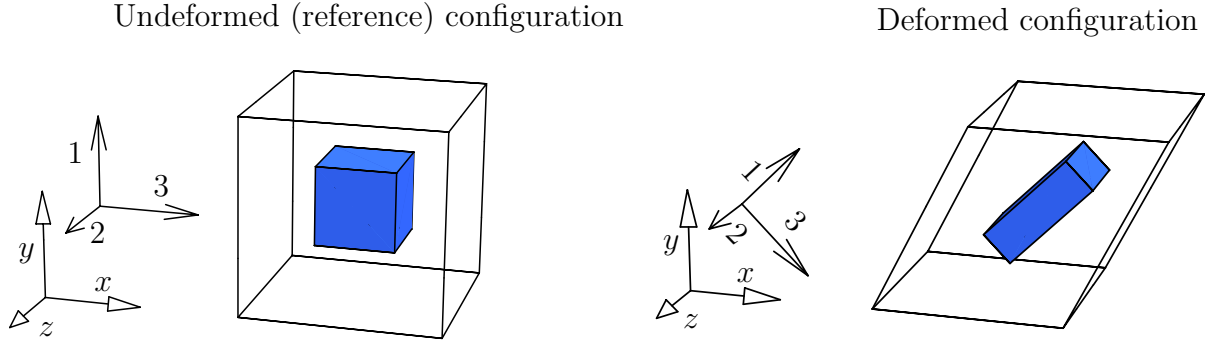
Figure 2.5: Visualisation of the eigen-directions for a simple shear deformation.

Further, one may split the strain tensors into their spherical and deviatoric parts. This mathematical operation is applied ot the Hencky strain tensor, by using Equation 2.11:

$$\underline{\underline{E}}_{\mathrm{H}} = \epsilon_{\mathrm{H}}\underline{\underline{I}} + \mathrm{dev}\,\underline{\underline{E}}_{\mathrm{H}} \tag{2.20}$$

$$with:\ \epsilon_{\mathrm{H}} = \frac{1}{3}\,\mathrm{tr}\,\underline{\underline{E}}_{\mathrm{H}} \tag{2.21}$$

This yields the following matrix representation, oriented to its principal directions:

$$\underline{\underline{E}}_{\mathrm{H}} = \begin{bmatrix} \ln\lambda_1 & & \\ & \ln\lambda_2 & \\ & & \ln\lambda_3 \end{bmatrix} = \begin{bmatrix} \epsilon_{\mathrm{H}} & & \\ & \epsilon_{\mathrm{H}} & \\ & & \epsilon_{\mathrm{H}} \end{bmatrix} + \begin{bmatrix} \ln\lambda_1 - \epsilon_{\mathrm{H}} & & \\ & \ln\lambda_2 - \epsilon_{\mathrm{H}} & \\ & & \ln\lambda_3 - \epsilon_{\mathrm{H}} \end{bmatrix}$$

$$with:\ \epsilon_{\mathrm{H}} = \frac{1}{3}(\ln\lambda_1 + \ln\lambda_2 + \ln\lambda_3)$$

Since $\underline{\underline{E}}_{\mathrm{H}}$ is a tensor measuring deformations, its spherical- and deviatoric part are also known as the dilatational and isochoric part. These two parts describe a pure volume-changing and pure distortional deformation, respectively. Figure 2.6 shows these two different kinds of deformation schematically on a simultaneously compressed and sheared cuboid.
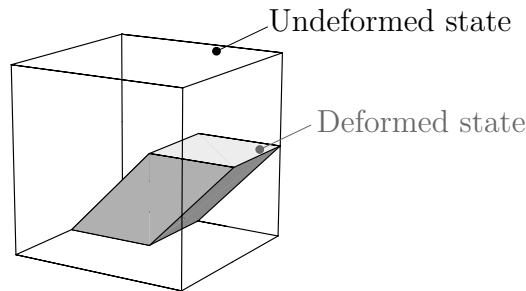
Figure 2.6: Compressed and sheared cuboid.

After the decomposition the dilatational part and isochoric part become visible:

Dilatational deformation   Isochoric deformation
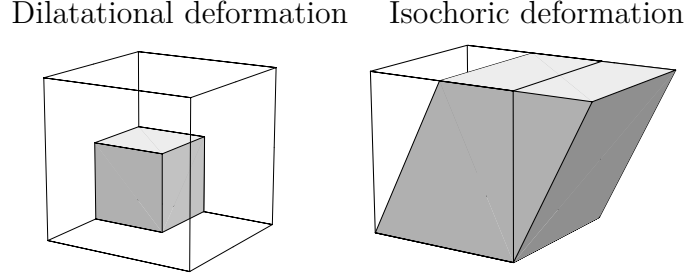
Figure 2.7: Deformation from Figure 2.6 decomposed in dilatational and isochoric parts.

In case of an incompressible material, the product of the stretches equals one:

$$\lambda_1 \lambda_2 \lambda_3 = 1 \tag{2.22}$$

Based on this law, one obtains a zero for the trace of $\underline{\underline{E}}$. For large deformations, $\mathrm{tr}\,\underline{\underline{E}}$ stays zero only when $\underline{\underline{E}}$ is defined by the Hencky strain concept, e.g. not for the nominal strain concept (see Equation 2.23).

$$\epsilon_{\mathrm{H}} = \frac{1}{3}\,\mathrm{tr}\,\underline{\underline{E}}_{\mathrm{H}} = 0 \tag{2.23}$$

This is because:

$$\epsilon_{\mathrm{H}} = \frac{1}{3}(\ln\lambda_1 + \ln\lambda_2 + \ln\lambda_3) = \frac{1}{3}(\ln(\lambda_1\lambda_2\lambda_3)) = 0 \tag{2.24}$$

The volume ratio J [10] is defined by:

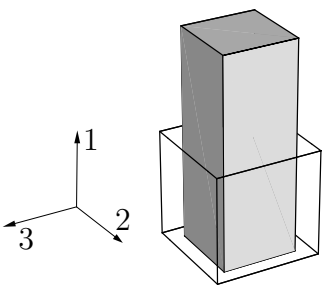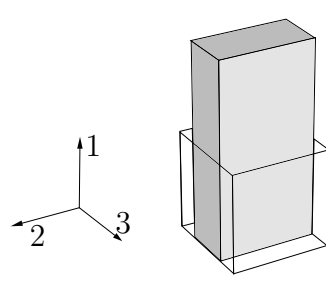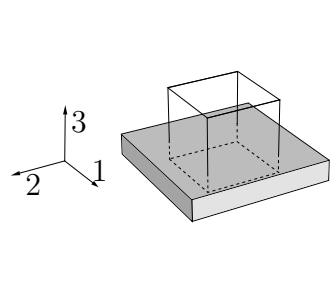$$J = \frac{\mathrm{d}v}{\mathrm{d}V} = \det\underline{\underline{F}} \tag{2.25}$$

with $\mathrm{d}v$ and $\mathrm{d}V$ as infinitesimal volume elements defined in the deformed and undeformed states, respectively. The Equation 2.25 leads to Equation 2.22, by using the diagonalised $\underline{\underline{F}}$. The volume ratio J is always equal to one for an incompressible material.

Strain-states

The basic strain-states are the uniaxial strain-state, plain strain-state and the equibiaxial strain-state [10]. As shown in Table 2.1, these strain-states are defined for an incompressible body with the three principal Hencky strains. An indicator for the different strain-states is the so-called biaxiality ratio B:

$$B = \frac{\varepsilon_{\mathrm{H.2}}}{\varepsilon_{\mathrm{H.1}}} \tag{2.26}$$

Uniaxial strain	Plain strain	Equibiaxial strain
$\varepsilon_{\mathrm{H.2}} = \varepsilon_{\mathrm{H.3}} = -\dfrac{1}{2}\varepsilon_{\mathrm{H.1}}$	$\varepsilon_{\mathrm{H.2}} = 0 \quad \varepsilon_{\mathrm{H.3}} = -\varepsilon_{\mathrm{H.1}}$	$\varepsilon_{\mathrm{H.2}} = \varepsilon_{\mathrm{H.1}} \quad \varepsilon_{\mathrm{H.3}} = -2\,\varepsilon_{\mathrm{H.1}}$
$B = -\dfrac{1}{2}$	$B = 0$	$B = 1$

Table 2.1: Strain-states defined by the biaxiality ratio B.

2.1.3 Stresses

Stresses are interior reactions, usually to exterior forces. The reference configuration is assumed to be free of both exterior and interior forces.

If a continuum body is deformed, a resistance occurs - a reaction force - that works against this deformation. Internal stresses become visible by using a plane that cuts the body [13]. They are defined as force per unit of area [10]. Figure 2.8 shows the body in the deformed state. Additionally, the body is cut to visualise the interior resistance in terms of forces and stresses.
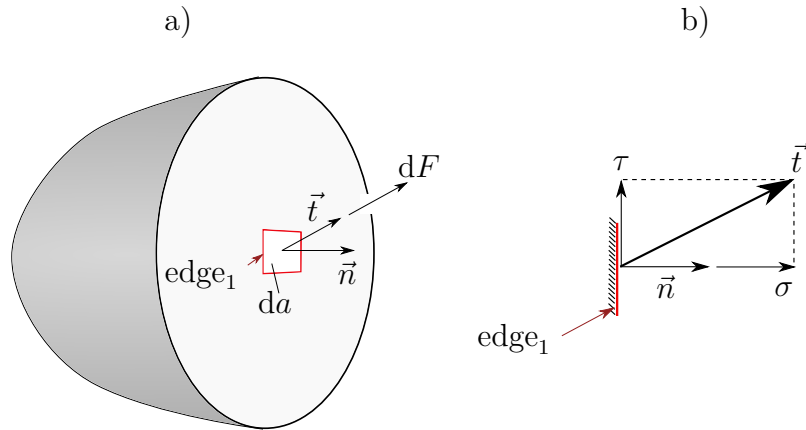
Figure 2.8: Traction vector and its decompostion in normal- and shear-stresses (referring to [9]).

In Figure 2.8-a) the traction vector $\vec{t}$ is shown. This vector is defined through the infinitesimal force vector $\mathrm{d}\vec{F}$ normalised by the infinitesimal surface area $\mathrm{d}a$:

$$\vec{t} = \frac{\mathrm{d}\vec{F}}{\mathrm{d}a} \tag{2.27}$$

Since the surface element (framed in red) is situated in the deformed configuration, $\vec{t}$ is labelled as the Cauchy traction vector [10].

The Figure 2.8-b) shows the decomposition of the Cauchy traction vector into the Cauchy normal stress σ (perpendicular to the surface element) and the Cauchy shear stress τ (tangential to the surface element):

$$\sigma = \vec{t} \cdot \vec{n} \; , \;\; \tau = \sqrt{\vec{t} \cdot \vec{t} - \sigma^2} \tag{2.28}$$

with $\vec{n}$ as normal of the surface element [9].

The following question may occur: What are the components of $\vec{t}$ in another cut plane however at the same spot? In order to obtain the full three-dimensional definition of the stress state, three independent cuts are needed. Figure 2.9 shows a material point with three independent cuts, including traction vectors for each cut.
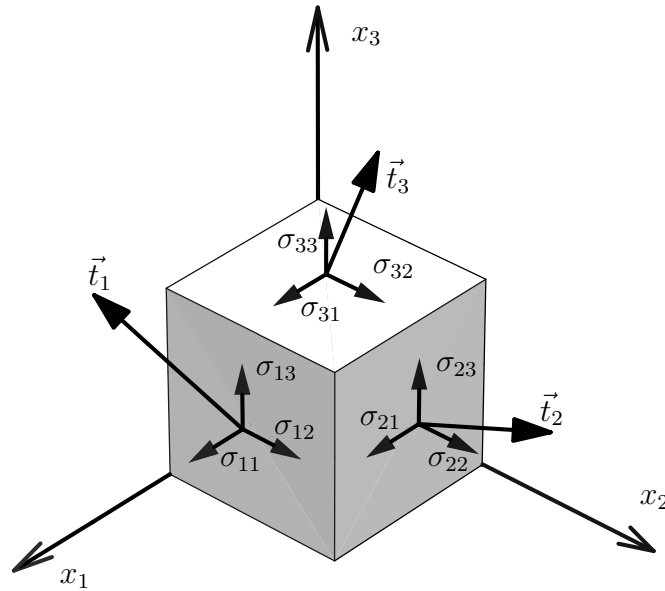
Figure 2.9: Stress components at a body cut by three independent planes.

Moreover, one may describe each traction vector by three components related to the cut axis x_1, x_2, x_3. For the axes x_i (with $i = 1, 2, 3$) $\vec{t_i}$ is defined [9]:

$$\vec{t_i} = \begin{bmatrix} \sigma_{i1} \\ \sigma_{i2} \\ \sigma_{i3} \end{bmatrix} \quad , \; i = 1, 2, 3 \tag{2.29}$$

According to Figure 2.9, the stress components σ_{ij} with $i = j$ are called normal stresses (with identifier σ) and those with $i \neq j$ shear stresses (with identifier τ). These stresses are still related to the surface area of the deformed configuration, hence they are labelled Cauchy normal stresses and Cauchy shear stresses, respectively.

In order to merge the information of the three cuts to one entity, the following matrix

notation is used:

$$\boldsymbol{\sigma} = [\vec{t}_1, \vec{t}_2, \vec{t}_3]^T = \begin{bmatrix} \sigma_{11} & \sigma_{12} & \sigma_{13} \\ \sigma_{21} & \sigma_{22} & \sigma_{23} \\ \sigma_{31} & \sigma_{32} & \sigma_{33} \end{bmatrix} = \begin{bmatrix} \sigma_{xx} & \tau_{xy} & \tau_{xz} \\ \tau_{yx} & \sigma_{yy} & \tau_{yz} \\ \tau_{zx} & \tau_{zy} & \sigma_{zz} \end{bmatrix} \tag{2.30}$$

with redefining the axes x_1, x_2, x_3 (see Figure 2.9) to x, y, z. The matrix $\boldsymbol{\sigma}$ is the matrix notation of the second-order tensor $\underline{\underline{\sigma}}$, called the Cauchy stress tensor. By using $\boldsymbol{\sigma}$, $\vec{t}$ may now be calculated for each arbitrary cut with the normal $\vec{n}$:
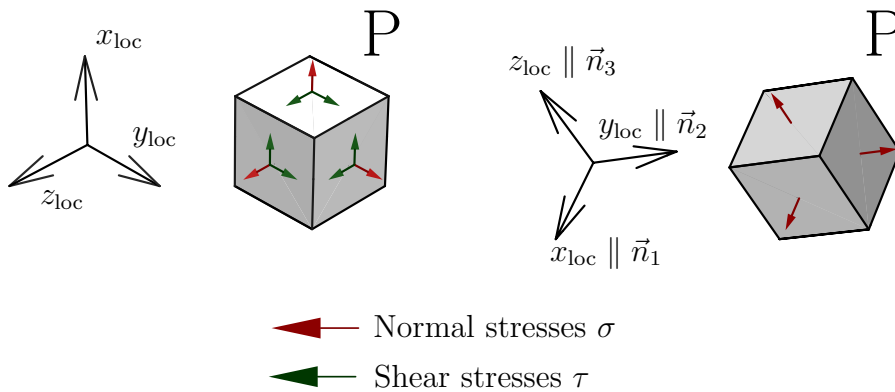
$$\vec{t} = \boldsymbol{\sigma}\vec{n} \tag{2.31}$$

Solving the eigenvalue problem for $\underline{\underline{\sigma}}$

$$(\underline{\underline{\sigma}} - \sigma_i \underline{\underline{I}})\vec{n}_i = \vec{0} \tag{2.32}$$

provides the eigenvalues σ_i and eigenvectors $\vec{n}_i$ from $\underline{\underline{\sigma}}$, with $i = 1$, 2, 3. Aligning $\underline{\underline{\sigma}}$ in the direction of its eigenvectors yields non-zero normal stresses only (see Figure 2.10).
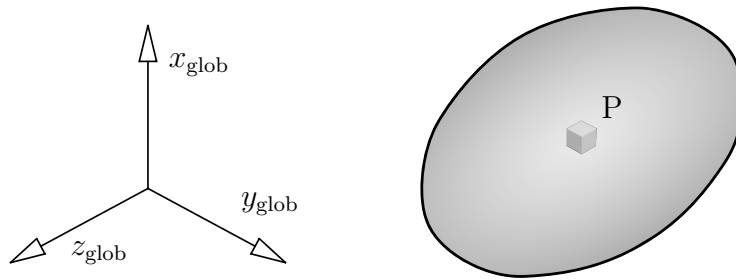
Stress state in point P visualized in two different coordinate systems.

Normal stresses σ

Shear stresses τ

Figure 2.10: The concept of eigendirections applied to the stress tensor.

Similar to the strain tensors, the Cauchy stress tensor $\underline{\underline{\sigma}}$ may be split into its spherical and deviatoric parts:

$$\underline{\underline{\sigma}} = \sigma_0 \underline{\underline{I}} + \text{dev}\,\underline{\underline{\sigma}} \tag{2.33}$$

$$with: \ \sigma_0 = \frac{1}{3}\,\text{tr}\,\underline{\underline{\sigma}} = -p \tag{2.34}$$

The spherical part $\sigma_0\underline{\underline{I}}$ is known as hydrostatic part, with σ_0 as the hydrostatic stress and p as hydrostatic pressure. Anticipating, this engineering value significantly influence the mechanical fatigue of rubber.

Cauchy stresses are related to the deformed configuration i.e. the deformed area $\text{d}a$ (see Equation 2.27). Stresses related to the area $\text{d}A$ of the reference/undeformed configuration are first Piola Kirchhoff stresses. We define these by defining first Piola Kirchoff tractions analogously to Cauchy tractions:

$$\vec{t}_{\text{PK}} = \frac{\text{d}\vec{F}}{\text{d}A} \tag{2.35}$$

From an experimental point of view, first Piola Kirchhoff stresses have their advantages against Cauchy stresses. They are more direct (without any assumption) accessible, since the initial area $\text{d}A$ stays constant by definition during the deformation of the body. The corresponding stress tensor $\underline{\underline{P}}$ is the first Piola Kirchhoff stress tensor and is consequently defined as:

$$\underline{\underline{P}} = [\vec{t}_{\text{PK.1}}, \vec{t}_{\text{PK.2}}, \vec{t}_{\text{PK.3}}]^T = \begin{bmatrix} P_{11} & P_{12} & P_{13} \\ P_{21} & P_{22} & P_{23} \\ P_{31} & P_{32} & P_{33} \end{bmatrix} \tag{2.36}$$

The transformation from the first Piola Kirchhoff stress tensor $\underline{\underline{P}}$ to the Cauchy stress tensor $\underline{\underline{\sigma}}$ is given by [10]

$$\underline{\underline{\sigma}} = J^{-1}\underline{\underline{P}}\,\underline{\underline{F}}^{T} \tag{2.37}$$

with J as volume ratio (see Equation 2.25).

This closes the necessary continuum mechanics as foundation for the subsequent elaborations of the present work.

2.2 Constitutive models

The purpose of this section is to provide mathematical descriptions of the stresses caused by a given strain for rubber materials (see Section 1.1). In order to *connect* the strains with the stresses (defined in Sections 2.1.2 and 2.1.3, respectively) a constitutive model is used. Our primary interest is in isochoric deformations, since unless the hydrostatic stress is very large, the dilatation is negligible and as is the relationship between isochoric deformations and deviatoric stresses (see Equations 2.20 and 2.33, respectively).

The isochoric stress-response ($\underline{\underline{P}}_{\text{iso}}$) of an elastic body to an isochoric deformation ($\underline{\underline{F}}_{\text{iso}}$) is formulated via the isochoric elastic free energy Ψ:

$$\underline{\underline{P}}_{\text{iso}} = \frac{\partial \Psi(\underline{\underline{F}}_{\text{iso}})}{\partial \underline{\underline{F}}_{\text{iso}}} \tag{2.38}$$

Elastomers show a non-linear stress-strain-behaviour for medium to large deformations. Such non-linear response of the stress for a given deformation can be modelled with the neo-Hookean material model.

$$\Psi = \frac{G}{2}(I_1 - 3) \tag{2.39}$$

This model contains one parameter only, the shear modulus G and describes a material with a linear shear-stress over strain behaviour to any strain [10]. For this model, the loading and unloading paths are identical regardless of how large the strain is; such models, and the idealised materials they describe, are said to be hyperelastic. Another hyperelastic constitutive model is the Arruda-Boyce material model. Its free energy is defined by [14]:

$$\Psi = G \left(\frac{1}{2}(I_1 - 3) + \frac{1}{20\,N}(I_1^2 - 9) \right.$$
$$\left. + \frac{11}{1050\,N^2}(I_1^3 - 27) + \frac{19}{7000\,N^3}(I_1^4 - 81) + \frac{519}{673750\,N^4}(I_1^5 - 243) \right) \tag{2.40}$$

with parameter G as shear modulus and N being associated with the average number of macromolecule-segments between two neighbouring cross-links. Figure 2.11 shows selected experimental data from a rubber material, as well as its numerical approximation with the neo-Hookean and Arruda-Boyce material model. In this example, the material model parameters are fitted separately for each amplitude (see Table 2.2). It appears that those two models are not able to capture all aspects of the material behaviour of the example material. Due to their pure hyperelastic nature, they are unable to describe the rubber-typical material softening, hysteresis and set. As realised in this example, the material softening can only be approximated by hyperelastic constitutive laws using several parameter sets.
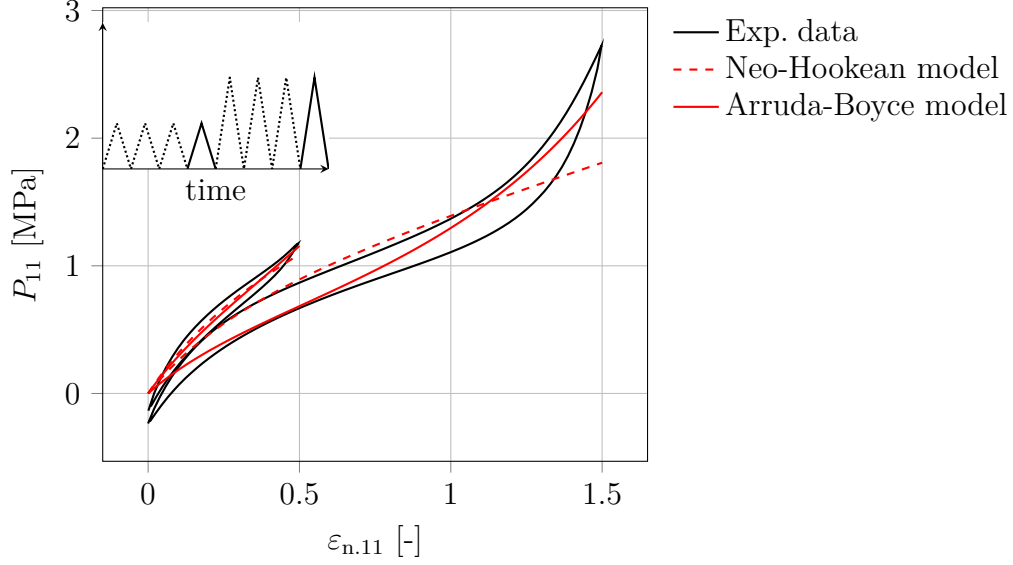
Figure 2.11: Experimental tension data of a filled NR material and its numerical approximation with the neo-Hookean and Arruda-Boyce material model.

	Neo-Hookean	Arruda-Boyce	
Strain range	G [MPa]	G [MPa]	N
$\varepsilon_{n.11} = 50\,\%$	0.9	0.55	2.10
$\varepsilon_{n.11} = 150\,\%$	0.74	0.41	3.13

Table 2.2: Material parameters of the data shown in Figure 2.11.

A material model that is able to capture many of the mechanical behaviour characteristics of rubber is the Plagge material model [15]. In its core, the stresses for a given deformation are defined by:

$$\underline{\underline{\sigma}} = (1 - \phi)\,\underline{\underline{\sigma}}_{\infty} + \phi\,\underline{\underline{\sigma}}_{\text{ve}} \tag{2.41}$$

where the parameter ϕ correlates with the amount of filler in the elastomer. For unfilled rubber $\phi = 0$, negligible viscoelastic properties are assumed; $\underline{\underline{\sigma}}_{\text{ve}}$ has no contribution. The strain energy function for the remaining $\underline{\underline{\sigma}}_{\infty}$ reads:

$$\Psi_{\infty} = \int\limits_{1}^{X_{\max}} P(X)\left(\Psi_{\text{p}}[X(I_1 - 3)] + \Psi_{\text{f}}[X^2(I_1 - 3)]\right)\mathrm{d}X \tag{2.42}$$

with X as amplification factor. The amplification stems from the presence of filler. As briefly discussed in Section 1.1, the filler is present in various aggregate-sizes within the polymer-matrix. The largest aggregates are associated with the strongest amplification ($X_{\max}$). This distribution of filler aggregate-sizes is given by distribution function:

$$P(X) = X^{-\chi}\frac{\chi - 1}{1 - X_{\max}^{1-\chi}} \tag{2.43}$$

with χ describing the shape of this distribution function. The maximum amplification $X_{\max}$ is reduced, associated with breakage of the largest filler aggregates, for newly reached maximum deformations and over time. This decrease of $X_{\max}$ over time describes the linear (in time-log-scale) material softening and is formulated as follows:

$$\dot{X}_{\max} = \exp(-e_{\mathrm{b}}) - \exp\Big(-e_{\mathrm{b}} + v_{\mathrm{b}} \left(\Psi_{\mathrm{p}}[X_{\max}(I_1 - 3)] + \Psi_{\mathrm{f}}[X_{\max}^2(I_1 - 3)]\right)\Big) \qquad (2.44)$$

where e_{b} stands for an energy threshold below which no significant softening occurs and v_{b} additionally scales the two energy functions.

Equation 2.42 contains two energy functions as well. On the one hand, Ψ_{p} models the mechanical response of the pure cross-linked polymer using a simplified version of the extended, non-affine hyperelastic tube-model [15, 16] (original tube-model: [17]):

$$\Psi_{\mathrm{p}} = \frac{G_{\mathrm{c}}}{2} \frac{I_1 - 3}{1 - \frac{1}{n}(I_1 - 3)} \qquad (2.45)$$

where G_{c} stand for the cross-link modulus and n for the elastically active chain length, similar to parameter N from the Arruda-Boyce model. On the other hand, the filler is assumed to behave like a neo-Hookean material with filler modulus G_{f}:

$$\Psi_{\mathrm{f}} = \frac{G_{\mathrm{f}}}{2} \left(I_1 - 3\right) \qquad (2.46)$$

Finally, the visco-elastic portion from Equation 2.41 is defined using the one-dimensional rheological model from Figure 2.12.
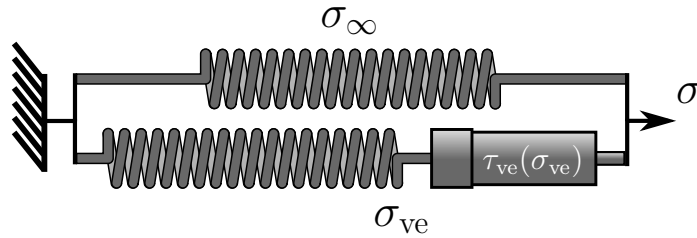
Figure 2.12: Rheological, for the sake of simplicity only one-dimensional, model of the constitutive law (see Equation 2.41) by Plagge [15].

Here the relaxation time τ_{ve} is not a constant but depends on the applied stress:

$$\tau_{\mathrm{ve}} = \tau_{\mathrm{ve.0}} \, \exp\left(-\frac{|\sigma_{\mathrm{ve}}|}{\sigma_{\mathrm{r}}}\right) \qquad (2.47)$$

with $\tau_{\mathrm{ve.0}}$ as initial relaxation time and σ_{r} as stress reduction factor.

Figure 2.13 demonstrates the capabilities of the Plagge-model to describe:

- the nonlinear material response (similar to the neo-Hookean and Arruda-Boyce model);

- the material softening with increasing deformation;

- the material softening with repetition of a constant deformation;

- the hysteresis;

- as well as the remaining deformation with unloading (set).

The interaction of these parameters cause phenomena like the non-constant strain over repeated displacement-controlled duty cycles (see Section 4.2). The Plagge-model will be used to describe this and other effects.
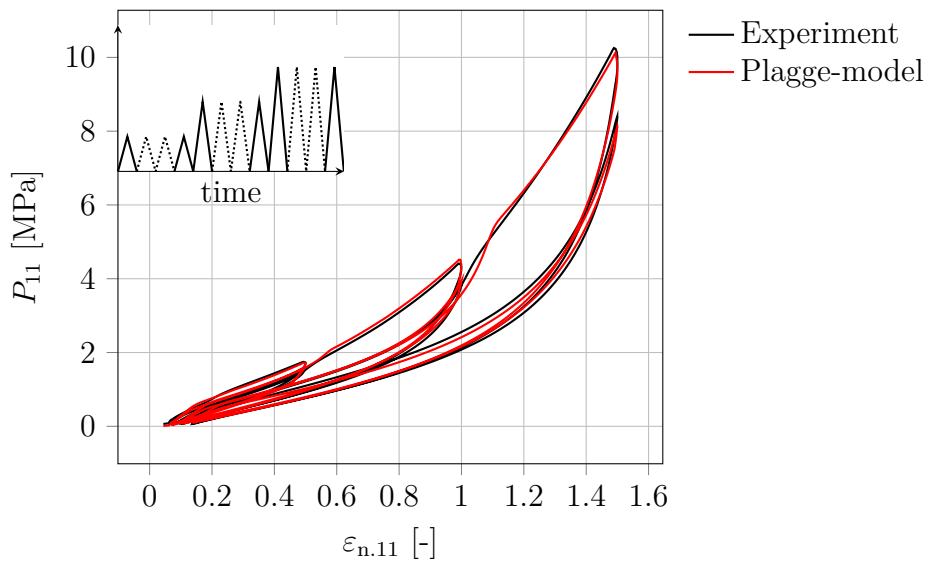
Figure 2.13: Experimental tension data of a rubber material and its numerical approximation with the Plagge-model.

Table 2.3 lists all nine parameter of the Plagge-model with a short description.

No.	Parameter	Description
1	ϕ	filler volume fraction
2	G_c	polymer cross-link modulus
3	G_f	filler modulus
4	n	elastically active chain length
5	χ	shape of filler aggregate distribution function
6	e_b	energy threshold for material softening
7	v_b	energy scale factor
8	$\tau_{ve.0}$	initial relaxation time
9	σ_r	stress reduction factor

Table 2.3: Overview of the parameters of the Plagge-model.

2.3 Statistics evaluation of fatigue test data

The Wöhler concept from Section 1.2 and generally deriving knowledge from fatigue test data only functions along-with a correct statistical evaluation of the experimental data, which have usually a limited sample size. In mechanical fatigue testing of rubber, using exactly the same load conditions, scattering with more than two orders of magnitude in number of cycles to failure is not unusual. This scattering depends on e.g. the material composition. In order to perform valid comparisons of e.g. different materials, the definition and choice of appropriate statistical parameters is crucial. Using the well known arithmetic average, with one or two standard deviations as measure for its *error*, might end in misleading statements.

Figure 2.14 illustrates the difference between a probability density function (PDF) and a cumulative distribution function (CDF). The CDF is here fitted at a sample of ten test pieces. Based on this sample, this CDF describes the failure probability for a chosen number of cycles. The differentiation of the CDF yields the PDF.
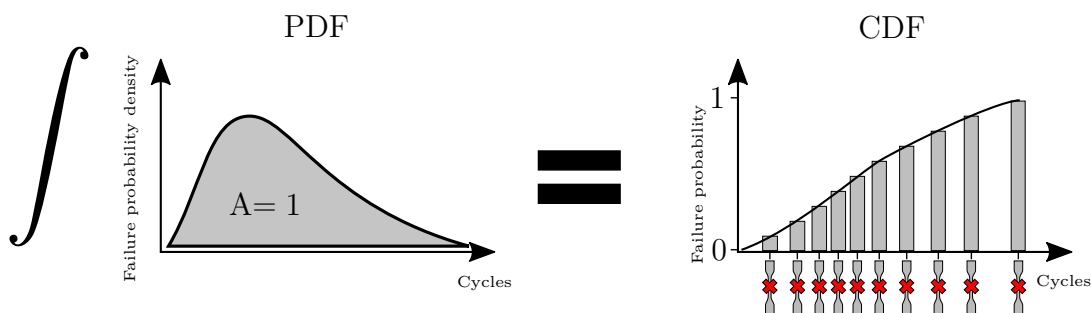

Figure 2.14: Difference between a probability density function (PDF) and a cumulative distribution function (CDF) and their correlation.

2.3.1 Mode, Median, Mean

These three terms are best defined via probability density functions (PDF). The number of cycles until failure for rubber often shows a non-symmetric density distribution. Different midpoint-like values for a later comparison of fatigue data can be defined for non-symmetric distributions. Figure 2.15 visualises the terms mode, median and mean for a sketched non-symmetric probability density function. For symmetric distributions (e.g. Gaussian distribution) these values are all equal.
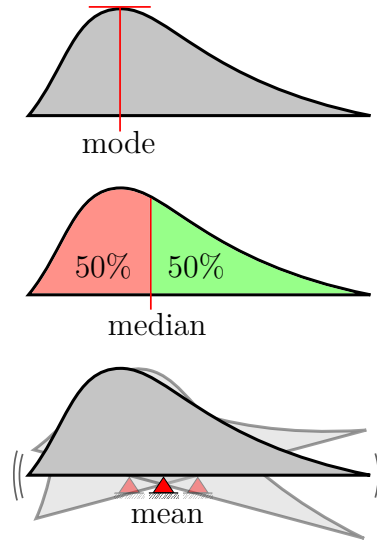
Figure 2.15: Visualisation of the mode, median and mean on an artificial probability density function (referring to [18]).

Only the median value is given for the statistical evaluation of the fatigue tests within this work. Applied to fatigue tests, it describes the number of cycles for which statistically half of the test pieces or components are considered as failed and the other half as still intact. Figure 2.15 visualises the definition of the mode and mean as well to demonstrate the difference among them.

Two of the most commonly used lifetime distributions are the log-normal and Weibull distributions [19]. They are introduced in the following Sections 2.3.3 and 2.3.4, respectively.

2.3.2 The normal distribution

As the foundation of the log-normal distribution, the normal distribution or Gaussian distribution is introduced. Its probability density function (PDF) reads [19]:

$$f_{\text{nor}}(x) = \frac{1}{\sigma_{\text{nor}}\sqrt{2\pi}} \exp\left(-\frac{(x-\mu_{\text{nor}})^2}{2\sigma_{\text{nor}}^2}\right) \tag{2.48}$$

The parameters μ_{nor} and σ_{nor} are endued with a subscripted 'nor' to exclude possible confusions with physical values for the e.g. friction coefficient or mechanical stress. For $\mu_{\text{nor}} = 0$ and $\sigma_{\text{nor}} = 1$ one obtains the PDF of the standard normal distribution f_{stn}.

$$f_{\text{stn}}(z) = \frac{1}{\sqrt{2\pi}} \exp\left(-\frac{z^2}{2}\right) \tag{2.49}$$

Equation 2.48 may be rewritten using the PDF of the standard normal distribution f_{stn}:

$$f_{\text{nor}}(x) = \frac{1}{\sigma_{\text{nor}}\sqrt{2\pi}} \exp\left(-\frac{(x-\mu_{\text{nor}})^2}{2\sigma_{\text{nor}}^2}\right) = \frac{1}{\sigma_{\text{nor}}} f_{\text{stn}}\left[\frac{x - \mu_{\text{nor}}}{\sigma_{\text{nor}}}\right] \tag{2.50}$$

The cumulative distribution function (CDF) of the normal distribution is [19],

$$F_{\text{nor}}(x) = \int\limits_{-\infty}^{x} f_{\text{nor}}(x)\mathrm{d}x = \int\limits_{-\infty}^{x} \frac{1}{\sigma_{\text{nor}}\sqrt{2\pi}}\exp\left(-\frac{(x-\mu_{\text{nor}})^2}{2\sigma_{\text{nor}}^2}\right)\mathrm{d}x \tag{2.51}$$

and with $\mu_{\text{nor}} = 0$ and $\sigma_{\text{nor}} = 1$ the CDF of the standard normal distribution F_{stn} becomes:

$$F_{\text{stn}}(z) = \int\limits_{-\infty}^{z} f_{\text{stn}}(z)dz = \int\limits_{-\infty}^{z} \frac{1}{\sqrt{2\pi}}\exp\left(-\frac{u^2}{2}\right)\mathrm{d}u \tag{2.52}$$

There is no simple closed form for these integrals [19]. Numerical methods are needed to obtain F_{nor} or F_{stn}. Values of F_{stn} are e.g. tabulated in [19]. As previously done for the PDF, one may rewrite the integral in Equation 2.51 using F_{stn}:

$$F_{\text{nor}}(t) = \int\limits_{-\infty}^{x} f_{\text{nor}}(x)\mathrm{d}x = F_{\text{stn}}\left[\frac{x - \mu_{\text{nor}}}{\sigma_{\text{nor}}}\right] \tag{2.53}$$

2.3.3 The log-normal distribution

The normal and standard normal distribution mathematically accept argument values from $-\infty$ to ∞. However, durability measured in number of cycles cannot be negative. This is one reason why fatigue results are better described by the log-normal distribution, which accepts argument values between 0 and ∞.

The probability density function (PDF) of the log-normal distribution is [20],

$$f_{\text{lgn}}(x) = \frac{1}{\sigma_{\text{lgn}}x\sqrt{2\pi}}\exp\left(-\frac{(\ln x-\mu_{\text{lgn}})^2}{2\sigma_{\text{lgn}}^2}\right) \tag{2.54}$$

and the corresponding CDF:

$$F_{\text{lgn}}(t) = \int\limits_{0}^{t} f_{\text{lgn}}(x)\mathrm{d}x = \int\limits_{0}^{t} \frac{1}{\sigma_{\text{lgn}}x\sqrt{2\pi}}\exp\left(-\frac{(\ln x-\mu_{\text{lgn}})^2}{2\sigma_{\text{lgn}}^2}\right)\mathrm{d}x \tag{2.55}$$

Similar to the normal distribution, the CDF of the log-normal distribution may be defined with the standard normal distribution (see Figure 2.52):

$$F_{\text{lgn}}(t) = F_{\text{stn}}\left[\frac{\ln t - \mu_{\text{lgn}}}{\sigma_{\text{lgn}}}\right] \tag{2.56}$$

In order to calculate the median of the log-normal distribution Φ_{lgn}, the inverse log-normal CDF $F_{\text{lgn.inv}}$ can be used. The median value, as shown in Figure 2.15, is given by:

$$\Phi_{\text{lgn}} = F_{\text{lgn.inv}}[50\,\%] \tag{2.57}$$

As for the log-normal CDF F_{lgn}, there is no simple closed form for $F_{\mathrm{lgn.inv}}$. Its solution can be determined numerically or is documented for certain probability values in tables (e.g. in [19]). Alternatively, the median of the log-normal distribution Φ_{lgn} can be calculated from the parameter μ_{lgn}:

$$\Phi_{\mathrm{lgn}} = e^{\mu_{\mathrm{lgn}}} \tag{2.58}$$

Estimate of μ_{lgn} and σ_{lgn}

A possible way to obtain estimates of μ_{lgn} and σ_{lgn} is to first linearise the CDF of the log-normal distribution [21]:

$$F_{\mathrm{stn.inv}}(P_{\mathrm{lgn.s}}) = \frac{1}{\sigma_{\mathrm{lgn}}} \ln(t) - \frac{\mu_{\mathrm{lgn}}}{\sigma_{\mathrm{lgn}}} \tag{2.59}$$

with $P_{\mathrm{lgn.s}}$ as an estimated probability. This estimated probability $P_{\mathrm{lgn.s}}$, e.g. for a presumed log-normal distribution, is [22]:

$$P_{\mathrm{lgn.s}} = \frac{3i - 1}{3n + 1} \tag{2.60}$$

The data of the taken sample are sorted in ascending order. Where in Equation 2.60 n stands for the sample size and i the position within the sorted data of the sample. Figure 2.16 shows an example of a linear regression of $F_{\mathrm{stn.inv}}(P_{\mathrm{lgn.s}})$ over $\ln(\text{Cycles})$ with $n = 12$.
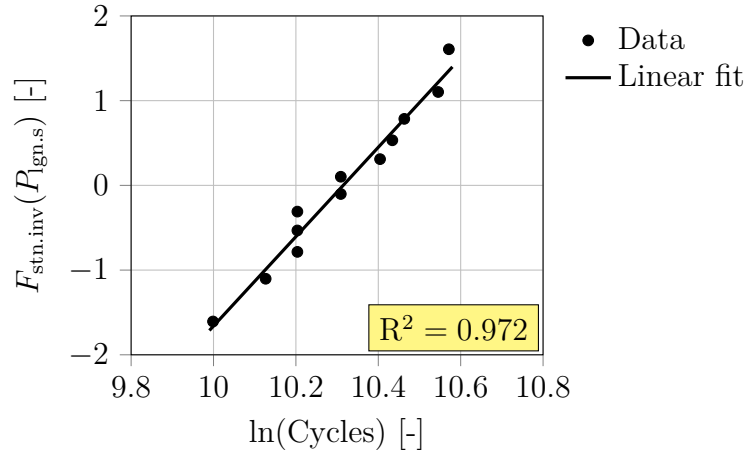
Figure 2.16: Linear regression of a sample with $n = 12$ within the linear environment based on Equation 2.59.

From the parameters of this linear regression, the estimates $\mu_{\mathrm{lgn.s}}$ and $\sigma_{\mathrm{lgn.s}}$, are calculated based on Equation 2.59. Additionally, the goodness of the linear regression provides information about how well the sample is approximated by the log-normal distribution. The shown data are a sample of the unknown population. Thus, the resulting $\mu_{\mathrm{lgn.s}}$ and

$\sigma_{\text{lgn.s}}$ are only estimates of the real, but always unknown (population based), parameters μ_{lgn} and σ_{lgn}. For this reason, a declaration of confidence limits to these estimates is mandatory.

Confidence limits for the median

Pivotal quantities are essential for the determination of confidence limits. A pivotal quantity is a random variable whose distribution does not depend on unknown parameters (see e.g. [23]). Further, the resemblance of the log-normal distribution to the Gaussian (normal) distribution is used again. For the normal distribution the unknown parameters are here the two parameters σ_{nor} and μ_{nor} of the population. The pivotal quantity for the normal distribution is given by [23]:

$$p_{\text{nor}}(n) = \frac{\mu_{\text{nor.s}} - \mu_{\text{nor}}}{\sigma_{\text{nor.s}}}\sqrt{n} \qquad (2.61)$$

with $\mu_{\text{nor.s}}$ and $\sigma_{\text{nor.s}}$ as estimates of the normal distribution parameters, based on a sample with sample size n. Figure 2.17 shows the corresponding estimates of 1000 random normal distributed samples of sample size n with given $\mu_{\text{nor}} = 0$ and $\sigma_{\text{nor}} = 1$. This deviation of $\mu_{\text{nor.s}}$ and $\sigma_{\text{nor.s}}$ from the given $\mu_{\text{nor}} = 0$ and $\sigma_{\text{nor}} = 1$ is independent from the, in reality, unknown population based μ_{nor} and σ_{nor} described by the pivotal quantity $p_{\text{nor}}(n)$. It is therefore unique for the normal distribution based estimates $\mu_{\text{nor.s}}$ and $\sigma_{\text{nor.s}}$.
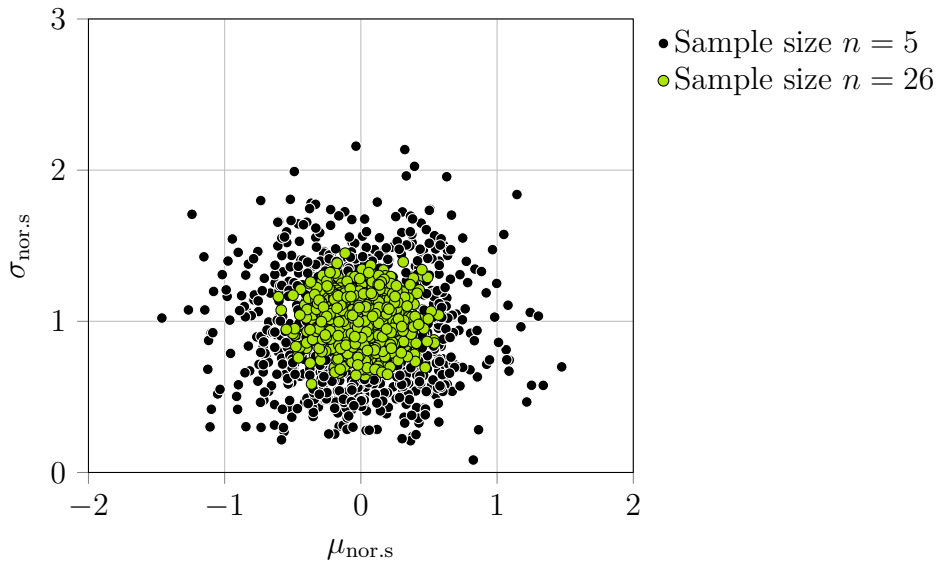

Figure 2.17: The sample standard deviation $\sigma_{\text{nor.s}}$ over the sample expectation $\mu_{\text{nor.s}}$ from 1000 normal distributed samples of size $n = 5$ and $n = 26$.

The Student's t distribution describes the behaviour of $p_{\text{nor}}(n)$ [24]. In case the 1000 corresponding values of p_{nor} are arranged according to size and are depicted in 1/1000 probability steps, the numerical Student's t cumulative distribution function $T_{\text{num}}()$ is

obtained.

Figure 2.18 shows $T_{\text{num.inv}}$ for the sample size n varied from $n = 2$ to $n = 26$ with step size 3. Additionally, the standard normal inverse CDF is depicted. The Student's t distribution approaches the standard normal distribution with increasing sample size [25].
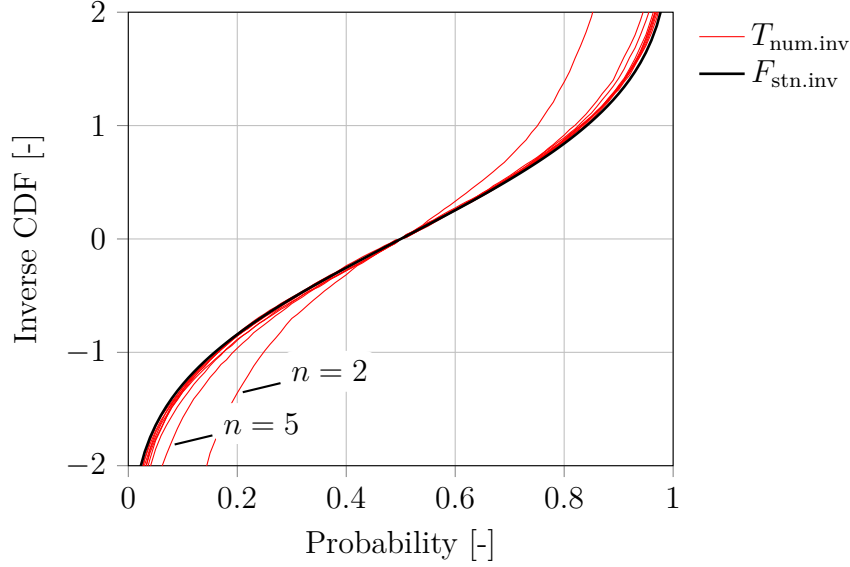
Figure 2.18: Numerically determined Student's t CDF with varied sample size n and the standard normal CDF $F_{\text{stn.inv}}$.

The upper and lower confidence limits for $\Phi_{\text{lgn.s}}$ are, respectively [19]:

$$\tilde{\Phi}_{\text{lgn.s}} = \exp\left(\ln\Phi_{\text{lgn.s}} + T_{\text{num.inv}}\left[\frac{1 + Probability}{2}, n\right]\frac{\sigma_{\text{lgn.s}}}{\sqrt{n}}\right) \tag{2.62}$$

$$\underset{\sim}{\Phi}_{\text{lgn.s}} = \exp\left(\ln\Phi_{\text{lgn.s}} - T_{\text{num.inv}}\left[\frac{1 + Probability}{2}, n\right]\frac{\sigma_{\text{lgn.s}}}{\sqrt{n}}\right) \tag{2.63}$$

With n as the sample size and $T_{\text{num.inv}}[\text{Input}_1, \text{Input}_2]$ as the Student's t inverse CDF. Since a two sided restriction is assumed, the term $\frac{1 + Probability}{2}$ is needed for Input_1 [19]. The parameter *Probability* describes with which likelihood the true (population based $\rightarrow$unknown) median is located within these confidence limits.

2.3.4 The two parametric Weibull distribution

The probability density function (PDF) of the Weibull distribution is given by [26, 27]:

$$f_{\text{WB}}(x) = \frac{\beta}{\eta}\left(\frac{x}{\eta}\right)^{\beta-1}\exp\left(-\left(\frac{x}{\eta}\right)^{\beta}\right) \tag{2.64}$$

In contrast to the normal or log-normal distribution, the cumulative distribution function (CDF) of the Weibull distribution can be given in closed analytical form:

$$F_{\text{WB}}(t) = \int_0^t f(x)\mathrm{d}x = 1 - \exp\left(-\left(\tfrac{t}{\eta}\right)^\beta\right) \tag{2.65}$$

with β as the so-called shape parameter and η as the scale parameter. The scale parameter η describes the number of cycles for which $63.2\,\%$ of the test pieces/components are failed:

$$F_{\text{WB}}(x = \eta) = 1 - \exp\left(-\left(\tfrac{\eta}{\eta}\right)^\beta\right) = 1 - \exp\left(-1\right) \approx 0.632 \tag{2.66}$$

Weibull's median $F_{\text{WB}}(t) = 0.5$ is given by:

$$\Phi_{\text{WB}} = F_{\text{WB.inv}}(0.5) = \eta(-\ln(0.5))^{1/\beta} \tag{2.67}$$

Estimate of η and β

Similar to the normal or log-normal distribution, estimates of η and β can be determined with a linear fit of the linearised Weibull CDF [20]:

$$\ln(-\ln(1 - P_{\text{s.WB}})) = \beta_{\text{s}} \ln(x) - \beta_{\text{s}} \ln(\eta_{\text{s}}) \tag{2.68}$$

The estimated probability $P_{\text{WB.s}}$, for sample size $n < 50$, is given by the so called Benard-method [28]:

$$P_{\text{WB.s}} = \frac{i - 0.3}{n + 0.4} \tag{2.69}$$

As for the log-normal distribution (see Section 2.3.3), i stands for the position within the sorted data of the sample.

Alternatively, the shape parameter β_{s} can be derived by solving a maximum likelihood equation, defined as [29]:

$$0 = \left(\sum_{i=1}^n x_i^{\beta_{\text{s}}}\right) \cdot \left(\frac{1}{\beta_{\text{s}}} + \frac{1}{n}\sum_{i=1}^n \ln(x_i)\right) - \sum_{i=1}^n x_i^{\beta_{\text{s}}} \ln(x_i) \tag{2.70}$$

With the known estimate β_{s}, the scale parameter η_{s} is given by [29]:

$$\eta_{\text{s}} = \left(\frac{1}{n}\sum_{i=1}^n x_i^{\beta_{\text{s}}}\right)^{1/\beta_{\text{s}}} \tag{2.71}$$

Confidence limits for the median

For the calculation of the confidence limits of the Weibull median, the pivotal quantities of the Weibull distribution are used. The pivotal quantity related to the scale parameter η is given by [29]:

$$p_{\text{WB}}(p,n) = \beta_{\text{s}} \ln \left(\frac{F_{\text{WB.inv}}(\eta_{\text{s}}, \beta_{\text{s}}, p)}{F_{\text{WB.inv}}(\eta, \beta, p)} \right) = \beta_{\text{s}} \ln \left(\frac{\eta_{\text{s}}(-\ln(1-p))^{1/\beta_{\text{s}}}}{\eta(-\ln(1-p))^{1/\beta}} \right) \tag{2.72}$$

and for the shape parameter β:

$$p_{\text{WB.2}}(n) = \frac{\beta_{\text{s}}}{\beta} \tag{2.73}$$

with failure probability p. The probability is set at $p = 0.5$ in order to calculate the confidence limits at the median. In order to determine the scatter behaviour of β_{s} and η_{s} for given β and η, here 10 000 samples are generated with sample size n, for given scale parameter $\eta = 1$ and shape parameter $\beta = 1$. After sizing the 10 000 pivotal quantities $p_{\text{WB}}(p,n)$, the upper and lower confidence limits for the median Φ_{WB} are defined by [29]:

$$\tilde{\Phi}_{\text{WB.s}} = F_{\text{WB.inv}}(0.5) \cdot \exp \left(-\frac{p_{\text{WB}} \left[\frac{(1-Probability)}{2}, n \right]}{\beta_{\text{s}}} \right) \tag{2.74}$$

$$\underset{\sim}{\Phi}_{\text{WB.s}} = F_{\text{WB.inv}}(0.5) \cdot \exp \left(-\frac{p_{\text{WB}} \left[\frac{(1+Probability)}{2}, n \right]}{\beta_{\text{s}}} \right) \tag{2.75}$$

The parameter *Probability* is the likelihood of the unknown population based Φ_{WB} to be located within $\tilde{\Phi}_{\text{WB.s}}$ and $\underset{\sim}{\Phi}_{\text{WB.s}}$.

2.3.5 Principal of Sudden-death testing using the Weibull distribution

Sudden-death testing describes the parallel testing of a group of identical test pieces. If one of the test pieces within this group fails, the test is considered as completed. Saving testing time is the main motivation behind sudden-death testing. Fatigue test data originating from this method are biased with respect to *one by one*-results. In order to compare sudden-death-based results with standard results, this bias needs to be considered. In the present work, this concept is adopted to enable the comparison of test pieces with different volumes. Details to this adoption will be given in Section 4.3.

A transformation can be given for CDFs based on *one by one*-tested test pieces to CDFs based on group or sudden-death tests [30]:

$$F_{\text{group}}(t) = 1 - (1 - F_{\text{single}}(t))^{n_{\text{group}}} \tag{2.76}$$

With n_{group} as the number of test pieces within the sudden-death group. For the case of given sudden-death data, a transformation to *one by one*-tested test pieces can be

conducted with the transposed Equation 2.76:

$$F_{\text{single}}(t) = 1 - (1 - F_{\text{group}}(t))^{1/n_{\text{group}}} \tag{2.77}$$

Equation 2.76 provides the transformation from *one by one* to group tested components or test pieces:

$$
\begin{aligned}
F_{\text{WB.group}}(t) &= 1 - (1 - F_{\text{WB.single}}(t))^{n_{\text{group}}} \\
&= 1 - \left(1 - \left(1 - \exp\left(-\left(\tfrac{t}{\eta}\right)^{\beta}\right)\right)\right)^{n_{\text{group}}} = 1 - \exp\left(-\left(\tfrac{n_{\text{group}}^{1/\beta} t}{\eta}\right)^{\beta}\right)
\end{aligned} \tag{2.78}
$$

The shape parameter β stays unaffected by the transformation from single to group tested data ($\beta_{\text{single}} = \beta_{\text{group}}$). Only the scale parameter η varies:

$$1 - \exp\left(-\left(\tfrac{t}{\eta_{\text{group}}}\right)^{\beta}\right) = 1 - \exp\left(-\left(\tfrac{n_{\text{group}}^{1/\beta} t}{\eta_{\text{single}}}\right)^{\beta}\right) \tag{2.79}$$

$$\eta_{\text{group}} = \eta_{\text{single}} \cdot n_{\text{group}}^{-1/\beta} \tag{2.80}$$

For the case of measured sudden-death group data and the need to calculate η_{single} for the virtual *one by one* test case, Equation 2.77 is applied:

$$\eta_{\text{single}} = \eta_{\text{group}} \cdot n_{\text{group}}^{1/\beta} \tag{2.81}$$

The median for the *one by one* case is defined, by use of Equation 2.81, as:

$$\Phi_{\text{WB.single}} = F_{\text{WB.single.inv}}(0.5) = \eta_{\text{group}} \cdot n_{\text{group}}^{1/\beta_{\text{group}}} \cdot (-\ln(0.5))^{1/\beta_{\text{group}}} \tag{2.82}$$

Sudden-death testing and confidence limits

In order to determine the sudden-death based confidence limits for the median of the Weibull distribution $\Phi_{\text{WB.single}}$, a modified pivotal function $p_{\text{WB.SD.1}}$ is needed. The shape parameter β related to the pivotal function $p_{\text{WB.2}}$ (see Equation 2.73), stays unaffected by the sudden-death transformations like the shape parameter β itself. The pivotal function $p_{\text{WB.SD.1}}$ is defined in [29] as:

$$p_{\text{WB.SD.1}}(p, n, n_{\text{group}}) = (1 - p_{\text{WB.2}}(n)) \ln(n_{\text{group}}) + p_{\text{WB.1}}(p, n) \tag{2.83}$$

The confidence limits for $\Phi_{\text{WB.single}}$ are:

$$\tilde{\Phi}_{\text{WB.single.s}} = F_{\text{WB.single.inv}}(0.5) \cdot \exp\left(-\frac{p_{\text{WB.SD.1}}\left[\frac{(1-Probability)}{2}, n\right]}{\beta_{\text{s}}}\right) \tag{2.84}$$

$$\Phi_{\text{WB.single.s}} = F_{\text{WB.single.inv}}(0.5) \cdot \exp\left(-\frac{p_{\text{WB.SD.1}}\left[\frac{(1+Probability)}{2}, n\right]}{\beta_{\text{s}}}\right) \tag{2.85}$$

3 Effects of temperature, cyclic loading, test piece geometry and dwell periods with focus on mechanical fatigue: State of the Art

The fatigue of rubber attracted a lot of scientific attention since one of the first studies from Cadwell et al. in 1940 [6]. In 2002 and 2004 Mars et al. published articles with the title *"A literature survey on fatigue analysis approaches for rubber"* [31] and *"Factors that affect the fatigue life of rubber: A literature survey"* [32]. Summed up, these two articles contain 243 citations with a certain but negligible overlap. Yun Lu Tee et al. [33] resumed this fatigue focused literature survey reviewing articles published between 2002 and 2018 (period of 16 years). They cite 198 articles, leading to 441 publications about rubber fatigue since Cadwell in 1940 to Yun Lu Tee in 2018. For this reason, sometimes only substitute-like publications are cited with a large amount of, existing but not cited, articles concluding similar statements.

3.1 Fatigue influence of temperature

Self-heating with cyclic deflection of test pieces made from filled rubber is inevitable due to the significant amount of lost energy within the material combined with its low thermal conductivity.

Already in one of the very first systematic investigations of filled natural rubber fatigue, the influence of the test piece temperature (range $-28\,°C$ to $60\,°C$) on lifetime was in focus [6]. The research on temperature and its implication on fatigue is still ongoing as evident by current projects (see e.g. [34, 35]). A. G. James measured a decrease in lifetime with two orders of magnitude for a temperature raise from $-30\,°C$ to $30\,°C$ for different SBR formulations [36]. With focus on NR, Charrier et el. performed a study on NR for a temperature range of $10\,°C$ to $102\,°C$ [37] and found a corresponding decrease in lifetime of about one order of magnitude. These studies demonstrate the significant influence of the material temperature on the fatigue and highlight the need to consider this factor in fatigue measurements. In the study of Ruellan et al. [38] a lot of effort is invested in the experimental database containing NR based Haigh diagrams (iso-lifetime curves in an amplitude-mean-load plot) for $23\,°C$, $90\,°C$ and $110\,°C$. They describe the challenges to ensure equivalent test piece temperatures within the three chosen ambient temperatures. The objective of the present work is not to study the influence of the temperature on the

fatigue of rubber, instead, the test piece temperature shall be held as constant as possible for all tests among the experimental databases in the subsequent chapters. An approach to ensure equivalent test piece temperatures is introduced in Section 4.1.

3.2 Effects of cyclic loading on rubber vulcanisates and its implication in fatigue tests

A state of the art of relaxation effects during cycling loading and awareness of their significance in fatigue tests on rubber shall be given. The intention is not to discuss fatigue testing in general, such as is available elsewhere [31, 32, 39].

Cyclic creep is an established phenomenon; for example, numerous studies (see e.g. [40, 41]) of it have been made for metallic materials. One of the first systematic investigations of the behaviour of rubber under prolonged cyclic loading was performed by Derham and Thomas in 1976 [42]. They revealed very much more creeping in the case of cyclic loading of their filled NR than would be anticipated from the static creep. The majority of this phenomenon was explained by rubber network reorganisation and permanent internal rupture caused by NR's significant ability to crystallise. Since, after the cyclic creep test with 50 cycles, swelling in solvent and then de-swelling the rubber failed to result in recovery to the virgin behaviour, they concluded that permanent internal rupture of the rubber network caused this effect. In contrast for static creep tests, swelling and then de-swelling resulted in full recovery of the rubber, indicating a purely topological basis of the creep. Derham and Thomas [42] did not elucidate the relative contributions of changes to the unstressed configuration (i.e. set) and of reduction in modulus to the phenomenon of enhanced creep caused by cyclic loading. Comparative cyclic creep tests by Davies et al. with SBR and NR showed a smaller effect for the SBR based material [43]. Pond and Thomas investigated the cause of the phenomenon for SBR using swelling. They found that half of the cyclic creep of SBR can be explained by breakage of crosslinks and that the other half probably originates from viscoelastically recoverable deformation [44]. Kingston and Muhr [45] studied the effects of the shape of the loading-waveform, frequency and minimum strain on the cyclic stress relaxation of filled and unfilled NR. They used nominal simple shear, a near-homogeneous deformation, so that differential effects in the test piece would have been very small.

Fatigue test pieces commonly contain a region of high deformation, wherein fatigue is intended to be intensified and studied. This region is typically as far as necessary away from the relatively lightly loaded regions of clamping or bonding to metal end-fixtures (see Section 3.3). The intention is to avoid initiation of the failure in the complicated and uncertain stress-field induced in the region of the clamps or bonding. However, a design like this causes loading inhomogeneities within the test piece, leading to the possibility of different rates of modulus reduction and set in the different regions, hence resulting in a

redistribution of stress [42]. The effect of shifting strain over cyclic deflection is considered in Standards e.g. ASTM D4482-11 [46] or ISO 6943 [47] for the fatigue determination of 2D-dumbbells. The former Standard recommends a measurement of the maximum strain and set at 1000 cycles only. However, the ISO 6943 suggests the measurement of the maximum strain and the set at every tenfold increase in the strain cycle count. The data of these measurements are incorporated in Equation 3.1 in ISO 6943 giving the maximum strain [47], reproduced here:

$$\varepsilon_N = \frac{L_N - l_N}{l_N} \tag{3.1}$$

cited from ISO 6943 [47]: *where, for dumbbell test pieces:*

l_N *is the unstrained reference length after the test piece has been fatigued for N cycles;*

L_N *is the distance between the reference lines at maximum clamp separation after the test piece has been fatigued for N cycles.*

However, ISO 6943 gives little guidance on how to take into account the evolution of the maximum strains ε_N in lifetime prediction using a Wöhler curve.
Narynbek Ulu et al. developed a concept for real stress controlled fatigue testing [39]. Even if not the main focus of their work, a discussion of the strain evolution over the cyclic loading is also given. It is stated that the strain decreases over repeated loading. This statement originates from the idea to always refer the reference length within the strain calculation to the unstressed configuration of the material. Thanks to the typical continuously increasing set, the reference length (at zero stress) also increases. A decreasing strain is the consequence in their theoretical deliberations.

3.3 Uniaxial fatigue test pieces

One may be surprised by the big variety of test piece geometries to measure one material property only: the fatigue for uniaxial deformation. In the early study of Cadwell et al. [6] multiple test piece geometries are used (see Figure 3.1). These test pieces were cyclically loaded along their symmetry axis until rupture. However, Cadwell et al. do not differentiate within this large amount of test piece shapes when evaluating their fatigue data.
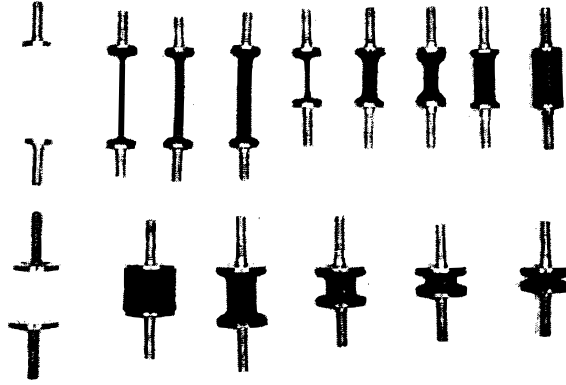
**Figure 3.1:** Test pieces geometries used by Cadwell et al. in [6].

Since Cadwell et al., many more studies followed focusing on different aspects of the fatigue behaviour of rubber using other test piece geometries. A common test piece used in the subsequent years is the 2D-dumbbell test piece (see Figure 3.2). This geometry has been used by, for example, Roberts and Benzies [48]. The 2D-dumbbell geometry is also suggested for fatigue testing of rubber by the Standards e.g. ASTM D4482 [46] or ISO 6943 [47].
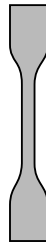
Figure 3.2: 2D-dumbbell test piece geometry.

The 2D-dumbbell test piece has beneficial properties in terms of low self-heating under cyclic loading thanks to the big surface area to volume ratio. The test piece is typically die-cut from a rubber sheet.

The rotationally symmetric version of the 2D-dumbbell is depicted in Figure 3.3. It is e.g. used by Abraham [49, 50] or Gehrmann et al. [51] to investigate in fatigue-influence of non-relaxing loadings on a synthetic elastomer. Compared to the 2D-dumbbell, the 3D-dumbbell has a significantly lower surface area to volume ratio, causing an increased heat build-up for equal amplitudes and frequencies.
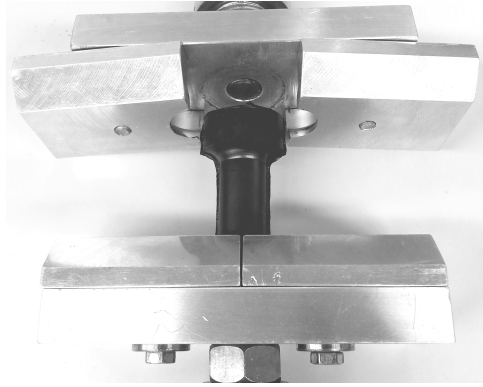
Figure 3.3: 3D-dumbbell test piece and its fixture.

As detailed in [32], there are many factors impacting the fatigue of rubber products. Several publications fatigued the two test piece geometries shown in Figure 3.4 to investigate the impact of these factors. Some of these studies were aimed to compare different fatigue predictors [52–60].
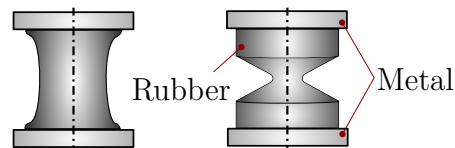

Figure 3.4: Diabolo and AE2 test piece.

The fatigue test piece in Figure 3.5 is related to the ones from Figure 3.4. It is e.g. applied in the studies from Flamm et al. [61].

Figure 3.5: Another diabolo-like test piece geometry.

Mars [62] carried out experimental work on multiaxial fatigue of strain-crystallising and non-crystallising rubber, using a test piece published in [63] (see Figure 3.6). This test piece does not exhibit distinct uniaxial deformation conditions at the locus of failure initiation. Nevertheless, it is listed due to its purpose to initiate cracks at the outer surface.

The database created by Mars [62] was used by other authors for the validations of fatigue predictors e.g. [64, 65].
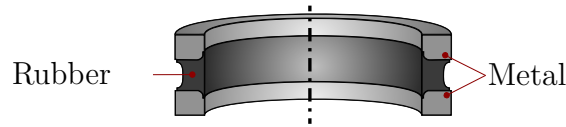

Figure 3.6: Ring test piece by Mars and Fatemi [63]. This schematic sketch shows only the half of the axis-symmetric test piece.

Yun Lu Tee et al. [33] give an overview of fatigue test pieces and their use in research published between 2002 and 2017. The most prominent geometries are shown in Figure 3.2 to 3.5. Besides these, Yun Lu Tee et al. mention a few more geometries. All test piece shapes shown in Figure 3.1 to 3.6 and listed in [33] are united by their propensity to failure initiation with locus at the surface.

Fatigue results from cracks initiating at the surface of the test piece may be significantly influenced by the surface finish of the mould or the properties of the partition lines or flash, which may create unexpected critical flaws at the surface.

A short clarification on the terminology *mould partition line* and *flash*: typically a vulcanisation mould has one or more partitions. The area of such mould partition that is in contact with the moulding made from rubber during the vulcanisation process, may be called mould partition line. The consequences of the mould partition line for the moulding, is a surface imperfection that might be a protrusion, and might be termed as flash.

These surface flaws introduce a variability that may significantly alter the fatigue behaviour of rubber and hence the accuracy of the corresponding lifetime estimates (see Section 1.2). Additionally, many real life components fail thanks to internally crack initiation [66]. Motivated by this observation, a uniaxial test piece with internal crack initiation was proposed by Brüger et al. (see Figure 3.7) [66]. The convex metallic inserts cause a concentration of the maximum deformation, when deformed along the symmetry axis, in the bulk of the test piece (see red region in Figure 3.7-a).
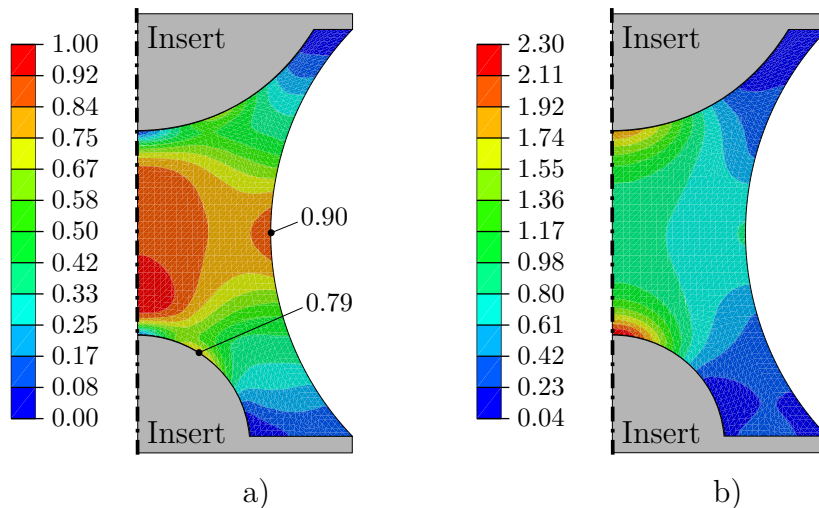
Figure 3.7: a) Maximum principal nominal strain $\varepsilon_{\text{n.max}}$ [-] and b) hydrostatic stress σ_0 [MPa] mapped on the non-deformed geometry.

However, for fully relaxing tensional loadings $R_{\text{u}} = {}^{d_{\sim.\text{min}}}/_{d_{\sim.\text{max}}} = 0$, the cracks initiate close to the insert (see Figure 3.7-a, spot labelled with 0.79) even if the local deformation at this spot is significantly lower ($\varepsilon_{\text{n.max}} = 0.79$) compared to the deformation at the centre of the bulk ($\varepsilon_{\text{n.max}} = 1.0$). The variables $d_{\sim.\text{min}}$ and $d_{\sim.\text{max}}$ stand for the minimum and maximum global deflection within a sinusoidal loading, respectively. In case of pure compressive loadings ($R_{\text{u}} = -\infty$), crack initiation in the centre of the test piece can be found. The spot of crack initiation for $R_{\text{u}} = -\infty$ is exposed to an equibiaxial deformation and for $R_{\text{u}} = 0$ to a shearing deformation state [66]. This spot at the insert is close to a region of hydrostatic loading (see Figure 3.7-b). An influence by cavitation effects on the failure of the test piece cannot be excluded [67]. Gent summarises the phenomenon called cavitation to:

If a rubber vulcanisate is subjected to a hydrostatic tension – that is, all three principal stresses are equal and tensile – then failure may take place by what appears to be a different mechanism, namely cavitation.

In order to justify a redevelopment of a test piece based on the Brüger geometry (see Section 4.3), a short assessment of the cavitation-risk is conducted. For the FE results shown in Figure 3.7 the neo-Hookean material model with a shear modulus $G = 0.8\,\text{MPa}$ is used (see Section 2.2). According to Ball [68] and Gent [67, 69] cavitation occurs for hydrostatic stresses greater than the critical hydrostatic stress $\sigma_{0.\text{crit}}$:

$$\sigma_{0.\text{crit}} = 5/6 \cdot E \tag{3.2}$$

For the chosen shear modulus ($G = 0.8\,\text{MPa}$), a critical hydrostatic stress of $\sigma_{0.\text{crit}} = 2\,\text{MPa}$ is calculated. As shown in Figure 3.7, the hydrostatic stress with $\sigma_0 = 2.3\,\text{MPa}$ exceeds $\sigma_{0.\text{crit}}$. For this reason, the crack initiation might be influenced by cavitation

effects for the given deflection.

Further on, for cases among which the numerical analysis is performed with the Plagge material model, the Young's modulus E is calculated from the initial shear modules at the tenth load cycle for $\varepsilon_{\mathrm{n.max}} < 5\,\%$.

3.4 Fatigue-influence of dwell periods

The new developed test piece from Section 4.3 shall not only be compared with other test piece geometries but also support the investigation of a possibly fatigue-influencing factor, namely dwell periods in an otherwise pure sinusoidal load signal.

In order to discuss the existing literature, the nomenclature from Harbour et al. is inherited [70], as shown in Figure 3.8.
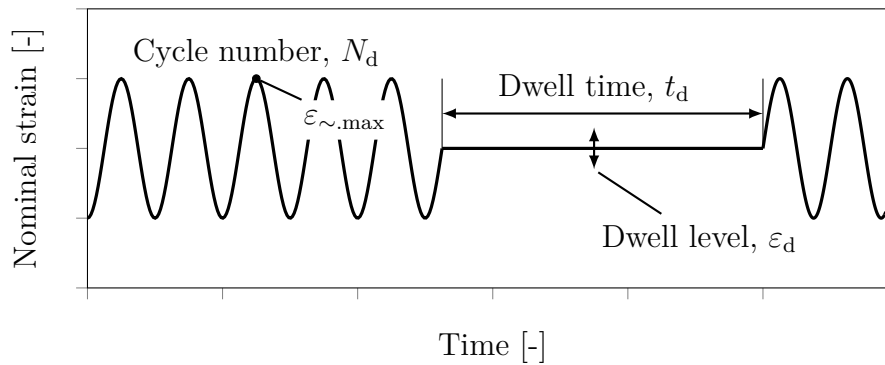
Figure 3.8: Nomenclature for fatigue testing with dwell periods (referring to [70]).

In reality, dynamic loads are not perfect continuously sinusoidal by nature. Motivated by this, Roland and Sobieski studied the influence of long dwell periods ($t_{\mathrm{d}} = 24\,\mathrm{h}$ - $t_{\mathrm{d}} = 72\,\mathrm{h}$) within a durability test on the fatigue behavior of rubber [71]. They found the maximum impact, a reduction of lifetime by factor 3 to 3.5 for unfilled NR and polyisoprene rubber (IR) for nearly unloaded ($\varepsilon_{\mathrm{d}} = 0.1 \cdot \varepsilon_{\sim.\mathrm{max}}$) dwell periods. In the case that $\varepsilon_{\mathrm{d}} = \varepsilon_{\sim.\mathrm{max}}$, the same or an even slightly greater lifetime compared to continuous periodic oscillation test was measured. Both effects were not detectable for their filled NR. Filled IR was not subject of their investigations.

Harbour et al. studied the impact of dwell periods on the crack growth rate of carbon black filled SBR and NR materials [70]. In detail, they investigated the influence of the parameters dwell time t_{d}, dwell level ε_{d} and number of cycles N_{d} between the dwell periods (see Figure 3.8). The crack growth tests were conducted at pure shear test pieces (dimension: width=150 mm, height=12.5 mm, thickness=1 mm) with a peak strain level of $\varepsilon_{\mathrm{d}} = 27.5\,\%$. Figure 3.9 shows a rapid increase of the crack growth rate with increasing dwell time t_{d}. This increase slows down to a near plateau-like behaviour for dwell times

$t_d > 10\,$s. In agreement with the results of Roland and Sobieski [71], Figure 3.10 shows an increasing crack growth rate with decreasing dwell level ε_d. The correlation, decreasing number of cycles between dwell periods N_d increases the lifetime, is shown in Figure 3.11. For the condition $N_d = 5$, $t_d = 10\,$s and $\varepsilon_d \approx 10\,\%$ a variation of the cyclic frequency from $0.5\,$Hz to $3.5\,$Hz did not impact the crack growth rate.

Within the investigation of Harbour et al. the dependency of the crack growth rate on the dwell time t_d for a fixed ratio between N_d and t_d was not studied.
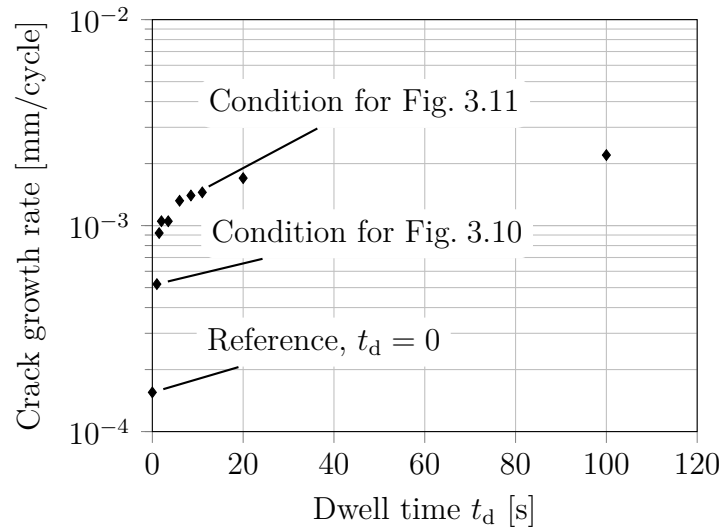
Figure 3.9: Carbon black filled SBR: Experimental data points of the crack growth rate over dwell time t_d (referring to [70]); Material: carbon black filled SBR; Constant parameters: $N_d = 5$ and dwell level $\varepsilon_d \approx 10\,\%$.
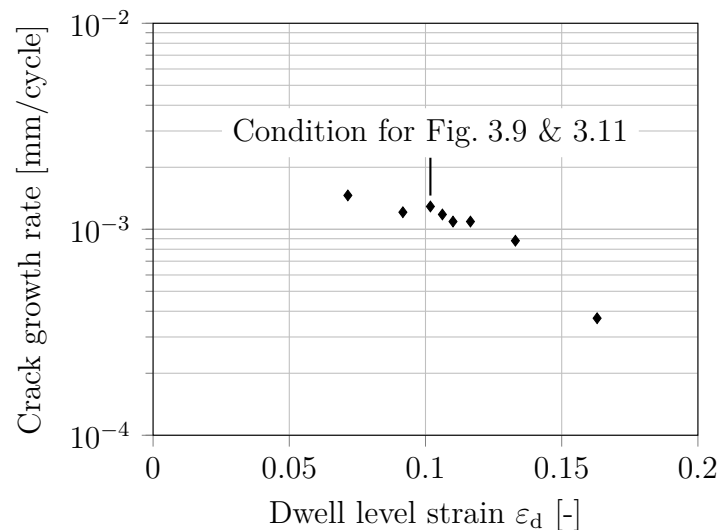
Figure 3.10: Carbon black filled SBR:Experimental data points of the crack growth rate over dwell level ε_d (referring to [70]); Constant parameters: dwell time $t_d = 1\,$s and $N_d = 5$.
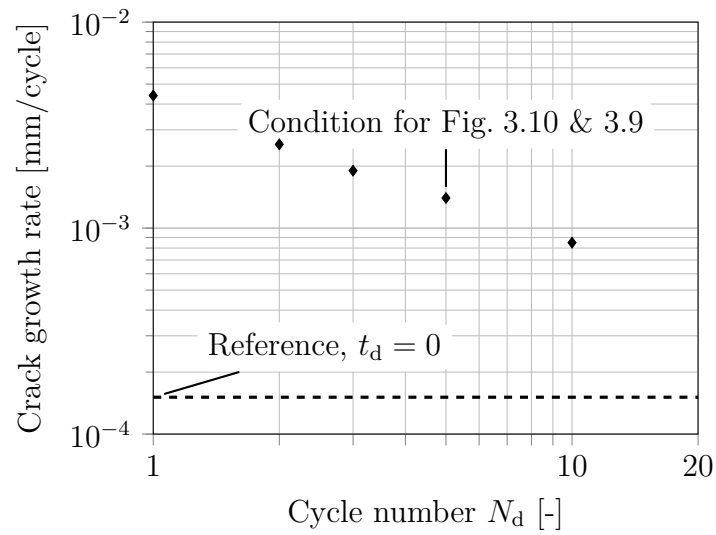
Figure 3.11: Carbon black filled SBR: Experimental data points of the crack growth rate over cycle number N_d (referring to [70]); Material: carbon black filled SBR; Constant parameters: dwell time $t_\mathrm{d} = 10\,\mathrm{s}$ and dwell level $\varepsilon_\mathrm{d} \approx 10\,\%$.

4 Improvements for the characterisation of fatigue

There is a large list of fatigue-influencing factors for rubber materials. In order to free of interference study them, the single fatigue-influencing factors should be to isolated. By this means, one is able to allocate the observations of the fatigue study to the isolated factor. New methods and improvements of existing methods for the isolation or consideration of certain fatigue-influencing factors are discussed in the present chapter.

4.1 Test piece temperature control for fatigue testing of filled elastomers

In agreement with the literature (see Section 3.1), Figure 4.1 shows the strong dependence of the mechanical fatigue on the ambient temperature of a technical rubber. The fatigue results are based on 3D-dumbbell test pieces. The experiment performed at an ambient temperature of $-30\,°\mathrm{C}$ was aborted for the lowest load-level (indicated by an arrow), due to limitations in the test duration.

As a result of internally dissipated energy in combination with the low surface area to volume ratio, significant self-heating occurs for the 3D-dumbbell test piece. For the lowest load-levels the fatigue test was performed with a loading frequency of $3\,\mathrm{Hz}$, whereas $1\,\mathrm{Hz}$ is chosen for all other load-levels. An approximate increase of one order of magnitude in lifetime for a decrease of $50\,°\mathrm{C}$ is shown in Figure 4.1.
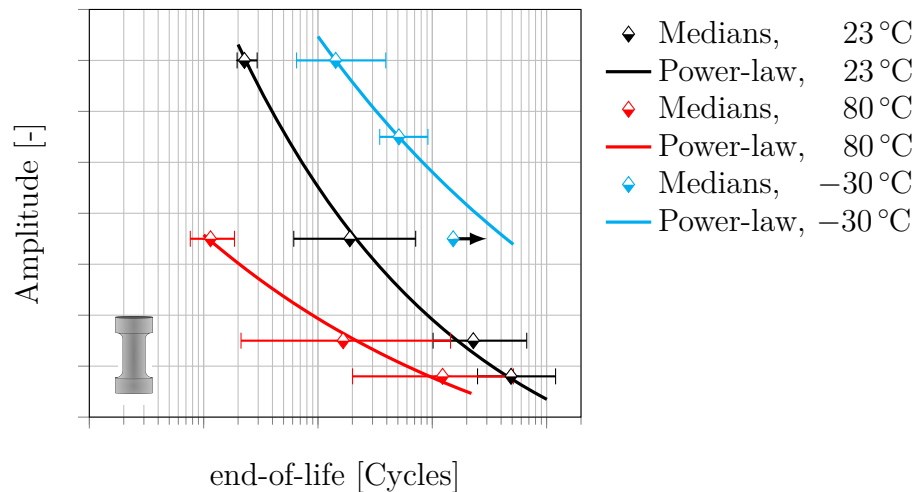
Figure 4.1: Impact of the ambient temperature on the fatigue behaviour of a technical rubber; 3D-dumbbell based measurements. All medians are endued with 95 % confidence limits.

4.1.1 Control of the surface temperature

As broached in Section 3.1, the temperature and its implication on the lifetime is not a main objective of the present study. Instead, the challenge is to maintain the test piece temperatures as constant as possible for all experiments within the experimental database. Moreover, it is decided that all investigated test pieces should not significantly heat-up beyond room temperature.

A suitable way to create an experimental database of fatigue data close to room temperature is the use of forced convection combined with an adaptation of load frequency for each load-level. The permanent usage of a temperature chamber to cool the test pieces was found to be too intricate.

Figure 4.2 shows the impact of forced convection on the surface temperature of a 3D-dumbbell. The test piece is oscillated with $130\,\mathrm{N} \pm 130\,\mathrm{N}$ with a frequency of $1.5\,\mathrm{Hz}$. A maximum surface temperature of greater than $50\,^\circ\mathrm{C}$ at thermal equilibrium without forced convection is measured using an infra-red sensor. The surface temperature rapidly drops below $30\,^\circ\mathrm{C}$ for an ambient temperature of $25\,^\circ\mathrm{C}$ after starting the air-flow.
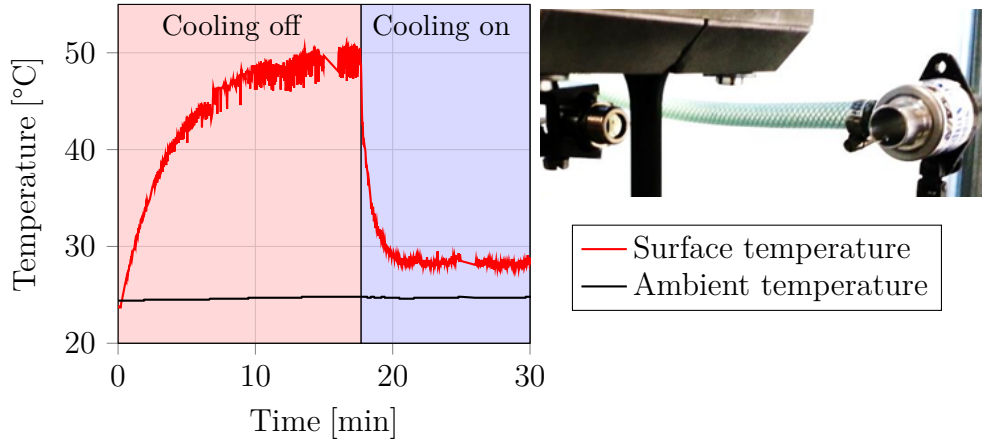
Figure 4.2: Cooling impact by forced convection at the example of a 3D-dumbbell.

For failure initiation with locus in the bulk material, thus not at the surface, not only the surface temperature but the also bulk temperature is of interest. The major question is if the bulk temperature decreases in the same way as the surface temperature when using forced convection. Equation 4.1 shows the general heat equation [72]:

$$\frac{\partial}{\partial t} T\left(\vec{x}, t\right) - \frac{\lambda_{\mathrm{cond}}}{\varrho c} \nabla T\left(\vec{x}, t\right) = \frac{\dot{q}(\vec{x}, t)}{\varrho c} \tag{4.1}$$

with T as the temperature and $\dot{q}$ as heat flow at the location $\vec{x}$ and time t, ∇ as Laplace operator and $\lambda_{\mathrm{cond}}, \varrho, c$ as thermal conductivity, density and heat capacity, respectively. For an infinite long cylinder, with an internal homogeneous heat source, in thermal equilibrium, the centre temperature is given by:

$$T_{r=0} = \frac{\dot{q}}{\lambda_{\mathrm{cond}}} \left(\frac{R}{2}\right)^2 + T_{r=R} \tag{4.2}$$

with R as the cylinder radius. It is assumed that the thermal conductivity λ_{cond} and heat flow $\dot{q}$ are independent on the temperature T. Based on these assumptions, the centre temperature $T_{r=0}$ decreases in the same way as the surface temperature $T_{r=R}$ once the fan is activated.

With the 3D-dumbbell geometry in mind, the assumption of an infinite long cylinder might appear quite inaccurate. In order to validate the applicability of Equation 4.2 on the 3D-dumbbell an interrupted fatigue test is performed. The test is terminated due to a sudden cut with a razor blade. This test is conducted with and without forced convection. In both cases, the cut is performed at thermal equilibrium and at the location of maximum surface temperature. The goal is to measure the centre temperature $T_{r=0}$ of the 3D-dumbbell with respect to its surface temperature $T_{r=R}$. Within the first deci-seconds after the cut, the centre temperature is captured by an infra-red camera, positioned in a steep angle to the cut surface of the test piece (see Figure 4.3).
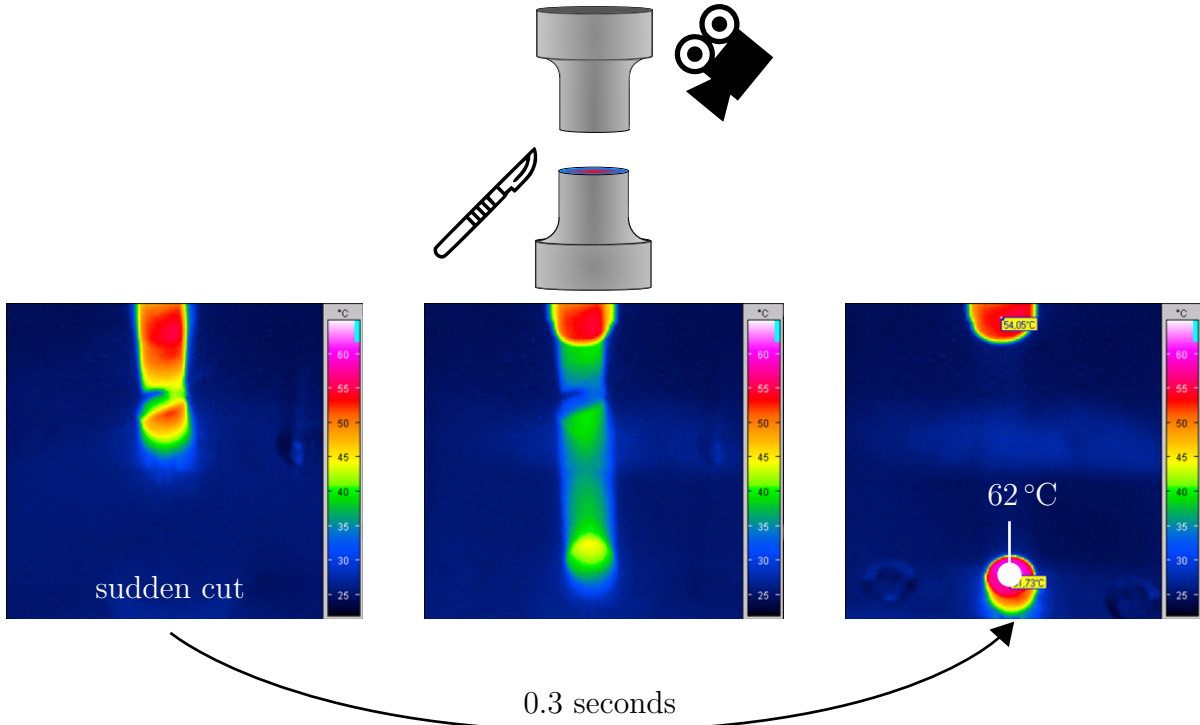
Figure 4.3: By a sudden cut with a razor blade, terminated fatigue test, recorded with an infrared camera.

The considered load conditions are $130\,\text{N} \pm 130\,\text{N}$ at $1.5\,\text{Hz}$ and $290\,\text{N} \pm 90\,\text{N}$ at $4.4\,\text{Hz}$. Figure 4.4 shows the measured surface temperatures and the corresponding centre temperatures with and without forced convection. A decrease of the centre temperature with the same magnitude as the surface temperature is measured for the uncooled and cooled test. For this reason, the assumptions from Equation 4.2 are reasonably correct. A small variation of the temperature difference between centre and surface for the uncooled and cooled $130\,\text{N} \pm 130\,\text{N}$ conditions ($T_{r=0} - T_{r=R} = 8\,°\text{C}$ and $T_{r=0} - T_{r=R} = 10\,°\text{C}$, respectively) is observed. Performing the razor blade cut at the location of maximum surface temperature while the running fatigue test is more difficult for this condition compared to the permanently stretched $290\,\text{N} \pm 90\,\text{N}$ case. In addition, the overall temperature drop is greater for the $130\,\text{N} \pm 130\,\text{N}$ case. Possible temperature dependencies of material properties like the thermal conductivity λ_{cond} must have a greater impact.

	130 N ± 130 N 1.5 Hz		Δ(Surface↔Centre)	290 N ± 90 N 4.4 Hz		Δ(Surface↔Centre)
	Surface	Centre		Surface	Centre	
	54 °C	62 °C	8 °C	31 °C	37 °C	6 °C
	27 °C	37 °C	10 °C	25 °C	31 °C	6 °C
Δ(~~fan~~ ↔fan)	27 °C	25 °C	2 °C	6 °C	6 °C	0 °C

Figure 4.4: Impact of forced convection on surface and volumetric centre temperature.

Here, a simplified test frequency adaptation is chosen. Within a Wöhler curve database one test condition (defined by: amplitude, mean load and frequency) is set as reference. For reasons of limits in test duration, this reference condition should be one for which cooling below a chosen threshold temperature is just possible. The frequency for all other load conditions is subsequently adopted based on the reference amplitude. The following rule is applied: double amplitude corresponds to halve load frequency. This significantly lowers the influence of temperature by self-heating but also causes approximately equal loading velocities among the database.

A more sophisticated approach would be based on equal dissipated power related to the test piece surface. The former approach is chosen for its simplicity. For each test condition the surface temperature at thermal equilibrium is monitored in order to detect possible transgressions of the chosen threshold temperature.

4.1.2 Conclusions

- Test piece temperature variations of some degrees influence the lifetime of the investigated elastomer significantly.

- A significant reduction of the surface temperature of a test piece close to ambient temperature can be achieved by forced convection.

- The bulk temperature decreases equally to the surface temperature for the investigated test piece geometry and loading conditions.

- Forced convection, combined with an amplitude dependent frequency adaption, is an effective method to control the test piece temperature among all fatigue tests in this work.

4.2 Displacement-controlled fatigue testing of rubber is not strain-controlled

Former Section 4.1 discusses the control of the test piece temperature in fatigue tests. The present section considers the findings from Section 4.1 and investigates the behaviour of the local strain during displacement-controlled cyclic loading. Information to the state of the art to this subject is given in Section 3.2.

4.2.1 Introduction

In research, tests with simple test pieces are used to quickly gather insights about the fatigue behaviour of rubber under the conditions of interest. In a more industrial environment, these kind of tests are often performed as a foundation for end-of-life prediction of components, using the procedure developed by August Wöhler [5] (see Section 1.2). Displacement-controlled fatigue testing is the most convenient way. The corresponding test rigs can be made in a purely mechanical way (e.g. with a simple eccentric as in [6]). No control loop such as, for example, for force-controlled testing is needed.

A procedure of displacement-controlled testing of the 2D-dumbbell (geometry defined in ISO 6943 [47]) is to establish first, using an auxiliary extension device and a single deformation, what displacement between the clamped dumbbell tabs is required to produce the desired elongation in the narrow portion of the 2D-dumbbell, and then adjust the fatigue machine to apply the same maximum displacement for each cycle. The assumption is that the maximum elongation of the narrow section is constant for all subsequent cycles. The validity of this assumption is quantitatively assessed in this work.

Section 4.2.2 provides information about the material composition, the test piece, the test set up, the test definition and the raw test results. Within Section 4.2.3 the test data are used to transform the experimentally measured varying strain to constant equivalent strain with Concept 1 (Page 63) and a more sophisticated alternative approach (Concept 2, Page 67). Additionally, the contribution of set to the evolution of maximum strain in the narrow test piece portion is discussed starting from Page 70, where the term set refers to change in the stress-free material configuration after application and removal of stress and not significantly recoverable in the period of the stress cycle.

A discussion and finite element analysis of the experiments can be found in Section 4.2.4. Finally, conclusions in the form of a numbered list are given in Section 4.2.5.

4.2.2 Experiments

In the present study the strain in the narrow section of a 2D-dumbbell was measured over the duration of cyclic loading conditions.

Material

Two materials are used. The compositions of the filled NR and SBR compound are shown in Table 4.1. They are the same as discussed in some previous publications, wherein additional aspects of properties may be found [73–78].

Name	NR	SBR
Ingredient	phr	
NR SMR CV60	100	
NR 1712		137.5
N330	45	
N339		77
SUNTHENE 410	4.5	
ZnO	3	3
Stearic acid	2	1
6PPD	3	3
CBS	0.6	
TMTD		0.2
TBBS		1.6
Sulphur	2.5	1.6

Table 4.1: NR and SBR formulations (phr ≡ parts per hundred of rubber, by mass)

Test piece

The chosen test piece is die-cut from a moulded sheet, nominally 2 mm thick, conforming to the (flat, not axisymmetric) 2D-dumbbell geometry defined in ISO 37:2011 [79]. Both ends of the test piece are clamped. To reduce the probability of failure initiation by the clamps, the 2D-dumbbell has a width of 12.5 mm at the ends, compared to 4 mm in the narrow portion.

Strain measurement

The cyclic loading is applied in a fatigue test rig with a simple adjustable eccentric to apply the varying displacement as shown diagrammatically in Figure 4.5. This machine incorporates a computerised logging system for the load transducers and a single displacement transducer for the motion of the bar to which the bottom clamps are fixed. Each load cell is mounted on a linear actuator with feedback control, for the option of maintenance of a peak maximum force, but this mode was not used for the work reported in this paper. Instead, the top clamps were fixed in position.
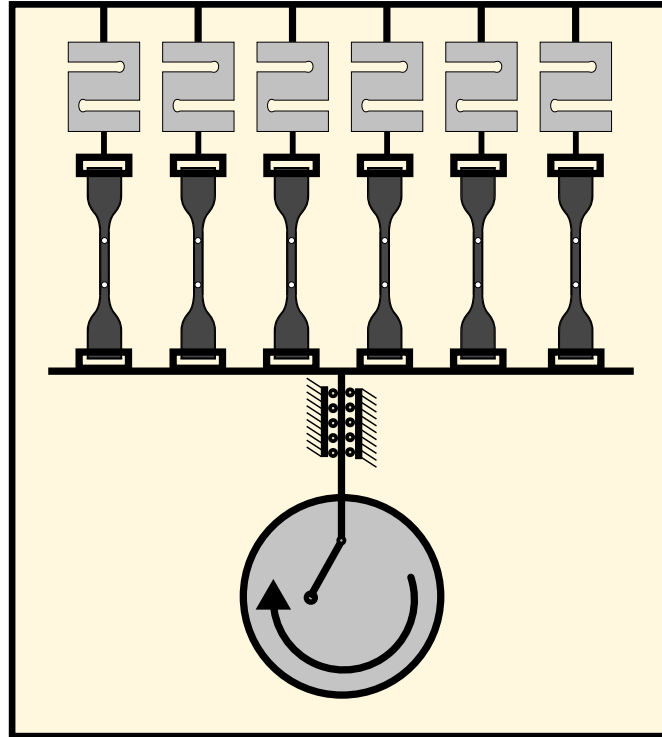
Figure 4.5: Test Rig. Top to bottom: load cells, test pieces attached to adjustable static clamps, lower moving clamps fixed to a common guided beam, eccentric drive.

Each dumbbell has two marked positions within the narrow section (see little white dots in Figure 4.5 and solid red arrow in Figure 4.6). To capture the separation between these two marks, a standard digital camera is used. Rulers placed in-plane serve as references for the separation measurements (see dashed arrow in Figure 4.6). A ruler is positioned next to each specimen to cover possible distortions in the images taken by the camera. For the evaluation of the separation measurements the closest ruler is chosen as reference, to convert the number of pixel to millimetre. In order to further convert these separation measurements into strains, the dumbbells are also measured with the photo camera method in the undeformed state before any displacement is applied.
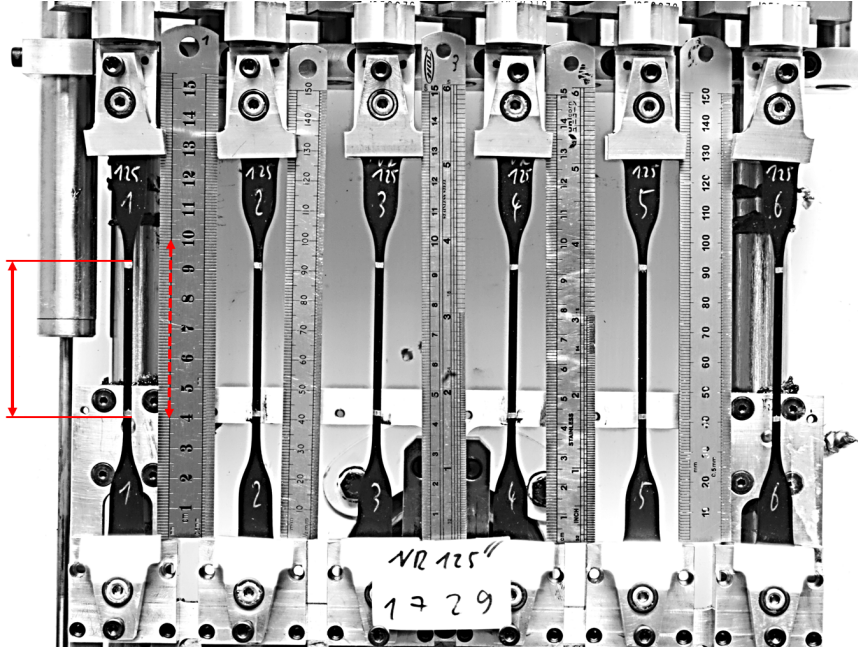
Figure 4.6: Photograph of the maximum deformed dumbbells to measure the strains in the narrow section. The solid arrow stands for the maximum separation of the narrow section whereas the dashed arrow serves for the conversion from pixel into millimetre.

The following measure of lengths, referring to ISO 6943, are given [47]:

l_N is the distance between the gauge marks at the zero load point of cycle N.

l_0 is the initial gauge mark separation (ref configuration) measured in undeformed state before any displacement is applied.

L_N is the distance between the gauge marks at maximum clamp separation at cycle N.

Based on these measures of lengths, stretches are defined:

$$\lambda_N = \frac{L_N}{l_N} \tag{4.3}$$

$$\lambda_{\text{set}.N} = \frac{l_N}{l_0} \tag{4.4}$$

$$\lambda_{\text{tot}.N} = \lambda_N \cdot \lambda_{\text{set}.N} = \frac{L_N}{l_0} \tag{4.5}$$

The nominal strains are consequently defined as:

$$\varepsilon_{\text{n}.N} = \lambda_N - 1 = \frac{L_N - l_N}{l_N} \qquad \rightarrow \text{equal to Equation 3.1} \tag{4.6}$$

$$\varepsilon_{\text{n.set.}N} = \lambda_{\text{set.}N} - 1 = \frac{l_N - l_0}{l_0} \tag{4.7}$$

$$\varepsilon_{\text{n.tot.}N} = \lambda_{\text{tot.}N} - 1 = \frac{L_N - l_0}{l_0} \tag{4.8}$$

Further, one may define:

$$\varepsilon_{\text{n.MS.}N} = \lambda_{\text{tot.}N} - \lambda_{\text{set.}N} = \frac{L_N - l_N}{l_0} \tag{4.9}$$

So that the total strain $\varepsilon_{\text{n.tot.}N}$ is split into set strain $\varepsilon_{\text{n.set.}N}$ and another part, here provisionally called material softening strain $\varepsilon_{\text{n.MS.}N}$:

$$\varepsilon_{\text{n.tot.}N} = \varepsilon_{\text{n.set.}N} + \varepsilon_{\text{n.MS.}N} \tag{4.10}$$

Test protocol

Four amplitudes are defined for both materials. All tests are performed in fully relaxing conditions, with respect to the global deflection ($R_{\text{u}} = {}^{d_{\sim.\,\text{min}}}\!/d_{\sim.\text{max}} = 0$). Buckling of the test pieces is not avoided. The amplitudes range from roughly $\varepsilon_{\text{n.tot.1}} = 90\,\%$ to $\varepsilon_{\text{n.tot.1}} = 180\,\%$ nominal strain. In general a standard displacement-controlled fatigue test is performed. The test rig is able to simultaneously cycle 12 dumbbells (Figure 4.5 only shows the half machine for simplicity). Only 6 of the total 12 2D-dumbbells are photographed for the strain evaluation. The fatigue test is interrupted for the time of recording the image after a selected number of cycles (the data from Chapter 6 prove the independence of the lifetime to these dwell periods). Except for the reference photo for the strain determination, all images are taken in the maximum deformed state of the specific test condition. This means that only L_N and l_0 (not l_N) were measured with the photo camera method. To minimize the influence of temperature by self-heating and different loading velocities the test frequencies are modified for each loading condition. For the smallest of the four amplitudes, corresponding to roughly $\varepsilon_{\text{n.tot.1}} = 90\,\%$, the maximum frequency of the fatigue machine is used (4.5 Hz). Accordingly, a frequency of 2.25 Hz is chosen for the largest amplitude, corresponding to roughly $\varepsilon_{\text{n.tot.1}} = 180\,\%$. Independent of the loading conditions, a fan is pointed on the specimens for all tests to reduce the maximum surface temperature to 28 °C or lower (see Section 4.1). The surface temperature is measured with an infra-red camera. Thanks to the large surface to volume ratio of the 2D-dumbbell it can be assumed that the bulk temperature approximately equals the surface temperature. The ambient temperature is controlled at 21 °C by an air conditioning system.

Test results

Figure 4.7 shows the strains $\varepsilon_{\mathrm{n.tot}.N}$ for each of the six evaluated positions in the test rig, as determined using the camera method. The results of the $\varepsilon_{\mathrm{n.tot}.1} \approx 90\,\%$ fatigue test of the NR mixture are chosen to illustrate the typical behaviour. The fatigue test was interrupted four times, including the first cycle, to record an image. All test pieces experience the same displacement-controlled amplitude. Nevertheless, the strains in the narrow section increase. The scattering of strain at maximum deflection among the test pieces originates from the manual clamping of the 2D-dumbbell; small deviations are inevitable when operated by a human. The ◇-symbol is the mean value for all test pieces for each time point.
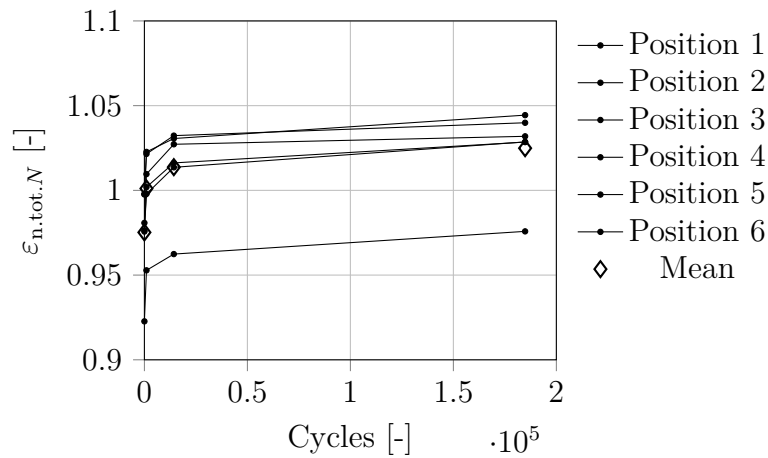
Figure 4.7: NR: Measured nominal strain $\varepsilon_{\mathrm{n.tot}.N}$ over Cycles.

Re-plotting Figure 4.7 in a semilog-plot reveals a logarithmic creep behaviour, in accord with the results of Derham and Thomas in their cyclic creep tests for a filled NR material [42]. All other measurements show the same nearly perfect logarithmic behaviour until the rupture of the dumbbell, independent of the loading condition and of the two filled materials. As a guideline for the eye, the mean values (◇) are fitted by a logarithmic function (see Equation 4.11).

$$\varepsilon_{\mathrm{n.tot}.N} \approx a \cdot \ln(N) + b \tag{4.11}$$

With N as number of cycles and a, b as parameters.
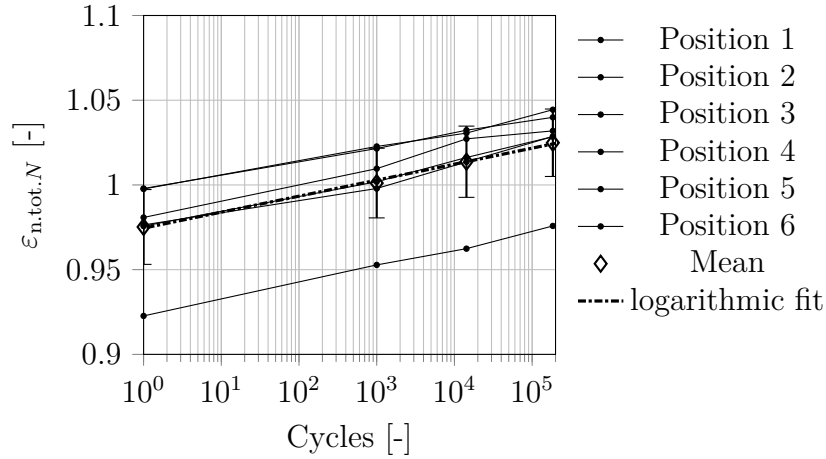
Figure 4.8: NR: Measured nominal strain $\varepsilon_{\text{n.tot.}N}$ over log(Cycles). Each mean is endued with 95 % confidence limits ($\perp, \top$), based on a Gaussian distribution.

Figure 4.9 shows the logarithmic fits for each loading condition and material. The plots are truncated at the mean number of cycles to failure (×-symbol). For the curves with the same symbol (●, ♦, ▲, ■), the same displacement-controlled amplitude is applied. The differences in material behaviour lead to significant variations in the strains even at the first loading cycle. The measured strains in the first cycle $\varepsilon_{\text{n.tot.}1}$ are used for the notation in the diagram's legend. The NR material shows larger strains in the narrow section of the 2D-dumbbell. In general, the NR-based material shows much greater creep-rates (strain change at maximum displacement over cycles) compared to the SBR-based material, as observed also by Davies et al. [43].
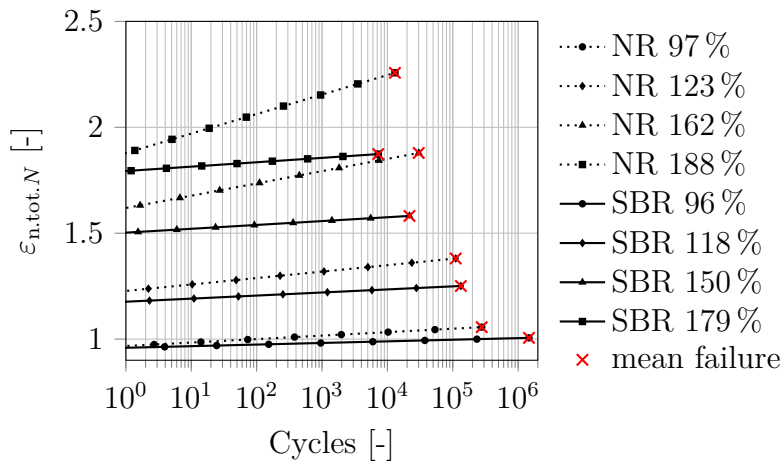
Figure 4.9: NR & SBR: Mean of the measured strains $\varepsilon_{\text{n.tot.}N}$ over cycles for all loading conditions. Only the fitted logarithmic curves are shown and plotted until the end-of-life. The legend gives the initial set-up strains $\varepsilon_{\text{n.tot.}1}$ (see Equation 4.8).

Table 4.2 provides the values of the fitted logarithmic function from Equation 4.11. The

parameter a describes the slope, mean creep-rate and parameter b the offset, here the strain at the first cycle $\varepsilon_{\text{n.tot.1}}$.

NR Material	a	b	SBR Material	a	b
NR 97 %	0.0071	0.9673	SBR 96 %	0.0033	0.9589
NR 123 %	0.0132	1.2273	SBR 118 %	0.0063	1.1764
NR 162 %	0.0252	1.6188	SBR 150 %	0.0079	1.5025
NR 188 %	0.04	1.8781	SBR 179 %	0.009	1.7934

Table 4.2: Parameter values of the fitted logarithmic function from Equation 4.11.

Even if the total strain $\varepsilon_{\text{n.tot}}$ steadily increases, the maximum reaction force decreases (see Figure 4.10). Here, the end-of-life or failure is reached if the dynamic stiffness drop cannot anymore be associated with the material specific viscoelastic stiffness drop (see Figure 4.10). This concept is applied for all fatigue tests throughout this work, not only in the current section and chapter.
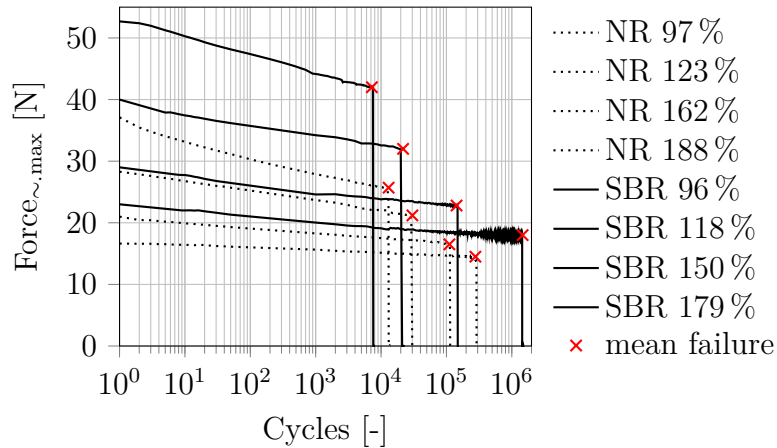
Figure 4.10: NR & SBR: Measured maximum reaction force over cycles (Force$_{\sim.\text{max}}$) for all loading conditions. Only one test piece data set, with the end-of-life as close as possible to the mean end-of-life, per load-level is shown. The legend gives the initial set-up strains $\varepsilon_{\text{n.tot.1}}$.

The Wöhler curves of the NR and SBR materials are shown in Figure 4.11. Each median is endued with 95 % confidence limits ($\vdash\dashv$ and $\perp, \top$). The vertical positions of the medians and the vertical confidence limits ($\perp, \top$) are based on a Gaussian distribution while the horizontal positions of the medians and the horizontal confidence limits ($\vdash\dashv$) are calculated based on the log-normal or Weibull distribution, depending on which of them describes best the statistics of the data-points. Information of statistics based on these two distribution can be found in Section 2.3. Each combination of horizontal median and confidence limits is based on 12 data points. Noting that the same number of data-points stands behind each confidence limit, the data for the SBR-based material can be surmised to have greater scattering in end-of-life, as is often seen; see e.g. [80]. For reasons of

demonstration, the strains $\varepsilon_{\text{n.tot.1}}$ of the first loading cycle are used for the depiction of the two Wöhler curves.
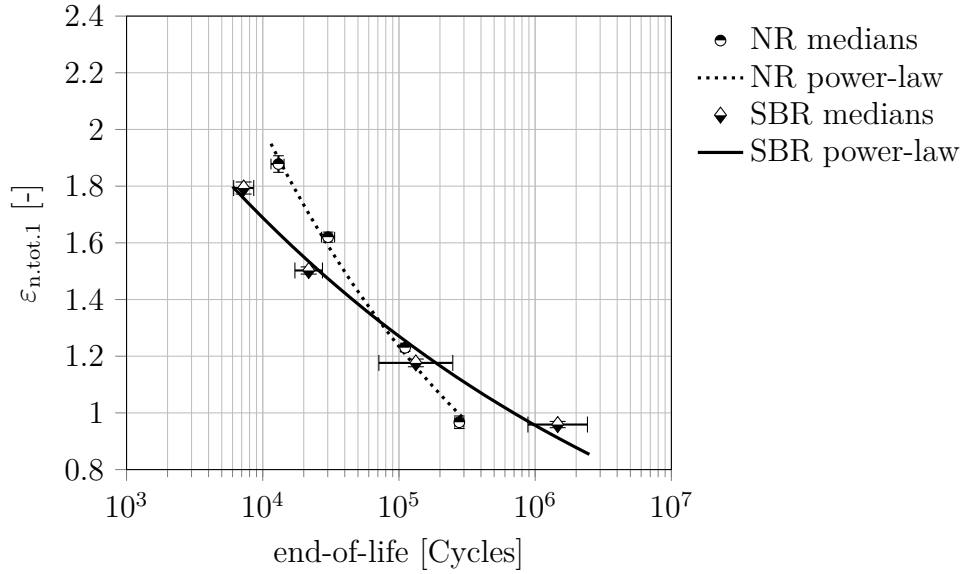
Figure 4.11: NR & SBR: Wöhler curves in comparison.

The median values are additionally listed in Table 4.3 and the power-law parameters in Table 4.4, Page 67.

NR Material	Median [Cycles]	SBR Material	Median [Cycles]
NR 97 %	277 309	SBR 96 %	1 463 538
NR 123 %	111 010	SBR 118 %	133 008
NR 162 %	30 162	SBR 150 %	21 747
NR 188 %	13 048	SBR 179 %	7 245

Table 4.3: Median end-of-life values of the NR and SBR materials from Figure 4.11.

4.2.3 Evaluation

From Section 1.2: *The Wöhler concept is to express lifetimes (measured in cycles to failure) as a function of the amplitude of a repeated mechanical duty cycle. A plot of the amplitude against log(lifetime) – the Wöhler curve – may then be interpolated or extrapolated to estimate the maximum amplitude consistent with a desired lifetime.* In the following a method is introduced to address the change of strain over cycles in the evaluation of the Wöhler curve data. A Wöhler curve is defined by:

$$\text{Load}(\cancel{N}) = \varepsilon(\cancel{N}) = \varepsilon_{\text{n.const}} = \alpha \cdot N_{\text{eol}}^{\gamma} \tag{4.12}$$

where N_{eol} (eol: end-of-life) is the lifetime and α, γ are power-law parameters. As indicated by the cancelled dependency of the duty cycle amplitude on the number of cycles

(N), see Equation 4.12), the Wöhler curve from its nature does not consider a changing amplitude over cycles or time. The conception is that from tests at a constant duty cycle, such as $\varepsilon_{\mathrm{n.const}}$, we find the corresponding values of N at which the end-of-life criterion is reached; these test results enable us, through interpolation and possibly extrapolation, to map from a given requirement for N_{eol} to the maximum duty cycle, or, for a given duty cycle, what value of lifetime would be achievable. However, our test data shows that, despite following the standard procedure, we do not achieve the ideal of a constant strain cycle. Thus, the increasing strain over cycles needs to be replaced by an equivalent constant strain, serving as a representative measure of the magnitude of a repeated duty cycle. This is quite extensively discussed here in two possible concepts with Chapter 5, 6 and Section 4.3 in the back of one's mind where different fatigue test pieces will be compared.

Concept 1: Consideration of varying strains

It is assumed that the law of linear damage accumulation holds within this study; this has been referred to as Miner's rule [81]. This assumption is reasonably applicable for the NR material [82, 83]. However, more to doubt for the SBR material [84]. It is further assumed that the current strain amplitude in the fatigue cycles serves as a measure of their propensity to cause *damage* to the material.

The aim is to transfer the constantly increasing strain to an equivalent constant strain value. It is assumed that cyclic straining accumulates damage in a linear way until the failure of the test piece, according to the law of linear damage accumulation. Figure 4.12 illustrates the concept for the NR 162 % loading condition; the area A_1 underneath the $\varepsilon_{\mathrm{n.tot.}N}$ curve over cycles is defined to be the accumulated damage. In case of the logarithmically changing strain described by Equation 4.11 the area is:

$$A_1 = \int_{0}^{N_{\mathrm{eol}}} \varepsilon_{\mathrm{n.tot.}N}(N)\mathrm{d}N = N_{\mathrm{eol}}(a \cdot \ln(N_{\mathrm{eol}}) + b - a) \tag{4.13}$$
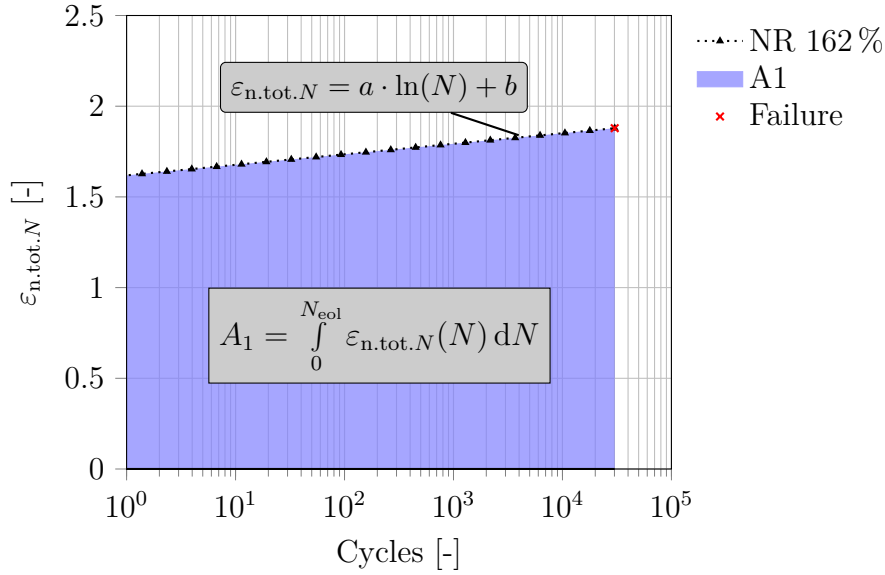
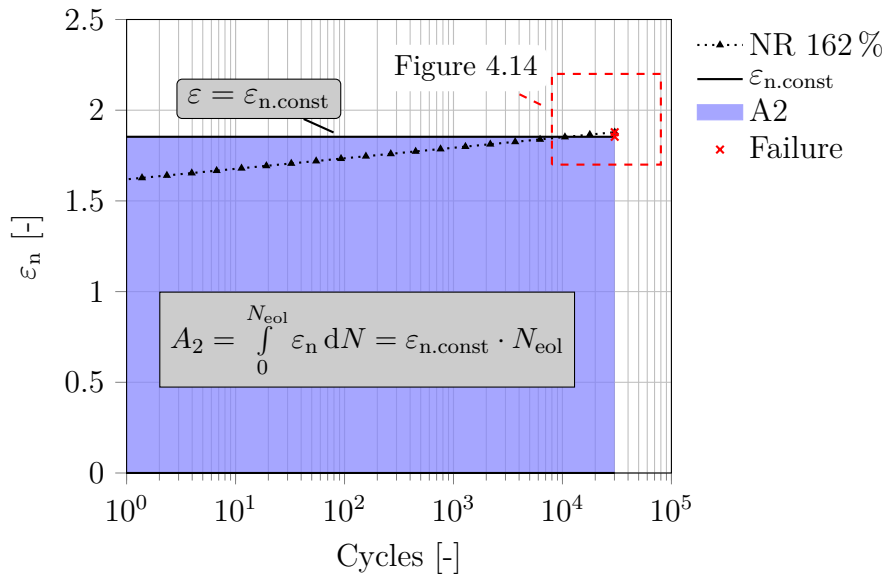**Figure 4.12: NR**: $\varepsilon_{\text{n.tot.}N}$ over cycles with blue highlighted measure of damage, area A_1.

In case of constant strain over cycles, the area is given by (see Figure 4.13):

$$A_2 = \int\limits_0^{N_{\text{eol}}} \varepsilon_\text{n}\,\mathrm{d}N = \varepsilon_{\text{n.const}} \cdot N_{\text{eol}} \tag{4.14}$$

In order to calculate the equivalent constant strain $\varepsilon_{\text{n.const}}$ the area (or damage) A_1 and A_2 are set equal (see Equation 4.15).

$$A_2 = A_1 \rightarrow \varepsilon_{\text{n.const}} = a \cdot \ln(N_{\text{eol}}) + b - a \tag{4.15}$$

The result for $\varepsilon_{\text{n.const}}$ based on Equation 4.15 is shown in Figure 4.13. A large magnification of Figure 4.13, shown in Figure 4.14, is necessary to be able to differentiate between the calculated $\varepsilon_{\text{n.const}}$ and the measured strains at the end of the fatigue test $\varepsilon_{\text{n.tot.}N_{\text{eol}}}$. The difference between the strains at end-of-life and $\varepsilon_{\text{n.const}}$ appears initially surprisingly small. A re-plot of Figure 4.13 with linear abscissa eliminates the initial surprise (see Figure 4.15).

Figure 4.13: NR: $\varepsilon_{\mathrm{n.tot.}N}$ and $\varepsilon_{\mathrm{n.const}}$ over cycles with blue highlighted measure of accumulated damage in case of constant strain $\varepsilon_{\mathrm{n.const}}$, area A_2.
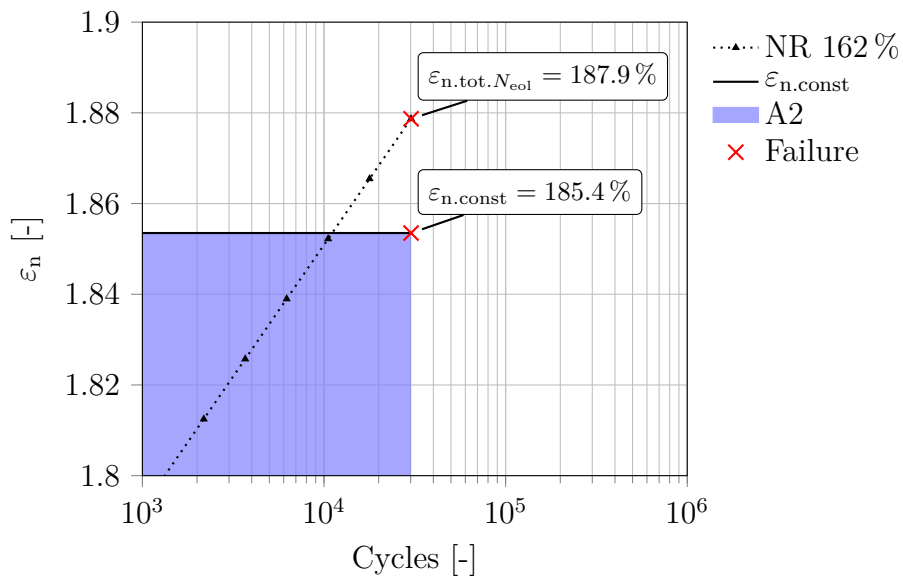

Figure 4.14: NR: Zoom of Figure 4.13 as highlighted.
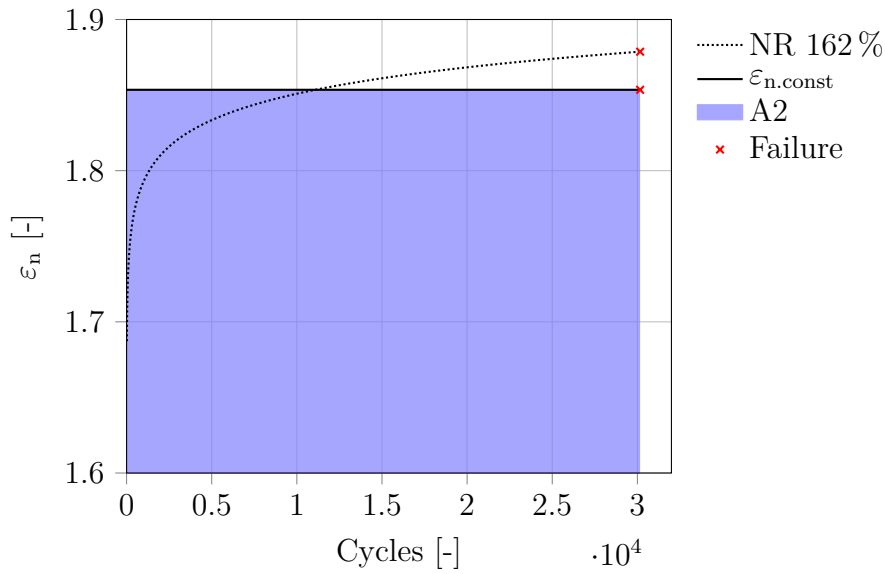
Figure 4.15: NR: Figure 4.13 with linear abscissa and enlarged ordinate.

Considering not only the strains from the first cycle $\varepsilon_{\text{n.tot.1}}$ (see Figure 4.11) but the increase of strain over cycles in the displacement-controlled fatigue test, leads to shifted Wöhler curves (see Figure 4.16). These Wöhler curves are plotted, based on $\varepsilon_{\text{n.const}}$ defined in Equation 4.15. The slope of the SBR material Wöhler curve stays almost unaffected compared to the NR material (see Table 4.4). This suggests that the modification of the Wöhler curve depends on the material as well. The values for $\varepsilon_{\text{n.const}}$ based on this concept are listed in Table 4.5.
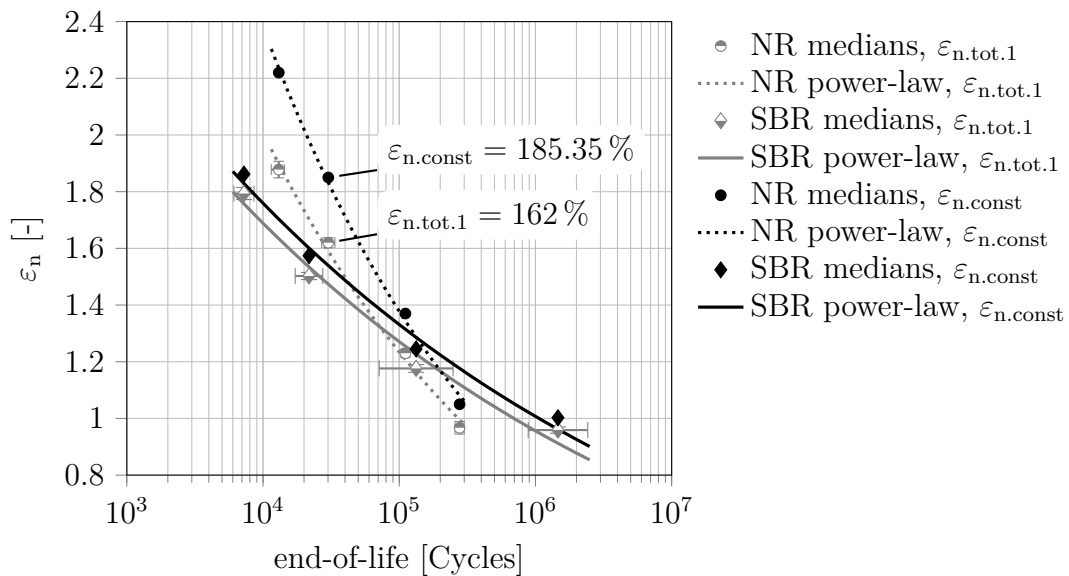
Figure 4.16: NR & SBR: Wöhler curves from Figure 4.11 using $\varepsilon_{\text{n.const}}$ instead of the strain from the first loading cycle $\varepsilon_{\text{n.tot.1}}$.

Material	α	γ
NR, $\varepsilon_{\mathrm{n.tot.1}}$	14.044	-0.2112
NR, $\varepsilon_{\mathrm{n.const}}$	21.265	-0.2377
SBR, $\varepsilon_{\mathrm{n.tot.1}}$	5.266	-0.1235
SBR, $\varepsilon_{\mathrm{n.const}}$	5.366	-0.1211

Table 4.4: NR & SBR: Wöhler curve / power-law parameters from Figure 4.16. The parameters are defined in Equation 4.12.

$\varepsilon_{\mathrm{n.tot.1}}$	$\varepsilon_{\mathrm{n.tot.}N_{\mathrm{eol}}}$	$\varepsilon_{\mathrm{n.const}}$
187.81 %	225.71 %	221.72 %
161.88 %	187.87 %	185.35 %
122.73 %	138.06 %	136.74 %
96.73 %	105.62 %	104.92 %

Table 4.5: NR: Strain comparison, starting with the strain measured in the first cycle $\varepsilon_{\mathrm{n.tot.1}}$, the cycle at end-of-life $\varepsilon_{\mathrm{n.tot.}N_{\mathrm{eol}}}$ and the equivalent constant strain $\varepsilon_{\mathrm{n.const}}$.

Concept 2: Consideration of varying strains

The small magnitude, but negative sign, of the Wöhler power law exponent γ (see Equation 4.12) implies that the propensity to damage increases very strongly with the cyclic strain amplitude. The possible significance of this statement, valid for $0 > \gamma > -1$, in choosing a representative value $\varepsilon_{\mathrm{n.const}}$ for the evolving strain magnitude observed in the fatigue tests was not considered in Concept 1 above so is considered here.

A virtual example, based on the slope $\gamma \approx -0.12$ of the Wöhler curve for SBR (see Table 4.4) makes the strength of the effect clear. For $\gamma \approx -0.12$, the lifetime at a strain amplitude of 200 % would be reduced by a factor of approximately 1/320 compared to that at an amplitude of 100 %, rather than halved. This simple property significantly complicates the concept introduced in Equation 4.15, but will turn out to have very little impact on the $\varepsilon_{\mathrm{n.const}}$. To meet this load sensitivity, a weight factor $\omega(N)$ is introduced in Equations 4.13 and 4.15 for the areas ($A1$) and ($A2$) underneath respectively the non-constant strain and the constant strain $\varepsilon_{\mathrm{n.const}}$:

$$A_1 = \int_0^{N_{\mathrm{eol}}} \varepsilon_{\mathrm{n.tot.}N} \cdot \omega(N)\, \mathrm{d}N \tag{4.16}$$

$$A_2 = \int_0^{N_{\mathrm{eol}}} \varepsilon_{\mathrm{n.const}} \cdot \omega(N)\, \mathrm{d}N \tag{4.17}$$

with:

$$w(N) = \frac{A_{\mathrm{ref}}}{A(N)} = \frac{\varepsilon_{\mathrm{n.ref}} \cdot N_{\mathrm{eol}}(\varepsilon_{\mathrm{n.ref}})}{\varepsilon_{\mathrm{n.tot.}N} \cdot N_{\mathrm{eol}}(\varepsilon_{\mathrm{n.tot.}N})} \tag{4.18}$$

where A_{ref} stands for the reference area. This reference area is based on the strain from the first cycle (see Figure 4.17). Using the example of the NR $\varepsilon_{\text{n.tot.1}} = 162\,\%$ case, the reference area is $A_{\text{ref}} = 162\,\% \cdot 27616$ cycles. The N_{eol} for $\varepsilon_{\text{n.ref}}$ differs somewhat from the value in Table 4.3 since it is calculated using the NR power-law (see Equation 4.12), fitted to the data points from Table 4.3. In the same way, the area at end-of-life can be calculated as $A_{\text{eol}} = 188\,\% \cdot 13648$ Cycles, and is highlighted in red in Figure 4.17. This example demonstrates that, based on the information of the NR Wöhler curve, the strains close to the time-point of rupture are 1.744 times more damaging compared to the strains at the beginning of the fatigue test:

$$w(N) = \frac{A_{\text{ref}}}{A_{\text{eol}}} = \frac{162\,\% \cdot 27616 \text{ Cycles}}{188\,\% \cdot 13648 \text{ Cycles}} = 1.744$$
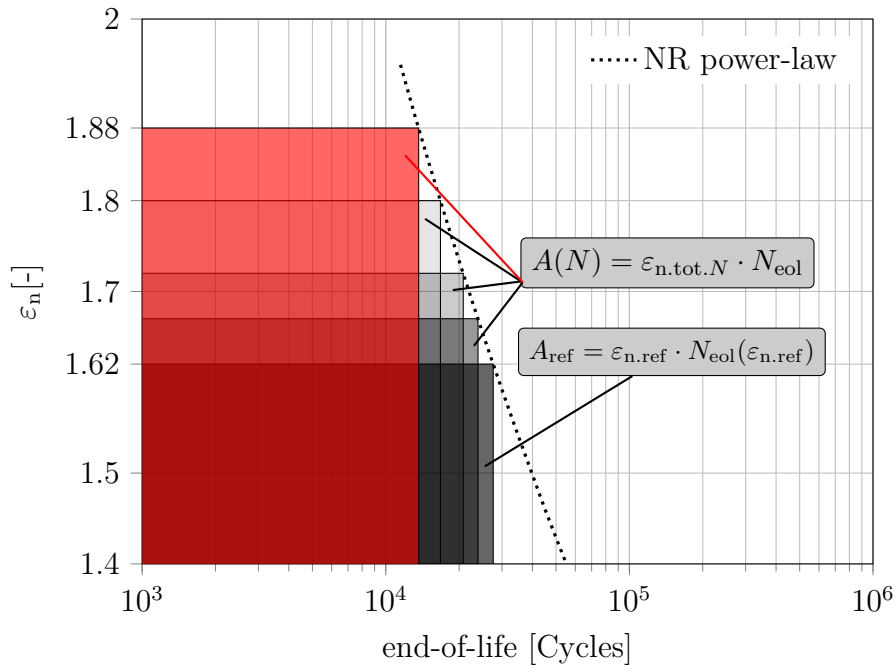
Figure 4.17: NR: Different areas representing damage with focus on the NR $162\,\%$ loading case. The area highlighted in red is the area based on the strain at end-of-life. The NR power-law used here is that fitted to the $\varepsilon_{\text{n.tot.1}}$ vs median values of N_{eol} given in Table 4.4.

This procedure needs to be performed continuously within the integrals from Equation 4.16 and 4.17. For that, the Wöhler curve power-law is plugged into Equation 4.18:

$$w(N) = \frac{A_{\text{ref}}}{A(N)} = \frac{\varepsilon_{\text{n.ref}} \cdot N_{\text{eol}}}{\varepsilon_{\text{n.tot.}N} \cdot N_{\text{eol}}(\varepsilon_{\text{n.tot.}N})} = \frac{\varepsilon_{\text{n.ref}} \cdot \exp\left(\frac{\ln(\varepsilon_{\text{n.ref}}/\alpha)}{\gamma}\right)}{\varepsilon_{\text{n.tot.}N} \cdot \exp\left(\frac{\ln(\varepsilon_{\text{n.tot.}N}/\alpha)}{\gamma}\right)} \tag{4.19}$$

As for Concept 1 the areas (damages) A_1 and A_2 are set equal:

$$A_1 = \int\limits_0^{N_{\mathrm{eol}}} \varepsilon_{\mathrm{n.tot}.N} \cdot \omega(N)\,\mathrm{d}N = \int\limits_0^{N_{\mathrm{eol}}} \varepsilon_{\mathrm{n.const}} \cdot \omega(N)\,\mathrm{d}N = A_2$$

Now, Equation 4.19 can be used to substitute for the weight factor $\omega(N)$:

$$\int\limits_0^{N_{\mathrm{eol}}} \varepsilon_{\mathrm{n.tot}.N} \cdot \frac{\varepsilon_{\mathrm{n.ref}} \cdot \exp\left(\frac{\ln(\varepsilon_{\mathrm{n.ref}}/\alpha)}{\gamma}\right)}{\varepsilon_{\mathrm{n.tot}.N} \cdot \exp\left(\frac{\ln(\varepsilon_{\mathrm{n.tot}.N}/\alpha)}{\gamma}\right)}\,\mathrm{d}N = \varepsilon_{\mathrm{n.const}} \int\limits_0^{N_{\mathrm{eol}}} \frac{\varepsilon_{\mathrm{n.ref}} \cdot \exp\left(\frac{\ln(\varepsilon_{\mathrm{n.ref}}/\alpha)}{\gamma}\right)}{\varepsilon_{\mathrm{n.const}} \cdot \exp\left(\frac{\ln(\varepsilon_{\mathrm{n.const}}/\alpha)}{\gamma}\right)}\,\mathrm{d}N$$

Partly solving and simplifying the above equation leads to:

$$\overbrace{\int\limits_0^{N_{\mathrm{eol}}} \exp\left(\frac{\ln(\varepsilon_{\mathrm{n.tot}.N}/\alpha)}{\gamma}\right)\mathrm{d}N}^{Integral} = N_{\mathrm{eol}} \cdot \exp\left(-\frac{\ln(\varepsilon_{\mathrm{n.const}}/\alpha)}{\gamma}\right)$$

The strain $\varepsilon_{\mathrm{n.tot}.N}$ depends on the number of cycles N, as described by the logarithmic Equation 4.11, making the integral on the left side analytically difficult to solve. It is solved numerically in MATLAB and for reasons of clarity labelled as *Integral*. Finally the equivalent constant strain $\varepsilon_{\mathrm{n.const}}$ considering the large load - small load sensitivity is defined as:

$$\varepsilon_{\mathrm{n.const}} = \alpha \cdot \exp\left(\gamma \cdot \ln(Integral/N_{\mathrm{eol}})\right) \tag{4.20}$$

A shift of the single load-levels and consequently of the complete Wöhler curve, by applying Equation 4.20, can be performed, as conducted for Concept 1 in Figure 4.16. The difference is now, that the definition of the equivalent constant strain $\varepsilon_{\mathrm{n.const}}$ (see Equation 4.20) contains the Wöhler curves power-law parameter. Therefore, the shift of the Wöhler curve happens in an iterative way until convergence is reached, as sketched in Figure 4.18.

New γ & α

$$\varepsilon_{\text{const}} = \alpha \cdot \exp\left(\gamma \cdot \ln\left(\frac{Integral}{N_{\text{eol}}}\right)\right)$$

ε_{n} [-]

end-of-life [Cycles]

New $\varepsilon_{\text{const}}$
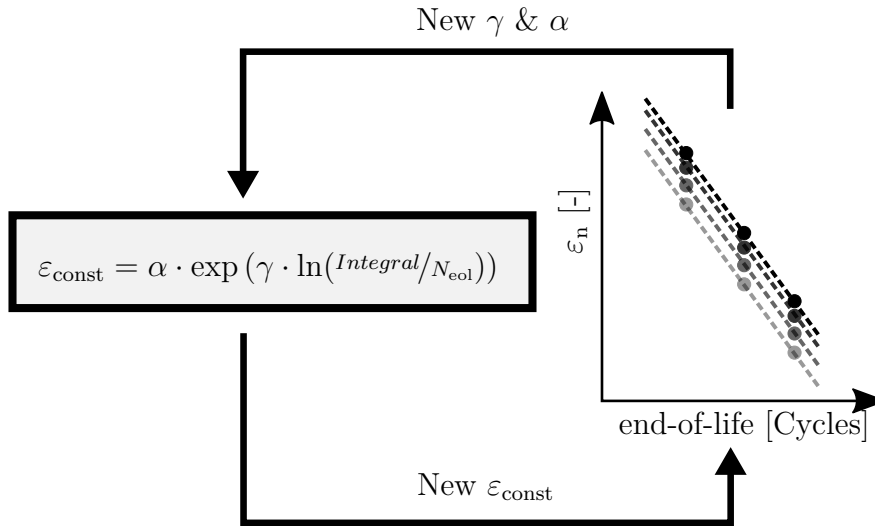
Figure 4.18: Iterative shift of the Wöhler curve.

One might expect a significantly stronger shift thanks to the extended Concept 2 in comparison with the simple Concept 1. The comparison in Table 4.6 shows only small differences in the values of $\varepsilon_{\text{n.const}}$ between the two concepts. For the NR 162 % case, 82 % of the entire strain increase takes place within the first 15 % of the lifetime. Because of the long period of approximately constant strain, the influence when comparing Concept 1 and Concept 2 is negligible. However, one would be making a mistake were one to choose to measure the strain for the evaluation in a Wöhler curve plot within the first quarter of the lifetime.

Strain at $N = 1$	Strain at $N = N_{\text{eol}}$	$\varepsilon_{\text{n.const}}$ based on Concept 1	$\varepsilon_{\text{n.const}}$ based on Concept 2
187.81 %	225.71 %	221.72 %	221.83 %
161.88 %	187.87 %	185.35 %	185.41 %
122.73 %	138.06 %	136.74 %	136.77 %
96.73 %	105.62 %	104.92 %	104.93 %

Table 4.6: NR: Strain comparison, starting with the strain measured in the first cycle, the cycle at end-of-life, followed by the equivalent constant strain $\varepsilon_{\text{n.const}}$ calculated based on Concept 1 and 2.

Share of the set on strain increase over cycles.

The phenomenon of the increasing strain $\varepsilon_{\text{n.tot.}N}$ over cycles is caused by different cyclic creep between narrow section (higher peak stress) and the wider clamping area (lower peak stress) of the 2D-dumbbell; it is consequently geometry dependent. In order to investigate the influence of the geometry on this effect three test piece geometries were chosen (see Figure 4.19). They vary in degree of non-uniformity of cross-sectional area along their lengths. The cross-section area is constant for the strip test piece. All test pieces

are die-cut from a 2 mm sheet. The cyclic deformation is applied using a Zwick/Roell Z010 equipped with an optical strain measure module. The marks for optical strain measurement were placed according to the Standard ISO 37 [79] in the narrow section. Using this Zwick machine provides the possibility to stretch the test pieces up to a given cross-head displacement and unload them to the unstressed state, rather than to the initial crosshead position. Reloading is resumed without significant pause. This enables the direct measurement of set in the narrow section. Such force-controlled unloading is not possible with the fatigue test rig sketched in Figure 4.5. Using the time-point of buckling from the fatigue force-displacement data to calculate the set turned out to be too imprecise. The cross-head displacements and the resulting $\varepsilon_{\mathrm{n.tot.1}}$ were chosen to replicate the load-levels of the fatigue tests. Only 3 out of the 4 fatigue test load-levels and one test piece were chosen per material and geometry to reduce test time. The test pieces were cycled with a frequency of $f \approx 0.01$ Hz, more than two orders of magnitude less than for the fatigue test conditions. The displacement-time histories were also triangular, rather than approximately sinusoidal, as for the TARRC fatigue machine from Figure 4.5.
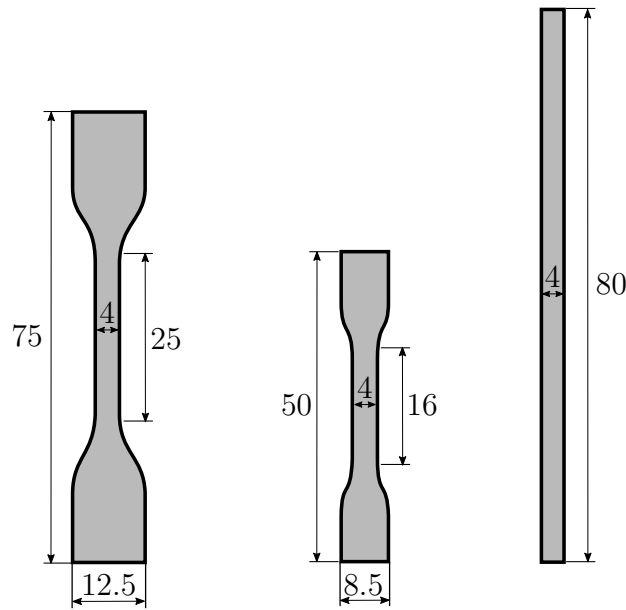
Figure 4.19: Geometry of 2D-dumbbell (see [79]), type 3 dumbbell (see [79]) and strip test pieces (f.l.t.r.).

Figure 4.20 shows $\varepsilon_{\mathrm{n.tot.}N}$ and $\varepsilon_{\mathrm{n.set.}N}$ for the three test pieces geometries. As for the strain data collected during the fatigue tests, the datapoints are fitted with a logarithmic regression (see Equation 4.11). For simplicity the single datapoints are displayed for the 2D-dumbbell only. Solely the regression function is plotted for the type 3 and strip test pieces for all diagrams within Figure 4.20.

The behaviour of $\varepsilon_{\mathrm{n.set.}N}$ is approximately equal for all geometries, since this value is measured in the stress-free state. Only in the case of a strong increase of $\varepsilon_{\mathrm{n.tot.}N}$ with

respect to the initial strain $\varepsilon_{\mathrm{n.tot.1}}$ can an impact of the test piece geometry be observed (see e.g. case NR 188 % in Figure 4.20). Since the material softening and the formation of set takes place uniformly within the strip, the strain at maximum deflection $\varepsilon_{\mathrm{n.tot.}N}$ cannot change over cycles, assuming perfect control and end clamping. The regression function shows an almost constant, slightly decreasing behaviour. This decrease might be a consequence of small movements/slippage from the test piece in the clamps, since the load on the clamping section of the strip is larger compared to the dumbbells. Another possible explanation are the small deviations in thickness of the mould sheet the strip is die-cut from, causing small material softening and set inhomogeneities.

Initially focusing on the lowest load-level, four times less increase of $\varepsilon_{\mathrm{n.tot.}N}$ over cycles for the SBR material compared to the NR material can be observed, although the increase in $\varepsilon_{\mathrm{n.set.}N}$ is very similar for both materials. Softening and set appear to distribute differently between narrow and wide sections, and, furthermore, this difference must be material-dependent. The basic statements made for the lowest load-level in Figure 4.20 hold for the higher load-level as well.

The increase of $\varepsilon_{\mathrm{n.tot.}N}$ is slightly stronger for the 2D-dumbbell compared to the type 3 dumbbell. The non-uniformity in local deformation is larger for the 2D-dumbbell. An overview over all creep rates with respect to $\ln(N)$ is given in Figure 4.21 for the NR material and in Figure 4.22 for the SBR material.
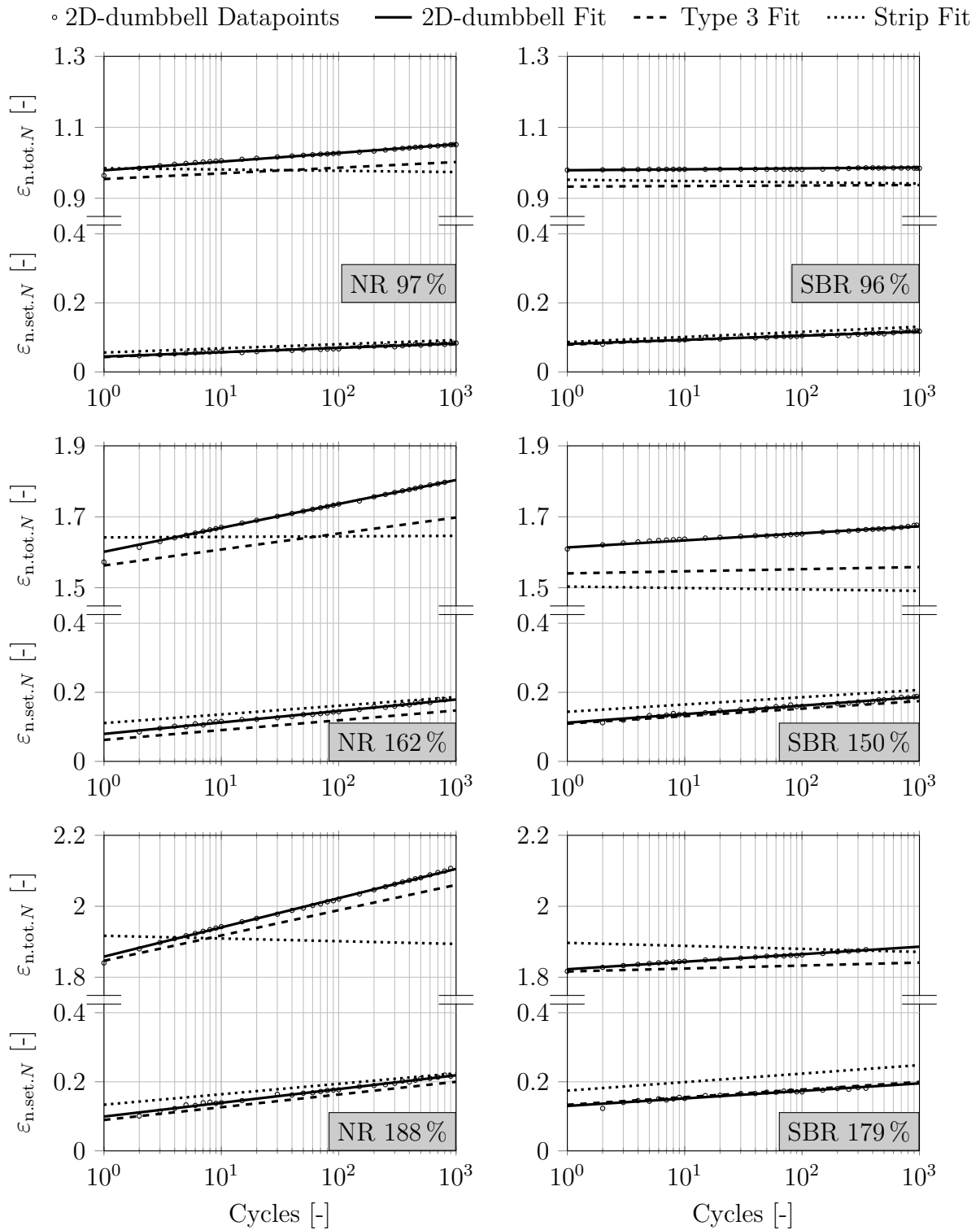
Figure 4.20: NR & SBR: $\varepsilon_{\mathrm{n.tot.}N}$ and $\varepsilon_{\mathrm{n.set.}N}$ of the three test piece geometries from Figure 4.19 measured with the Zwick test rig. Maximum deformations are intended to be equal to fatigue load cases labelled in the box within the each diagram.

The creep rate with respect to $\ln(N)$, slope of the lines in Figure 4.20, is given by:

$$\Delta\varepsilon = \frac{\mathrm{d}\,\varepsilon}{\mathrm{d}\ln(N)} \tag{4.21}$$

These creep rates are shown for the different load-level, geometries and for the strains $\varepsilon_{\mathrm{n.tot.}N}$ and $\varepsilon_{\mathrm{n.set.}N}$ in Figure 4.21 for NR and in Figure 4.22 for SBR. The data from the fatigue tests with the dumbbell (—┼—) match the data from the hundred times slower Zwick test rig (—┼—) especially for the higher load-level well, since the camera method becomes more accurate with larger strains. It is concluded that the creep rate $\Delta\varepsilon_{\mathrm{n.tot.}N}$ is much more dependent on the number of cycles rather than on time for the investigated materials. For this reason Thomas and co-workers referred to the phenomenon as cyclic creep, distinct from time-dependent creep [42].

Independent from the load-level, geometry and material, the creep rates of the set $\Delta\varepsilon_{\mathrm{n.set.}N}$ (—┼—,-▫-,···▯···) coincide. Additionally, the creep rate $\Delta\varepsilon_{\mathrm{n.tot.}N}$ of the 2D-dumbbell is always greater than the creep rate $\Delta\varepsilon_{\mathrm{n.tot.}N}$ of the type 3 dumbbell, since the the deformation is more uniform in the type 3 dumbbell. The strip test pieces always shows creep rates $\Delta\varepsilon_{\mathrm{n.tot.}N}$ close to, or slightly below, zero based on its entire uniform deformation field.
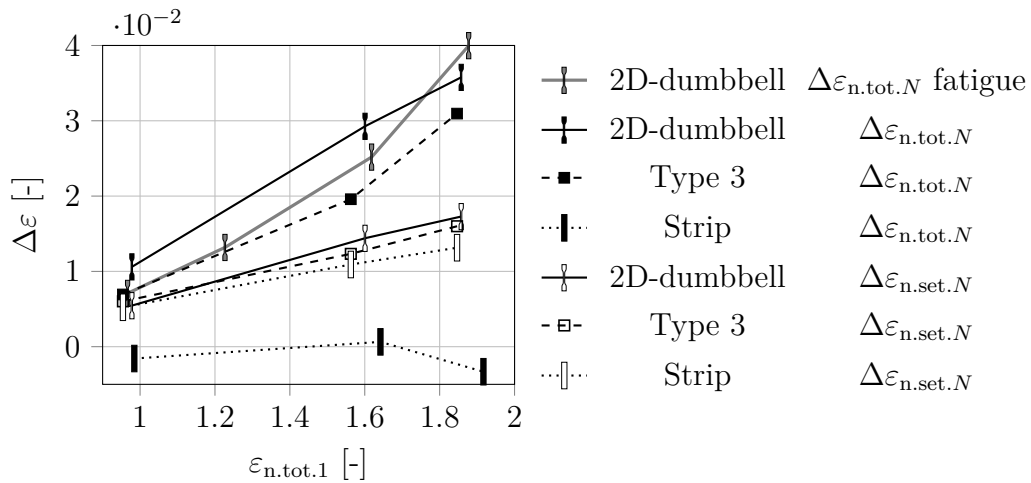
Figure 4.21: NR: Creep rates $\Delta\varepsilon$ with respect to $\ln(N)$ for the different load-level and test piece geometries. The data from the fatigue tests with the 2D-dumbbell are shown as well.
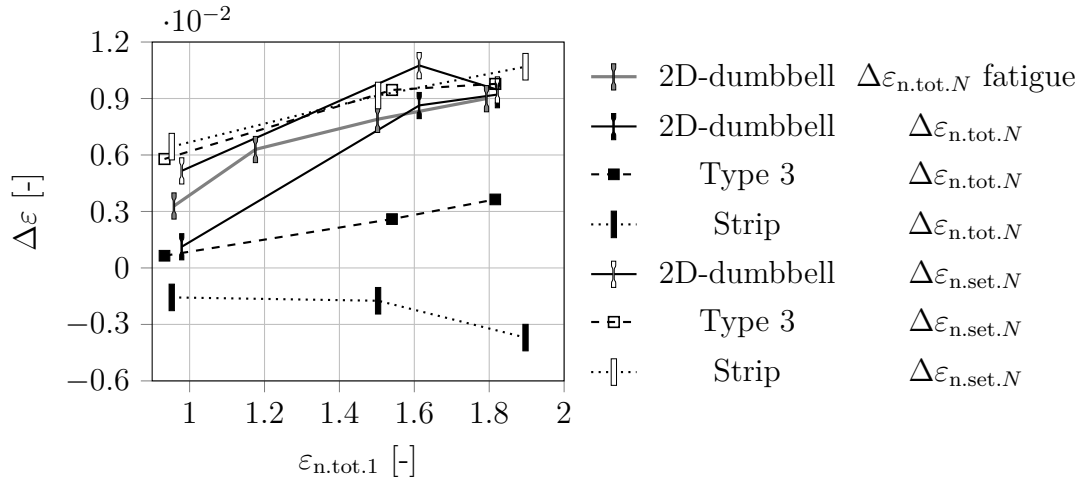
Figure 4.22: SBR: Creep rates $\Delta\varepsilon$ with respect to $\ln(N)$ for the different load-level and test piece geometries. The data from the fatigue tests with the 2D-dumbbell are shown as well.

A major difference between the NR and SBR material is the ratio of $\Delta\varepsilon_{\text{n.tot.}N}$ and $\Delta\varepsilon_{\text{n.set.}N}$ for the two types of dumbbell test pieces. For the NR material the creep rate $\Delta\varepsilon_{\text{n.tot.}N}$ is up to 3 times greater than $\Delta\varepsilon_{\text{n.set.}N}$ whereas for SBR the creep rate $\Delta\varepsilon_{\text{n.tot.}N}$ is less than $\Delta\varepsilon_{\text{n.set.}N}$ for all load-levels. Having Equation 4.10 (Page 58) in mind, the latter observation for SBR ($\Delta\varepsilon_{\text{n.tot.}N} < \Delta\varepsilon_{\text{n.set.}N}$) might be unexpected. In order to consider the interaction of the narrow with the wide section of the dumbbells and their role in the relation of $\Delta\varepsilon_{\text{n.tot.}N}$ to $\Delta\varepsilon_{\text{n.set.}N}$ a simplified linearised dumbbell model is used.

Simple dumbbell model

To word qualitative statements about the share of $\Delta\varepsilon_{\text{n.set.}N}$ on $\Delta\varepsilon_{\text{n.tot.}N}$ a simplified model of a dumbbell is introduced. The idea is to evaluate the ratio of $\Delta\varepsilon_{\text{n.tot.}N}$ and $\Delta\varepsilon_{\text{n.set.}N}$ for certain assumptions, including that of infinitesimal elastic and set strains, and afterwards qualitatively compare the results with the experimental data from Figure 4.21 and 4.22. Within the simplified model the wide section and narrow sections are replaced by linear spring-like elements. Linear springs are assumed to be sufficient since only the moments of maximum deflection are of interest using this model. These spring elements are allowed to have different moduli (E_{na}, E_{wi}), different sets ($\varepsilon_{\text{n.set.na}}, \varepsilon_{\text{n.set.wi}}$) and different initial lengths ($l_{\text{na}}, l_{\text{wi}}$). As a consequence, they undergo different deflections ($d_{\text{tot.na}}, d_{\text{tot.wi}}$) or total strains ($\varepsilon_{\text{n.tot.na}}, \varepsilon_{\text{n.tot.wi}}$), if a global deflection (d_{ovl}) is applied.
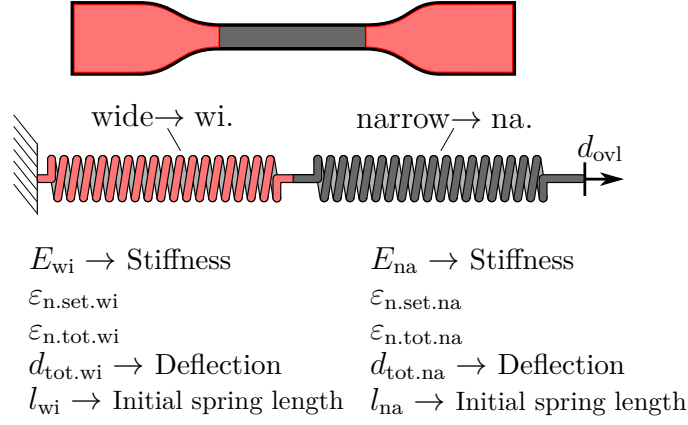
Figure 4.23: Simplified model of a dumbbell test piece.

Eliminating the stress on the simplified dumbbell in favour of the total deformation d_{ovl}, the total deflection $d_{\text{tot.na}}$ of the spring, representing the narrow section of the dumbbell, is given by:

$$d_{\text{tot.na}} = l_{\text{na}} \cdot \varepsilon_{\text{n.tot.na}} = \frac{d_{\text{ovl}} - l_{\text{na}} \cdot \varepsilon_{\text{n.set.na}} - l_{\text{wi}} \cdot \varepsilon_{\text{n.set.wi}}}{1 + \frac{E_{\text{na}}}{E_{\text{wi}}}} + l_{\text{na}} \cdot \varepsilon_{\text{n.set.na}} \qquad (4.22)$$

In order to investigate the impact of the set creep rate $\Delta\varepsilon_{\text{n.set.}N}$ on $\Delta\varepsilon_{\text{n.tot.}N}$, differentiation with respect to $\ln(N)$ of Equation 4.22 is conducted. It is initially assumed that: a) $\varepsilon_{\text{n.set.na}}$ follows a logarithmic behaviour with slope $\Delta\varepsilon_{\text{n.set.na}}$, b) $\varepsilon_{\text{n.set.wi}}$ is neglected, c) the ratio of the moduli is constant and equal to one:

$$\text{a) } \varepsilon_{\text{n.set.na}} = \Delta\varepsilon_{\text{n.set.na}} \cdot \ln(N) + b \qquad \text{b) } \varepsilon_{\text{n.set.wi}} \approx 0 \qquad \text{c) } \frac{E_{\text{na}}}{E_{\text{wi}}}(\cancel{N}) \approx 1$$

Performing the differentiation of Equation 4.22 based on these assumptions one obtains:

$$\Delta\varepsilon_{\text{n.tot.na}} = \frac{-\Delta\varepsilon_{\text{n.set.na}}}{2} + \Delta\varepsilon_{\text{n.set.na}} = 0.5 \cdot \Delta\varepsilon_{\text{n.set.na}} \qquad (4.23)$$

Based on Equation 4.23 the creep rate of $\varepsilon_{\text{n.tot.na}}$ is half of the creep rate of $\varepsilon_{\text{n.set.na}}$. A positive $\Delta\varepsilon_{\text{n.set.wi}}$ smaller than $\Delta\varepsilon_{\text{n.set.na}}$ would lower this ratio since its set is subtracted from the global deflection d_{ovl}.

This result is compared with a case where the ratio of the modulus is constant over cycles and equal to 0.32, being the ratio of the width of the narrow to the wide section (4/12.5) of the 2D-dumbbell:

$$\text{a) } \varepsilon_{\text{n.set.na}} = \Delta\varepsilon_{\text{n.set.na}} \cdot \ln(N) + b \qquad \text{b) } \varepsilon_{\text{n.set.wi}} \approx 0 \qquad \text{c) } \frac{E_{\text{na}}}{E_{\text{wi}}}(\cancel{N}) \approx 0.32$$

The differentiation of Equation 4.22 results in:

$$\Delta\varepsilon_{\text{n.tot.na}} = \frac{-\Delta\varepsilon_{\text{n.set.na}}}{1.1} + \Delta\varepsilon_{\text{n.set.na}} = 0.\overline{24} \cdot \Delta\varepsilon_{\text{n.set.na}} \qquad (4.24)$$

Lowering the ratio of the modulus leads to a lower impact of $\Delta\varepsilon_{\text{n.set.na}}$ on $\Delta\varepsilon_{\text{n.tot.na}}$. Even if the model from Figure 4.23 is a strong simplification of the dumbbell test piece made from filled rubber one can deduce, that for the extreme case of the modulus ratio of one and no significant $\varepsilon_{\text{n.set.wi}}$, the e.g. half (or more) of $\Delta\varepsilon_{\text{n.tot.na}}$ must originate from the change in modulus (material softening) ratio between narrow and wide sections of the NR 2D-dumbbell (see Figure 4.22). A much larger share of $\Delta\varepsilon_{\text{n.set.na}}$ on $\Delta\varepsilon_{\text{n.tot.na}}$ must result from change in modulus ratio for the SBR 2D-dumbbell and type 3 dumbbell. For quantitative statements about the share of $\Delta\varepsilon_{\text{n.set.na}}$ on $\Delta\varepsilon_{\text{n.tot.na}}$ it is necessary to measure $\Delta\varepsilon_{\text{n.set.wi}}$ as well. These data are missing in the present study. Even if simplified to the limits, the dumbbell model from Figure 4.23 demonstrates the vital importance of the interaction between narrow and wide dumbbell section for phenomena like $\Delta\varepsilon_{\text{n.tot.}N} < \Delta\varepsilon_{\text{n.set.}N}$.

4.2.4 Discussion and Outlook

The 2D-dumbbell is a very suitable test piece for an optical measurement of the deformation of its narrow section with a photo camera and some rulers. The quantification of the relative significances of set and material softening as contributions to change in $\varepsilon_{\text{n.tot.}N}$ suggests that only a minor share of the overall $\varepsilon_{\text{n.tot.}N}$ change originates from the set, in the case of the highest cyclic deformation of the NR material. Significantly more of the $\varepsilon_{\text{n.tot.}N}$ change originates from the set in case of the NR material. The set and material softening ratios change between the narrow and the clamping area of the dumbbell are material, loading and geometry dependent. Even for displacement-controlled testing, the changes of $\varepsilon_{\text{n.tot.}N}$ over cycles are not comparable between different but similar test piece geometries. For the exact same material the rate of $\varepsilon_{\text{n.tot.}N}$ increase might be significantly different for a diabolo to that for an AE2 test piece (e.g. used in [52,53,58–60,85,86]), since both test pieces differ in their overall load inhomogeneity (see Figure 4.24).
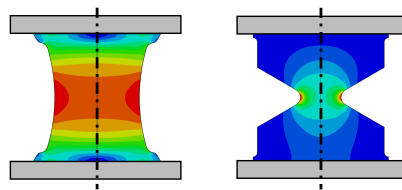
Figure 4.24: Diabolo and AE2 test piece. Both with $100\,\%$ maximum principal nominal strain $\varepsilon_{\text{n.max}}$ at the spot of maximum deformation.

A possible solution for the imponderables that follow from the non-constant strain over cycles comes from appropriate material models implemented in a finite element (FE) software. One of these models - the Plagge-model - is introduced in Section 2.2; other possible appropriate models can be found in [87]. The suitability of Plagge's model originates from its approximately linear stress relaxation behaviour over log(time), as

observed in the test data reported here and in the prior literature. The model's material parameters are fitted using the strain-controlled uniaxial tensile test data containing different amplitudes, loading velocities as well as dwell times at different loads (see Figure 4.31 within the subsequent Section 4.3). The simple symmetric geometry of the 2D-dumbbell and the axis-symmetric geometries of the diabolo and AE2 test piece allows a simulation of 1,000 load-cycles in an acceptable time. Only the lowest and the uppermost load-level is simulated in case of the dumbbell (see Figure 4.25). The level of agreement between the fatigue test data and numerical results is acceptable, having in mind that the loading velocities in the fatigue tests are very much greater than in the test campaign used for the parameter identification. For the simulations of the diabolo and AE2 test piece an arbitrary, but similar for the first cycles, amplitude is chosen; the Plagge model was used with NR material properties. The strong influence of the load inhomogeneity is shown in Figure 4.26.
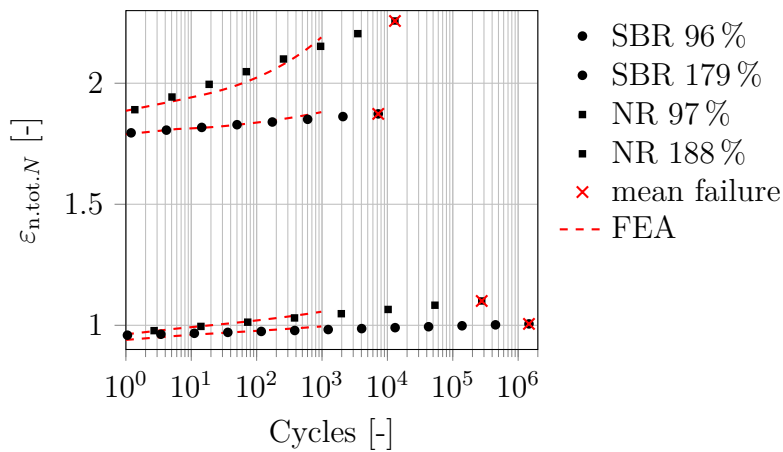
Figure 4.25: NR & SBR: Comparison of the measured (•, ▪ symbols) with the predicted (FEA; Plagge model) $\varepsilon_{\mathrm{n.tot.}N}$ over cycles for the 2D-dumbbell.
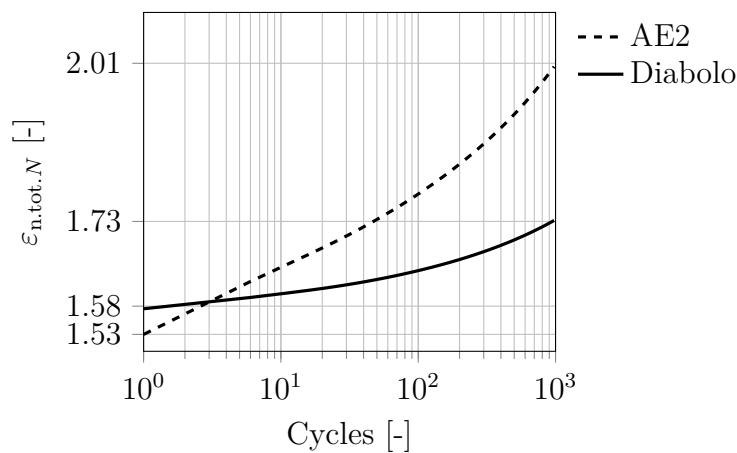
Figure 4.26: NR: Comparison of the diabolo and AE2 test piece FEA results, Plagge model. The simulations are based on the NR material parameters.

4.2.5 Conclusions

- For filled rubber test pieces and engineering components with inhomogeneous strain fields but undergoing constant end-to-end displacement cycles, the local strains depend not only on the current overall displacement, but also on the number of times it has been applied.

- This change of distribution of local strain during cyclic loading with constant displacement amplitude is strongly material and amplitude dependent.

- Moreover it is found that not only the magnitudes but also the relative significances of set and material softening are material and strain-amplitude dependent. A filled NR suffers greater softening, but similar set to, a filled SBR.

- Neither of the contributions (set and material softening) can be neglected for the investigated materials.

- The stress-dependence of the relative material softening and increase in set results in inhomogeneous softening and set evolution between, for example, wide and narrow sections of a dumbbell.

- As a result, the strength of the strain shift must also depend on the geometry of the cyclically loaded test piece or engineering component. In detail, it must depend on the ratio of deformation in the highly stressed and lightly stressed cross sections.

- In order to accurately calculate the strain evolution over cycles for a general engineering component, FE-analyses using an advanced material model, able to describe the cyclic relaxation, softening and set, is necessary.

- If constant stress or strain are not accessible within fatigue tests, a transfer of continuously changing strains into Wöhler curve-compliant constant equivalent strain is necessary. Two methods are proposed to transfer the continuously changing strains into constant equivalent strain, and lead to approximately the same result. Both calculated constant equivalent strain are close to the strains measured just before to the failure of the dumbbell.

4.3 A new fatigue test piece

The design of a new test piece stems from the currently available choice of fatigue test piece geometry. As discussed in Section 3.3, the majority of the fatigue test pieces suffer from crack initiations with locus at their surface. Fatigue results using these test pieces might be significantly influenced (even biased) by the surface finish of the mould or more specific the properties of the partition line. In order to approach this issue, Brüger et al. [66] introduced a fatigue test piece with two-sided bonded convex shaped inserts, to shift the maximum deformation from the surface to the bulk material. This test piece serves as foundation for the design of a new geometry within this section. Having Wöhler's principal of end-of-life prediction in mind (see Section 1.2), these simple test pieces should be free of crack initiations with locus at surface features, unless the very same quality of surface features is present at the component or test piece to be compared with. However, the surface properties of the simple test pieces, used as surrogates for real components, are likely to be significantly different to the surface properties of components. In some cases, the components may even fail due to crack initiation within the bulk material.

As an additional requirement for the new test piece, a uniaxial strain-state shall be present at the locus of failure initiation, to enable a direct comparison of the lifetime results of this new test piece with a selection of the previously introduced ones (see Section 3.3).

4.3.1 Material and its numerical description

The two filled NR and SBR compounds from Section 4.2, shown in Table 4.1, are used. Their stress-strain-characteristic is determined via a strain-controlled quasi-static multi-hysteresis test with six different load-levels and five cycles per load-level. As a first step, the design of the new test pieces is based on pure hyperelastic material-models only. The neo-Hookean and Arruda-Boyce material models are chosen to describe the average stress-strain-behaviour of the NR and SBR material (see Section 2.2). As shown in Figure 4.27 and 4.28, hysteresis loops need to be chosen from the whole data volume when using pure hyperelastic material-models. For the determination of material parameters, only the last (assumed to be *softened*), of the five cycles from three chosen load-levels are considered. This is done because the design is conduced in the framework of fatigue testing with many load-cycles applied on the test piece.
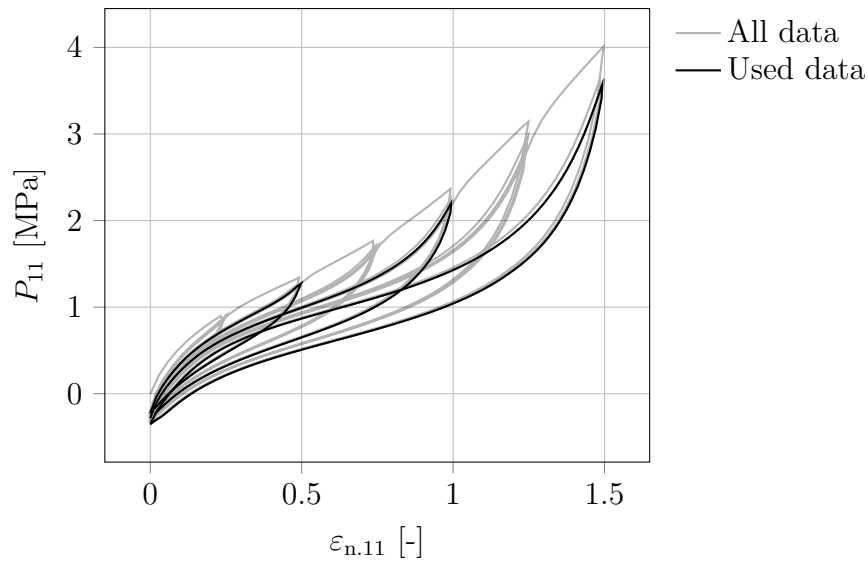
Figure 4.27: SBR: Data of a pure shear quasi-static multi-hysteresis test.
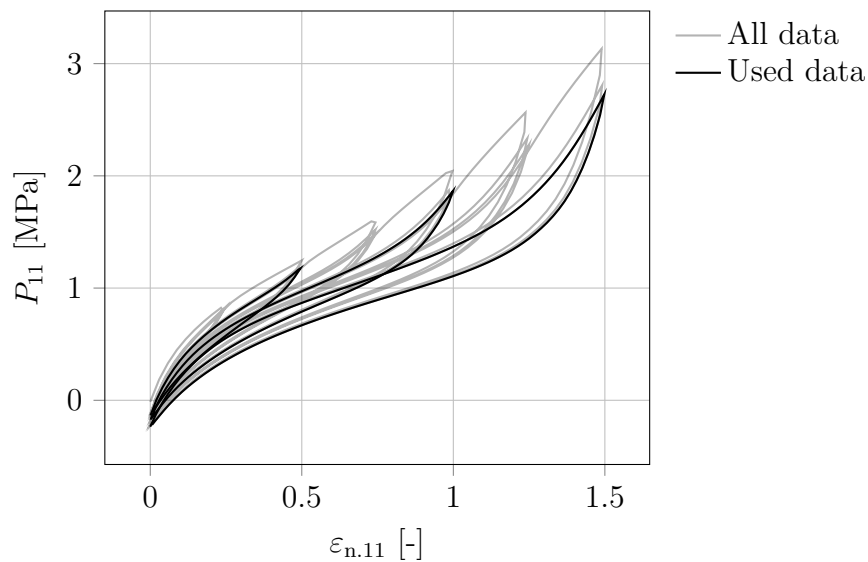
Figure 4.28: NR: Data of a pure shear quasi-static multi-hysteresis test.

However, not only one set of parameters is determined for the chosen *softened* data per material and material model. Instead, one fit is performed for each load-level to take the material-softening into account (see Figure 4.29 and 4.30). The parameters are listed in Table 4.7.
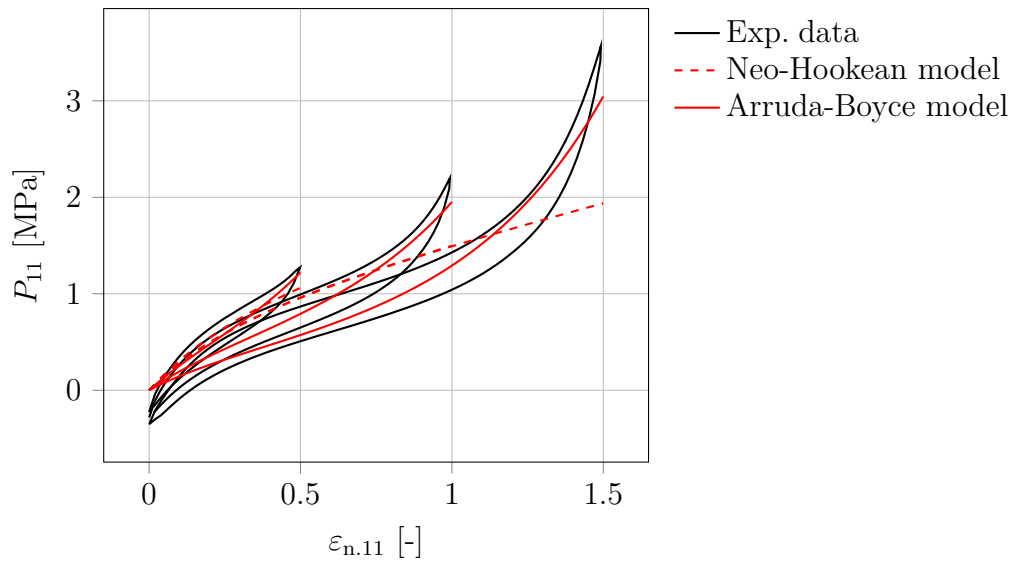
Figure 4.29: SBR: The data are fitted with the hyperelastic neo-Hookean and Arruda-Boyce model based on the selected test data from Figure 4.27. A fit is performed for each hysteresis loop (see material parameter in Table 4.7).
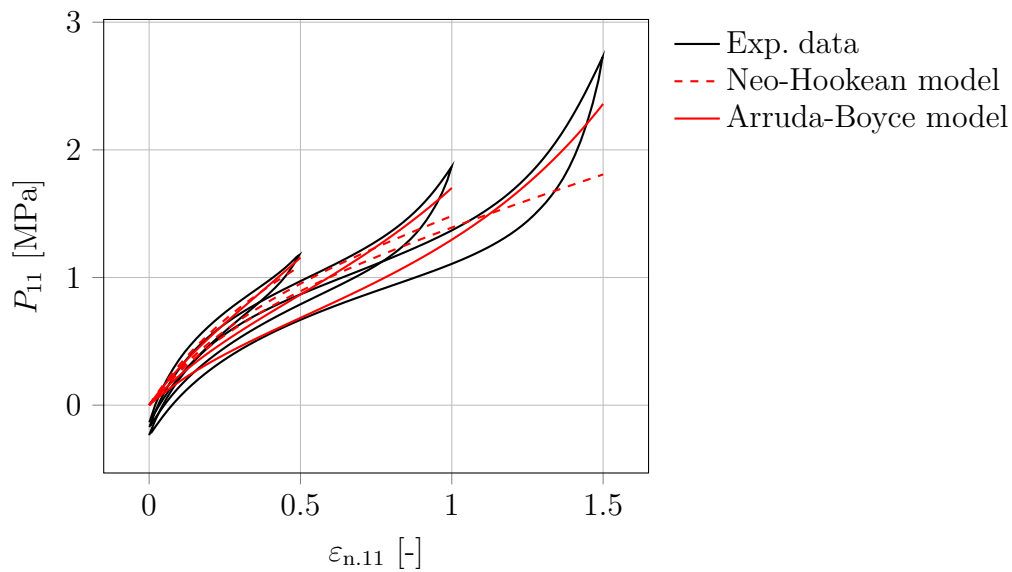
Figure 4.30: NR: The data are fitted with the hyperelastic neo-Hookean and Arruda-Boyce model based on the selected test data from Figure 4.28. A fit is performed for each hysteresis loop (see material parameter in Table 4.7).

		Neo-Hookean	Arruda-Boyce	
	Hys. loop	G [MPa]	G [MPa]	N
NR	50 %	0.9	0.55	2.10
	100 %	0.8	0.5	2.86
	150 %	0.74	0.41	3.13
SBR	50 %	0.88	0.27	1.17
	100 %	0.8	0.34	1.85
	150 %	0.8	0.28	2.13

Table 4.7: Material parameters of Figure 4.29 and 4.30. The column labelled with 'Hys. loop' indicates the hysteresis loops on the basis of the maximum strain within the single loops.

The Arruda-Boyce model with the material parameters listed in Table 4.7 is used in Section 4.3.2 for a manual geometry parameter study, as well as in Section 4.3.3 for the automated design of the new test piece. Within the automated design, the optimisation algorithm performs up to tens of thousands single finite element simulations of an eight parametric optimisation problem. The Arruda-Boyce model provides an acceptable compromise between accuracy and numerical computation time. However, the neo-Hookean material model is chosen to calculate the critical hydrostatic stress $\sigma_{0.\mathrm{crit}}$ for the appearance of damage by cavitation, since this model more accurately describes the initial stiffness (see Figure 4.29 and 4.30, up to 20 % strain). Deformations are rather small in regions of cavitational damage risk due to the near incompressible material behaviour of rubber. This approach is supposed to consider the reduced material softening in the regions of small deformations.

For the determination of the local $\varepsilon_{\mathrm{n.max}}$-values for the Wöhler plots in Section 4.3.5 and 4.3.7, a more sophisticated material model, the Plagge-model, is chosen (see Section 2.2). Apart from the calculation of the strain-field, the Plagge-model is applied for the geometry optimisation for the second version of the new test piece (see Section 4.3.6). For this optimisation only three geometry parameters are varied. Thus, much less FE-simulations are performed by the optimisation algorithm. For the material parameter identification multi-hysteresis tests including dwell-periods and a variation in strain-rates (see Figure 4.31 and 4.32) are conducted. Within each load-level, the test piece is cycled ten times with strain rates of $\dot{\varepsilon}_{\mathrm{n.11}} = 7\,\frac{\%}{\mathrm{s}}$, $\dot{\varepsilon}_{\mathrm{n.11}} = 3\,\frac{\%}{\mathrm{s}}$ and $\dot{\varepsilon}_{\mathrm{n.11}} = 0.7\,\frac{\%}{\mathrm{s}}$. All cycle-blocks end with an one hour long relaxation section for each load-level. In addition to the experimental data, the fitted Plagge-model is shown as well in Figure 4.31 and 4.32. Prior, the strong impact of cyclic relaxation compared to static relaxation on the material softening was discussed in Section 4.2. For an accurate description of the experimental data the model needs to be able to correctly differentiate between cyclic and static relaxation. However, the Plagge-model currently predicts incorrectly stronger relaxation for static loading compared to an oscillating load.

The fits in stress-strain-space are shown in Figure 4.33 and 4.34. For reasons of clarity, only

the first and last cycle for each load-level is shown. The physically motivated Plagge-model does not include specific definitions covering the NR's significant ability to strain-crystallise. This results in overall less accurate fits for the NR material.
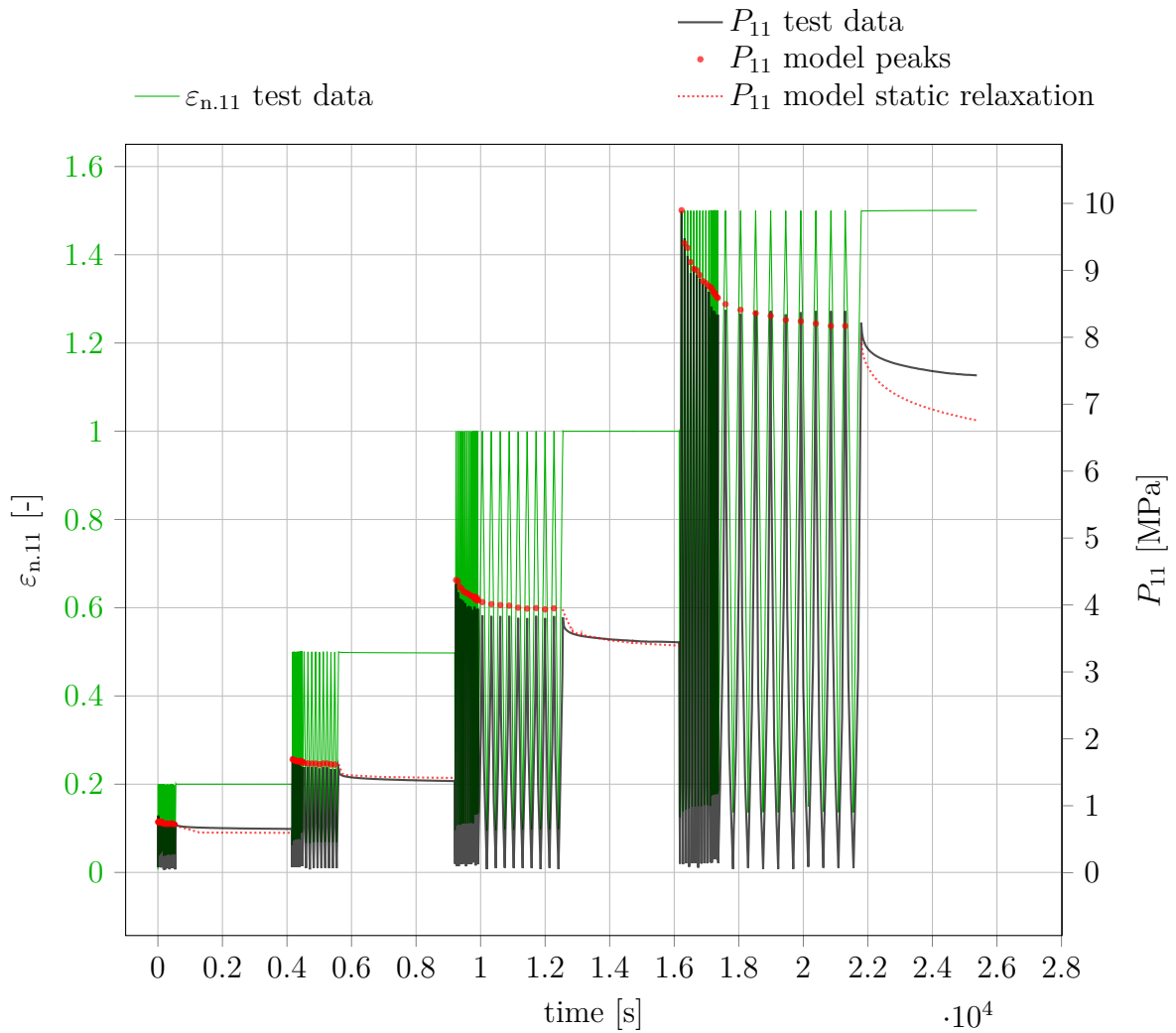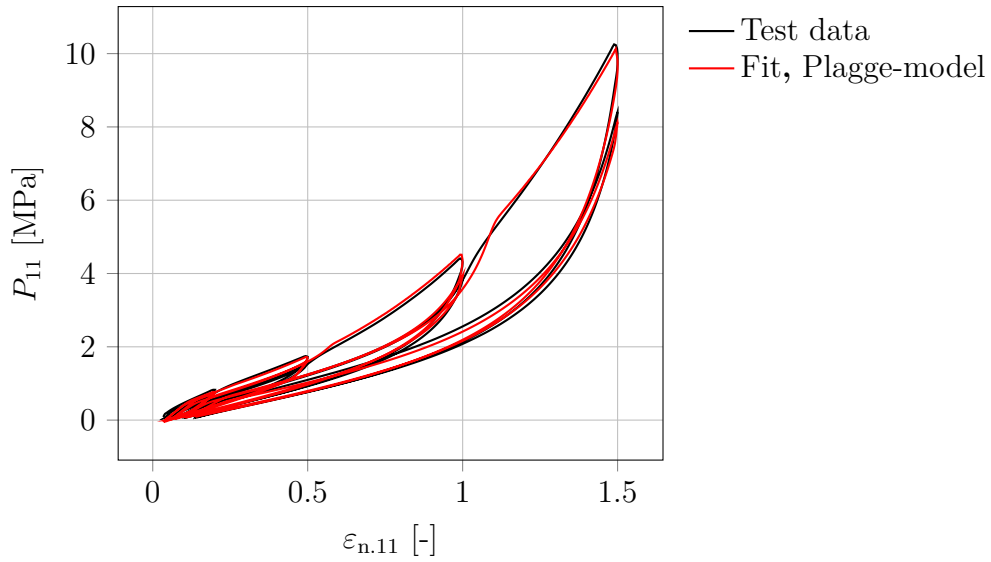

Figure 4.31: SBR: Test protocol used for the material parameters determination of the Plagge model. The measurements are performed with a uniaxial test piece.
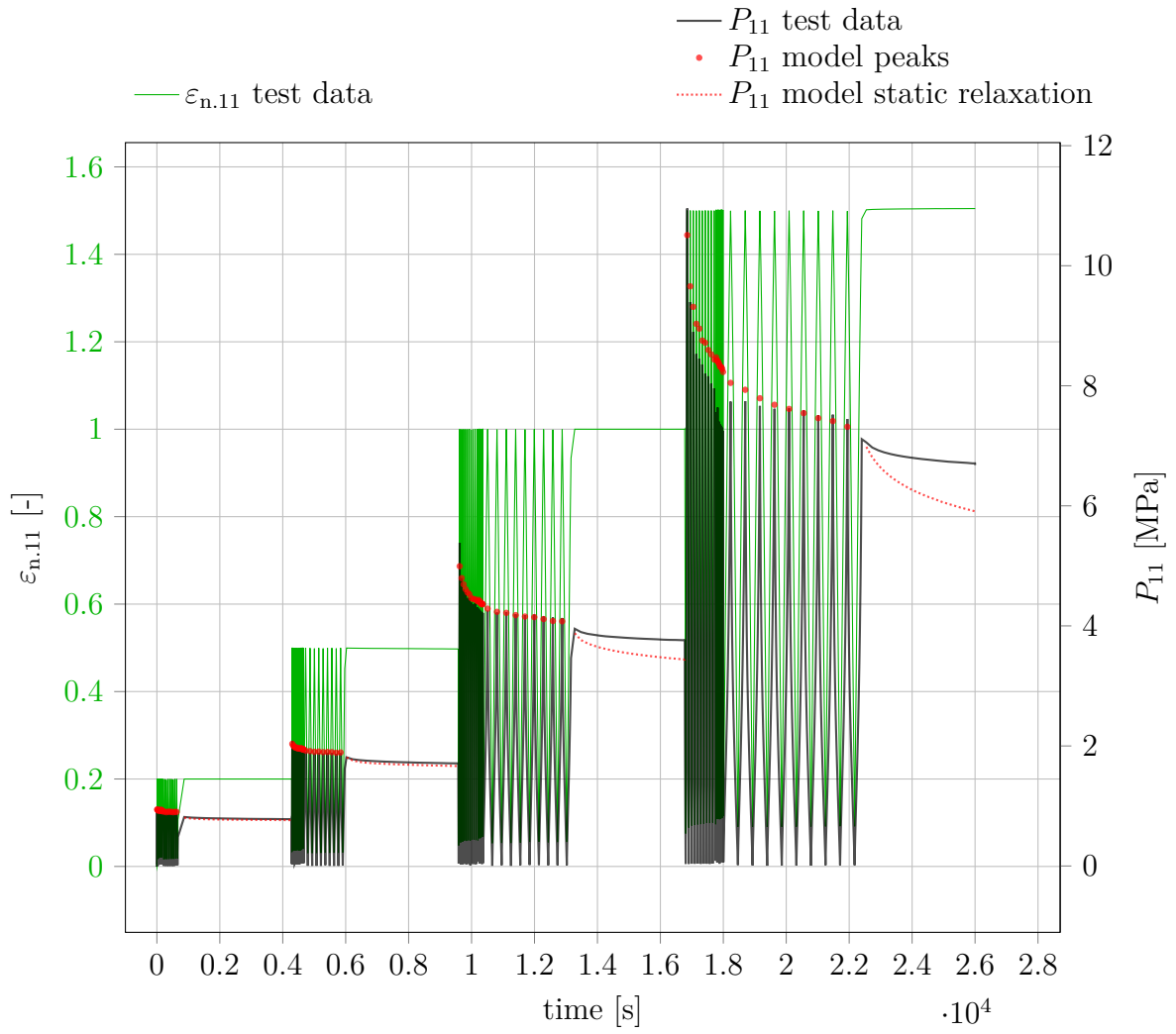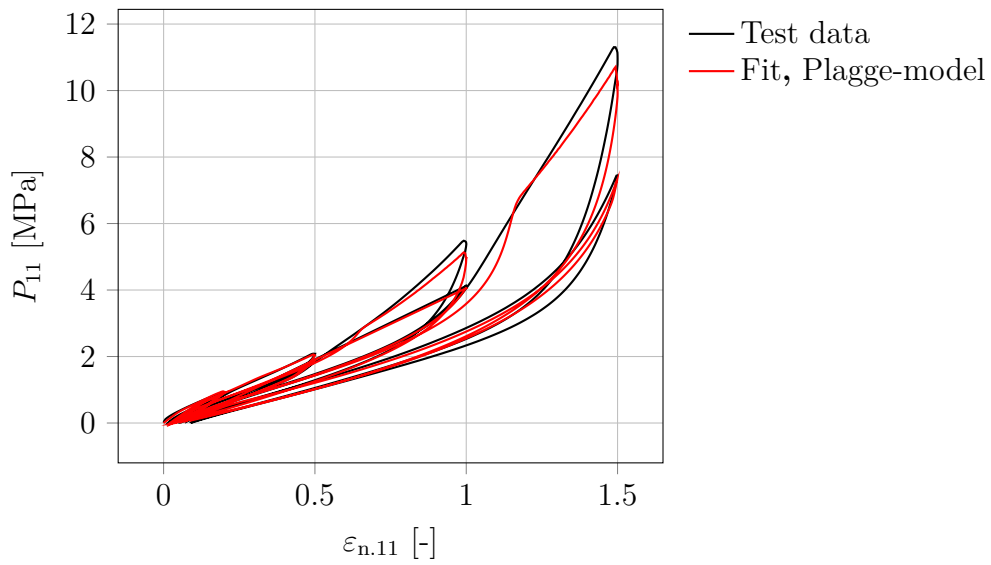
Figure 4.32: NR: Test protocol used for the material parameters determination of the Plagge model. The measurements are performed with a uniaxial test piece.

Figure 4.33: SBR: Data and fit based on a uniaxial quasi-static multi-hysteresis test (see test protocol in Figure 4.31).

Figure 4.34: NR: Data and fit based on a uniaxial quasi-static multi-hysteresis test (see test protocol in Figure 4.32).

No.	Parameter	NR	SBR
1	ϕ	0.38	0.57
2	G_c	0.38 MPa	0.61 MPa
3	G_f	0.1 MPa	0.11 MPa
4	n	36.86	19.04
5	χ	2.84	2.96
6	e_b	15.12	18.78
7	v_b	0.11	0.45
8	$\tau_{ve.0}$	473.80 s	271.33 s
9	σ_r	0.048 MPa	0.044 MPa

Table 4.8: Parameters of the Plagge-model from Figure 4.31 to 4.34.

4.3.2 Design of the new test piece - *manual* study

The design of the new test piece originates from the rotational symmetric test piece publicised by Brüger et al. [66] (see Section 3.3, Figure 3.7, Page 44). In contrast to this geometry, the two convex inserts from the test piece designed in the present study, shall be identical. Another plane of symmetry is the consequence. Figure 4.35 shows a sketch of the new test piece, considering rotational symmetry, with the six parameters needed to describe its geometry. The dashed-dotted line on the left hand side indicates the axis of rotational symmetry. The radii R_1 and R_2 describe the convex and oval geometry of the symmetric inserts. Whereas radii R_3 and R_4 dimension the curvature of the free surface.
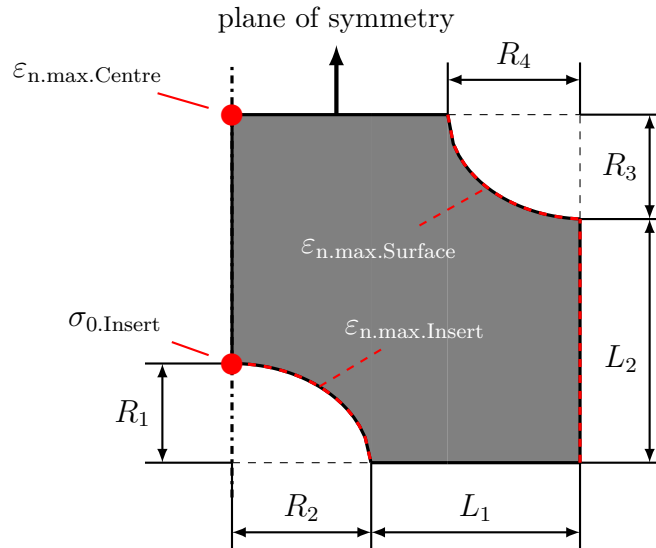
Figure 4.35: Six parametric sketch of the new test piece with a dashed-dotted line indicating the rotational symmetric axis and with a labelled plane of symmetry. Additionally, this sketch contains relevant strain and hydrostatic stress values.

Firstly, a *manual* parameter study is performed to study the impact of each geometry parameter on some chosen strain and stress values, introduced in the following. This manual study serves as foundation for the automated parameter optimisation conducted in Section 4.3.3. The hyperelastic Arruda-Boyce material model with material parameters fitted at the NR 100 % load-level ($G = 0.5$ MPa and $N = 2.86$, see Table 4.7) is applied. Using the same experimental dataset to fit the neo-Hookean material law gives a shear modulus of $G = 0.8$ MPa. As reasoned in Section 4.3.1 this neo-Hookean-based shear modulus is used to calculate the, for cavitation, critical hydrostatic stress, based on Equation 3.2 ($\sigma_{0.\text{crit}} = 2.0$ MPa).

In Figure 4.35:

- $\varepsilon_{\text{n.max.Centre}}$ is the maximum principal nominal strain at the geometrical centre of the test piece;

- $\varepsilon_{\text{n.max.Insert}}$ are the maximum principal nominal strains values along the insert contour (see red dotted line Figure 4.35), where $\max(\varepsilon_{\text{n.max.Insert}})$ yields the maximum value along the insert contour;

- $\varepsilon_{\text{n.max.Surface}}$ are the maximum principal nominal strains values along the outer surface contour (see red dotted line Figure 4.35), where $\max(\varepsilon_{\text{n.max.Surface}})$ yields the maximum value along the surface contour;

- $\sigma_{0.\text{Insert}}$ is the hydrostatic stress at the poles of the inserts.

Three evaluation criteria are chosen for the parameter study:

- Ratio of $\max(\varepsilon_{\text{n.max.Insert}})$ to $\varepsilon_{\text{n.max.Centre}}$;

- Ratio of $\max(\varepsilon_{\text{n.max.Surface}})$ to $\varepsilon_{\text{n.max.Centre}}$;

- $\sigma_{0.\text{Insert}}$.

Since the overall aim of the new test piece is the focus of the maximum deformation towards its centre, unaffected by cavitation, all three listed criteria should be simultaneously as small as possible. As a reminder, possible crack initiation at the insert shall be avoided since the region of cavitation risk is in immediate vicinity. A later judgement of the impact of the cavitation on the failure initiation would be aggravated. Futhermore, a plain strain-like deformation-state at the insert's region of maximum deformation is present. However, a uniaxial deformation-state at the location of main failure initiation is intended.

For the entire manual parameter study, the evaluation criteria are determined for $\varepsilon_{\text{n.max.Centre}} = 100$ %. Table 4.9 is an overview of the parameter study and the corresponding figures.
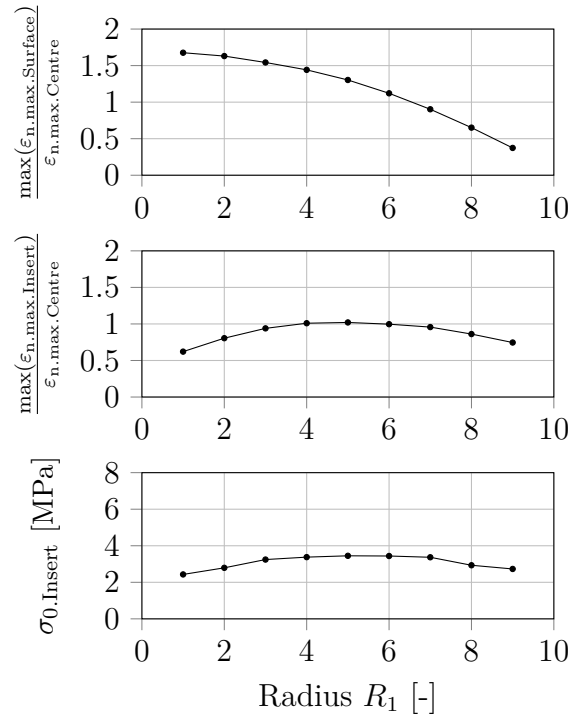
Varied Parameter	Impact on geometry	Impact on evaluation criteria
R_1	Figure 4.36	Figure 4.37
R_1 & R_2	Figure 4.38	Figure 4.39
R_4	Figure 4.40	Figure 4.41
R_3 & R_4	Figure 4.42	Figure 4.43
L_2	Figure 4.44	Figure 4.45

Table 4.9: Overview of the figures for the parameter study.

The radii R_1 - R_4 are varied while the total size of the geometry is kept constant. The parameter L_1 and L_2 are adapted to meet this restriction (except for the variation of L_2 itself). Figure 4.36 shows the geometry variation of the test piece while varying R_1 only. The impact of this variation on the three evaluation parameters is shown in Figure 4.37. A distinct decrease of $\max(\varepsilon_{\text{n.max.Surface}})$ compared to the $\varepsilon_{\text{n.max.Centre}}$ with increasing R_1 is shown. Evaluating $\max(\varepsilon_{\text{n.max.Insert}})$ with respect to $\varepsilon_{\text{n.max.Centre}}$ shows an increasing and for $R_1 > 5$ a decreasing behaviour. Considering simultaneously all three evaluation parameters, yields a great value for R_1 as best compromise. However, the value for $\sigma_{\text{0.Insert}} = 2.73\,\text{MPa}$ for $R_1 = 9$ might cause cavitation since a critical hydrostatic stress of $\sigma_{\text{0.crit}} = 2.0\,\text{MPa}$ was determined.
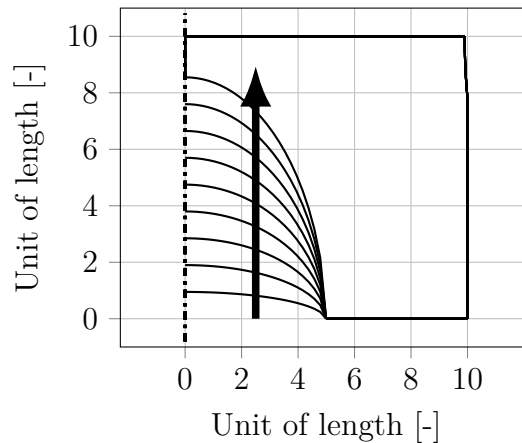
Figure 4.36: Variation of the geometry parameter R_1; change of geometry. The increase of R_1 is indicated with an arrow.

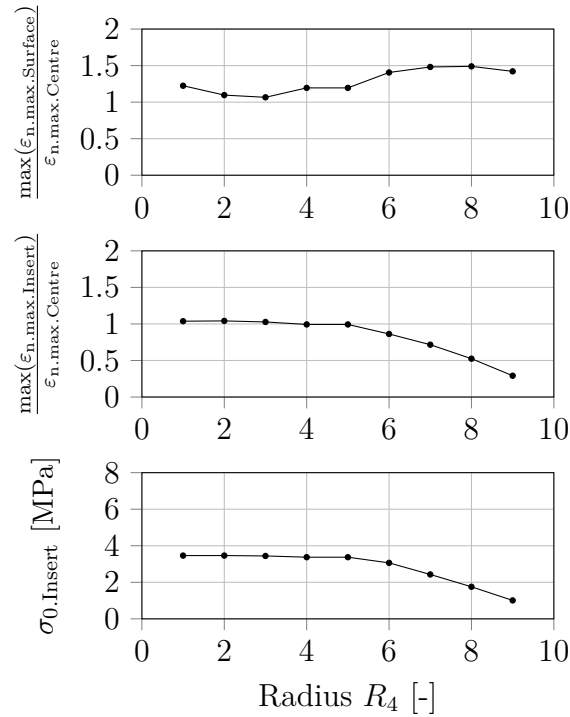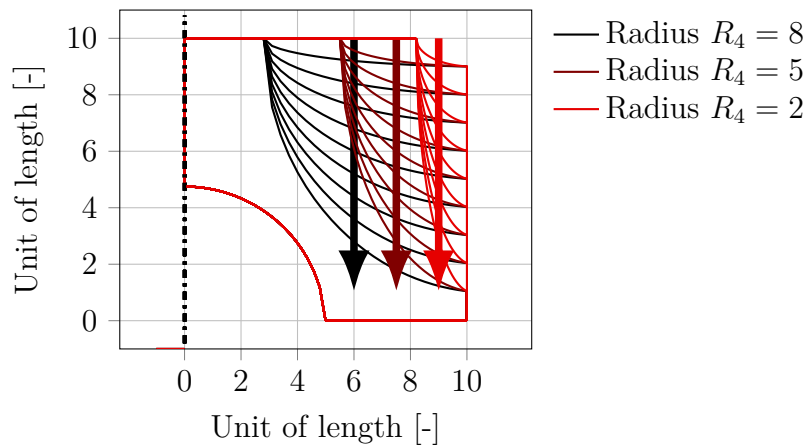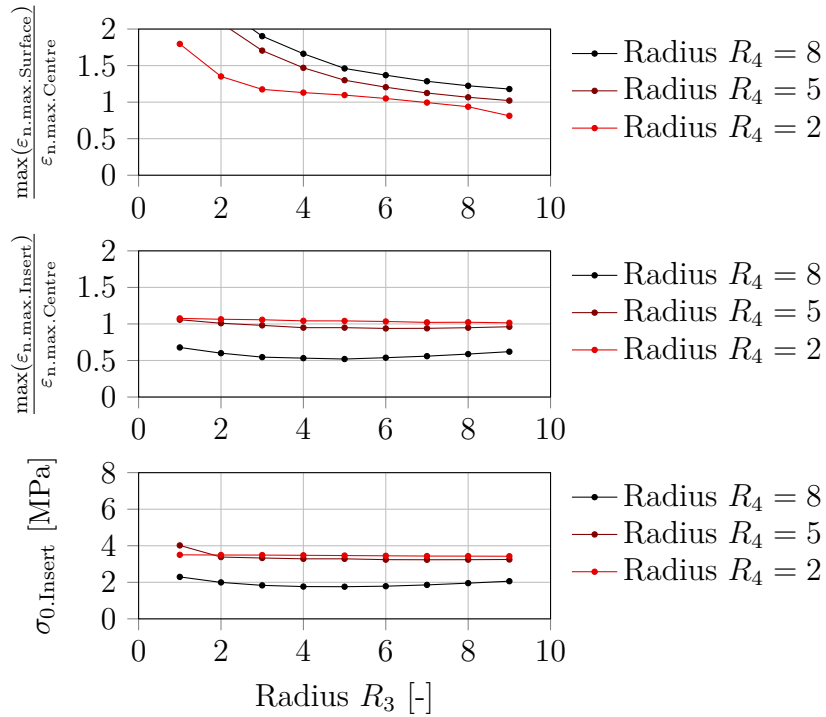**Figure 4.37:** Variation of the geometry parameter R_1; impact on the evaluation parameter.

In Figure 4.38, the change of geometry for a range of R_2 and $R_1 = 2, 5, 8$ is shown. The evaluation is done in Figure 4.39. An increase of R_2 has a positive impact on all three evaluation criteria. Solely the ratio of $\max(\varepsilon_{\text{n.max.Insert}})$ to $\varepsilon_{\text{n.max.Centre}}$ slightly increases with increasing R_2 and $R_1 = 2$. For $R_2 > 4$, $\sigma_{0.\text{Insert}}$ stays rather unaffected by any further increase of R_2 for all R_1. Overall, the increase of R_1 greatly improves all (except in one case) evaluation criteria.
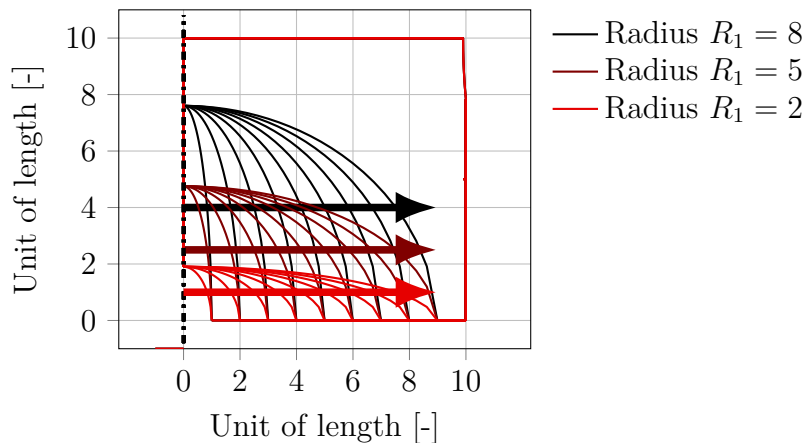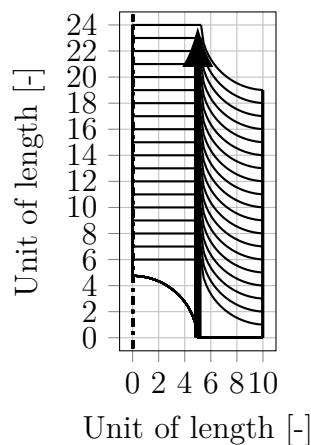

Figure 4.38: Variation of the geometry parameter R_2 and R_1; change of geometry. The increase of R_2 is indicated with an arrow.
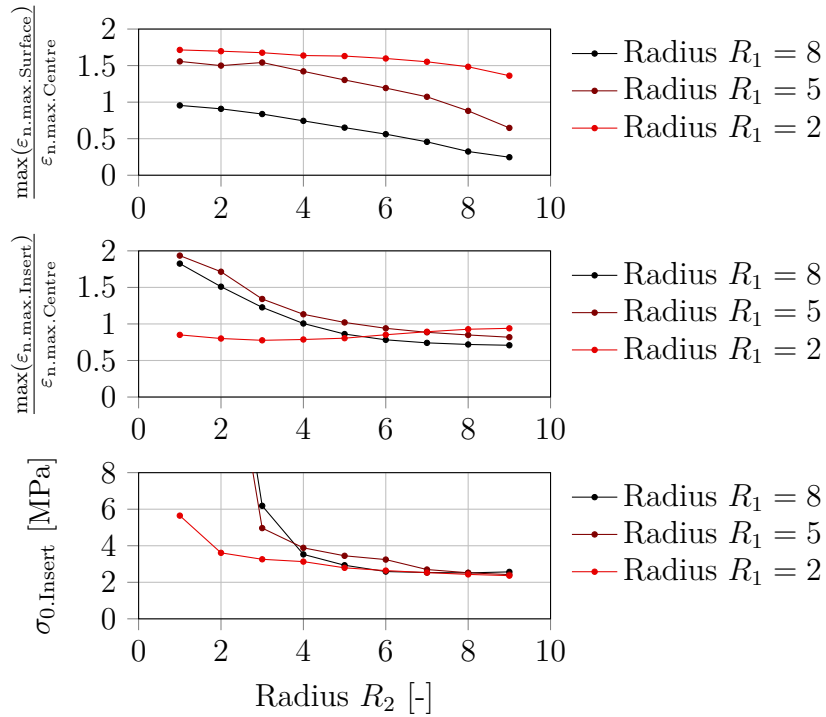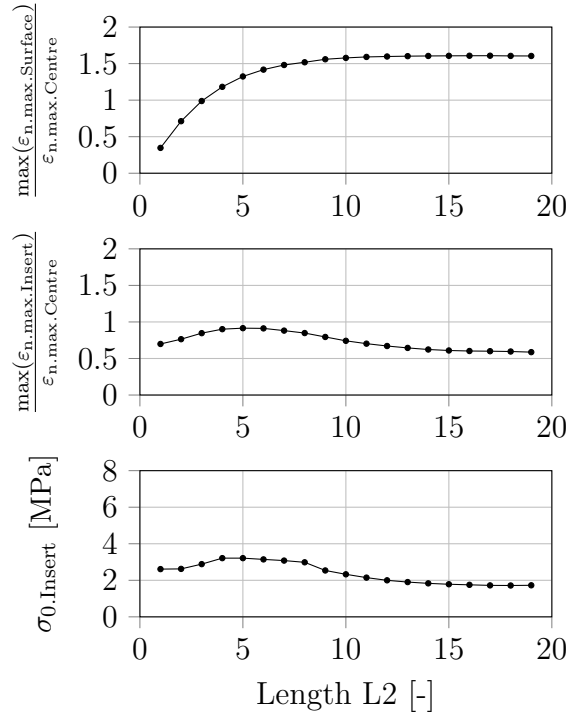
Figure 4.39: Variation of the geometry parameter R_2 and R_1; impact on the evaluation parameter.

An increase of R_4, as shown in Figure 4.40, has almost no influence up to $R_4 = 5$ (see Figure 4.41). Beyond $R_4 = 5$ the insert region becomes unloaded. Decreasing $\max(\varepsilon_{\text{n.max.Insert}})$ and $\sigma_{0.\text{Insert}}$ are the consequence. However, the deformation at the surface compared to the deformation at the centre is slightly increasing, up to a ratio of 1.5, where as < 1.0 is desired.
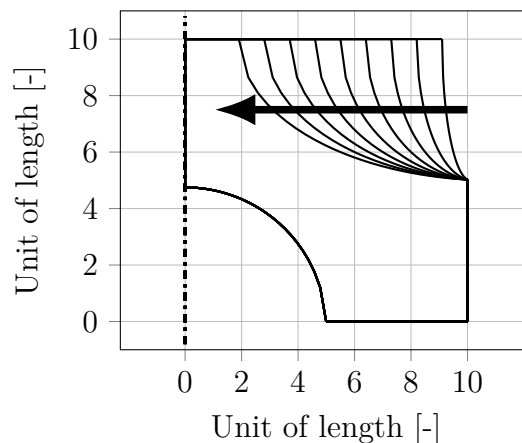
Figure 4.40: Variation of the geometry parameter R_4; change of geometry. The increase of R_4 is indicated with an arrow.

Figure 4.41: Variation of the geometry parameter R_4; impact on the evaluation parameter.

Figure 4.42 shows the variation of R_3 for three different R_4 ($R_4 = 2$, $R_4 = 5$, $R_4 = 8$). This variation is evaluated in Figure 4.43. An increase of R_3 has a positive effect on the ratio of $\max(\varepsilon_{\mathrm{n.max.Surface}})$ to $\varepsilon_{\mathrm{n.max.Centre}}$; their ratio decreases. This ratio shifts towards lower (better) values with decreasing R_4. In contrast, a decrease in R_4 yields an increase of the $\max(\varepsilon_{\mathrm{n.max.Insert}})/\varepsilon_{\mathrm{n.max.Centre}}$-ratio and $\sigma_{\mathrm{0.Insert}}$. These two evaluation parameters stay almost unaffected by the variation of R_3.

Figure 4.42: Variation of the geometry parameter R_3 and R_4; change of geometry. The increase of R_3 is indicated with an arrow.

Figure 4.43: Variation of the geometry parameter R_3 and R_4; impact on the evaluation parameter.

The last investigated parameter is the length L_2 (see Figure 4.35). Compared to the investigations of the radii R_1 - R_4, the total size of the test piece changes while varying L_2 (see Figure 4.44). The impact of the radii R_1 - R_4 on the ratio of $\max(\varepsilon_{\text{n.max.Surface}})$ to $\varepsilon_{\text{n.max.Centre}}$ is more and more lost with the increase of L_2. For $L_2 > 10$ the influence on all three evaluation criteria vanishes.

Figure 4.44: Variation of the geometry parameter L_2; change of geometry. The increase of L_2 is indicated with an arrow.

Figure 4.45: Variation of the geometry parameter L_2; impact on the evaluation parameter.

Summing up the parameter variation:

- The ratio of $\max(\varepsilon_{\text{n.max.Surface}})$ to $\varepsilon_{\text{n.max.Centre}}$ may be strongly decreased/improved by increasing $\uparrow R_1$.

- All three evaluation criteria are positively affected by a large curvature ($\uparrow R_2$ and $\uparrow R_3$).

- With increasing $\uparrow R_4$ the insert region is unloaded and therefore the ratio of $\max(\varepsilon_{\text{n.max.Insert}})$ to $\varepsilon_{\text{n.max.Centre}}$ and $\sigma_{0.\text{Insert}}$ decreases. However, the $\max(\varepsilon_{\text{n.max.Surface}})$ increases with $\uparrow R_4$.

- The length L_2 needs to be in balance with the size of the curvatures at the surface and insert. Otherwise, the ability of the insert curvature to shift the highest deformation away from the surface to the inside of the test piece, is lost for too large L_2.

In general, a balance of all geometric parameters needs to be found. No straight forward way of decreasing all three evaluation criteria at the same time to a satisfying level was found in the parameter study.

4.3.3 Design of the new test piece - automated

Based on the insights from the manual parameter investigation from the former Section 4.3.2, an automated parameter optimisation is set up. Two additional parameters (S_1

and S_4) are introduced to allow the optimisation algorithm more freedom, especially for generating large curvatures at the surface and insert.
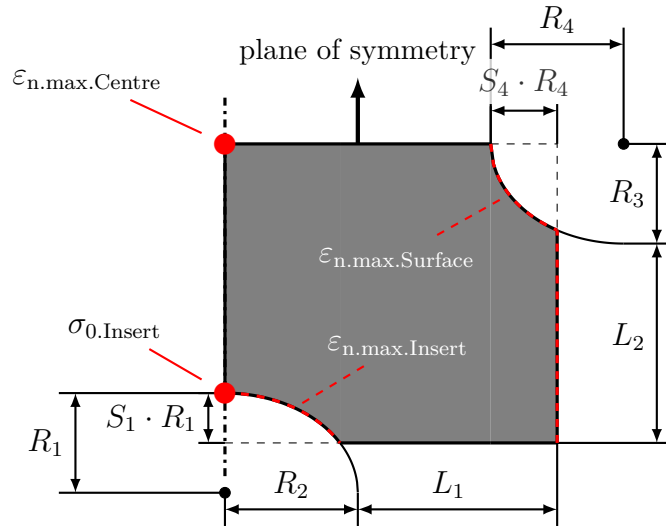
Figure 4.46: Eight parametric sketch of the new test piece with a dashed-dotted line indicating the rotational symmetric axis and with a labelled plane of symmetry. Additionally this sketch contains relevant strain and hydrostatic stress values.

The optimisation is performed using a Python-script which operates a finite element software. Within this Python-script the Differential Evolution optimisation algorithm from the *scipy.optimize* Python-package is chosen [88]. From Scipy's documentation about the Differential Evolution algorithm [89]: *Finds the global minimum of a multivariate function. Differential Evolution is stochastic in nature (does not use gradient methods) to find the minimum, and can search large areas of candidate space, but often requires larger numbers of function evaluations than conventional gradient-based techniques.* The advantages of the chosen optimisation algorithm are:

- The differential evolution algorithm is a global optimisation algorithm. It doesn't *get stuck* in local minima. First rehearsals applying an algorithm searching for local minima, turned out to be stopped dead before reaching an acceptable result.

- Upper and lower bounds for the single parameter (here for the eight geometry parameters) can be defined.

- No derivatives or similar extra information need to be provided.

However, the downside is an increased number of function calls (here, FEAs) compared to other algorithm as described in [89].

The six parameters (R_1, R_2, R_3, R_4, L_1 and L_2) are chosen to be restricted between 1 and 20. Whereby the shift-parameters (S_1, S_4) are only allowed to take on values between 0.1 and 1. The target function to be minimised within the optimisation is defined as:

$$f_{\text{target}} = f\left(\frac{\max(\varepsilon_{\text{n.max.Surface}})}{\varepsilon_{\text{n.max.Centre}}}\right) + f\left(\frac{\max(\varepsilon_{\text{n.max.Insert}})}{\varepsilon_{\text{n.max.Centre}}}\right) + \frac{\sigma_{0.\text{Insert}}}{\sigma_{0.\text{crit}}} \tag{4.25}$$

Function $f()$ is defined as shown in Figure 4.47. It returns the value 0.6 for input values smaller than 0.6. Thanks to that, the algorithm focusses on the reduction of $\sigma_{0.\text{Insert}}$ for ratios of $\max(\varepsilon_{\text{n.max.Surface}})/\varepsilon_{\text{n.max.Centre}}$ or $\max(\varepsilon_{\text{n.max.Insert}})/\varepsilon_{\text{n.max.Centre}}$ less than 0.6. The threshold value of 0.6 is initially arbitrary since no data are available to judge the influence of surface inhomogeneities on the lifetime.
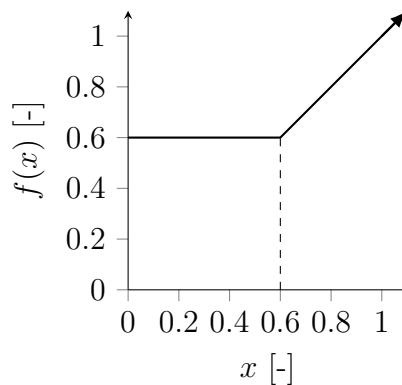
Figure 4.47: Function $f()$.

The optimisation is performed for the NR material, SBR material and three different $\varepsilon_{\text{n.max}}$ at the centre of the test piece (see Table 4.10). For each of these cases, material parameters for the Arruda-Boyce material model are given in Table 4.7.

	NR	SBR
	50 %	50 %
$\varepsilon_{\text{n.max.Centre}}$	100 %	100 %
	150 %	150 %

Table 4.10: Optimisations are performed for the shown six conditions.

Figure 4.48 shows the optimisation results for the six cases from Table 4.10.
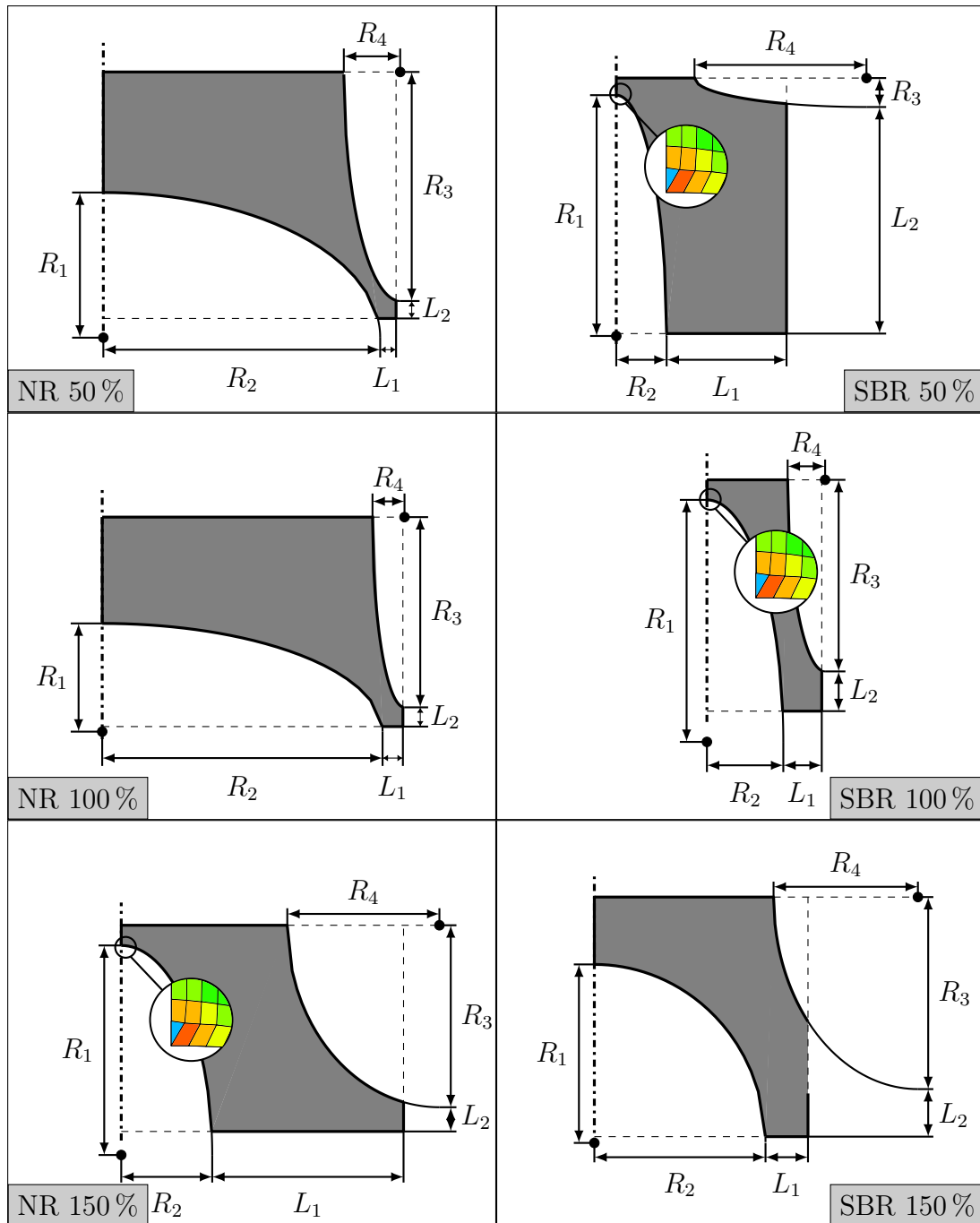
Figure 4.48: Calculated optimum for the given target function, materials and strain levels at the center.

Unfortunately, three of the six solutions show issues with the finite element mesh. The optimisation algorithm found a geometry where the automatic finite mesh generator places a triangle element at the position where $\sigma_{0.\text{Insert}}$ is evaluated. Too low values for $\sigma_{0.\text{Insert}}$ is the consequence, leading to an erroneously reduced target value. Nonetheless, the optimisations are not repeated with improved settings for the mesh generator since the remaining results are satisfactory and one optimisation run takes up to one or two weeks. Especially the results for the NR 50 % and NR 100 % case are matching the insights from

the manual parameter study well (see summary of Section 4.3.2). The algorithm chooses a big curvature for the surface and for the insert. The result from the NR 100 % case is chosen as foundation for a manual fine-tuning.

For the Brüger test piece only a small difference between surface and centre strain (ratio = 0.9) can be found, as shown in Figure 3.7 (see Section 3.3). However, no surface crack initiations are reported by Brüger et al. [66]. Instead, cracks initiate at the insert close to a region with risk of damage by cavitation. Because of these findings, the focus of the manual fine-tuning is to further reduce $\sigma_{0.\mathrm{Insert}}$, $\max(\varepsilon_{\mathrm{n.max.Insert}})$ and shift the locus of maximum $\max(\varepsilon_{\mathrm{n.max.Insert}})$ further away from the point of maximum σ_0 at the insert. The last measure simplifies the later distinction between cavitation and non-tri-axial deformation caused crack initiation. The result of the manual fine-tuning is shown in Figure 4.49. Compared to the Brüger test piece, the hydrostatic stress reduces from $\sigma_0 = 2.30\,\mathrm{MPa}$ to $\sigma_0 = 1.77\,\mathrm{MPa}$ ($\sigma_{0.\mathrm{crit}} = 2.0\,\mathrm{MPa}$, Equation 3.2) for $\varepsilon_{\mathrm{n.max.Centre}}{=}100\,\%$. This reduction is partly achieved by adding a small concave section at the insert. Focusing on the result of the NR 100 % case in Figure 4.48, the low values of L_1, L_2 and R_4 stand out. The optimisation algorithm approached the lower bonds for these parameters to generate the large curvatures of the insert and the free surface. In order to further increase these curvatures, L_1 and L_2 are set zero and the free surface changed to a flat (infinite curvature) section. A convex design for this section has been considered as well, however, failed to reduce the deformation at the surface.
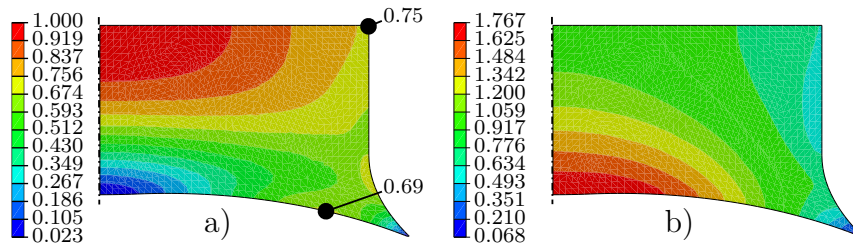
Figure 4.49: NR: New final test piece geometry after manual fine-tuning; a) Strain $\varepsilon_{\mathrm{n.max}}$ and b) hydrostatic stress σ_0 mapped on the non-deformed geometry.

4.3.4 Reference Experiments - 2D-dumbbell test piece

The fatigue results from the new test piece (objective: crack initiation with locus in the bulk) designed in the former section, is benchmarked with the fatigue results of the 2D-dumbbell test piece.

On the one hand, the 2D-dumbbell is chosen as reference since it is recommended by the Standard ISO6943 [47]. On the other hand, the corners of the 2D-dumbbell are subjected to large deformations during the die-cut from a sheet. Because of that, a certain propensity of the cracks to the surface is assumed. In former Section 4.2, a detailed assessment of the fatigue results can be found. Yet, an evaluation of the locus of failure initiation is missing

and is completed subsequently.

A tremendous difference in cracking behaviour between the NR and SBR material is found. The 2D-dumbbells made from NR, show the often reported (e.g. [57]) multi-crack initiation (the SBR-based dumbbells do not) as shown in Figure 4.50. Moreover, these multi-cracks preferentially initiate at the corner of the 2D-dumbbell's cross-section.
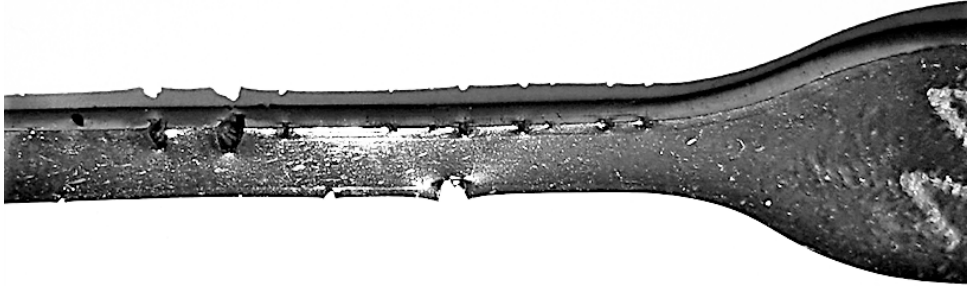

Figure 4.50: NR: Typical multi-crack initiation at the 2D-dumbbell.

The locus of the crack initiation of the main crack, responsible to for final rupture of the dumbbell, is investigated with a microscope (see Figure 4.51). As statistically evaluated in Figure 4.52, the majority of the cracks start in the corner of the fracture surface.
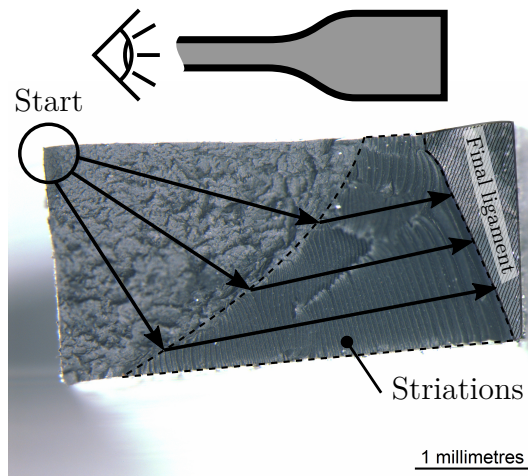
Figure 4.51: NR: Typical fracture surface of the 2D-dumbbell.

Half of the fracture surface area exhibits striation patterns, as shown in Figure 4.51. The ratio between striation area and cross section area increases with the load-level. Figure 4.51 shows an example of the uppermost load level. This very regular pattern is often associated with NR's ability to form crystals during straining. However, they have no further relevance for the present study. Additional information to striations can be found in Poisson et al. [78], Le Cam and Toussaint [90], Flamm et al. [61], Munoz et al. [91], Le Cam et al. [92] or Ruellan et al. [93].
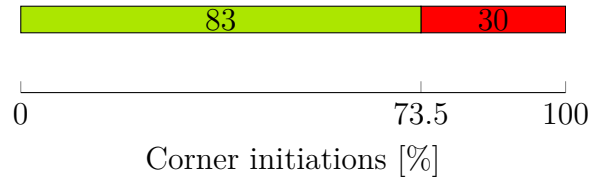
Figure 4.52: **NR**: Corner initiations (yes: green) of the 2D-dumbbell in number of test pieces in the bar and percent at the axis label. Results from the NR material. Hence, the colour red is associated with crack initiation with locus in the bulk material or at the edges in between the corners.

The corner cracks of the NR-based 2D-dumbbell initiate preferably at the side that is facing the punch knife, indicating the die-cutting and the associated large deformations at this corner as causal for the results from Figure 4.51.

In contrast to the NR surface/corner cracks, the main cracks of the dumbbells made from the SBR material initiate with a probability of 97 % at particles (see Figure 4.53). The distribution of these critical particles was found to be perfectly random over the fracture surface; there is no propensity of cracks to initiate at particles close to the surface (Figure 4.53-right) or within the bulk material (Figure 4.53-left) of the dumbbell. Opposed to NR's multi-crack initiation, there is only one single macro-crack per dumbbell found being responsible for the final fracture of the test piece.
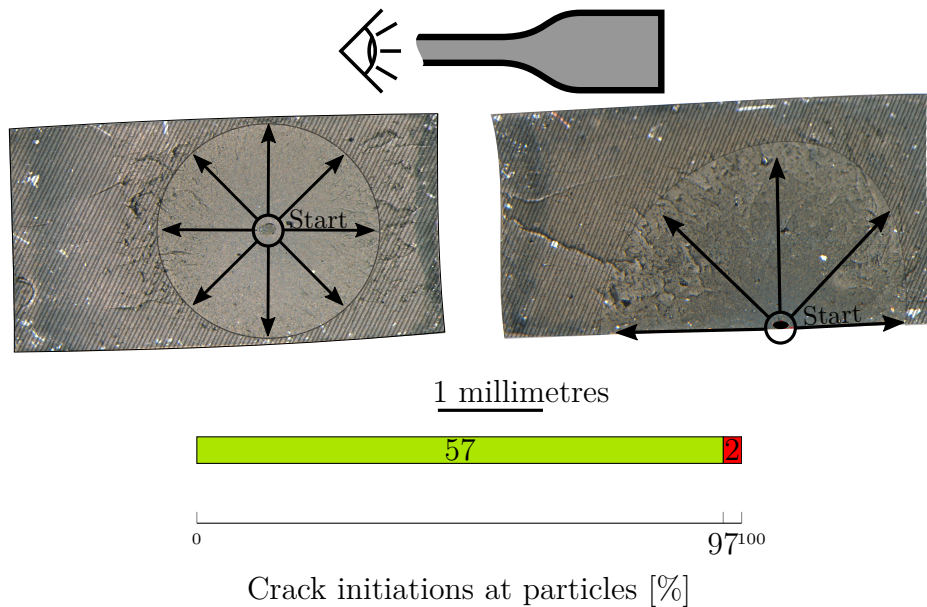

Figure 4.53: **SBR**: Crack initiations at particles (yes: green) in number of test pieces in the bar and percent at the axis label. Hence, the colour red is associated with crack initiation with locus not at the particles but e.g. at the corner.

This crack initiation behaviour of the SBR material, enables an evaluation of the influence of the particle size on the number of the cycles to failure (see Figure 4.54). The

evaluation is performed for each of the four load-levels. No distinct correlation between maximum visible particle size and number of cycles to failure is evident as shown in Figure 4.54. Same was found for another filled synthetic elastomer by Balutch et al. [94]. However, instead of the maximum visible size of the particle, they used a representative dimension defined as the "*square root of the area of a defect projected in the direction of the maximum tensile stress*" (first proposed by Murakami and Endo [95]). This measure is not used in the present work since the length of a slim but long object is assumed to damage its surrounding polymer matrix stronger, compared to its projected area.
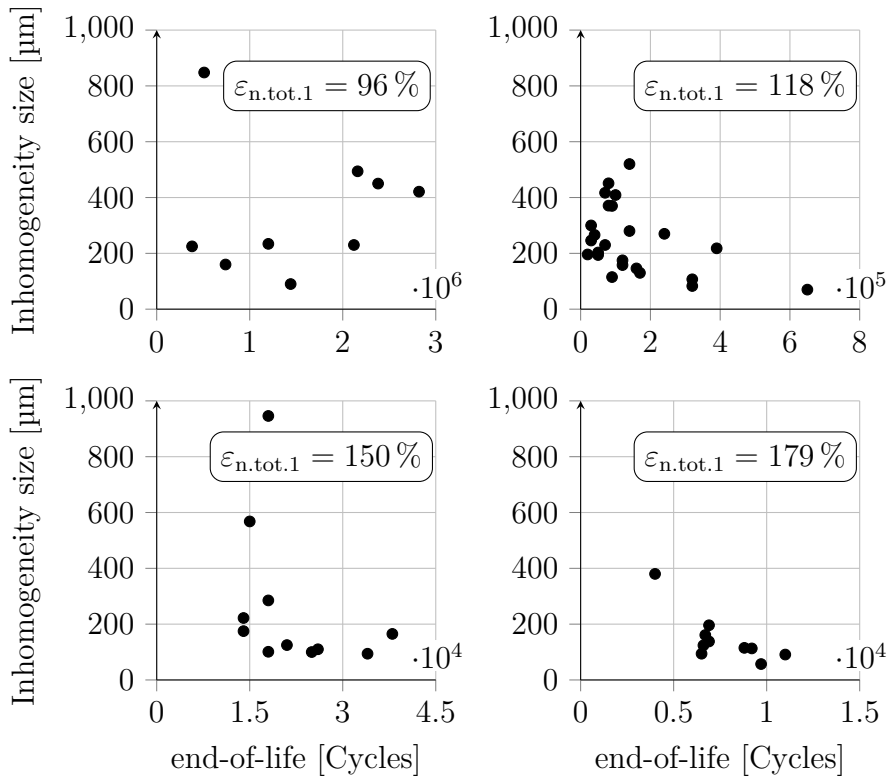
Figure 4.54: SBR: Maximum visible particle size over number of cycles to end-of-life. The label of the load-levels are shown within the single plots. Only the data of the clear evaluable particles are shown.

One of the many evaluated fracture surfaces strengthens the weak dependency of the lifetime on the pure particle size. Figure 4.55 shows a fracture surface with a small (72 µm) particle and a more than two times larger (161 µm) loosely attached particle. Nonetheless, the crack initiated at the small particle.
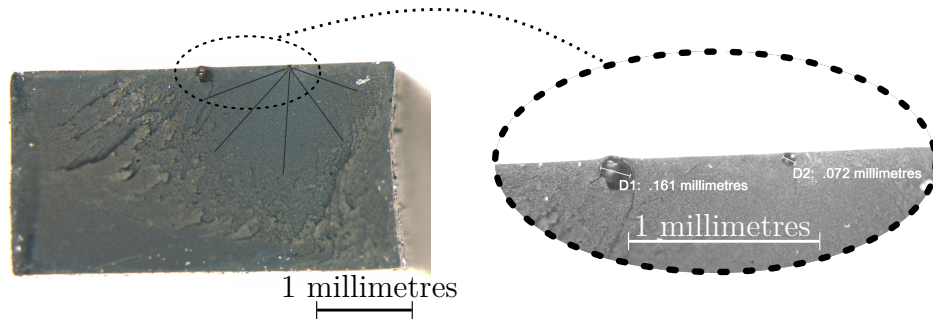
Figure 4.55: SBR: Unique fracture surface of a 2D-dumbbell with in-plane small and two times bigger particle. This examples originates from the lowest load-level.

### 4.3.5 Fatigue results of the new test piece

Objective of the new test piece is to fail due to surface-independent fatigue cracks with locus in the bulk material. The material load in the centre compared to the surface shall be high enough so that crack initiation in the bulk reliably dominates possible surface crack initiations.

Figure 4.56 shows the typical crack initiation behaviour of the new test piece made from the NR material (see Figure 4.49). Even if the deformation of the material is $\Delta\varepsilon_{\mathrm{n.max}} \approx 20\,\%$ greater in the centre, many cracks appear at the surface.


Figure 4.56: NR: Typical multi-crack initiation at the new test piece; shown in the deflected state.

Like for the 2D-dumbbell in Section 4.3.4, the locus of failure initiation of the major cracks is researched with a reflected light microscope. The statistical evaluation confirms the first impression from Figure 4.56. Many major cracks initiate at the surface. Similar was found for the NR material-based 2D-dumbbell (see Figure 4.52).

Surface crack initiations [%]
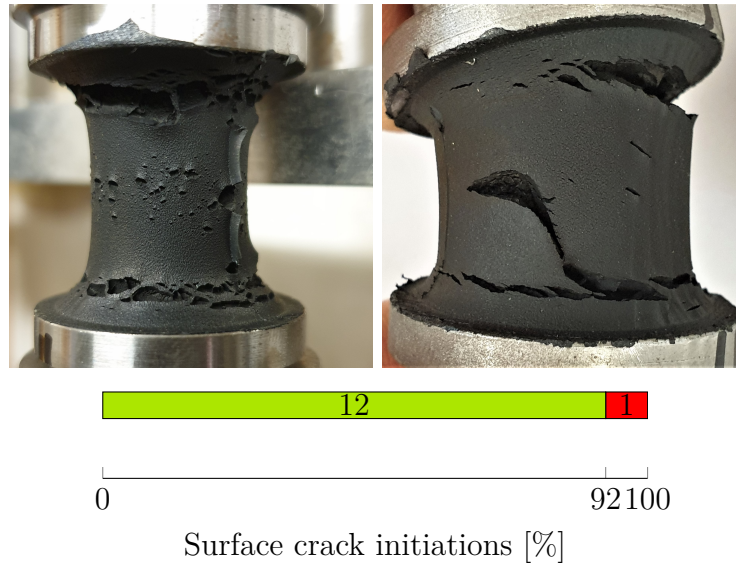
Figure 4.57: NR: Surface initiations (yes: green) in number of test pieces in the bar and percent at the axis label. Hence, the colour red is associated with macro crack initiation with locus in the bulk material only.

However, because of the multi-crack initiation behaviour of the NR material, large cracks with locus in the bulk material are found as well (see Figure 4.58). In the most cases no single dominant crack, clearly responsible for the global failure of the test piece, can be identified.
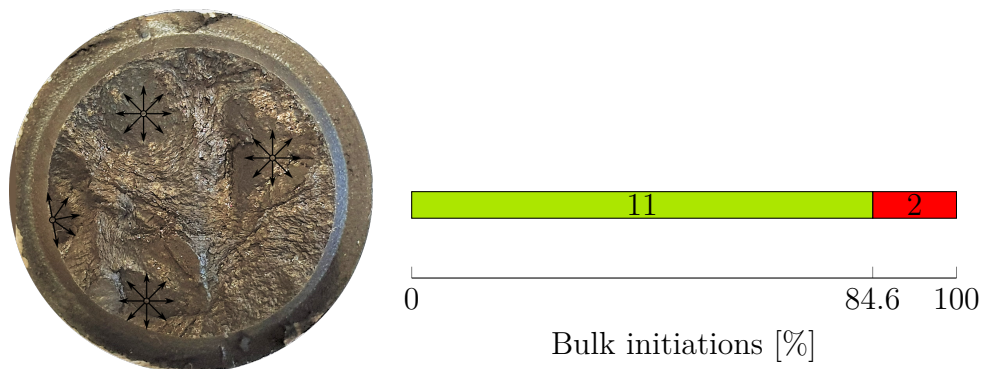
Bulk initiations [%]

Figure 4.58: NR: Crack initiations in the bulk material (yes: green) in number of test pieces in the bar and percent at the axis label. Hence, the colour red is associated with macro crack initiation with locus on the surface only.

Before comparing the Wöhler curves of the NR material-based 2D-dumbbell and the new test piece, the volumes of the two test pieces are evaluated. This is done, because there is a volume size effect on the durability of materials (for rubber materials see e.g. [96]). The effect can be summarised to: with increasing volume, the probability to apply critical loading to a matrix damaging inhomogeneity increases as well. Following this principle, regions of the test piece that are almost undeformed if the test piece is globally deflected

should not be considered in the estimation of the test piece volume. Figure 4.59 shows the two test pieces with regions in colour that are deformed greater than 75 % of the maximum $\varepsilon_{\text{n.max}}$; this is assumed to be the significantly loaded volume. The threshold of 75 % is chosen for no particular reason. Only criteria is that the regions at the surface of the new test piece, where crack initiation takes place (see Figure 4.56), should be included. Additionally, other threshold values did not distinctly change the ratio of the loaded volume between the two test pieces. Same is true for different global deflections. The size of the loaded volume of the new test piece is approximately 10 times greater compared to the 2D-dumbbell.
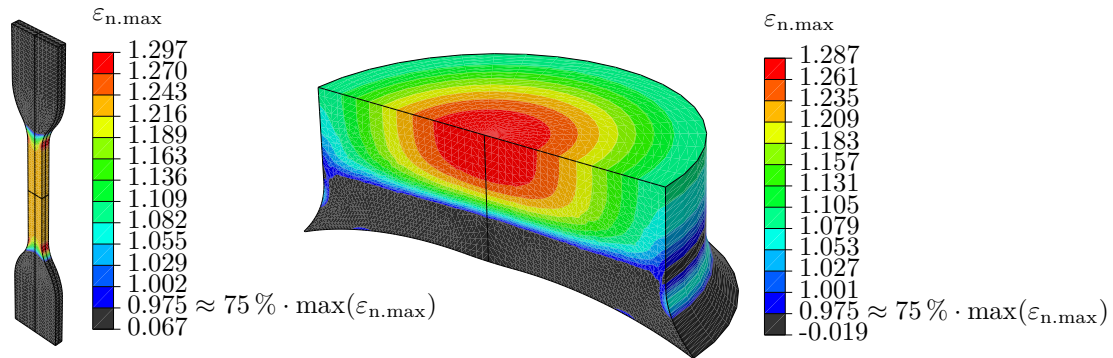
Figure 4.59: Comparison of the significantly loaded volume size of the 2D-dumbbell and the new test piece. Only a quarter of the new test piece is displayed. The test pieces are not shown in the same scale.

The principals of the Sudden Death (SD) testing are used to consider the loaded volume differences for the two test pieces within the fatigue results (for Sudden Death testing see Section 2.3). As a reminder, in case a fatigue test is considered as completed if one within a group of equally loaded identically test pieces fails, it is designated as a Sudden Death test. In a practical application this is often applied for rolling bearings, since the whole bearing fails if one of its balls fails (see e.g. [97]). In the theory of the Sudden Death testing, the test results of a group can be transformed in test results for the virtual case of *one by one*-tested test pieces, using their cumulative failure distribution functions (see Equation 2.77 in Section 2.3.5).

The following property of elastomers is fundamental for the way forward: the crack growth rate increases with crack size (see e.g. [1, 98]; explanatory framework: one-sided notched stripe test piece). For this reason, cracks are small in size during the majority of the lifetime and only reach macro crack dimension towards the final rupture of the test piece. This leads to a major impact of the conditions of the very initial failure initiation on the final lifetime. These failure initiations are distributed over the loaded volume for the NR material (see Figure 4.58). The most unfavourable failure initiations lead to critical macro cracks. As mentioned above, the likelihood to initiate such critical failure increases with the size of the loaded volume.

In order to consider the loaded volume difference between the 2D-dumbbell to the new test piece, it is assumed that ten small new test pieces (with 1/10 of the volume of the original test piece) were fatigued and the test was stopped after the first of the 10 small test pieces had failed. By using Equation 2.77 this biased *group-tested* result can be transformed into a result of 1/10 - volume test pieces, fatigued one by one. Like that, one obtains a virtual test result which equals the test results from the 2D-dumbbell regarding the size of loaded volume.

Figure 4.60 shows the original test data (◼) and the test data with volume correction based on the Sudden Death approach (◼). Each load-level consists of four test pieces only; visible in the wide confidence limits, compared the 2D-dumbbell data (see Figure 4.61). Within the Sudden Death procedure, the complete cumulative distribution function (see Equation 2.77) is considered, but is determined using only four data points. This should be considered when evaluating the data from Figure 4.60 or 4.61.

Similar to the 2D-dumbbell test piece (see Section 4.2), the local strains of the new test piece increase with ongoing cyclic globally constant deflection. The varying strains are converted into the equivalent constant strain ($\varepsilon_{\text{n.const}}$) for data with ◄-symbol. See Section 4.2 for more details about $\varepsilon_{\text{n.const}}$. Compared to the 2D-dumbbell test pieces (see Figure 4.16, Page 66) the conversion from $\varepsilon_{\text{n.max.tot.1}}$ to $\varepsilon_{\text{n.const}}$ yields less shift of the Wöhler curve for the new test piece. The new test piece has a more homogeneous deformation field than the 2D-dumbbell which lowers the strain increase over the cycles. The $\varepsilon_{\text{n.max.tot.}N}$ for the new test piece are derived using finite element simulations of 1000 amplitudes under application of the Plagge-model (see Section 4.3.1).
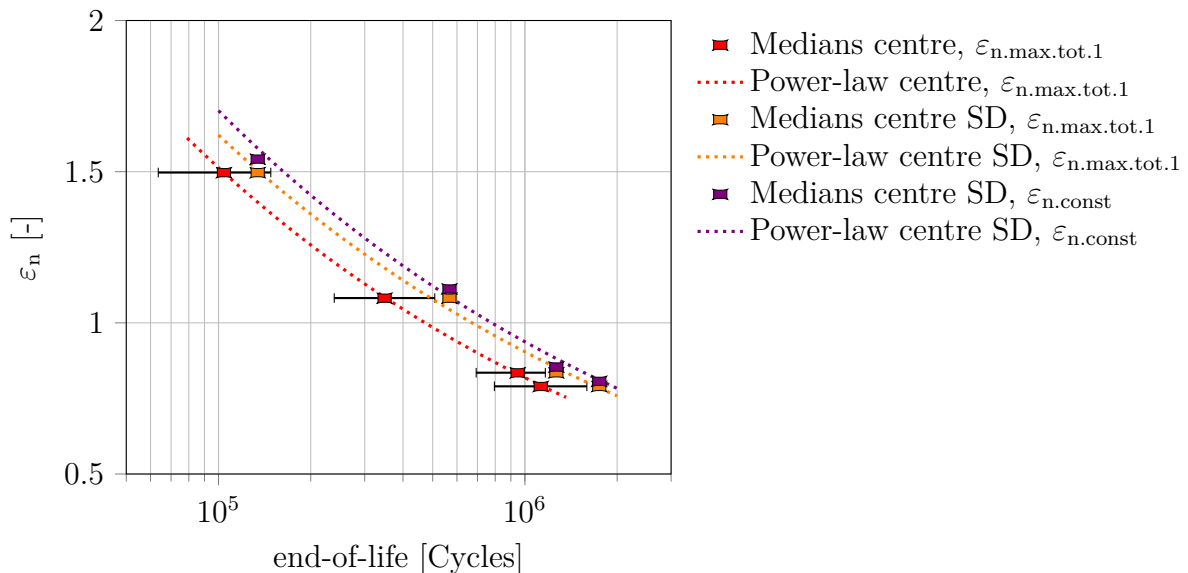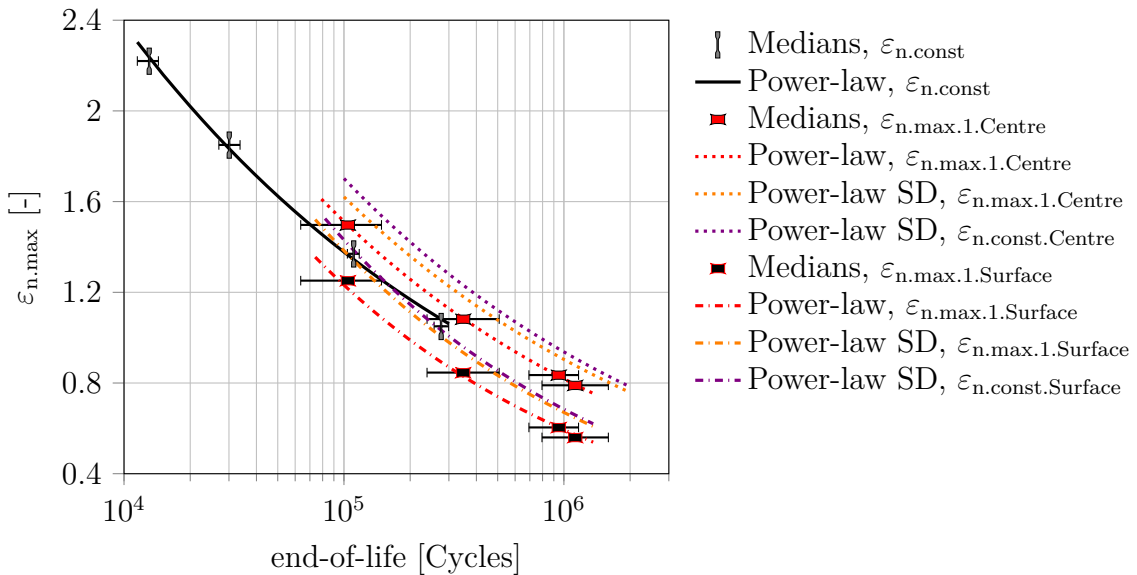

Figure 4.60: NR: Wöhler curve of the new test piece with different evaluation methods. SD is the acronym for Sudden Death. The ◼-symbol represents the silhouette of the new test piece. The medians with ◄-symbol are endued with 95 % confidence limits (⊢⊣).

All data shown in Figure 4.60 are based on the maximum principal nominal strain ($\varepsilon_{\text{n.max.Centre}}$) in the centre. Additionally, Figure 4.61 includes the data of the new test pieces based on $\max(\varepsilon_{\text{n.max.Surface}})$ (see ·-··· curves in Figure 4.61) and the Wöhler curve of the 2D-dumbbell (see —— curve). The data of $\varepsilon_{\text{n.max.Centre}}$ and $\max(\varepsilon_{\text{n.max.Surface}})$ are simultaneously shown since macro cracks are present in both regions at end-of-life of the new test piece (see Figure 4.57 and 4.58). Global failure is caused by the coalescence of cracks from both regions.

The on first sight unnecessary amount of data from the new test piece in Figure 4.61 is shown, since non of the six new test piece Wöhler curves is claimed to be the only correct Wöhler curve. The unknown correct new test piece Wöhler curve is located somewhere in between these six Wöhler curves.

The Wöhler curves from both test pieces are approximately aligned. This suggests that the multi-crack driven fatigue behaviour of the NR material is quite robust against the choice of test piece geometry.


Figure 4.61: NR: New test piece Wöhler curves based on different evaluation methods compared with the 2D-dumbbell Wöhler curve. SD is the acronym for Sudden Death. The ⊨-symbol and ⌶-symbol represent the silhouette of the new test piece and the 2D-dumbbell, respectively. All shown medians are endued with 95 % confidence limits (⊢⊣).

Similar to the 2D-dumbbell, no multi-crack initiation is found for the SBR material-based new test piece. The typical crack initiation behaviour is shown in Figure 4.62. Cracks initiate almost always at the test piece's surface (see Figure 4.63), preferably at the radius. From there, the cracks grow towards the centre of the test piece, following the path of maximum deformation.
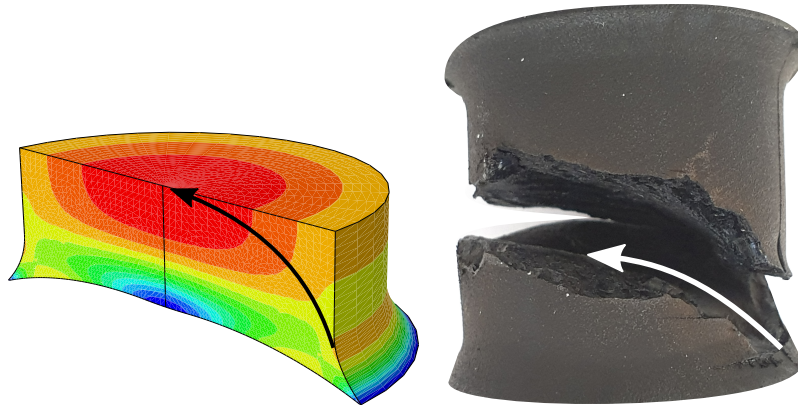
Figure 4.62: SBR: Typical crack-initiation at the new test piece. Experimental failure compared with numerical $\varepsilon_{\mathrm{n.max}}$-field.

The data from Figure 4.63 to Figure 4.65 are gathered using a microscope. Within the large amount of surface-crack initiations (94 %, see Figure 4.63), the majority (66 %) of these 31 surface cracks initiate at the flash. This large amount of surface-crack initiations for the new test piece is in strong contrast to the randomly distributed initiations at particle-like inhomogeneities for the SBR-based 2D-dumbbells (see Figure 4.53, Page 100). Randomly distributed, even if the corners of the 2D-dumbbell are strongly deformed when die-cut from a sheet. However, this die-cut appears to be less damaging than the flash of the new test piece. The damage of the flash dominates the $\varepsilon_{\mathrm{n}} \approx 20\,\%$ greater deformation in the test piece's centre and the most other surface inhomogeneities.
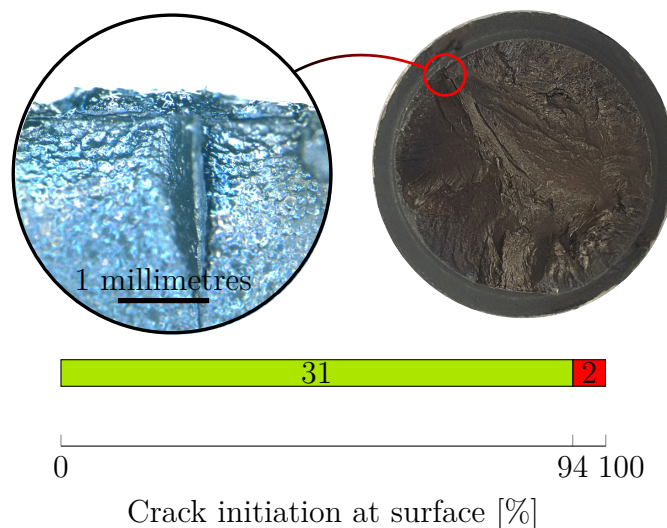
Figure 4.63: SBR: Surface initiations (yes: green) in number of test pieces in the bar and percent at the axis label. Hence, the colour red is associated with crack initiation with locus in the bulk material.

As a consequence, almost no cracks initiate within the bulk material of the new test

piece (see Figure 4.64). Three out of the five crack initiations in the bulk are caused by non-natural inhomogeneities (e.g. metal particles, right in Figure 4.64). Inhomogeneities that are not based on the ingredients of the material are judged to be non-natural, therefore not considered in the fatigue data or within the evaluation in Figure 4.63. They are only considered one-time in Figure 4.64.
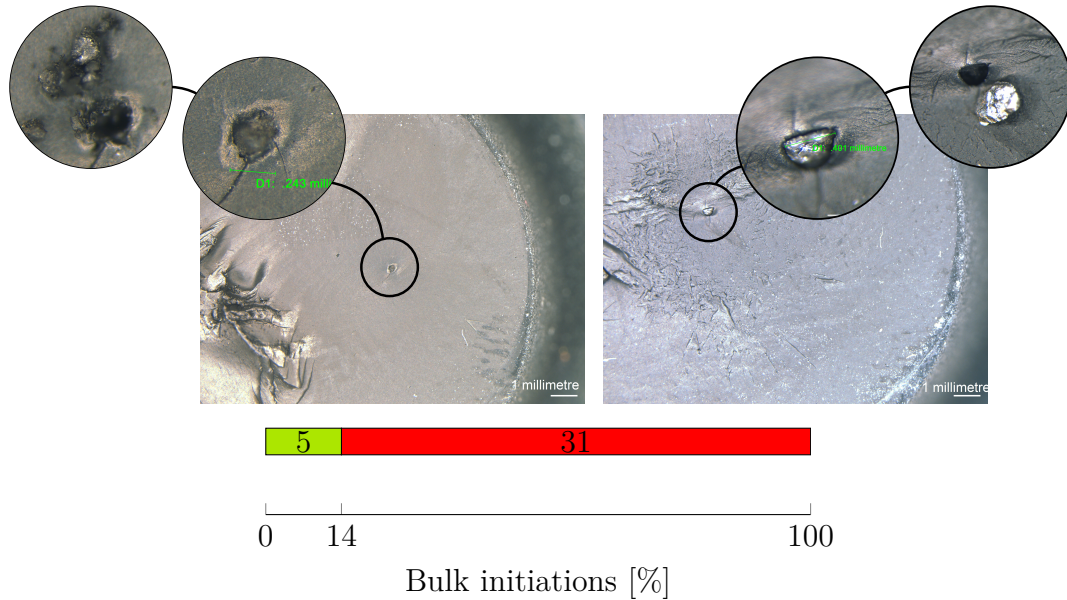
Figure 4.64: SBR: Crack initiations in the bulk material (yes: green) in number of test pieces in the bar and percent at the axis label. Hence, the colour red is associated with crack initiation with locus on the surface. In the outer circular shaped images the particles are pushed aside with a needle.

For the SBR material-based new test piece, the appearance of cavitation is investigated. Cavitation as shown in Figure 4.65 is always found for the uppermost load-level near the inserts only. However, in only one out of eight cases, cavitation is involved in the critical crack causing the failure of the entire test piece.
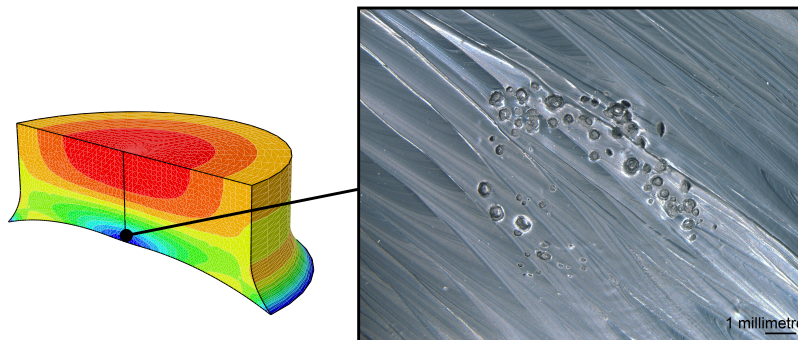
Figure 4.65: SBR: Cavitational damage at the metallic of the new test piece. Experimental failure compared with numerical $\varepsilon_{\mathrm{n.max}}$-field.

Figure 4.66 shows the SBR material-based Wöhler curves of the 2D-dumbbell and the new test piece. Like for the NR material, several Wöhler curves are shown for the new test piece. However, the Sudden Death method to consider different volumes is not performed. For the SBR material, the crack initiation is not spread over the loaded volume of the new test piece, but is concentrated on the surface, in particular on the flash. Therefore it is assumed that a loaded volume size correction should not be applied. For the same reason, the two Wöhler curves based on $\varepsilon_{n.Surface}$ are judged to be more relevant compared to $\varepsilon_{n.Centre}$. A huge difference, of factor 50 in lifetime, is measured between the 2D-dumbbell and the surface-based new test piece data (see arrow in Figure 4.66). A devastating damage effect of surface inhomogeneities, especially of the flash, is quantified in Figure 4.66. The ratio between $\varepsilon_{n.Surface}$ to $\varepsilon_{n.Centre}$ of approximately 0.8 is not sufficient to dominate the damage of the surface inhomogeneities. Nevertheless, the data from Figure 4.66 provide fundamental and unique information for a second design of the new test piece.
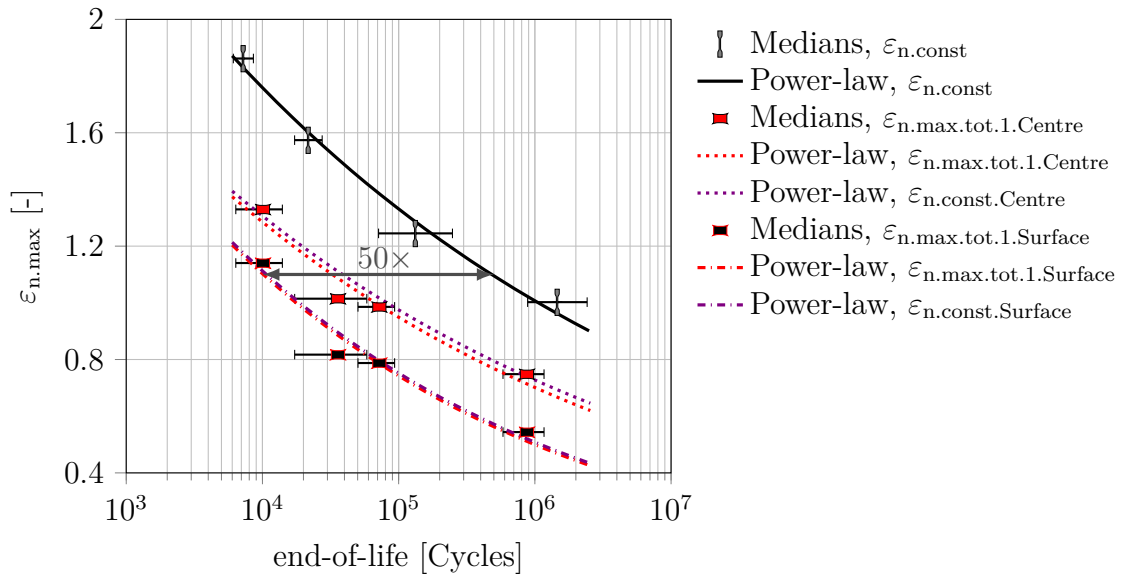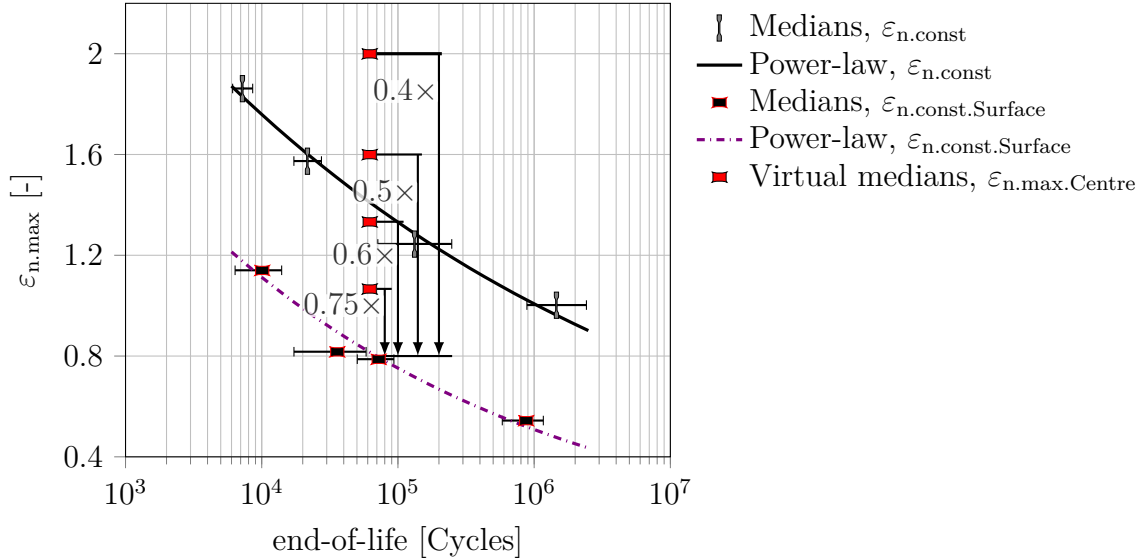

Figure 4.66: SBR: New test piece Wöhler curves compared with the 2D-dumbbell Wöhler curve. All shown medians are endued with 95 % confidence limits (⊢⊣).

4.3.6 Design of the new test piece - version 2

The second design of the new test piece has its origin in the fatigue data of the SBR material shown in the former section. Based on the complete randomly distributed crack initiation locus for the 2D-dumbbell (see Figure 4.53, Page 100), it is assumed, that the according Wöhler curve represents the bulk material. One might remark, that the objective of surface-independent fatigue results is achieved with the dumbbell. However, as shown for the NR material, the 2D-dumbbell test piece is not consequently delivering surface-independent fatigue results. Additionally, the usage of the die-cut dumbbell is

refused at times, based on its discrepancy in manufacture to components. The former is die-cut from a compression-moulded sheet in contrast to injection-moulded components. Figure 4.67 shows the Wöhler curve of the 2D-dumbbell compared with the Wöhler curve of the first version of the new test piece, based on the maximum strain on the surface; the main locus of crack initiation. Additionally, virtual centre strains, based on different $\max(\varepsilon_{n.max.Surface})$ to $\varepsilon_{n.max.Centre}$ ratios, are indicated. A ratio of 0.5 or less is necessary to dominate the surface inhomogeneities (including the flash) of the first version of the new test piece.


Figure 4.67: SBR: New test piece Wöhler curve compared with the 2D-dumbbell Wöhler curve with indicated virtual centre strains, based on different $\varepsilon_{n.max.Surface}$ to $\varepsilon_{n.max.Centre}$ ratios. All shown medians are endued with $95\,\%$ confidence limits ($\vdash\dashv$).

Instead of the hyperelastic Arruda-Boyce model, the Plagge material model with the parameters fitted in Figure 4.31 to 4.34 is used for the second geometry optimisation (see Page 84). Triangle shaped finite elements are disabled to avoid the mesh issues shown in Figure 4.48. The data for the target function are taken from the second loading-cycle. Based on the Plagge-model an initial shear modulus of $G = 1.48\,\mathrm{MPa}$ is estimated by applying a small simple shear load on a cube. Using Equation 3.2, a critical hydrostatic stress for cavitation of $\sigma_{0.crit} = 3.7\,\mathrm{MPa}$ is calculated. A hydrostatic stress of $\sigma_{0.Insert} = 4.7\,\mathrm{MPa}$ and $\sigma_{0.Insert} = 3.1\,\mathrm{MPa}$ is calculated based on the SBR material parameter at the insert of the new test piece V1 for the uppermost and next lower load-level, respectively. Only for the highest load-level, cavitation at the insert, as shown in Figure 4.65, can be found. This supports the validity of the determined critical hydrostatic stress of $\sigma_{0.crit} = 3.7\,\mathrm{MPa}$. The design of the second version of the test piece is performed using the same automated procedure as described for the first version in Section 4.3.3. The function $f_2()$,

within the modified target-function f_{target} (see Equation 4.26), is defined according to the $^{\max(\varepsilon_{\text{n.max.Surface}})}/\varepsilon_{\text{n.max.Centre}}$-ratios from Figure 4.67 (see Figure 4.68). In addition to the threshold value of 0.6, two more threshold values of 0.5 and 0.4 are applied (see Figure 4.68 and compare to Figure 4.47). Since no crack initiation at the location of $\max(\varepsilon_{\text{n.max.Insert}})$ is reported within former Section 4.3.5, the definition of $f()$ for the $^{\max(\varepsilon_{\text{n.max.Insert}})}/\varepsilon_{\text{n.max.Centre}}$-ratio keeps its definition with a threshold value of 0.6.

$$f_{\text{target}} = f_2\left(\frac{\max(\varepsilon_{\text{n.max.Surface}})}{\varepsilon_{\text{n.max.Centre}}}\right) + f\left(\frac{\max(\varepsilon_{\text{n.max.Insert}})}{\varepsilon_{\text{n.max.Centre}}}\right) + \frac{\sigma_{0.\text{Insert}}}{\sigma_{0.\text{crit}}} \tag{4.26}$$
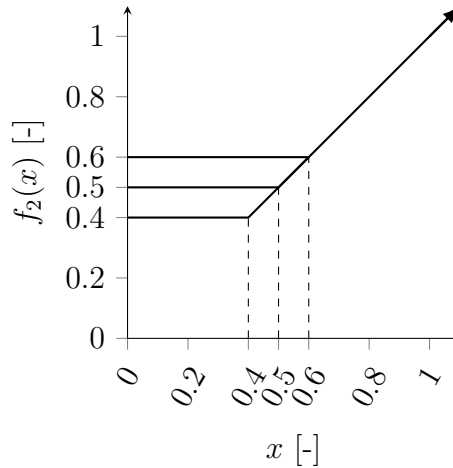
Figure 4.68: Function $f_2()$.

Besides the threshold value variation within $f_2()$, the geometry optimisation is perform for three different $\varepsilon_{\text{n.max.Centre}}$ values (75 %, 100 % and 130 %), for one threshold value of 0.5 within $f_2()$. In order to not alter the damage behaviour of the mould-specific surface imperfections, the mould from test piece V1 is used. Thus, the surface geometry is kept constant between test piece V1 and V2. Consequently, the amount of geometry parameters reduces from eight (see Figure 4.46, Page 95) to three (S_1, R_1 and R_2).
On the left hand side (a) of Figure 4.69 the results of the threshold value variation are shown, whereas, the right hand side (b) of Figure 4.69 shows the results of the $\varepsilon_{\text{n.max.Centre}}$ variation for a $f_2()$ threshold value of 0.5.
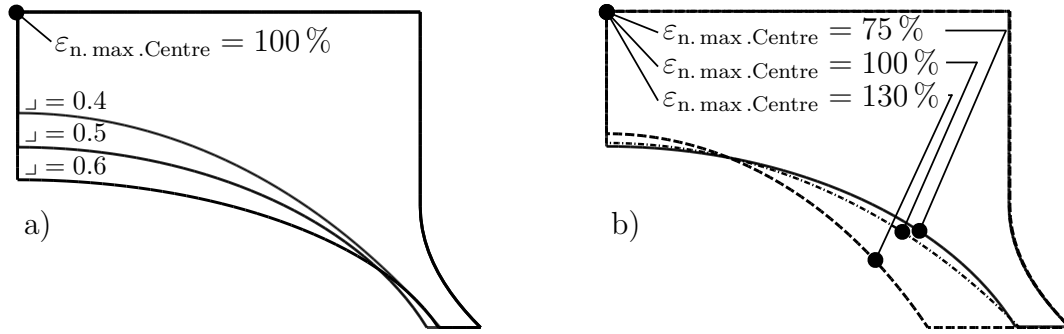
Figure 4.69: Geometry optimisation results for a) the three threshold values 0.4, 0.5 and 0.6 within $f_2()$ and b) different $\varepsilon_{\mathrm{n.max.Centre}}$ values of 75 %, 100 % and 130 % for a constant threshold values of 0.5. The ⌐-symbol symbolises the threshold value from Figure 4.68.

Table 4.11 lists the optimisation criteria values for the three versions from the Figure 4.69-a). The version with the ratio between $\max(\varepsilon_{\mathrm{n.max.Surface}})$ and $\varepsilon_{\mathrm{n.max.Centre}}$ of ≈ 0.5 is chosen, since it is the best compromise between an as low as possible $\sigma_{0.\mathrm{Insert}}$ and a great enough $\max(\varepsilon_{\mathrm{n.max.Insert}})/\varepsilon_{\mathrm{n.max.Centre}}$-ratio to reliably dominate the surface inhomogeneities (based on the Wöhler curves of 4.67). The variation of the $\varepsilon_{\mathrm{n.max.Centre}}$ for the threshold value 0.5 is shown in Figure 4.69-b). Almost the same geometry is found for $\varepsilon_{\mathrm{n.max.Centre}} = 75\,\%$ and $100\,\%$. For $\varepsilon_{\mathrm{n.max.Centre}} = 130\,\%$ the algorithm found the target function's f_{target} minimum for a reduced radius parameter R_2. Nevertheless, strain values of 75 % or 100 % are assumed to be more relevant for this study and therefore the geometry found for $\varepsilon_{\mathrm{n.max.Centre}} = 100\,\%$ is eventually chosen. Figure 4.70 compares the $\varepsilon_{\mathrm{n.max}}$-fields of the second test piece's version with the first.

Case	≈ 0.4	≈ 0.5	≈ 0.6
$\dfrac{\max(\varepsilon_{\mathrm{n.max.Surface}})}{\varepsilon_{\mathrm{n.max.Centre}}}$	0.404	0.498	0.599
$\dfrac{\max(\varepsilon_{\mathrm{n.max.Insert}})}{\varepsilon_{\mathrm{n.max.Centre}}}$	0.653	0.640	0.633
$\dfrac{\sigma_{0.\mathrm{Insert}}}{\sigma_{0.\mathrm{crit}}=3.7\,\mathrm{MPa}}$	1.044	0.982	0.922

Table 4.11: Optimisation criteria values for threshold value variation from Figure 4.69-a).

A fourth parameter was temporarily used to introduce a concave section to the insert, like manually found to cause a significant decrease of $\sigma_{0.\mathrm{Insert}}$ for the first version (see Section 4.3.3). This fourth parameter was chosen by the optimisation algorithm such that this concave section disappears. Thus, a concave section at the insert for the second version of the new test piece was not further considered.
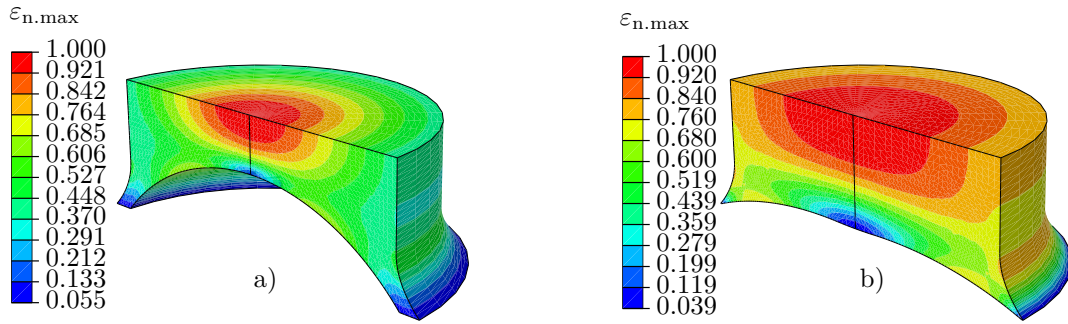
Figure 4.70: Comparison of the strain fields of the V1 (b) and V2 (a) new test piece. Only a quarter of the test pieces is depicted.

4.3.7 Fatigue results concerning interbatch variation and comparison of new test piece - version 1 and 2

The loaded volume, based on the $\varepsilon_{\text{n.max}}$-field with a threshold value of $75\,\%\cdot\max(\varepsilon_{\text{n.max}})$, of the new test piece V2 is approximately equal compared to the 2D-dumbbell. A correction of the fatigue test data using the Sudden Death method is not necessary. However, additional rubber batches prepared at different institutions were used for the fatigue tests with the new test piece V2. To be able to compare the fatigue data of the 2D-dumbbell with the new test piece V2, the different material batches need to be compared first. However, test results with the former material batch (B_{TARRC}) and the current batch ($B_{\text{DIK-2}}$), are only available for the new test piece V1 (see Table 4.12). The institution initials are used in the subscripts of the batch labels.

As shown in Figure 4.71, the NR material made in the TARRC institution withstands a greater dynamic load for $\approx 100\,000$ cycles and shows the same fatigue resistance against lower dynamic loads for $\approx 1\,000\,000$ cycles.

Test piece	B_{TARRC}	$B_{\text{DIK-1}}$	$B_{\text{DIK-2}}$
2D-dumbbell	☑	☐	☐
new test piece V1	☑	☐	☑
new test piece V2	☐	☑	☑

Table 4.12: Overview of the combination of batches and test pieces.
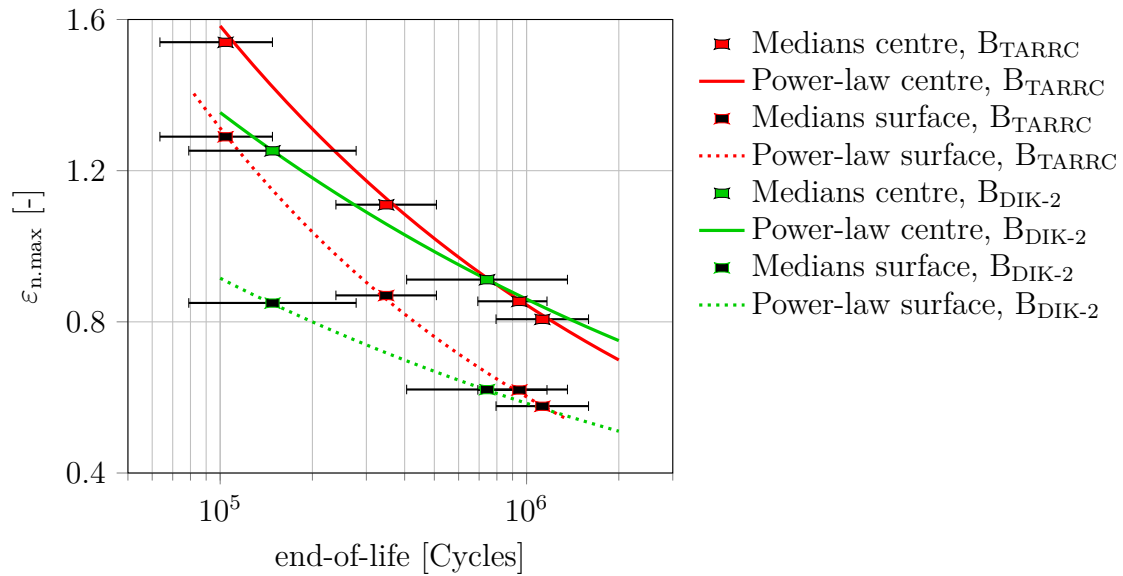
Figure 4.71: NR: New test piece V1 Wöhler curves based on the TARRC batch (B_{TARRC}) and the DIK batch (B_{DIK-2}). All shown medians are endued with 95 % confidence limits (⊢⊣) and $\varepsilon_{n.const}$-based.

Roughly the same fatigue behaviour for the SBR material is shown in Figure 4.72.
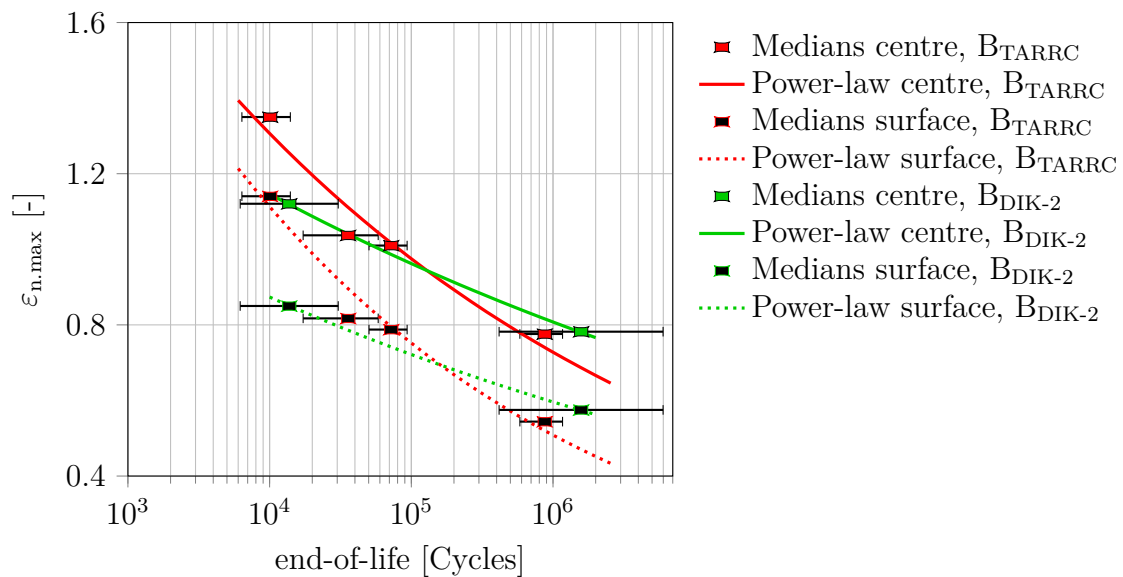
Figure 4.72: SBR: New test piece V1 Wöhler curves based on the TARRC batch (B_{TARRC}) and the DIK batch (B_{DIK-2}). All shown medians are endued with 95 % confidence limits (⊢⊣) and $\varepsilon_{n.const}$-based.

In addition to the naked number of cycles to end-of-life, the locus of failure initiation is investigated too. For the NR material the amount of surface crack initiations and crack initiations in the bulk material is equal (see Figure 4.73). However, the most of the bulk crack initiations for the DIK batch (B_{DIK-2}) are located in direct vicinity to the metallic

inserts with large and lengthy shaped inhomogeneities (see Figure 4.74). This conspicuity might originate from a faulty bonding system, leading to the slightly reduced lifetimes shown in Figure 4.71.
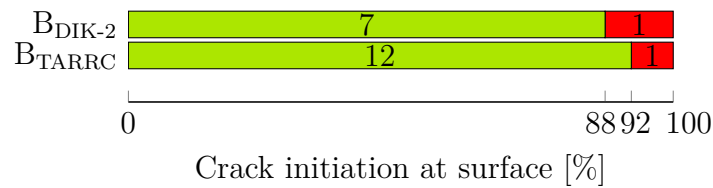
Figure 4.73: NR: Surface initiations (yes: green) in number of test pieces in the bar and percent at the axis label for the TARRC batch (B_{TARRC}) and the DIK batch (B_{DIK-2}). Hence, the colour red is associated with macro crack initiation with locus in the bulk material only.
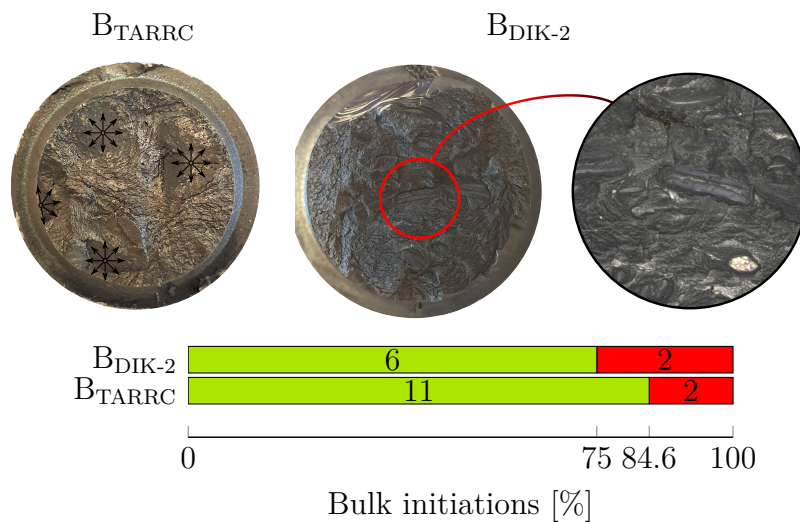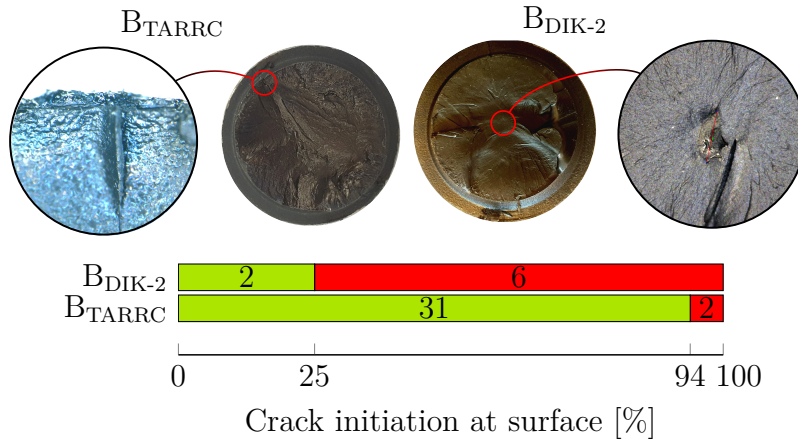

Figure 4.74: NR: Crack initiations in the bulk material (yes: green) in number of new test pieces V1 in the bar and percent at the axis label for the TARRC batch (B_{TARRC}) and the DIK batch (B_{DIK-2}). Hence, the colour red is associated with macro crack initiation with locus on the surface only.

Figure 4.75 shows a different fatigue crack initiation behaviour for the SBR material-based new test pieces V1. The majority of the test pieces made from the DIK batch (B_{DIK-2}) failed due to bulk material cracks instead of surface material cracks (B_{TARRC}). The main differences between the B_{DIK-2} and B_{TARRC}-based tests are that:

- not the exact same polymer types for both SBR batches could be used;

- wear at the mould of the new test piece was eradicated between the manufacture B_{DIK-2} and B_{TARRC}-based test pieces;

- the conditions while mixing the rubber might have been different, potentially leading to more damaging particles within the B_{DIK-2}, able to dominate the surface inhomogeneities.


Figure 4.75: SBR: New test piece V1 surface initiations (yes: green) in number of test pieces in the bar and percent at the axis label for the TARRC batch (B_{TARRC}) and the DIK batch (B_{DIK-2}). Hence, the colour red is associated with macro crack initiation with locus in the bulk material only.

Subsequent to the assessment of the batch impact on the lifetime and the fracture surfaces, the new test piece V2 may be compared with the 2D-dumbbell (see Figure 4.76). Independent of the batch, all major cracks of the new test piece V2 initiate in its bulk material. Thus, only the Wöhler curves using $\varepsilon_{n.max.Centre}$ are shown. The probable bonding faults also occur for the B_{DIK-2}-based new test piece V2. This bonding problem is not present for the B_{DIK-1}-batch as will be shown in the subsequent Chapter 5.

The indirect comparison for the NR material in Figure 4.76 of the new test piece V2 with the 2D-dumbbell suggest longer lifetimes for the new test piece. Unfortunately, only an indirect comparison can be conducted since both test pieces are made from different batches (see Table 4.12).
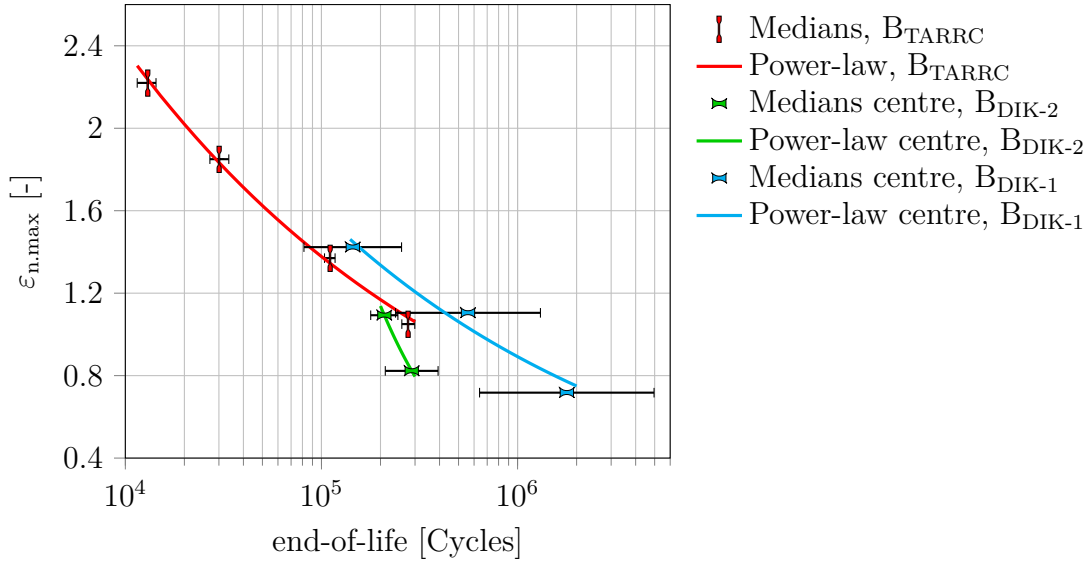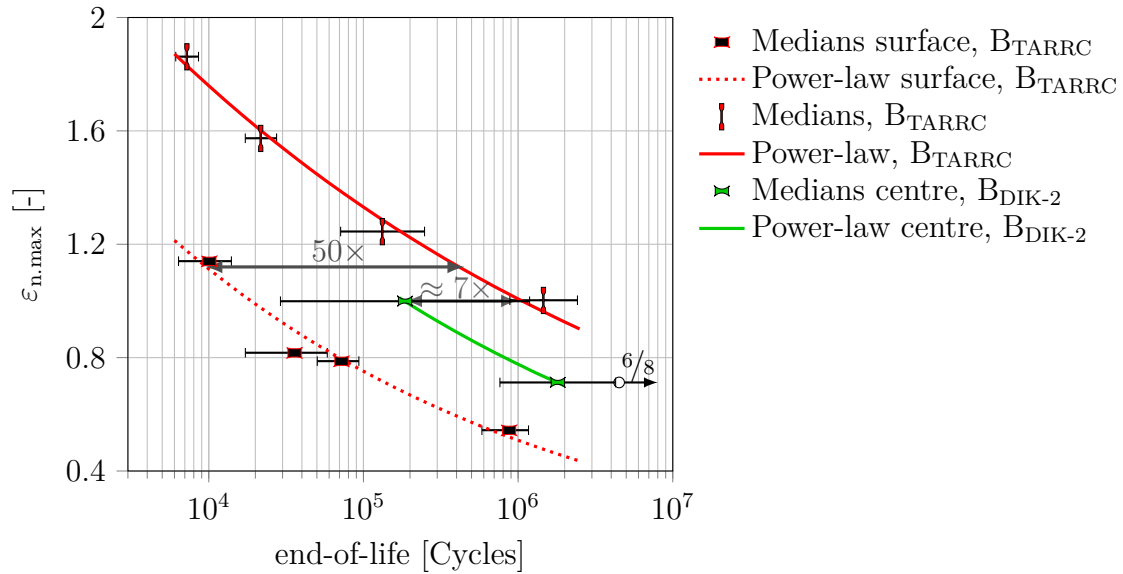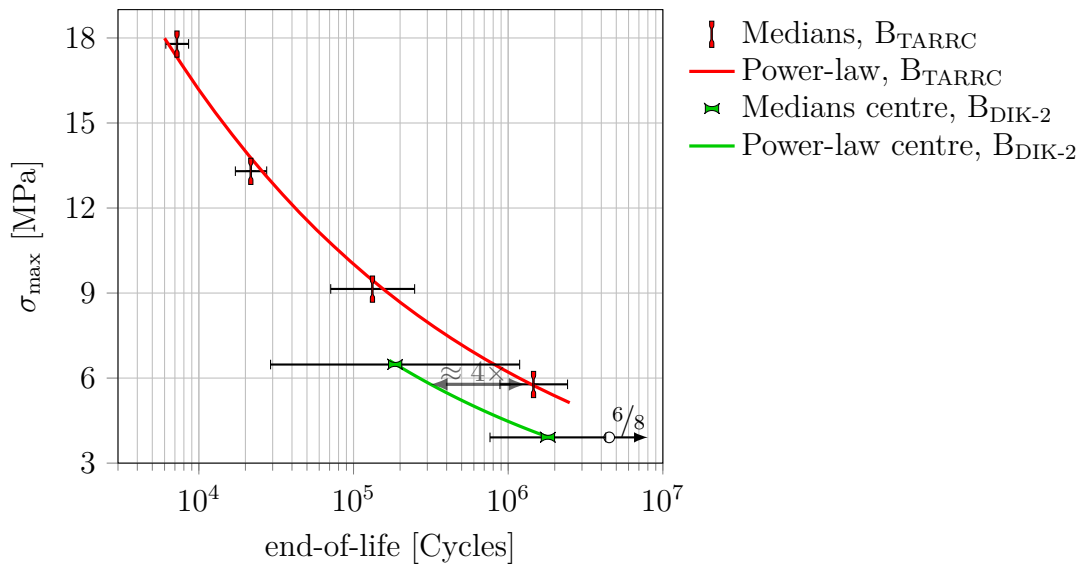
Figure 4.76: NR: Wöhler curves of the 2D-dumbbell ⌶ and new test piece V2 ⋈ based on the TARRC batch ———, DIK batch Nr. 2 ——— and DIK batch Nr. 1 ———. All shown medians are endued with 95 % confidence limits (⊢⊣) and all shown data are $\varepsilon_{\text{n.const}}$-based.

Also for the new test piece V2, made from the SBR material, only bulk crack initiations occurred. However, still less number of cycles to end-of-life are measured in this indirect comparison with the 2D-dumbbell shown in Figure 4.77. However, the difference reduces to factor ≈ 7 compared to the factor of ≈ 50 for the new test piece V1.

In addition to the inaccuracy due to the different batches, this comparison might be influenced by the choice of fatigue criterion ($\varepsilon_{\text{n.max}}$ for Figure 4.77). The 2D-dumbbell (free contraction while deflection) differs from the new test piece V1 and V2, with their stiff metallic inserts, in the magnitude of hydrostatic stress σ_0 in the loaded volume. The new test piece are characterised by a lower length to width ratio, leading to less free contraction while deflection. Differences in hydrostatic stress σ_0 are almost not considered by $\varepsilon_{\text{n.max}}$ due to the near incompressible behaviour of rubber. However, σ_0 influences the maximum principal stress σ_{max}. For this reason, the Wöhler curve of the new test piece V2 ⋈ moves towards the 2D-dumbbell ⌶-based Wöhler curve in case σ_{max} as fatigue criterion instead of $\varepsilon_{\text{n.max}}$ (see Figure 4.78). Still, a small difference remains between these two test pieces.

Figure 4.77: SBR: Wöhler curves of the 2D-dumbbell ▯, new test piece version one ▬ and new test piece version two ⋈ based on the TARRC batch ▬ and DIK batch Nr. 2 ▬. All shown medians are endued with 95 % confidence limits (⊢⊣) and all shown data are $\varepsilon_{\mathrm{n.const}}$-based. The $^{\mathrm{X}}/_{\mathrm{Y}}$ stands for X non-failed from Y total test pieces.

Figure 4.78: SBR: Wöhler curves of the 2D-dumbbell ▯ and new test piece version two ⋈ based on the TARRC batch ▬ and DIK batch Nr. 2 ▬. All shown medians are endued with 95 % confidence limits (⊢⊣) and all shown data are $\sigma_{\mathrm{n.const}}$-based. The $^{\mathrm{X}}/_{\mathrm{Y}}$ stands for X non-failed from Y total test pieces.

4.3.8 Conclusions

A high level of reliability of statements about the mechanical fatigue of rubber is not easy to ensure. The consequences for an experimental database in case fatigue tests are

conducted at different institutions with different material batches combined with slight changes on a mould are shown.

From the further development of the fatigue test piece of Brüger et al. [66] the subsequent can be concluded: An overview of generic statements about the lifetime difference and the figures where these findings can be deduced from is given in Table 4.13.

- Within the manual study of the geometry parameters, it was shown that large curvatures at the surface and inserts support the objective of failure initiations with locus in the bulk material. However, a straight forward way to find optimum values of the six geometry parameters could not be identified.

- For this reason, an automated parameter optimisation was set-up. The results of this optimisation reflected the insights from the *manual* study.

- The 2D-dumbbell chosen as reference test piece for the new test piece turned out to only systematically initiate failures at the surface for the NR material probably due to the die-cut process.

- Unlike observed for the NR material, failures initiated randomly over the cross section for the 2D-dumbbell made from SBR.

- The failure initiations of the new test piece V1 made from NR are spread over its loaded volume, leading to a similar lifetime as measured for the 2D-dumbbell.

- However, for the new test piece V1 made from SBR, a focus of the failure initiation on the flash was found. This behaviour led to a 50 times shorter lifetime of the new test piece compared to the 2D-dumbbell.

- The new test piece V2 showed the desired failure initiation behaviour with locus in the bulk material. A significant increase in lifetime for the SBR material compared to the new piece V1 is the consequence.

- Finally, reliable conclusions from the comparison of the second version new test piece with the 2D-dumbbell are hampered due to differences in the batch. Motivated by this, a benchmark of several uniaxial test pieces is performed in Chapter 5.

	NR material			SBR material		
	⌇	▥	⋈	⌇	▥	⋈
⌇	—	⌇ ≈ ▥ Figure 4.61	⌇ ≈ ⋈ Figure 4.76	—	⌇ < ▥ Figure 4.78	⌇ ≈ ⋈ Figure 4.78
▥	⊡	—	▥ ≈ ⋈ Figure 4.61 & 4.76	⊡	—	▥ > ⋈ Figure 4.78
⋈	⊡	⊡	—	⊡	⊡	—

Table 4.13: Overview of the material-dependent lifetime differences between the test pieces under neglect of any batch influence. The test pieces are depicted using the symbols ⌇, ▥ and ⋈ for 2D-dumbbell, new test piece V1 and new test piece V2. For reasons of symmetry, the cells with ⊡-symbol are not filled.

5 Benchmark uniaxial test pieces

## 5.1 Why another test piece benchmark?

The main objective of the former Section 4.3 is the design of a fatigue test piece with uniaxial deformation conditions at the locus of failure initiation in the bulk material. This test piece should serve as reference for other test pieces with preferential surface failure initiations. However, this comparison turned out to be partly invalid for two reasons:

- The chosen test piece with preferential surface failure initiations (2D-dumbbell) does not show this expected behaviour. Only for the natural rubber material a certain propensity of crack initiations towards the corner for the cross-section is ascertained.

- Only an indirect comparison of the 2D-dumbbell and the new test piece V2 was possible because they were made from different batches.

In order to still obtain reliable insights into the lifetime-impact of flashes or, more generally, surface-based failure initiations compared to failure initiations in the bulk material, an additional benchmark study is performed.

Figure 5.1 shows $\varepsilon_{\mathrm{n.max}}$-fields and a schematic silhouette-like depiction of the investigated fatigue test pieces. The requirement on the test pieces is a uniaxial strain-state at the locus of failure. This hotspot is identical for each test piece whether determined based on $\sigma_{\max}$ or maximum strain energy density Ψ. Unfortunately, the 2D-dumbbell was not available for this study.

Except the 3D-dumbbell test piece, all test pieces are bonded to metal inserts. The concave shape of the inserts of the $\mathrm{TDS_{Concave}}$ causes a shift of the fatigue hotspot from the bulk (see $\mathrm{TDS_{V2}}$) to the surface. The same mould is used for the production of these two test pieces, therefore the surface properties are not altered. Only one of the four investigated materials was tested using the $\mathrm{TDS_{Concave}}$, since as few as eight concave inserts were available.

| 3D-Dumbbell | Boge Test piece | TDS$_{V2}$ | TDS$_{Concave}$ |
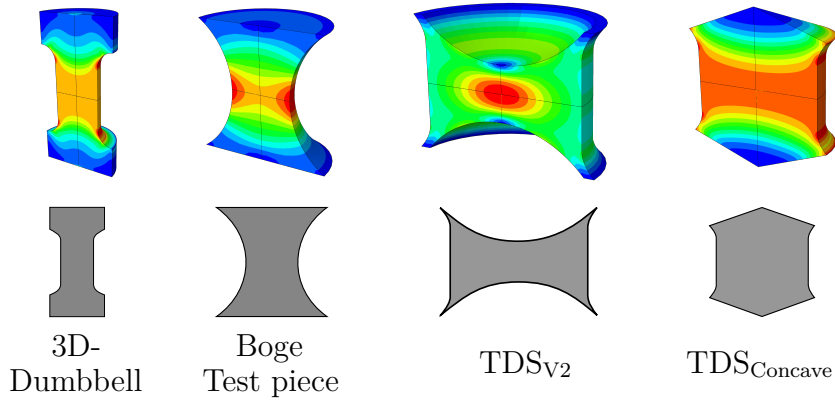
Figure 5.1: $\varepsilon_{n.max}$ fields, mapped on half models, and a schematic silhouette-like depiction of the investigated fatigue test pieces. The silhouettes are used within the Wöhler-diagrams. BOGE is the name of the company where the BOGE test piece got tested and TDS stands for **T**ARRC-**D**IK-**S**pecimen; this abbreviation is chosen since 'new test piece' is too long and imprecise for this comparison.

5.2 Material and its numerical description

The material formulations from the former Section 4.2 and 4.3 are employed again. Additionally an unfilled version of each compound is investigated (see NR 0 and SBR 0 in Table 5.1). The labels 'NR material' and 'SBR material' used in Section 4.2 and 4.3 are extended by the amount of filler in the mixture, expressed by parts per hundred of rubber.
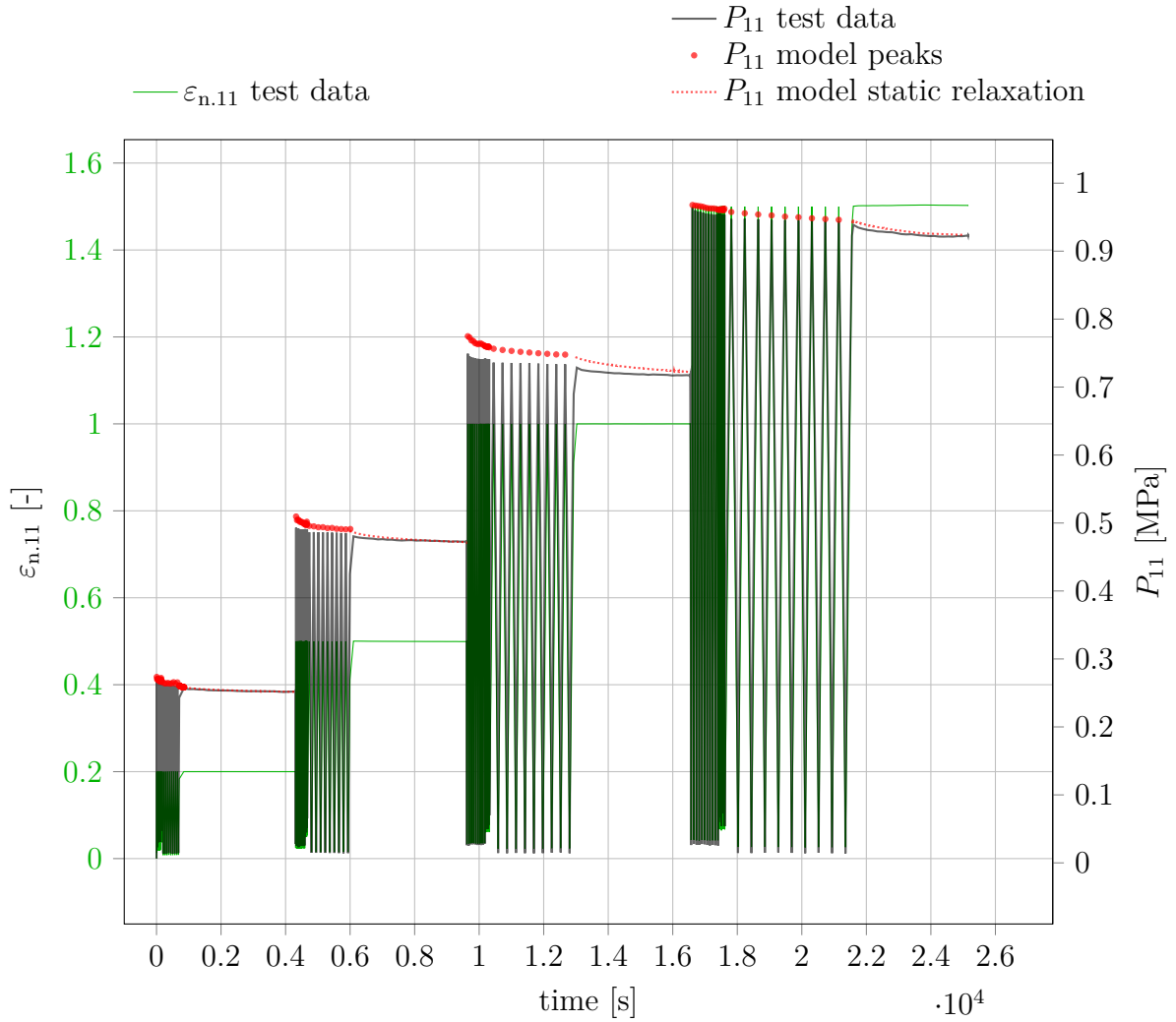
Name	NR 45	SBR 77	NR 0	SBR 0
Ingredient	phr			
NR SMR CV60	100		100	
SBR 1723/1793		137.5		137.5
N330	45			
N339		77		
SUNTHENE 410	4.5			
ZnO	3	3	3	3
Stearic acid	2	1	2	1
6PPD	3	3	3	3
CBS	0.6		0.6	
TMTD		0.2		0.2
TBBS		1.6		1.6
Sulphur	2.5	1.6	2.5	1.6

Table 5.1: Recipes of the investigated NR and SBR-based mixtures. The batch B$_{DIK-1}$ contains SBR 1723 whereby B$_{DIK-2}$ needed to be made of SBR 1793 (phr $\equiv$ parts per hundred of rubber, by mass). The formulations of the NR 45 and the SBR 77 compounds are equal to the ones called NR and SBR material in former Section 4.2 and 4.3.

In order to conduct finite element analyses of the chosen test pieces, the Plagge material model is used. The material parameters for this material model are determined with the same procedure as described in Section 4.3.1 and are listed in Table 5.2. Compared to the filled NR 45 and SBR 77 material, the unfilled compounds show much less cyclic as well as static relaxation (see Figure 5.2 & 5.3 and compare with Figure 4.31 & 4.32 on Page 84).
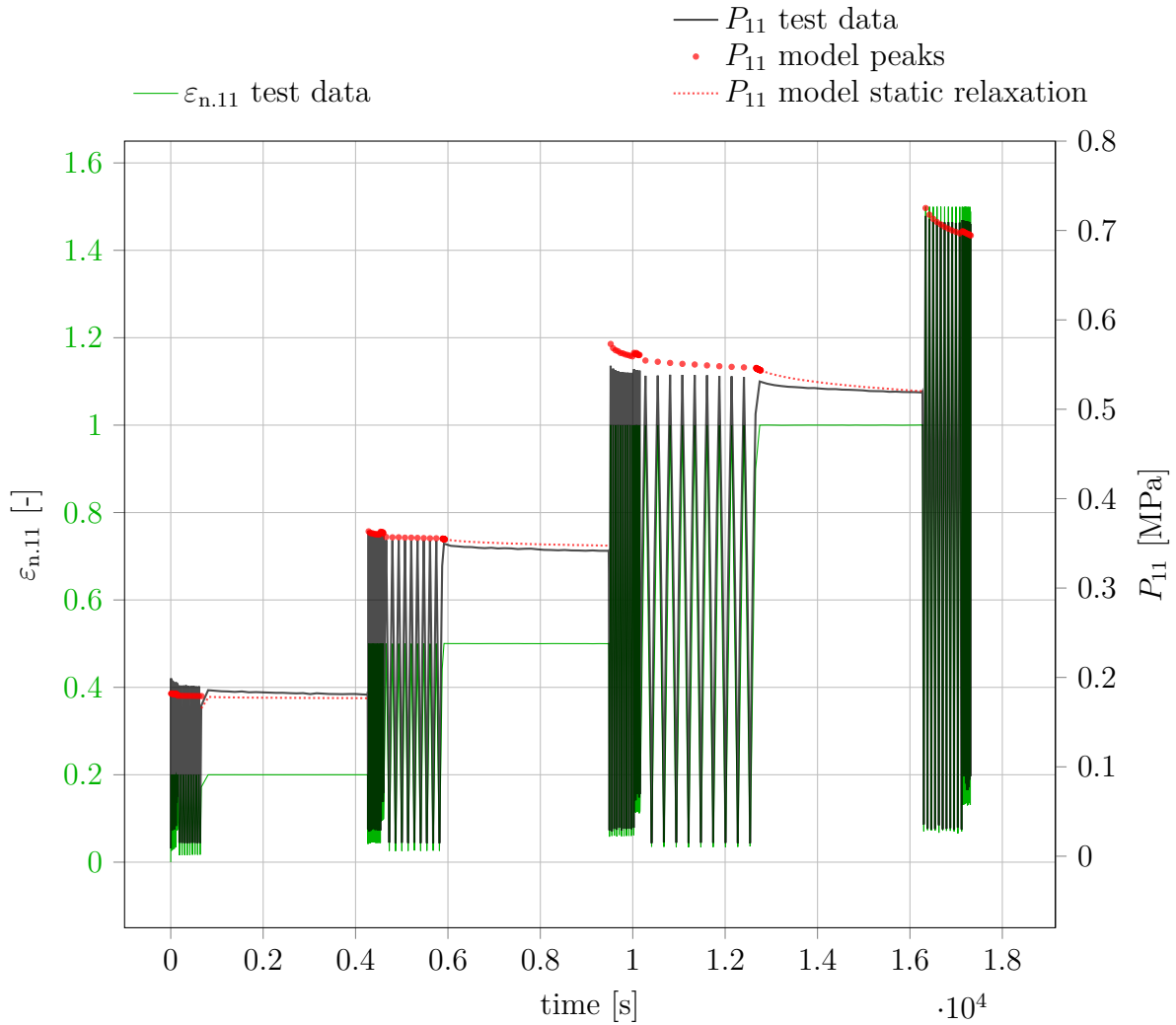
Figure 5.2: SBR 0: Test protocol used for the material parameters determination of the Plagge model. Experimental data are based on a uniaxial test piece. The test is interrupted after a few cycles with $\varepsilon_{n.11} = 1.5$.

Figure 5.3: NR 0: Test protocol used for the material parameters determination of the Plagge model. Experimental data are based on a uniaxial test piece.

No.	Parameter	NR 45	SBR 77	NR 0	SBR 0
1	ϕ	0.38	0.57	0.17	0.14
2	G_{c}	0.38 MPa	0.61 MPa	0.48 MPa	0.33 MPa
3	G_{f}	0.1 MPa	0.11 MPa	0.037 MPa	0.015 MPa
4	n	36.86	19.04	193.44	194.16
5	χ	2.84	2.96	2.99	2.92
6	e_{b}	15.12	18.78	19.22	17.07
7	v_{b}	0.11	0.45	0.72	1.07
8	$\tau_{\text{ve.0}}$	473.80 s	271.33 s	0.49 s	2.55 s
9	σ_{r}	0.048 MPa	0.044 MPa	0.01 MPa	0.01 MPa

Table 5.2: Parameters of the Plagge-model from Figure 5.2 and 5.2. The parameter for the filled materials, determined in Section 4.3.1, are shown as well.

5.3 Fatigue test protocol

As in Section 4.2 and 4.3 all tests, except for the BOGE test piece, are conducted in fully relaxing conditions, with respect to the global deflection ($R_{\mathrm{u}} = {}^{d_{\sim.\min}}/d_{\sim.\max} = 0$); they are displacement-controlled. The amplitude is chosen such that approximately the same range of maximum local deformation is calculated in the finite element analysis for all test pieces. Likewise to the fatigue tests in Section 4.2, the test frequencies are modified for each load-level. The reference frequency is chosen such that independent of the load-level, the surface temperature of the test pieces can be kept below 30 °C with the assistance of forced convection. This is ensured with infra-red sensor measurements. Eventually, the frequencies range between 1 Hz and 6 Hz. As shown in Section 4.3, the TDS$_{\mathrm{V2}}$ fails exclusively due to crack initiations in the bulk material. A critical question here is how the temperature in the bulk material develops with respect to the surface temperature. Estimating simulations of the temperature-field in thermal equilibrium resulted in negligible temperature difference between surface bulk material temperature, mainly due to the effective heat transfer over the metallic inserts.

Force-controlled fatigue tests are performed with the BOGE test piece for all four materials since displacement-controlled testing is not available within the facilities of BOGE Elastmetall GmbH. As an additional obstacle, forced convection was not available neither. Infra-red measurements show surface temperatures greater than 50 °C after 30 min cyclic loading for the filled SBR 77 and NR 45 material. Fortunately, surface temperatures of approximately 20 °C are measured for the unfilled materials. Because of the negligible cyclic creep and self-heating of the unfilled materials, it is assumed that the forced-controlled fatigue test data from the BOGE test piece are valid for the comparison with the other displacement-controlled test pieces made from SBR 0 and NR 0. The fatigue test results for the BOGE test pieces made from the filled SBR 77 and NR 45 material is discarded. For them, the temperature difference to the remaining data is too significant and the cyclic creep behaviour yields a very strong continuous increase of the global deflection and accordingly of the local strain.

The test pieces from Figure 5.1 differ in size of the loaded volume. However, a shift of certain fatigue data due to these differences is not conducted since all test pieces except the TDS$_{\mathrm{V2}}$ suffer from failure initiation at the flash. A clear definition of a loaded volume is not possible for these cases.

5.4 Fatigue test results

Figure 5.4 shows the fatigue results for the 3D-dumbbell ⫯, BOGE test piece ⬚ and TDS$_{\mathrm{V2}}$ ⋈ based on the DIK batch Nr. 1 —— and DIK batch Nr. 2 —— for the unfilled SBR material. The existence of several batches has been briefly addressed in Section 4.3. Initially focusing

on the greatest load-level of the BOGE test piece, only data from two test pieces were available. This leads to a very great confidence limit ($\vdash\dashv$).

A difference of roughly two decades in lifetime is measured between the 3D-dumbbell and the TDS_{V2}. The lifetime of the BOGE test piece ranges in between these two samples. Comparing the two batches B_{DIK-1} and B_{DIK-2} shows a reduced lifetime of the 3D-dumbbell made from B_{DIK-2}. However, longer or similar lifetimes are measured for the TDS_{V2}. Fatigue tests based only on the B_{DIK-2} batch are performed for the BOGE test piece.
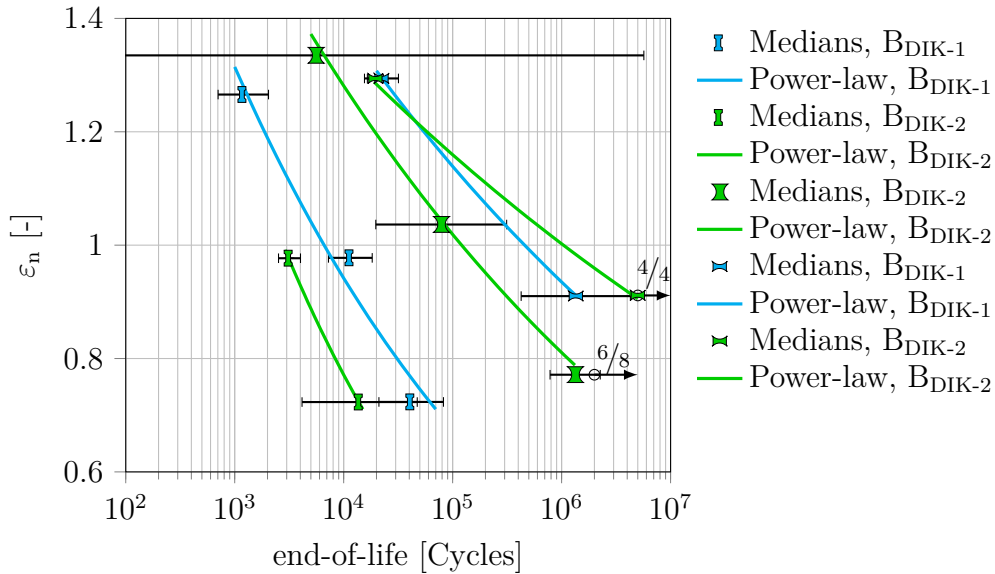

Figure 5.4: SBR 0: Wöhler-curves of the 3D-dumbbell ⲐＩ, BOGE test piece ⲐＸ and TDS_{V2} ⲐＫ based on the DIK batch Nr. 1 —— and DIK batch Nr. 2 ——. All shown medians are endued with 95 % confidence limits ($\vdash\dashv$) are $\varepsilon_{n.const}$-based. The X/Y stands for X non-failed from Y total test pieces.

In order to possibly explain the measured differences in lifetime, a microscopical investigation of the failure origin is conducted. Figure 5.5 shows representative fracture surfaces of the test samples. The quantitative evaluation is shown in Figure 5.6 and Figure 5.7. Evaluating whether the major crack initiated at the surface or in the bulk material verifies the functionality of the TDS_{V2}. In contrast to the 3D-dumbbell and BOGE test piece, all failures initiate in the bulk material of this new test piece. Figure 5.7 shows how many of the surface initiated major fatigue cracks started growing at the flash or somewhere else at the surface. The majority of the cracks initiate at the flash for the surface crack initiating 3D-dumbbell and BOGE test piece.
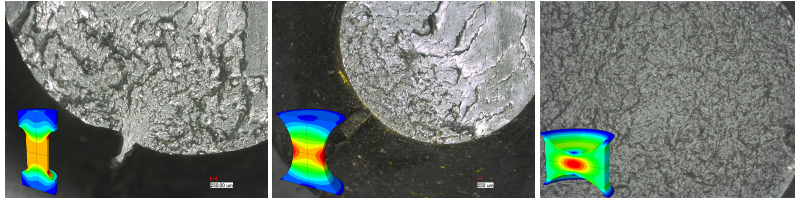
Figure 5.5: SBR 0: Representative examples of fracture surfaces of the dumbbell, BOGE and TDS$_{V2}$ test piece.
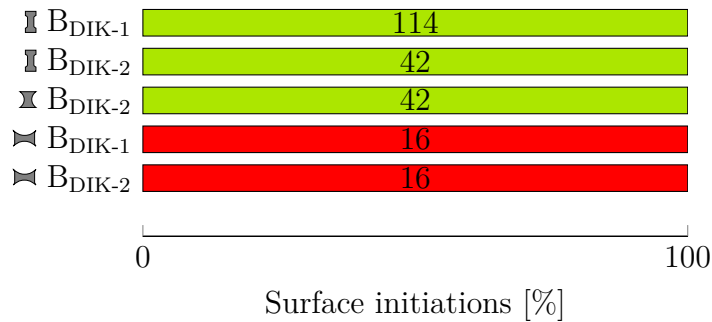
Figure 5.6: SBR 0: Crack initiations at the surface material (yes: green) in number of test pieces in the bar and percent at the axis label. Hence, the colour red is associated with crack initiation with locus in the bulk material.
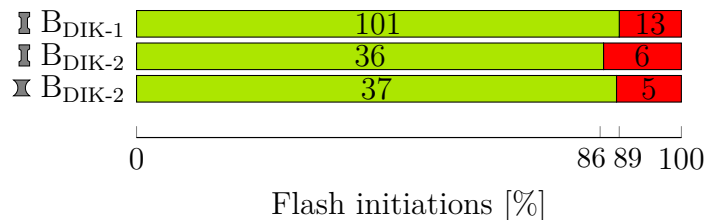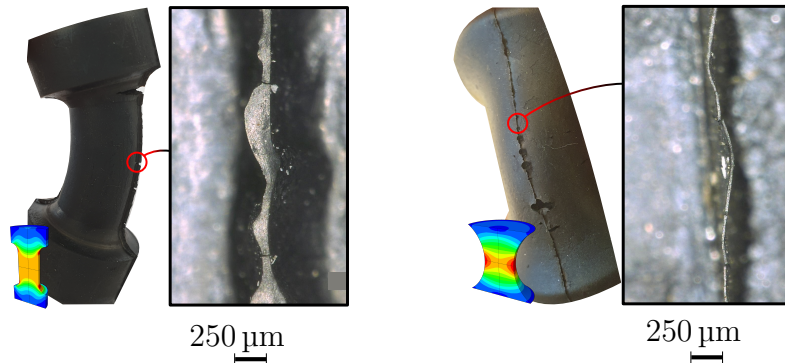

Figure 5.7: SBR 0: Crack initiations at the flash (yes: green) in number of test pieces in the bar and percent at the axis label. Hence, the colour red is associated with crack initiation elsewhere on the surface.

The focus of the fatigue cracks on the flash for the 3D-dumbbell and BOGE test piece explains the reduced lifetimes compared to the TDS$_{V2}$ since all other regions (general surface or bulk material) of these two test pieces are still intact macroscopically at the moment of crack initiation at the flash. However, an even greater lifetime difference is measured between 3D-dumbbell and BOGE test piece. Figure 5.8 shows the difference of their flashes; the difference of their major locus of crack initiation. The two microscopic pictures in Figure 5.8 are equal dimensionally scaled. The 3D-dumbbell mould seems to be more worn, leading to a thicker and on first sight more patchy geometry. The cracks preferentially initiate at the thinner regions of the flash of the dumbbell (close look to

Figure 5.8). Motivated by this, a very simplified finite element model is created. It assumes a repeating narrow and three times thicker flash section (formed by rubber protruding into the mould partition). Only one thick-narrow-thick section of flash is shown in Figure 5.9 on Page 129. In the case the body attached to the flash, representing the main test piece corpus, is deformed with 100 % nominal strain, a deformation of 140 % nominal strain within the narrow section and 174 % nominal strain at the transition region from thin to thick flash is calculated with the finite element analysis. An increase of 40 % nominal strain causes a decrease in lifetime with a factor of ten for the SBR 0 material as shown in Figure 5.4.

The geometry of the shown finite element model is scalable to any arbitrary absolute dimension. Even if not visible for the shown magnification of the BOGE test piece, its flash might show similar thickness variations using a greater magnification. However, the fatigue results shown in Figure 5.4 suggest a less pronounced ratio between thickness of the thick and narrow flash sections, assuming this to be relevant for the lifetime differences. Another possible influence on the lifetime might originate from the average thickness of the flash. The two test pieces show a great difference in this geometrical property. A much stronger orientation of the macro molecules for the thin flash of the BOGE test piece is conceivable. Unfortunately, to the knowledge of the author, there is no research available investigating the effect of thickness of thin rubber films on the lifetime.

Figure 5.8: Crack initiation at the flash of the dumbbell and BOGE test piece.
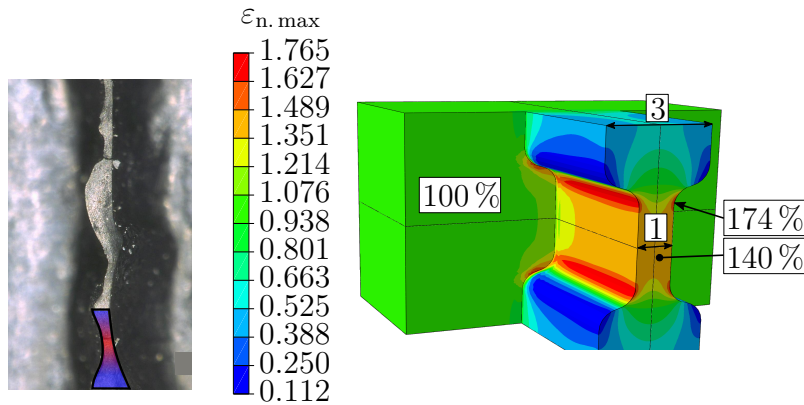
Figure 5.9: Exemplary deformation concentration due to the varying thickness of the flash. This example is motivated by 3D-dumbbell-based observations. Within the micrograph one segment of the flash is overlain by colours to highlight areas with potentially small (blue) and large (red) deformation.

Figure 5.10 shows the fatigue results for the 3D-dumbbell ⬛, TDS_{V2} ⋈ and $TDS_{Concave}$ ⬛ based on the filled SBR 77 material. The results from the BOGE test piece are discard for the SBR 77 as reasoned in Section 5.3.

As for the unfilled SBR 0, longer lifetimes are measured for the TDS_{V2} compared to the 3D-dumbbell and $TDS_{Concave}$. The latter two show the same fatigue behaviour. However, the lifetime difference of the 3D-dumbbell made from different batches, observed for the SBR 0 in Figure 5.4, disappears for the SBR 77 as shown in Figure 5.10. Adding filler only, seems to extinguish the lifetime reducing effects observed for SBR Type 1793 (B_{DIK-2}), compared to SBR Type 1723 (B_{DIK-1}).

Table 5.3 helps to keep the overview in the subsequent discussion. The lifetime difference for the lowest load-level (see Figure 5.10) of the TDS_{V2}, made from SBR 77, is present for SBR 0 in Figure 5.4 as well. For the TDS_{V2}, a significant more rigid fatigue test machine was used for the tests with the batch B_{DIK-2} compared to the tests based on the B_{DIK-1}. The overall less rigid fatigue machine from the B_{DIK-1} tests causes an increase in stroke and therefore global deflection as soon as one of the four simultaneously tested TDS_{V2} fails. The given deflection is set up within the first cycles, with four intact TDS_{V2}. For this reason, tests using the less rigid fatigue machine tend to result in biased data with shorter lifetimes. This effect has more impact with increasing stiffness of the test piece, possibly explaining the less pronounced effect for the softer SBR 0-based TDS_{V2}, although it is still present. While the stiffness differences of the fatigue machines give a possible answer to the effect shown for the lowest load-level, no lifetime difference is measured of the uppermost load-level of the TDS_{V2} and the two batches. However, the microscopic investigation of the fracture surfaces of the TDS_{V2} a general shift, for B_{DIK-2} compared with B_{DIK-1}, of the locus of crack initiation towards the metallic insert is salient especially for the highest load-level. This possibly raised sensitivity for hydrostatic loadings is detected for the NR-based material too (see Section 4.3.7 or the following evaluations in this section). The

possible issues with the bonding system might compensate the effects originating from the stiffness differences of the fatigue machines.
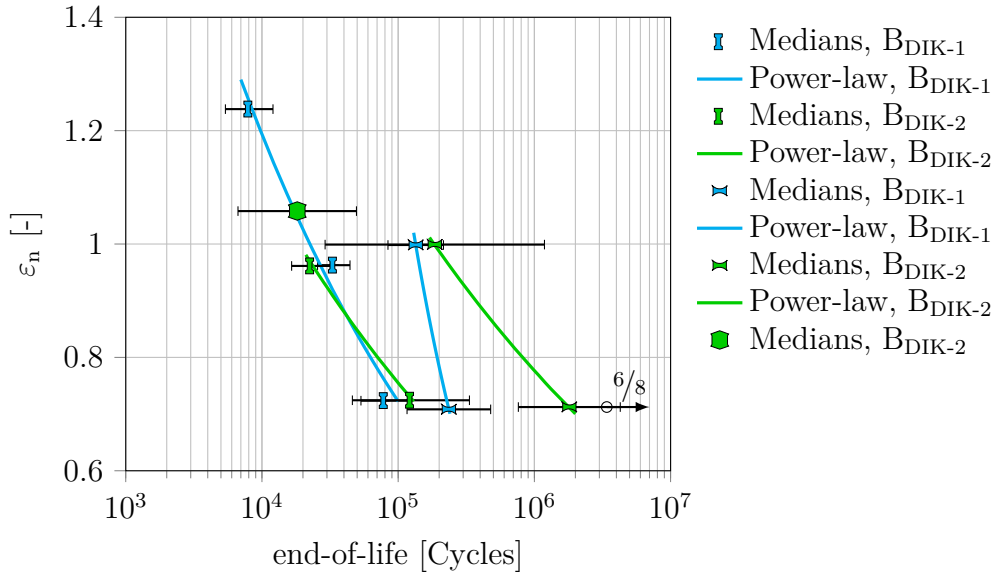

Figure 5.10: SBR 77: Wöhler-curves of the 3D-dumbbell ⚍, TDS_{V2} ⋈ and $\text{TDS}_{\text{Concave}}$ ⬡ based on the DIK batch Nr. 1 —— and DIK batch Nr. 2 ——. All shown medians are endued with 95 % confidence limits (⊢⊣) and are $\varepsilon_{\text{n.const}}$-based. The $^{\text{X}}/_{\text{Y}}$ stands for X non-failed from Y total test pieces.

	SBR 77 $\text{B}_{\text{DIK-1}}$ ⋈	SBR 77 $\text{B}_{\text{DIK-2}}$ ⋈
Possible bonding defects	No	Yes
Test rig stiffness	Low	High

Table 5.3: SBR 77: Overview of the fracture surface abnormalities and test rig properties for tests on the TDS_{V2} made from $\text{B}_{\text{DIK-1}}$ and $\text{B}_{\text{DIK-2}}$.

Figure 5.11 shows generic examples of crack surfaces of the SBR 77 based on the 3D-dumbbell, $\text{TDS}_{\text{Concave}}$ and TDS_{V2}. All cracks initiated at the surface for the 3D-dumbbell and for the $\text{TDS}_{\text{Concave}}$ whereas each crack initiates within the bulk material for the TDS_{V2} (see Figure 5.12). As shown for SBR 0 in Figure 5.4 on Page 126 and corresponding evaluation, failures initiating in the bulk material instead of at the surface raise the lifetime; same is measured for SBR 77 (see Figure 5.10). In detail for SBR 77, the majority of the surface cracks of the 3D-dumbbell start at the flash (see Figure 5.13). Figure 5.13 shows an equal amount of free surface and flash initiations for the $\text{TDS}_{\text{Concave}}$. However, this finding is based on a very small amount (four) of test pieces.
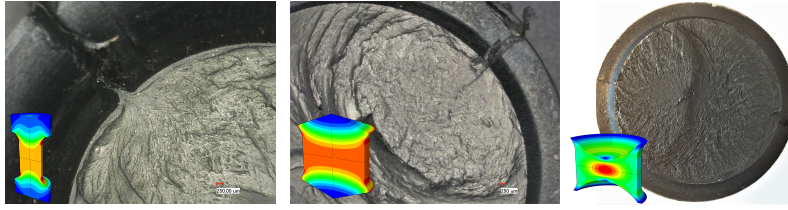
Figure 5.11: SBR 77: Representative examples of fracture surfaces of the dumbbell, TDS$_{\text{Concave}}$ and TDS$_{\text{V2}}$ test piece.
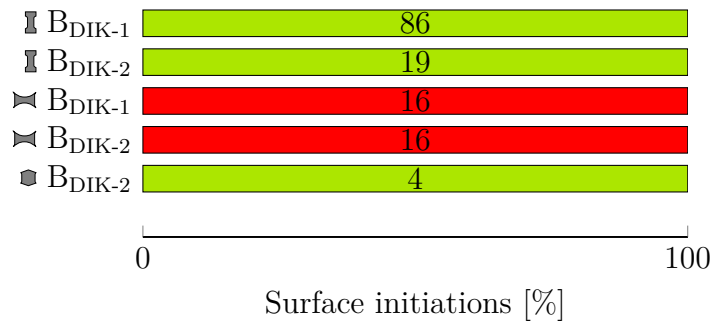

Figure 5.12: SBR 77: Crack initiations at the surface material (yes: green) in number of test pieces in the bar and percent at the axis label. Hence, the colour red is associated with crack initiation with locus in the bulk material.
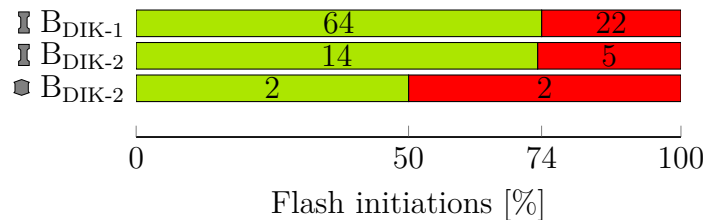
Figure 5.13: SBR 77: Crack initiations at the flash (yes: green) in number of test pieces in the bar and percent at the axis label. Hence, the colour red is associated with crack initiation elsewhere on the surface.

Figure 5.14 shows fatigue results of the 3D-dumbbell ⚎, BOGE test piece ⚏ and TDS$_{\text{V2}}$ ⋈ based on NR 0. The arrangement of the Wöhler curves is reminiscent of the results for the SBR 0 shown in Figure 5.4, because the TDS$_{\text{V2}}$ shows the longest and the 3D-dumbbell the shortest lifetime with the BOGE test piece in between. Nonetheless, Figure 5.14 contains several details that need elucidation. First of all, the possible bonding issues of the TDS$_{\text{V2}}$ made from B$_{\text{DIK-2}}$ yield much shorter lifetimes compared to the B$_{\text{DIK-1}}$-based TDS$_{\text{V2}}$ (⋈ vs. ⋈). The results of the 3D-dumbbell prove an otherwise similar fatigue behaviour of both batches (⚎ vs. ⚎). An even stronger lifetime-reducing effect is found for the uppermost load-level of the TDS$_{\text{V2}}$ based on B$_{\text{DIK-2}}$. As indicated by the depiction of the fracture

pattern acquired at the insert, failure by cavitation took place. Solely for this load-level, material and test piece, the present hydrostatic stress σ_0 at the insert exceeds the critical hydrostatic stress $\sigma_{0.\text{crit}}$ calculated using Equation 3.2 on Page 44. For all other test pieces and materials (SBR 0, SBR 77, NR 45) the hydrostatic stress σ_0 is less than $\sigma_{0.\text{crit}}$ at any region of the test pieces. For this reason, only the two lower load-levels are consider in the fit of the power-law for the TDS_{V2} from $\text{B}_{\text{DIK-1}}$.
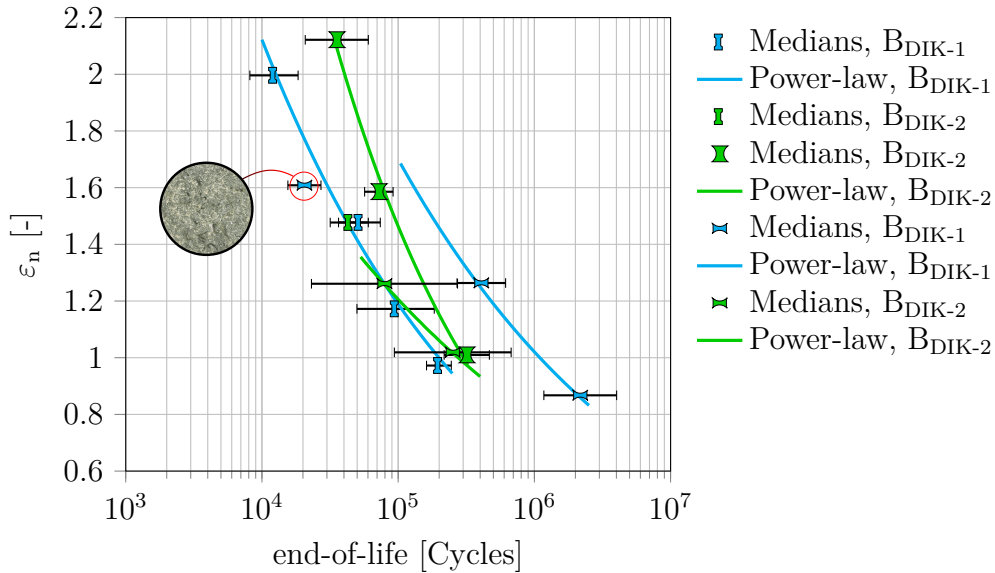

Figure 5.14: NR 0: Wöhler-curves of the 3D-dumbbell ⧛, BOGE test piece ⧓ and TDS_{V2} ⋈ based on the DIK batch Nr. 1 —— and DIK batch Nr. 2 ——. All shown medians are endued with 95 % confidence limits (⊢⊣) and are $\varepsilon_{\text{n.const}}$-based. Picture of the fracture surface with cavitation for the uppermost load-level of ⋈.

The detailed analysis of the fracture surfaces of the TDS_{V2} solidifies the assessment of cavitational damage for uppermost load-level of the TDS_{V2} based on $\text{B}_{\text{DIK-2}}$. For this test condition each failure initiated in direct vicinity of the metallic insert; unlike initiation for the two lower load-levels.

Figure 5.15 shows representative examples of fracture surfaces indicating the focus of the crack initiation on the surface and flash for the 3D-dumbbell and BOGE test piece (see Figure 5.16 and 5.17). As for the SBR materials only bulk material initiations are found for the TDS_{V2} (see Figure 5.16). Yet, the properties of the first batch $\text{B}_{\text{DIK-1}}$ and second batch $\text{B}_{\text{DIK-2}}$ differ. Except for the uppermost load-level (cavitation) of the TDS_{V2} the cracks initiate in the region of maximum $\varepsilon_{\text{n.max}}$ for the $\text{B}_{\text{DIK-1}}$. The possible bonding issues, firstly addressed in Section 4.3.7, with the $\text{B}_{\text{DIK-2}}$ batch occur here as well. One might remark that the bonding issues, in common with caviation, both have the failure locus close to the metallic insert, which complicates distinguishably. This is further discussed in the subsequent evaluation of the NR 45-based fatigue data while the differences between

both phenomena are more distinct there.
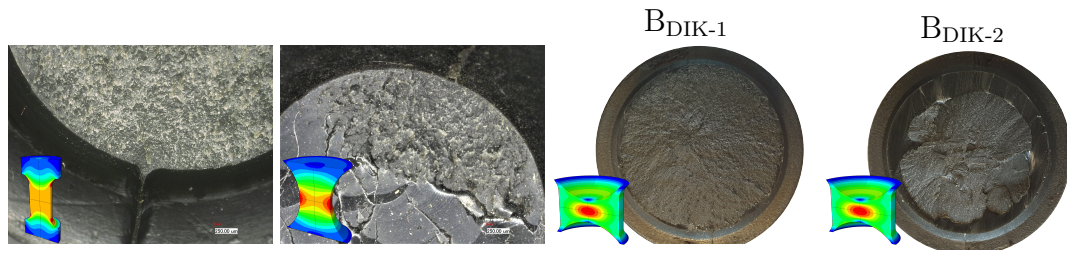
Figure 5.15: NR 0: Representative examples of fracture surfaces of the dumbbell, BOGE and TDS$_{V2}$ test piece.
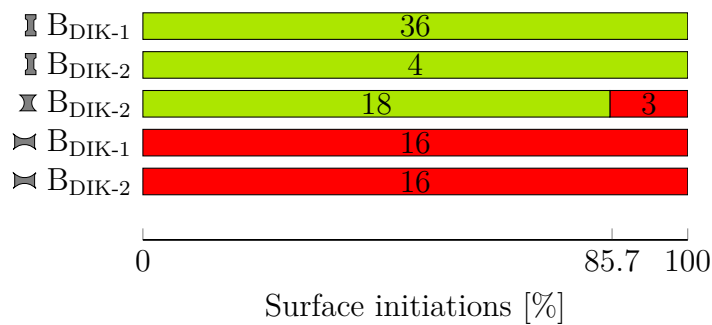

Figure 5.16: NR 0: Crack initiations at the surface material (yes: green) in number of test pieces in the bar and percent at the axis label. Hence, the colour red is associated with crack initiation with locus in the bulk material.
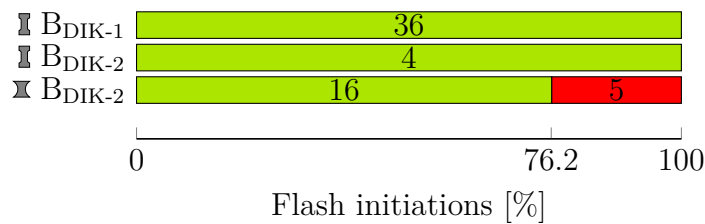
Figure 5.17: NR 0: Crack initiations at the flash (yes: green) in number of test pieces in the bar and percent at the axis label. Hence, the colour red is associated with crack initiation elsewhere on the surface.

Solely the 3D-dumbbell ⚎ and TDS$_{V2}$ ⋈-based Wöhler curves are available for NR 45 (see Figure 5.18). No lifetime difference is measured between the two batches B$_{DIK-1}$ and B$_{DIK-2}$ based on the 3D-dumbbell. However, as for the unfilled material NR 0, a (five times) shorter lifetime is measured for the TDS$_{V2}$ made from B$_{DIK-2}$ in comparison with the B$_{DIK-1}$-based TDS$_{V2}$.
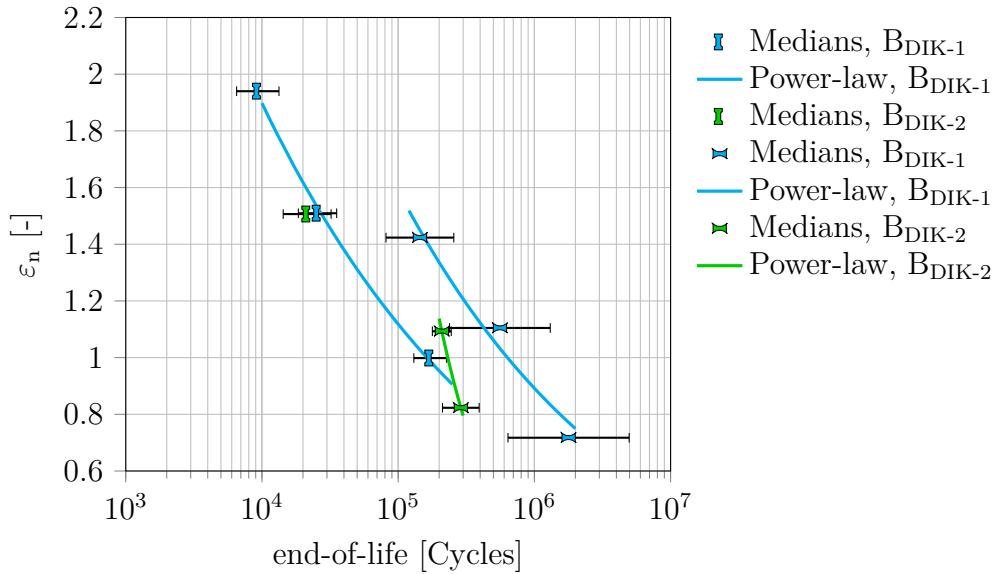
Figure 5.18: NR 45: Wöhler-curves of the 3D-dumbbell ⚏ and TDS_{V2} ⋈ based on the DIK batch Nr. 1 —— and DIK batch Nr. 2 ——. All shown medians are endued with 95 % confidence limits (⊢⊣) and are $\varepsilon_{n.const}$-based.

Different fracture surfaces are associated with the different lifetimes between the TDS_{V2} of the two batches, as shown Figure 5.19. The B_{DIK-2}-based TDS_{V2} might remind of cavitation because the fracture surface is in direct vicinity of the metallic insert. Nevertheless the close-up analysis with a microscope reveals distinct differences between the fracture surface of the B_{DIK-2}-based TDS_{V2} and a *classical* cavitation damage.

Figure 5.20 shows magnifications of fracture surfaces from the B_{DIK-2} and B_{DIK-1}-based TDS_{V2}. The cavitation damage of the B_{DIK-1} example occurred for the uppermost load-level and was found by cutting the test piece close to the insert only. This cavitation damage is not involved in the major failure of the test piece. As a first difference between the two investigated cases in Figure 5.19 and 5.20, the cavitation-like patterns for B_{DIK-2} occur independent of the load-level; even if the hydrostatic stress σ_0 is much lower than the critical hydrostatic stress $\sigma_{0.crit}$. Secondly, the *classical* cavitation damage from the B_{DIK-1}-based TDS_{V2} is characterised by pronounced crater-like patterns, as shown by the three-dimensional depiction acquired with a confocal microscope in Figure 5.20. In contrast to this, the cavitation-like patters of the B_{DIK-2}-based TDS_{V2} are rather flat. Additionally, this pattern spreads over the complete insert surface in case of B_{DIK-2}, in contrast to the localised (at maximum σ_0) occurrence of the B_{DIK-1}-based patterns. Hence, the results of the B_{DIK-1}-based TDS_{V2} are assumed to be relevant for the comparison with the 3D-dumbbell results; less relevant are the results of the B_{DIK-2}-based TDS_{V2} due to the suspicion of bonding based failure.
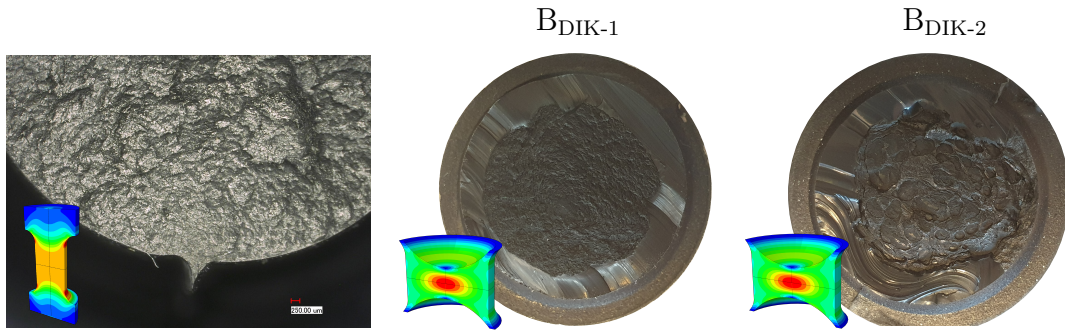
Figure 5.19: NR 45: Representative examples of fracture surfaces of the dumbbell and TDS$_{V2}$ test piece.
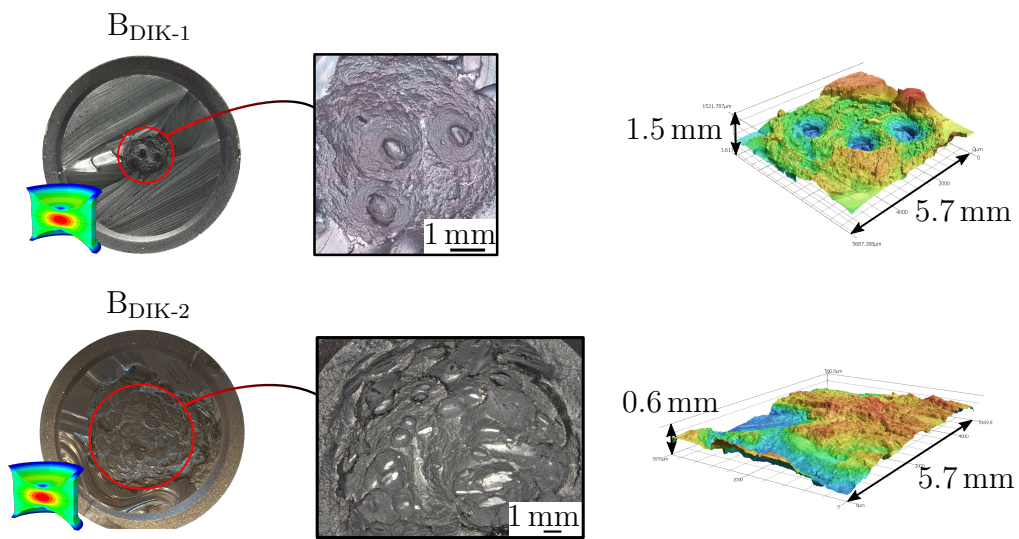
Figure 5.20: Failure initiation at the insert for TDS$_{V2}$; comparison between DIK batch Nr. 1 (B$_{DIK-1}$) and Nr. 2 (B$_{DIK-2}$). The topographical figures at the right hand side are rotated relative to the micrographs.

The reduced lifetime of the 3D-dumbbell and TDS$_{V2}$ is attributed to the dumbbell's propensity for crack initiation at the flash (see Figure 5.21 and 5.22).
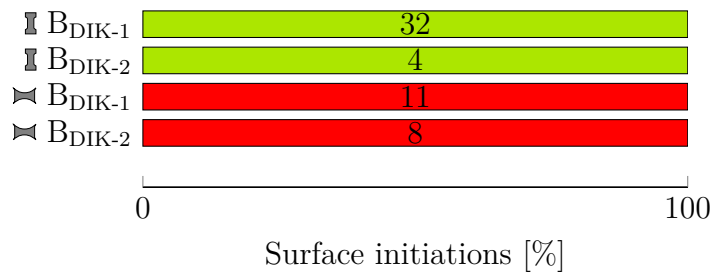
Figure 5.21: NR 45: Crack initiations at the surface material (yes: green) in number of test pieces in the bar and percent at the axis label. Hence, the colour red is associated with crack initiation with locus in the bulk material.
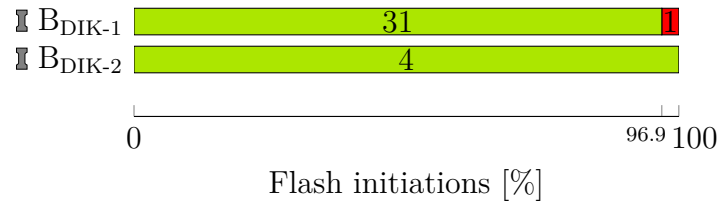
Figure 5.22: NR 45: Crack initiations at the flash (yes: green) in number of test pieces in the bar and percent at the axis label. Hence, the colour red is associated with crack initiation elsewhere on the surface.

5.5 Conclusions

Summing up Chapter 5:

- The mechanical failure of the TDS_{V2} is caused by cracks initiating in the bulk material, independent of the load-level and material. TDS_{V2} fatigue test results are therefore surface texture and flash-independent.

- Test pieces with propensity to crack initiation at the flash tend to have shortened lifetimes.

- The comparison of the BOGE test piece with the 3D-dumbbell in Figure 5.4, Page 126 and 5.14, Page 132 shows a different impact of their flashes on the lifetime. Since the flash is the only known varied fatigue-influencing parameter in this case, the fatigue of rubber must significantly depend on the properties of the corresponding mould partition line. This might be less true for filled rubber materials as indicated by the equal lifetimes of the $TDS_{Concave}$ and 3D-dumbbell for SBR 77 in Figure 5.10, Page 130. However, comprehensive results are pending for the $TDS_{Concave}$.

- The damage by tri-axial tensile loads influences the fatigue much more strongly compared to the *classic* failure initiation at inhomogeneities in e.g. uniaxial-dominated stress-fields. Even if much more sophisticated cavitation criteria can be found in literature (see e.g. Fond's review [99]), the applied criterion from Ball and Gent [67,68] (see Equation 3.2, Page 44) shows good performance in the present study.

Note that, for the 3D-dumbbell made from filled EPDM, in the study from Gehrmann et al. [51], a less distinct focus of the cracks on the flash is encountered. This can be possibly explained by much more damaging particle-like inhomogeneities in this rubber material, dominating the damage potential of the flash.

Conclusively of Chapter 5 it needs to be emphasised that the differences in hydrostatic stress σ_0 are negligible between the 3D-dumbbell, $TDS_{Concave}$ and BOGE test piece for a given strain. The re-plot of the corresponding lifetime results using stress instead of

strain would therefore not alter the location of the corresponding Wöhler curves with respect to each other. A much bigger difference in hydrostatic stress σ_0 at the average locus of crack initiation is present for the TDS_{V2}, compared to the other three test piece geometries. Independent of the material, longer lifetimes are found for the TDS_{V2} in strain-lifetime-plots. The depiction of these data in a stress-lifetime-plot would only increase the gap in lifetime between the TDS_{V2} and the others. The same statement holds for a strain energy density based depiction. The fatigue results are primarily plotted using strains throughout this study since strain-values are assumed to be less susceptible for the description of the displacement-controlled experiments against e.g. the chosen material model.

6 Influence of dwell periods on the mechanical fatigue of rubber

Chapter 6 examines dwell periods within cyclic loading and their implication on the lifetime. This investigation is motivated by components loaded in service. These real-life loadings are rarely of continuous cyclic nature. However, the Wöhler concept based end-of-life prediction of components commonly uses fatigue results of simple test pieces exposed to continuous cyclic loading. A systematic inaccuracy in end-of-life prediction of components might be the consequence. Prior to the study of this possibly fatigue-influencing factor, the accuracy of mechanical fatigue testing itself was improved with the methods from Section 4.1 and 4.2, as well as by the development of a test pieces geometry delivering surface quality-independent lifetime results. The study of the dwell periods took place parallel to the development of the new test piece. For this reason, the majority of the results within this chapter are produced with the 3D-dumbbell.

## 6.1 Fatigue testing with dwell periods - Test protocol

Section 3.4 lists two studies approaching the influence of dwell periods on the fatigue of rubber. Roland and Sobieski performed fatigue tests with 24 h to 72 h long single dwell periods. A maximum influence in number of cycles to failure with a factor of 3.5 was found for unfilled NR. More significant influence was measured by Harbour et al. with crack growth tests (growth of a preexisting macroscopic crack under cyclic loading) [70]. They found a factor of ten in crack growth per cycle for their carbon black filled SBR for much shorter dwell periods, of only a few seconds, but constantly recurring in between a few load-cycles (see Section 3.4).

The fatigue of rubber was successfully correlated to fracture mechanics more than 55 years ago [98]. Therefore the study of Harbour et al. is used as main template for the test protocol definition of the present study. Five cycles $N_\mathrm{d} = 5$ between dwell periods of $t_\mathrm{d} = 10\,\mathrm{s}$ length is chosen to be performed for all materials (nomenclature is shown in Figure 3.8 on Page 45). It is a compromise between test duration and maximized impact of the dwell periods on the fatigue (see Figures 3.9 to 3.11 starting on Page 46). Moreover, this test condition is applied with loaded ($\varepsilon_\mathrm{d} = \varepsilon_{\sim.\mathrm{max}}$) and unloaded ($\varepsilon_\mathrm{d} = 0$) dwell periods. In addition to the ($N_\mathrm{d} = 5$ - $t_\mathrm{d} = 10\,\mathrm{s}$) - combination, for some materials, experiments with longer dwell periods but same $N_\mathrm{d}/t_\mathrm{d}$-ratio (e.g. $N_\mathrm{d} = 100$ - $t_\mathrm{d} = 200\,\mathrm{s}$) as well as changed $N_\mathrm{d}/t_\mathrm{d}$-ratio (e.g. $N_\mathrm{d} = 2000$ - $t_\mathrm{d} = 5\,\mathrm{min}$) are conducted.

Further, all four materials from Chapter 5 (same two batches), shown in Table 5.1, are investigated in this study about the influence of dwell periods. As before, all fatigue tests are conducted using force convection, frequency adaptation for each load-level, and are displacement-controlled loading. The results in the following figures that originate from finite element simulations use the Plagge material model with corresponding fits shown in Section 4.3.1 and 5.2.

6.2 Static relaxation vs. Cyclic relaxation

A dwell period is nothing more than a static relaxation step. In order to research the static relaxation properties, the reaction force of a uniaxial compressed cylinder $\varepsilon_{n.11} = -25\%$ with an undeformed height of $8\,\text{mm}$ and diameter of $12\,\text{mm}$ is measured over time according to ISO 3384 [100]. The static relaxation rates of the SBR and NR material are approximately equal (see Figure 6.1).
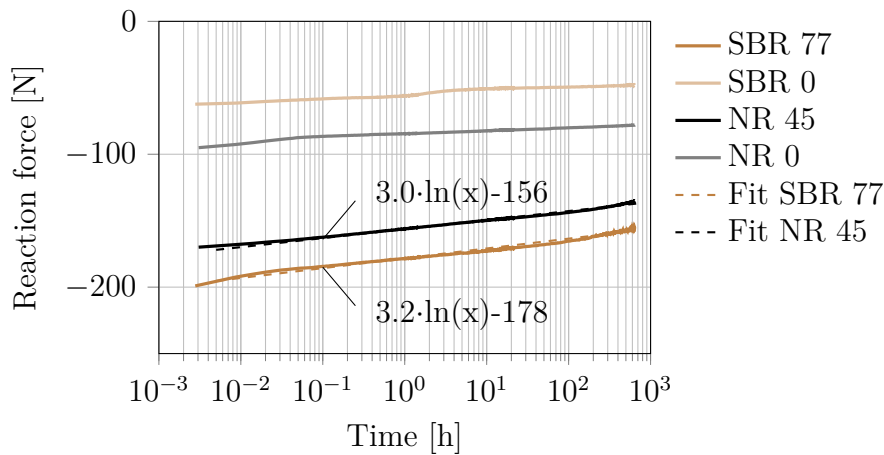
Figure 6.1: Static relaxation of a compressed cylinder.

For the cyclic relaxation tests - the fatigue tests - four 3D-dumbbells are cycled simultaneously in one fixture, attached to one load-cell. For this reason, the data from Figure 6.2 to 6.9 are averaged over four to eight (eight in case of repeated experiments) test pieces. Figure 6.2 shows the maximum reaction force $\text{Force}_{\sim.\text{max}}$ within the cyclic deflection of the 3D-dumbbell for the NR 0 material. The reaction force tends to greater values for unloaded dwell periods (see blue lines in Figure 6.2). This propensity is measured for all materials and is dedicated more focus to for the NR 45 material, which shows a much more pronounced effect. The colour-code:

  black $\Rightarrow$ no dwell periods
    red $\Rightarrow$ loaded dwell periods
  blue $\Rightarrow$ unloaded dwell periods

is used for the Figures 6.2 to 6.15.

The reason for greatest value of Force$_{\sim.\mathrm{max}}$ for the continuously cycled case (——) and the $N_\mathrm{d} = 2000$ case (–·–··) is not fully understood within this dataset. A possible reason originates from the circumstance that these two measurements are performed as the very first ones from the complete dataset. All other tests were conducted one month later. Small impacts of aging, even if the test pieces were stored at $-25\,°\mathrm{C}$, might show an influence on the reaction force when deflected. The deviations of Force$_{\sim.\mathrm{max}}$ in Figure 6.2 are in general fairly small compared to the filled NR 45 or SBR 77 materials.

The finite element analysis (FEA) lies in the region of the test data. FE simulations are performed consistently for all materials and load-level for the continuously cycled case. Within these FEAs, 700 continuous displacement cycles are simulated. By way of example, FEAs with dwell periods are only conducted for the NR 45 material and are discussed at Figure 6.4. As broached in Section 3.2 and discussed in Section 4.2, cyclic relaxation dominates static relaxation for the here investigated filled elastomers and mainly depends on the number of times the load has been applied and not on the e.g. load frequency or more general, the time the load has been applied. The validity of this assumption is shown in Figure 6.3 and 6.6. Within these data plotted against load-cycles, based on the rate of decrease of Force$_{\sim.\mathrm{max}}$, one cannot distinguish between the different test conditions with and without dwell periods. This pure dependency of the relaxation should be less true for e.g. unfilled NR according to Derham and Thomas [42]. However, no clear assertion can be made from the corresponding data in Figure 6.2.
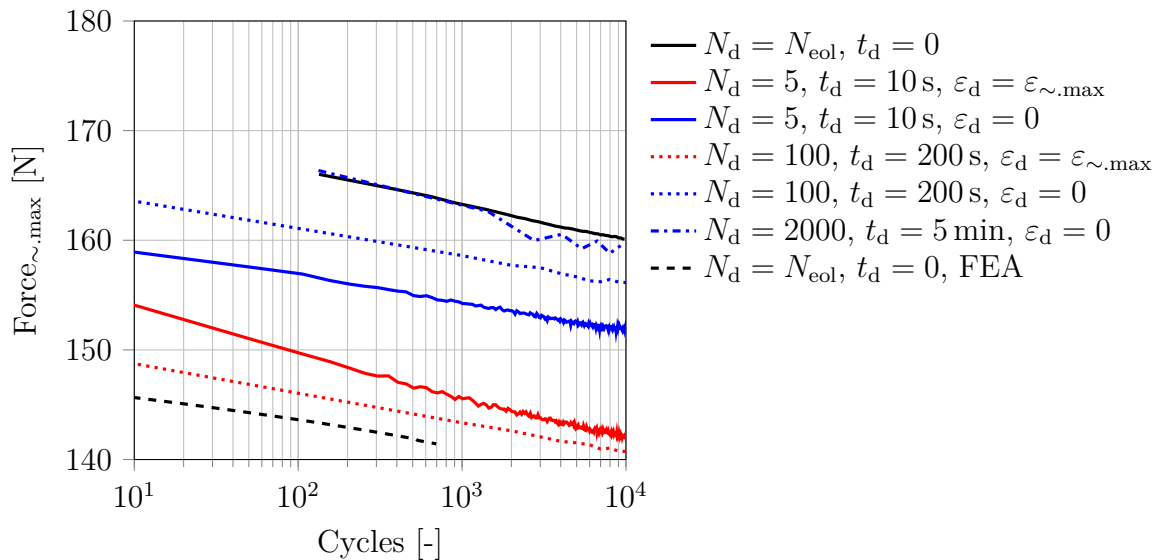
Figure 6.2: NR 0: Cyclic relaxation of the 3D-dumbbell with $\varepsilon_{\sim.\mathrm{max}} \approx 150\,\%$ for all cases. For the cases with the $N_\mathrm{d} = 5$ and $N_\mathrm{d} = 100$ the Force$_{\sim.\mathrm{max}}$ is taken from the third for $N_\mathrm{d} = 2000$ from the last cycle. The data from the (——) and the (–·–··) case are only available starting from more than hundred cycles, due to a different test procedure.

Focusing on the cases with $N_{\mathrm{d}} = 5$, a much more pronounced Force$_{\sim.\max}$ increase effect due to unloaded dwell periods is measured for NR 45 compared to NR 0 (see Figure 6.3 and compare with 6.2). Figure 6.4 can be considered as an extract from Figure 6.3. It shows the data from two cycle-dwell periods at approximately 2500 load-cycles against time. The loaded $\varepsilon_{\mathrm{d}} = \varepsilon_{\sim.\max}$ or unloaded $\varepsilon_{\mathrm{d}} = 0$ holding determines whether an increasing or decreasing characteristic is measured for Force$_{\sim.\max}$ within the dynamic periods (here five cycles) and has a significant impact on the total average level of Force$_{\sim.\max}$ (● vs. ●). For unloaded $\varepsilon_{\mathrm{d}} = 0$ dwell periods, the material recovers in the undeformed state causing greater reaction force within the first subsequent cyclic loads. After 175 load-cycles, this effect almost disappears and ⋯⋯ in Figure 6.3 is therefore close to ⋯-⋯. The case $N_{\mathrm{d}} = 5$ with loaded and unloaded dwell periods is simulated in an FEA using the Plagge model for in total 100 load-cycles. Similar to the test-data from Figure 6.4, an increasing and decreasing Force$_{\sim.\max}$ trend is calculated within the 5 load-cycles for loaded and unloaded dwell periods, respectively. A similar deviation in average Force$_{\sim.\max}$ is obtained as well. Although the FEA based on the Plagge model calculates too large reaction forces, as shown in Figure 6.3, the deviation of about $10\,\%$ between continuous cyclic loading ▬ and $N_{\mathrm{d}} = 5$ with $\varepsilon_{\mathrm{d}} = 0$ ▬ is correctly predicted by this material model.

With reference to the fatigue results from subsequent Section 6.3, the behaviour of the local strains and stresses at the average spot of failure initiation of the 3D-dumbbell shall estimated with the simulations using the Plagge model. Although the global reaction force significantly increases for the test $N_{\mathrm{d}} = 5$ and $\varepsilon_{\mathrm{d}} = 0$, with respect to the continuous cyclic loading, the global deflection in this displacement-controlled FE-simulation stays unaffected. For this reason, it is hardly surprising that the local strain does almost not differ between these two load-cases. On the other hand, in the increase of $10\,\%$ in Force$_{\sim.\max}$ is almost fully passed on to the local stress; the local maximum principal Cauchy stress increases with $8\,\%$. Therefore, the experiments of the present chapter provide the unique possibility to obtain fatigue measurements with different local stress values and at the same time almost unaltered local strains.

The position of the ▬ curve below the other data could not be conclusively resolved. Possible reasons are an impact of the $5\,°\mathrm{C}$ to $10\,°\mathrm{C}$ greater test piece temperature during the ongoing cyclic deformation, stiffness fluctuations among the test pieces or the more precise displacement control of the servo-hydraulic fatigue test rig for continuous cyclic loadings.
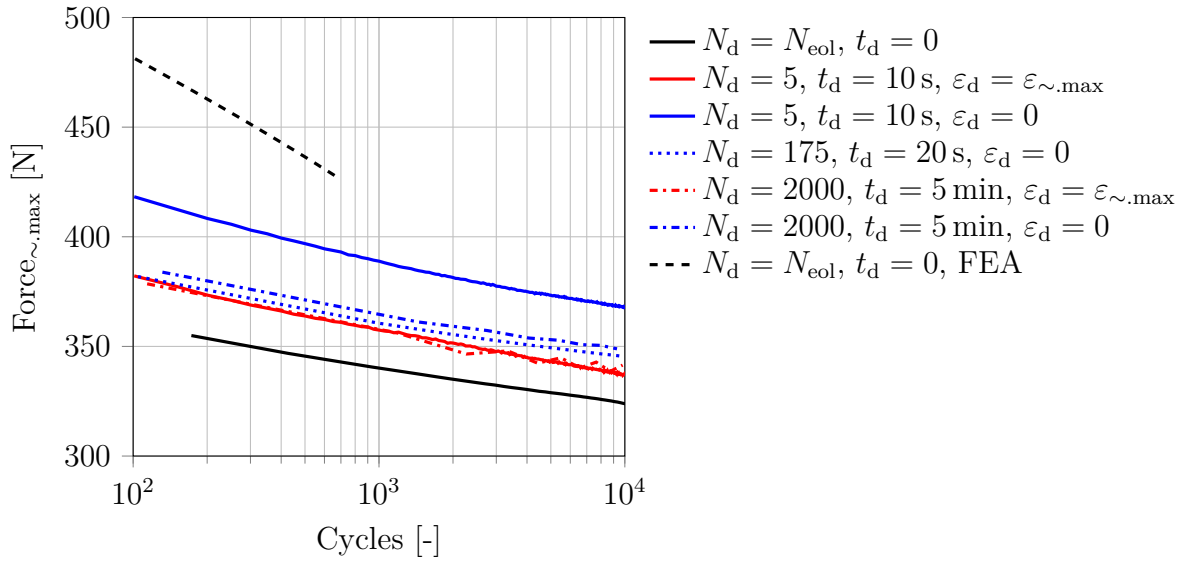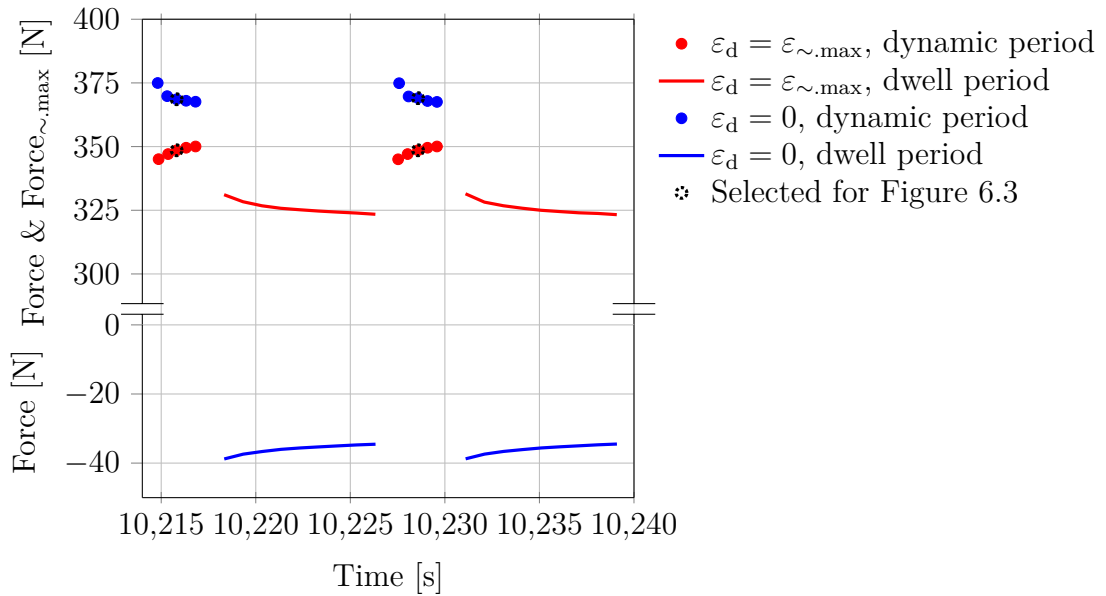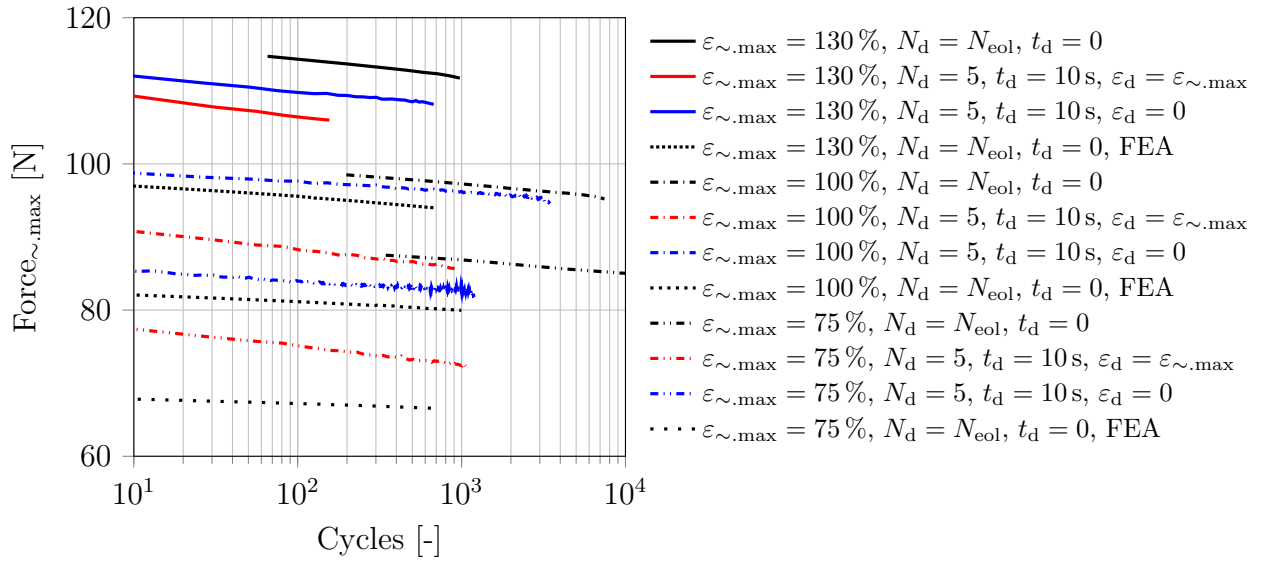
Figure 6.3: **NR 45**:Cyclic relaxation of the 3D-dumbbell with $\varepsilon_{\sim.\text{max}} \approx 150\,\%$ for all cases. For the cases with the $N_\text{d} = 5$ the Force$_{\sim.\text{max}}$ is taken from the third for $N_\text{d} = 2000$ and $N_\text{d} = 175$ from the last cycle.

Figure 6.4: **NR 45**: Details of two cyclic loadings and dwell periods from the $N_\text{d} = 5$, $t_\text{d} = 10\,\text{s}$, $\varepsilon_\text{d} = \varepsilon_{\sim.\text{max}}$ and $N_\text{d} = 5$, $t_\text{d} = 10\,\text{s}$, $\varepsilon_\text{d} = 0$ load cases from Figure 6.3.

For the SBR 0 and SBR 77 material, the data for the cyclic relaxation are not limited on only one load-level (see Figure 6.5 and 6.6). As with the NR materials, the dynamic force peaks Force$_{\sim.\text{max}}$ are significantly greater if the dwell periods are without strain (see —, $\text{-}\cdot\text{-}\cdot$, $\text{-}\cdots$ in Figure 6.5 and 6.6). For the filled material SBR 77, the Force$_{\sim.\text{max}}$ from the tests with unloaded dwell periods (100 % $\text{-}\cdot\text{-}\cdot$, 75 % $\text{-}\cdots$) are even close to the Force$_{\sim.\text{max}}$

from the next greater load-level of the tests with loaded dwell periods (130 % ——, 100 % ----).

Figure 6.5: SBR 0: Cyclic relaxation of the 3D-dumbbell for different load-level and load cases. Force$_{\sim.\text{max}}$ originates from the third load-cycle for fatigue tests with dwell periods.
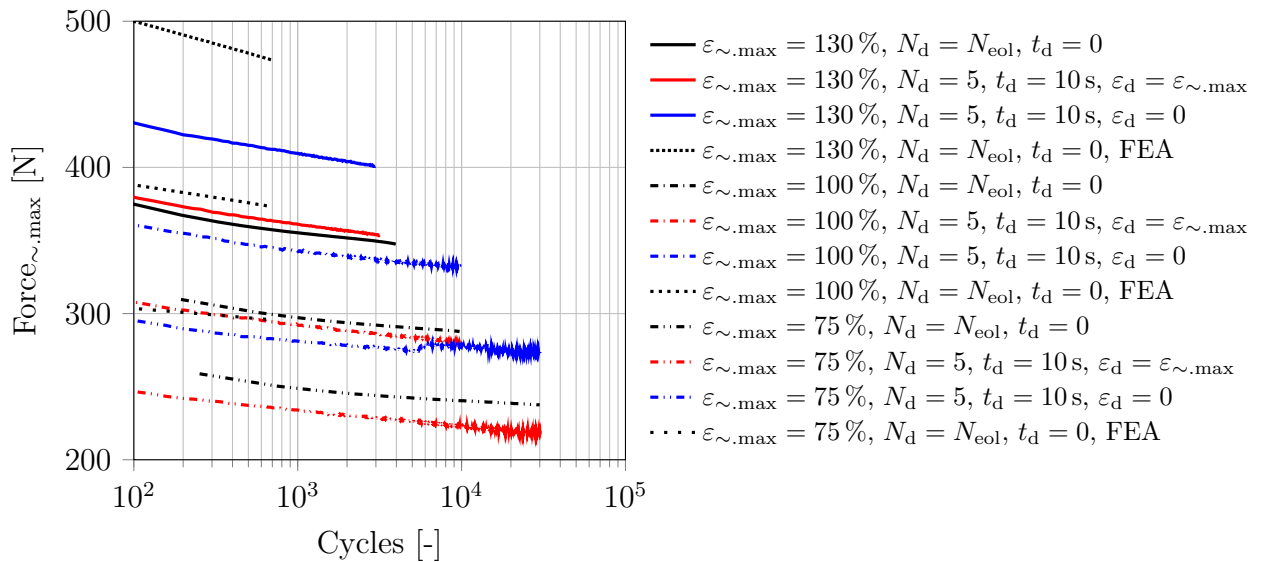
Figure 6.6: SBR 77: Cyclic relaxation of the 3D-dumbbell for different load-level and load cases. Force$_{\sim.\text{max}}$ originates from the third load-cycle for fatigue tests with dwell periods.

Summing up the results for the cyclic relaxation with loaded dwell periods and unloaded dwell periods:

- The average maximum cyclic reaction force Force$_{\sim.\text{max}}$ is always greater in case of unloaded dwell periods compared to loaded dwell periods.

- This stays true independent of the material or load-level and becomes less pronounced with increasing number of cycles subsequent to the dwell periods N_{d} in case the latter cycle of N_{d}-block is evaluated (see cases with $N_{\text{d}} = 175$ or $N_{\text{d}} = 2000$).

- In fact, the significant differences in Force$_{\sim.\text{max}}$ for the unloaded and loaded dwell periods for the exact same global deformation provides the unique possibility to induce greater local stress for the same local strain.

The static relaxation experiments with the compressed cylinder according to ISO 3384 [100] from Figure 6.1 are only contingently comparable with the 3D-dumbbell loaded in tension. As a result, static relaxation experiments using the 3D-dumbbell are conducted, however, only for the SBR materials.

The data in Figure 6.2 to 6.6 are plotted against load-cycles. To be able to plot the cyclic and static relaxation data in one figure, an "effective time" is introduced (see Figure 6.7). As defined in Equation 6.1, this variable describes the time of true loading. For instance, the effective time of a pure sinusoidal load (between zero & one) signal is taken to be one half of the effective time of a pure static relaxation test with load one (simply one times length of test).

In advance of the static relaxation periods, 200 cyclic deformations are performed to soften the material. Figure 6.8 shows the SBR 77 based static relaxation with the cyclic relaxation data over effective time for the uppermost load-level only. In agreement with the results from Section 4.2, a greater decrease of Force$_{\sim.\text{max}}$ from the cyclic relaxation tests in comparison with the decrease of the static reaction force is shown in Figure 6.8. Due to the visco-elastic material behaviour of rubber, the static reaction force is lower than the dynamic reaction force Force$_{\sim.\text{max}}$. For the unfilled SBR 0 - material less distinct tendencies in consequence of the relatively small reaction forces and much less general relaxation (see Figure 5.2 on Page 123) are found.
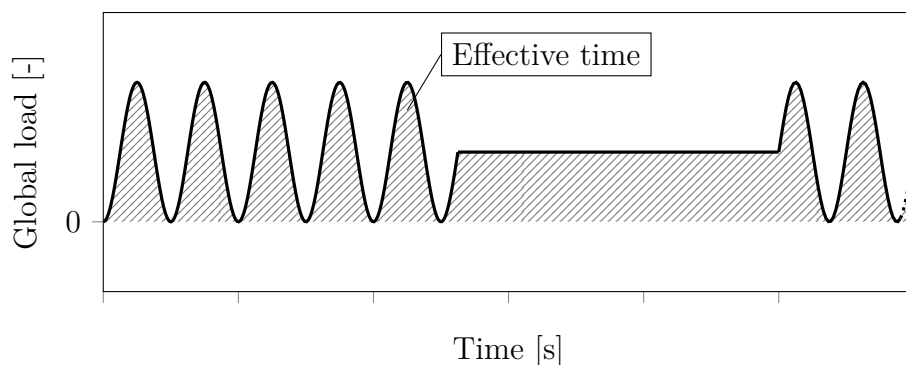
Figure 6.7: Illustration of the effective time.

$$\text{Effective time} = \int\limits_0^{\text{trial period}} \frac{\text{global deflection}(t)}{\max(\text{global deflection})} \, \mathrm{d}t \qquad (6.1)$$
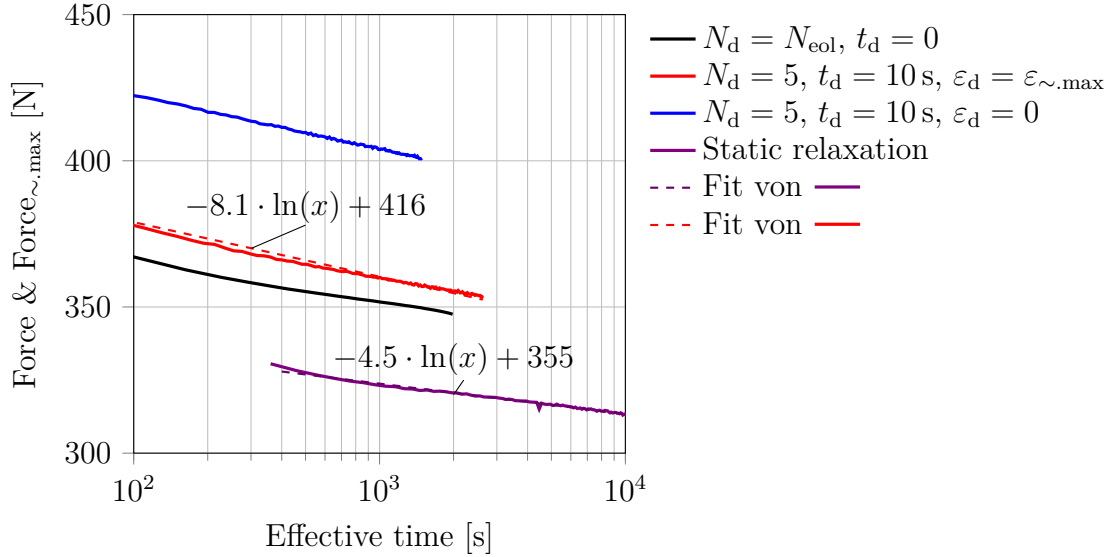
Figure 6.8: SBR 77: Cyclic relaxation vs. static relaxation of the 3D-dumbbell with equal global deflection ($\varepsilon_{\text{static}} = \varepsilon_{\sim.\text{max}} \approx 130\,\%$). Force$_{\sim.\text{max}}$ originates from the third load-cycle for fatigue tests with dwell periods.
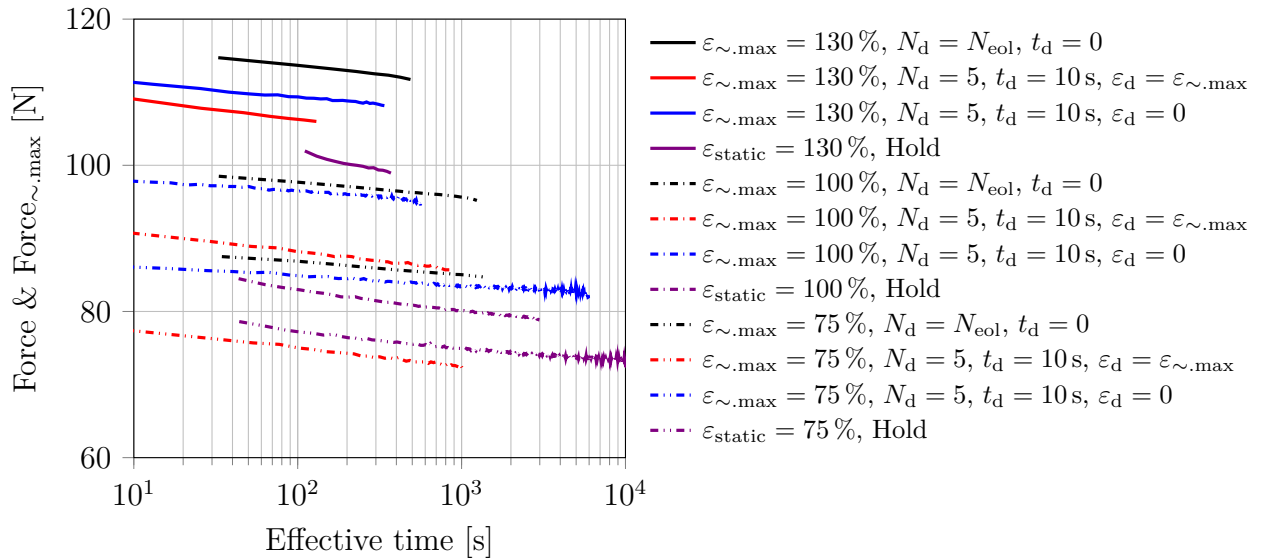
Figure 6.9: SBR 0: Cyclic relaxation vs. static relaxation of the 3D-dumbbell with equal global deflection for different load-level and load cases. Force$_{\sim.\text{max}}$ originates from the third load-cycle for fatigue tests with dwell periods.

6.3 Fatigue test results

Figure 6.10 shows the NR 0 based fatigue results. The different variations of dwell periods do not influence the number of cycles to end-of-life. In addition to the tests with short dwell periods, motivated from Harbour et al. [70], the test protocol from Roland and Sobieski [71] is applied as well. Solely the test condition with the most significant lifetime impact of factor 3.4 is repeated. This test protocol starts with 200 load-cycles, followed by a single $t_d = 48\,h$ dwell period and ends with cycling the test piece until end-of-life. However, only a factor of 1.8 is measured between continuous cyclic test ◆ and the test with the single 48 h long dwell period ◇. Yet, their factor of 3.4 is still statistically possible with respect to the size of the 95 % confidence limits (see enlargement in Figure 6.10). However, a very large number of test pieces would be necessary to work out these relatively small lifetime impacts.
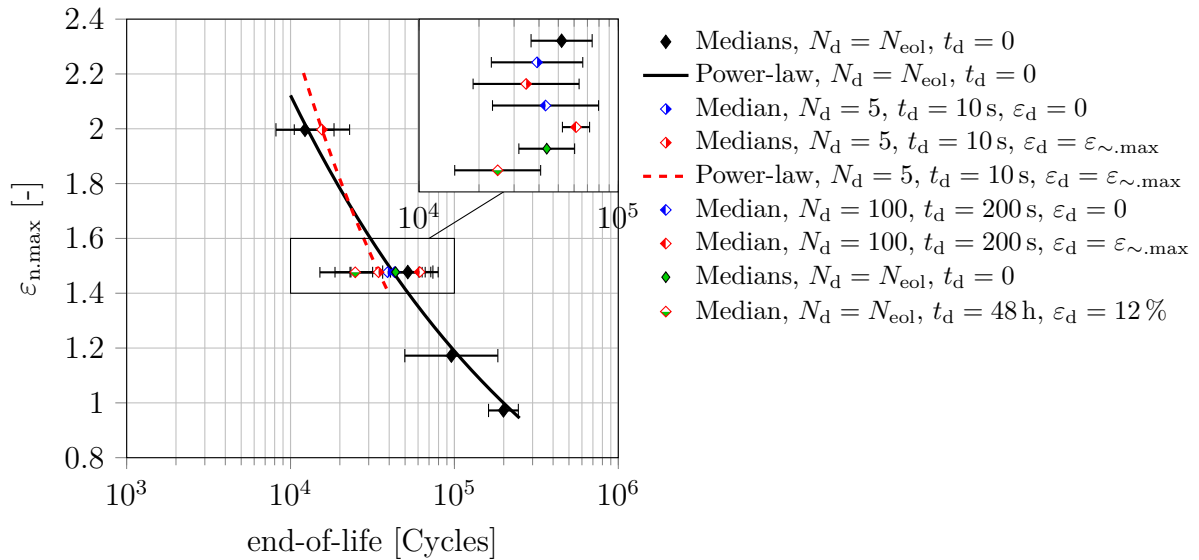
Figure 6.10: NR 0: Fatigue test data of the 3D-dumbbell with and without dwell periods. For reasons of clarity, a zoom of the load-level $\varepsilon_{n.max} \approx 150\,\%$ is shown in the corner. Within this enlargement the data-points are vertically shifted. All shown medians are endued with 95 % confidence limits (⊢⊣) and all shown data are B_{DIK-1} and ε_{const}-based. Only ◆ and ◇ are measured based on B_{DIK-2}.

The effect of increased peak reaction force for unloaded dwell periods is much more distinct for NR 45 compared to NR 0 (see Figure 6.2 and 6.3 starting on Page 140). Figure 6.3 shows an up to 10 % increased average Force$_{\sim.max}$ for unloaded dwell periods compared to loaded dwell periods. A load difference of 10 % causes an approximate lifetime decrease of 50 %, assuming the slope of the power-law from Figure 6.11. Nevertheless, only small lifetime differences are found in Figure 6.11 for all load cases.
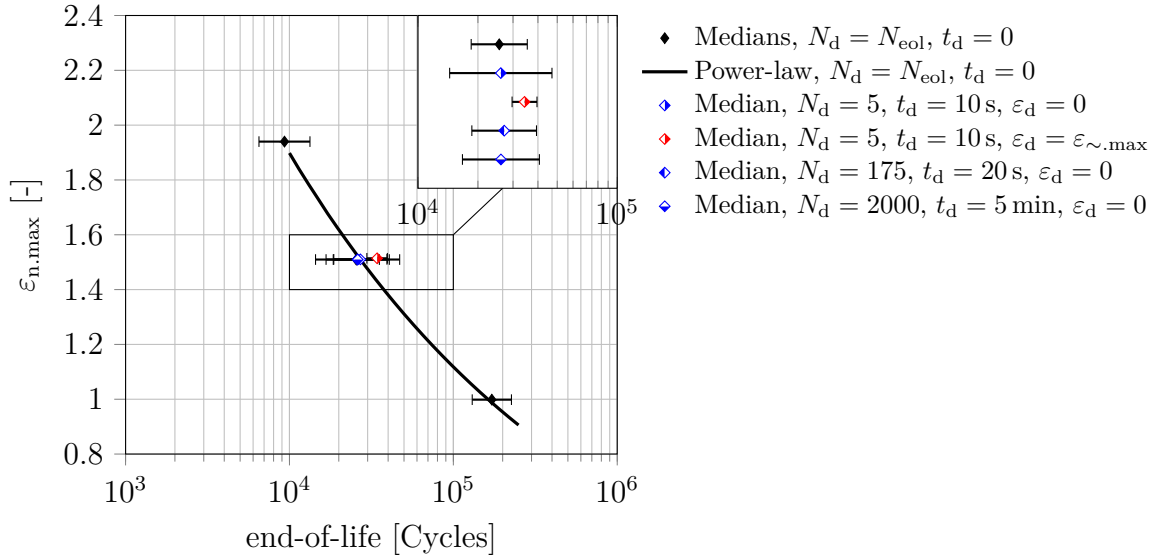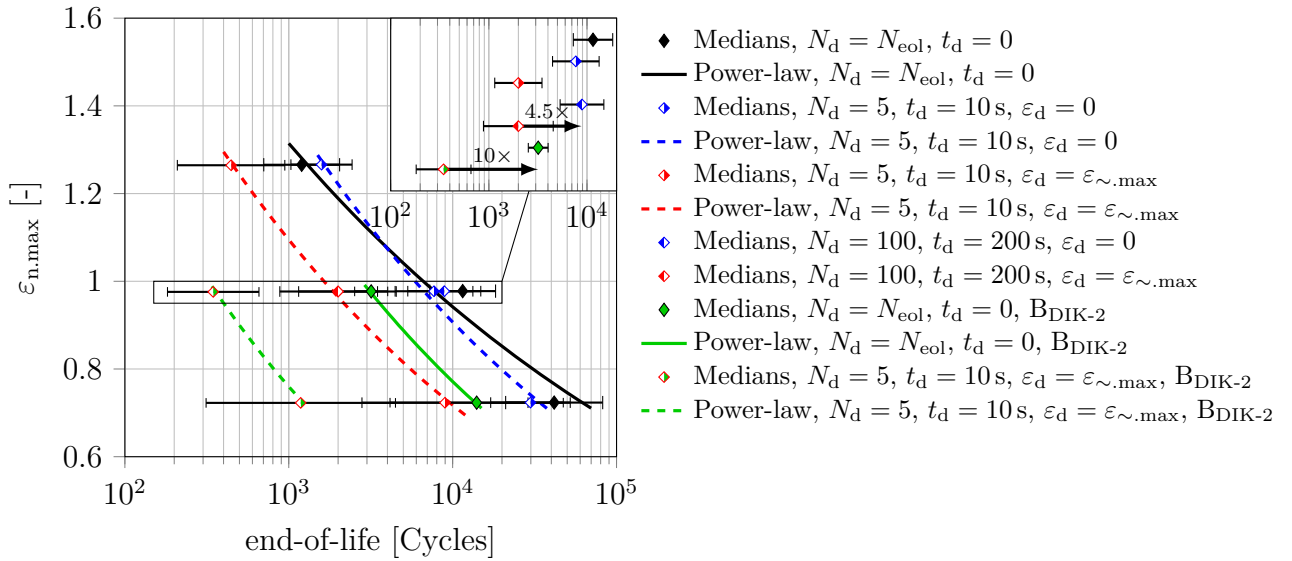
Figure 6.11: NR 45, B$_{\text{DIK-1}}$: Fatigue test data of the 3D-dumbbell with and without dwell periods. For reasons of clarity, a zoom of the load-level $\varepsilon_{\text{n.max}} \approx 150\%$ is shown in the corner. Within this enlargement the data-points are vertically shifted. All shown medians are endued with 95% confidence limits ($\vdash\dashv$) and all shown data are $\varepsilon_{\text{const}}$ based.

A very significant fatigue influence due to dwell periods is measured for the unfilled SBR compound (see Figure 6.12). However, in a converse direction as might be excepted from the Force$_{\sim.\text{max}}$ shown in Figure 6.5 on 143 and the results of Harbour et al. [70]. Their results state a greater crack growth rate in case of nearly unloaded dwell periods compared to loaded dwell periods. By contrast, the lifetime decreases with a factor of 4.5 (B$_{\text{DIK-1}}$) and even ten (B$_{\text{DIK-2}}$) for loaded dwell periods compared to unloaded dwell periods in Figure 6.12 for all load-levels. An almost negligible implication on the lifetime, with the continuous test as reference, is measured in case of unloaded dwell periods. In general, lower lifetimes are measured for the second batch B$_{\text{DIK-2}}$ material as discussed earlier in Section 5.4 and shown in Figure 5.4 on Page 126. In addition to the Harbour et al. conditions $N_{\text{d}} = 5$, $t_{\text{d}} = 10\,\text{s}$, an upscaled load-condition with $N_{\text{d}} = 100$, $t_{\text{d}} = 200\,\text{s}$ is applied. This load-condition allows for longer static relaxation time for the same $N_{\text{d}}/t_{\text{d}}$-ratio. The equal lifetimes are found with the upscaled load-condition compared to the ($N_{\text{d}} = 5$, $t_{\text{d}} = 10\,\text{s}$)-case, suggesting a crucial relevance of the $N_{\text{d}}/t_{\text{d}}$-ratio for the mechanical fatigue for unfilled SBR.

Figure 6.12: SBR 0: Fatigue test data of the 3D-dumbbell with and without dwell periods. For reasons of clarity, a zoom of the load-level $\varepsilon_{n.max} \approx 100\%$ is shown in the corner. Within this enlargement the data-points are vertically shifted. All shown medians are endued with 95% confidence limits ($\vdash\dashv$) and all shown data are B_{DIK-1} and ε_{const} based. Only the green colored data (e.g. ♦) are measured based on B_{DIK-2}.

The same lifetime shortening effect of loaded dwell periods is measured for the TDS_{V2} (see Figure 6.13). For this reason, the dwell period effect for the SBR 0 is not exclusively found for test pieces with crack initiations at the flash, represented by the 3D-dumbbell. For one load-level of the TDS_{V2}, a continuous cyclic fatigue test with $f = 1\,Hz$ ⋈ and $f = 6\,Hz$ ⋈ is conducted. The lifetime for the $f = 1\,Hz$ test is significantly shorter than for the $f = 6\,Hz$ case.
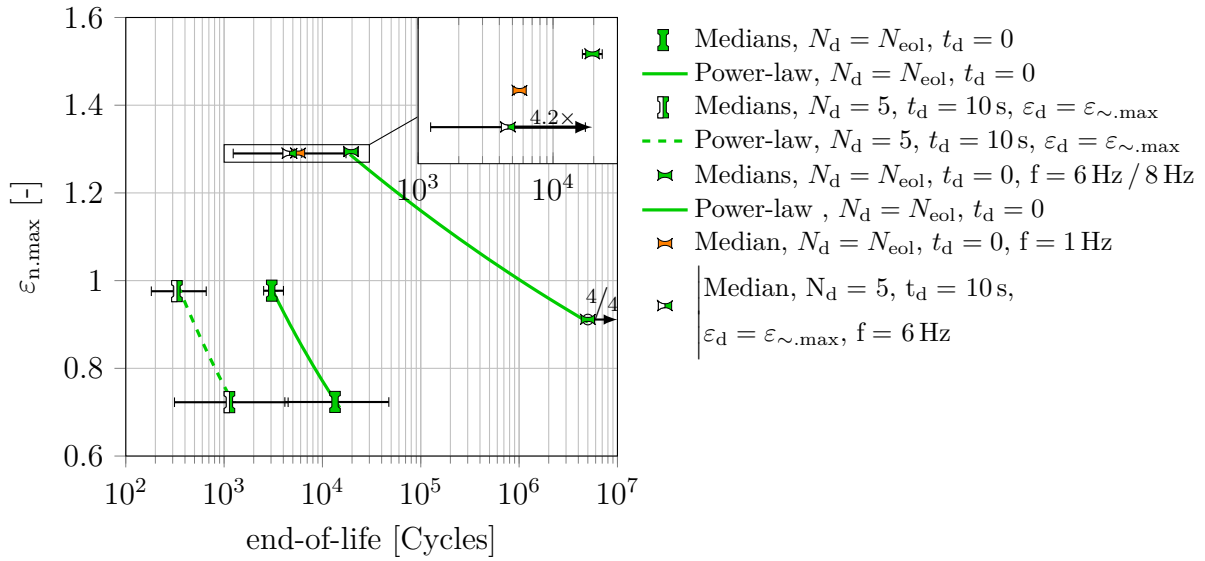
Figure 6.13: SBR 0, B$_{\text{DIK-2}}$: Fatigue test data of the 3D-dumbbell ⚏ and TDS$_{\text{V2}}$ ⋈ with and without dwell periods. For reasons of clarity, a zoom of the load-level $\varepsilon_{\text{n.max}} \approx 130\,\%$ from the TDS$_{\text{V2}}$ is shown in the corner. Within this enlargement the data-points are vertically shifted. All shown medians are endued with 95 % confidence limits (⊢⊣) and all shown data are $\varepsilon_{\text{const}}$ based. The $^{\text{X}}/_{\text{Y}}$ stands for X non-failed from Y total test pieces.

This frequency dependency and the lifetime shortening effect of loaded dwell periods suggest an influence by the time of load, measured by the effective time (see Equation 6.1). Figure 6.14 shows the lifetime data from the tests with continuous sinusoidal duty cycles, with dwell periods and also with the time until failure for the static relaxation experiments. The statically loaded 3D-dumbbells fail due to static crack propagation (aka. time-dependent crack propagation [101]). Note that only one out of four test pieces failed for the lowest load-level due to static crack propagation. Unlike the dynamic failure, static crack propagation seems to take place only for loads above a certain threshold. Similar results were obtained by Lake and Lindley in e.g. [102, 103]. This threshold is situated here for the 3D-dumbbell between the $\varepsilon_{\text{n.max}} \approx 75\,\%$ and $\varepsilon_{\text{n.max}} \approx 100\,\%$ load-level. The plot of the fatigue data, with and without dwell periods, over the effective time, yields a superposition of the fatigue data, confirming the strong dependency of the end-of-life on the effective time of loading for the SBR 0 material. However, this statement holds only for the dynamic fatigue experiments. Figure 6.14 still shows a gap in lifetime between all dynamic fatigue data and the pure static fatigue tests.
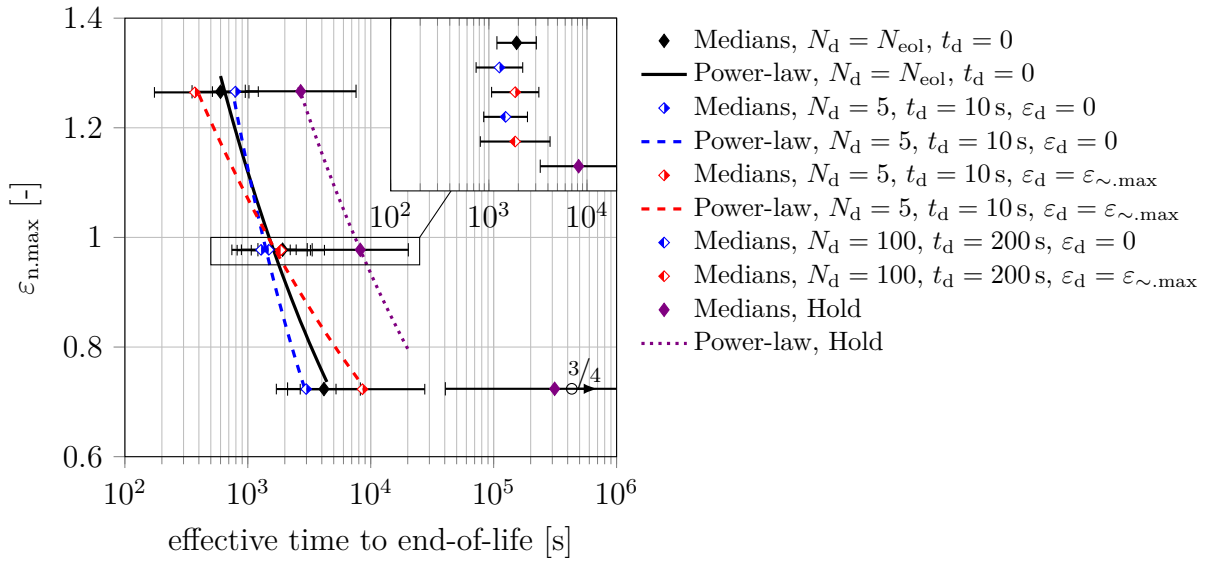
Figure 6.14: SBR 0, B$_{\text{DIK-1}}$: Fatigue test data of the 3D-dumbbell with and without dwell periods plotted over effective time instead of cycles. For reasons of clarity, a zoom of the load-level $\varepsilon_{\text{n.max}} \approx 100\,\%$ is shown in the corner. Within this enlargement the data-points are vertically shifted. All shown medians are endued with 95 % confidence limits ($\vdash\dashv$) and all shown data are $\varepsilon_{\text{const}}$ based. The $^{\text{X}}/_{\text{Y}}$ stand for X non-failed from Y total test pieces.

Adding carbon black completely suppresses the effects of dwell periods under static stress measured for the unfilled SBR. As shown in Figure 6.15, the Wöhler curves for the different test conditions align. This does not only hold for the 3D-dumbbell but for the TDS$_{\text{V2}}$ as well. Moreover, the increase in crack growth rate with nearly one order of magnitude between tests with dwell periods and continuous crack growth tests measured by Harbour et al. [70] is nowhere near found in the present data. This finding might be disputed with the argument of a wrong criterion ($\varepsilon_{\text{n.max}}$) on the ordinate of the Wöhler-diagram. Stress might be a better criterion due to its ability to differentiate between test conditions with and without dwell periods (see Section 6.2.) However, in case the data from Figure 6.15 would be replotted in a Cauchy stress σ_{max} based Wöhler diagram, the medians ⫫ from the tests with unloaded dwell periods would approximately shift as indicated by the blue arrows, with respect to the tests with unloaded dwell periods. The shift factors originate from the maximum cyclic reaction force Force$_{\sim.\text{max}}$ difference in Figure 6.6 on Page 143 between cyclic relaxation data with loaded (red lines) and unloaded (blue lines) dwell periods. In fact, a stress based Wöhler-plot would therefore even lead to the opposite crack growth based conclusion made in Harbour et al. [70]; unloaded dwell periods, significantly increase the lifetime. Re-plotting the data using the strain energy density yields a similar trend as indicated in a stress-based Wöhler-diagram.

In the present study a carbon black filled SBR (SBR 77) is tested. However, the SBR 77 has in detail a different formulation to the material of Harbour et al.
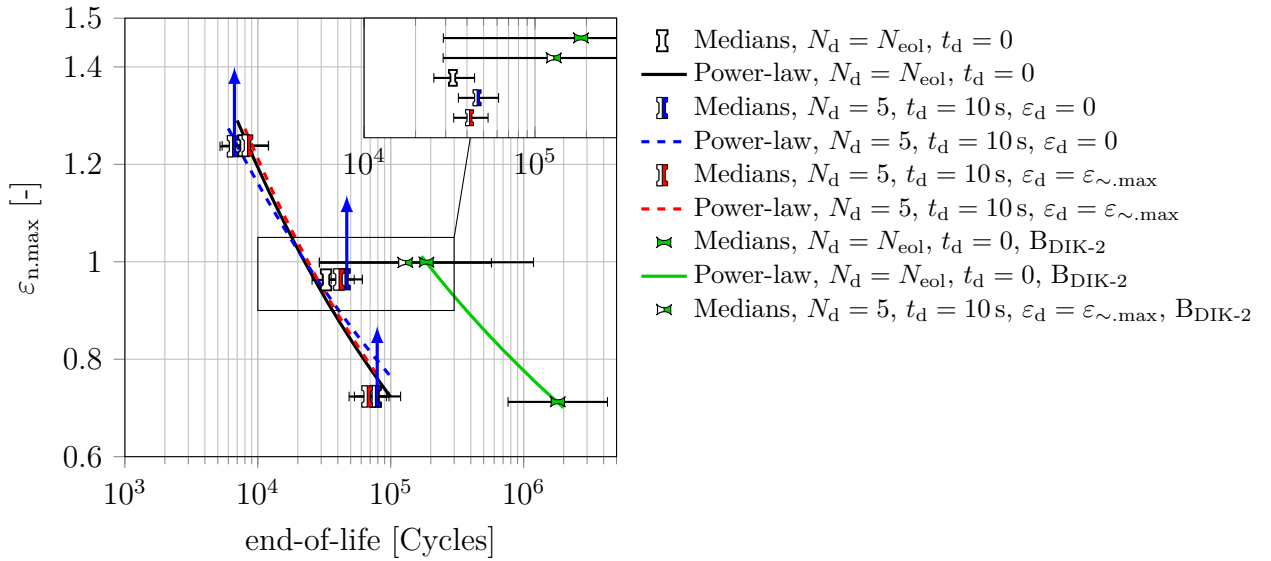
Figure 6.15: SBR 77: Fatigue test data of the 3D-dumbbell ⚏ and TDS$_{V2}$ ⋈ with and without dwell periods. For reasons of clarity, a zoom of the load-level $\varepsilon_{n.max} \approx 100\%$ is shown in the corner. Within this enlargement the data-points are vertically shifted. All shown medians are endued with 95% confidence limits (⊢⊣) and all shown data are B$_{DIK-1}$ and ε_{const} based. Only the green colored data are measured based on B$_{DIK-2}$. The blue arrows indicate the location of ⚏ with respect to ⚏ in a stress based Wöhler-plot.

In order to verify whether the significant dwell period impact on the crack growth rate is not only a phenomenon measurable with the SBR formulation of Harbour et al., their tests are here partially repeated with the present SBR 77 material. For this reason, crack growth tests with two-sided notched pure shear test pieces (dimension: width= 40 mm, height= 4 mm, thickness= 0.85 mm) are conducted. Five test pieces are cycled simultaneously via a common guided beam (see Figure 6.16). The test machine is basically set up in a similar manner as the 2D-dumbbell test rig shown in Figure 4.5 (Section 4.2), with the only difference of a freely controllable electric actuator replacing the eccentric drive.
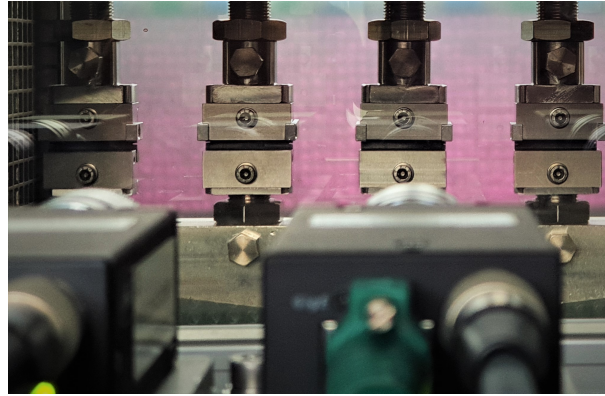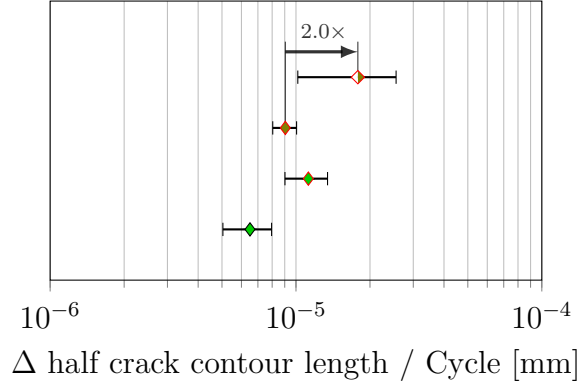
Figure 6.16: Set-up for crack growth measurements. Four out of five two-sided notched pure shear test pieces in a temperature chamber monitored by one camera per test piece.

Unfortunately it is not possible to perform a $N_d = 5$, $t_d = 10\,$s - load signal throughout the test run. The camera system, tracking the crack length, is unable to photograph all five test pieces within only five load-cycles. One is forced to insert sections of 200 continuous sinusoidal cycles in the load-signal. These 'recording-sections' repeat every $150 \times (N_d = 5,$ $t_d = 10\,$s). Thus, $71\,\%$, with respect to the number of cycles, of the test is running with the desired conditions. An additional imprecision is incorporated by complete software crashes every $4\,$h to $5\,$h, leading to several hours long standstills. The maximum test frequency for the test rig with this dwell period procedure is limited on $1\,$Hz. In order to avoid buckling of the $0.85\,$mm thin test pieces, the minimum dynamic force within the sinusoidal deflection and the dwell periods is maintained at $0\,$N by stepper motors.

Figure 6.17 shows the crack growth rate (crack length increase per cycle) for the NR 45 material. In accord with the results from Harbour et al. [70], a minor increase of the crack growth rate is measured in case that unloaded dwell periods are included in the load-signal. See the caption of Figure 6.17 for further details.

$\diamond\, \varepsilon_{\sim.\mathrm{max}} = 50\,\%,\ N_{\mathrm{d}} = 5,\ t_{\mathrm{d}} = 10\,\mathrm{s},\ \sigma_{\mathrm{d}} = 0,\ \mathrm{B_{DIK\text{-}2\text{-}old}}$

$\diamond\, \varepsilon_{\sim.\mathrm{max}} = 50\,\%,\ \mathrm{B_{DIK\text{-}2\text{-}old}}$

$\diamond\, \varepsilon_{\sim.\mathrm{max}} = 50\,\%,\ \mathrm{B_{DIK\text{-}2}}$

$\diamond\, \varepsilon_{\sim.\mathrm{max}} = 37.5\,\%,\ \mathrm{B_{DIK\text{-}2}}$
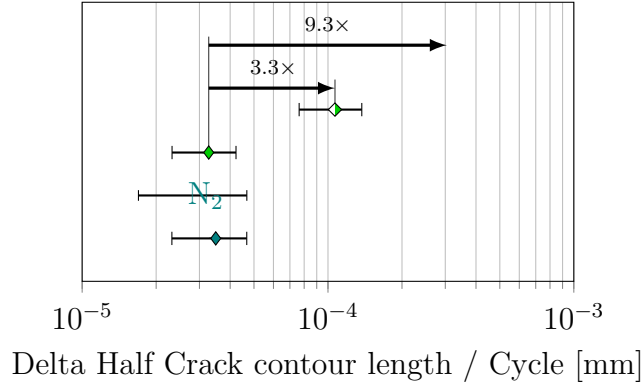

Figure 6.17: NR 45: Half crack contour increase per cycle. Data points labelled with $\mathrm{B_{DIK\text{-}2}}$ originate from test pieces vulcanised one week after material mixing, whereas data labelled with $\mathrm{B_{DIK\text{-}2\text{-}old}}$ originate from test pieces vulcanised three months after material mixing.

Yet, also for the SBR 77 material a minor impact of dwell periods is shown in Figure 6.18, relative to the Harbour et al. results. The factor of 9.3, found by Harbour et al., between the continuously cycled test pieces and the data-points originating from tests with dwell periods is marked with an arrow in Figure 6.18.

Deviating temporarily from the subject of dwell periods, additionally the crack growth rate in nitrogen atmosphere (O_2-concentration $< 1\,\%$) is measured. This is motivated by the large lifetime differences between the 3D-dumbbell and the $\mathrm{TDS_{V2}}$, found in Chapter 5. In addition to the possible reasons for this phenomenon in Chapter 5, the implication on the lifetime of a more significant exposure to oxygen of surface cracks compared to bulk cracks shall be investigated with the crack growth measurements in nitrogen atmosphere. However, unlike often observed for NR materials (see e.g. [1]), there is no difference to the crack growth rates in air (much higher oxygen content) as ambient medium ($\diamond$ vs. $\mathrm{N_2}$). A possibly sufficient concentration of oxygen dissolved in the rubber to mask an effect of the different atmospheres, even during the nitrogen tests, was not studied.

Coming back to the subject of dwell periods, the compromises in the test-signal or the different material compositions are possible reasons for the gap in crack growth rate between the data from Harbour et al. and the data from Figure 6.18. It is assumed that for a $100\,\%$ and not only $71\,\%$ correct test-signal, the crack growth rate increases so that $\diamond$ moves towards the results from Harbour et al.

◇ $N_\mathrm{d} = 5$, $t_\mathrm{d} = 10\,\mathrm{s}$, $\sigma_\mathrm{d} = 0$, B$_\mathrm{DIK\text{-}2}$
◆ B$_\mathrm{DIK\text{-}2}$
N$_2$ B$_\mathrm{DIK\text{-}1}$, Nitrogen
◆ B$_\mathrm{DIK\text{-}1}$


Delta Half Crack contour length / Cycle [mm]

Figure 6.18: SBR 77: Half crack contour increase per cycle. All tests are performed for a peak strain of $\varepsilon_{\sim.\mathrm{max}} = 37.5\,\%$. A factor of 9.3 is found by Harbour et al. between the continuous tests and the tests with dwell periods. The test for data-point N$_2$ is performed in nitrogen atmosphere.

However, not even the (probably too low) factor of 3.3 can be observed in the fatigue tests with the 3D-dumbbell (see Figure 6.15 or with relevant data only in Figure 6.19). The factors from the crack growth experiments can be directly applied to the 3D-dumbbell fatigue tests assuming crack growth dominated lifetime in a uniaxial deformed environment. The crack growth Equation 6.2, only containing relevant quantities, shows the inversely proportional relation of the crack growth rate ΔC to the number of cycles $N_{c_1 \to c_2}$ from crack size c_1 to crack size c_2 [1].

$$N_{c_1 \to c_2} = \mathrm{Multiplier} \cdot \frac{1}{\Delta C} \cdot \left(\frac{1}{c_1^{\mathrm{Exponent}}} - \frac{1}{c_2^{\mathrm{Exponent}}} \right) \tag{6.2}$$

The near superposition of the data-points from the fatigue tests with the 3D-dumbbell in e.g. Figure 6.19 with and without dwells periods raises the question as to what extent insights from crack growth tests are applicable to fatigue phenomena. One possible explanation, at least for the SBR material, is that the failure initiation process of the later macro cracks cannot be described with *classical* crack growth. These macro cracks eventually yield the final failure of the test piece or component.
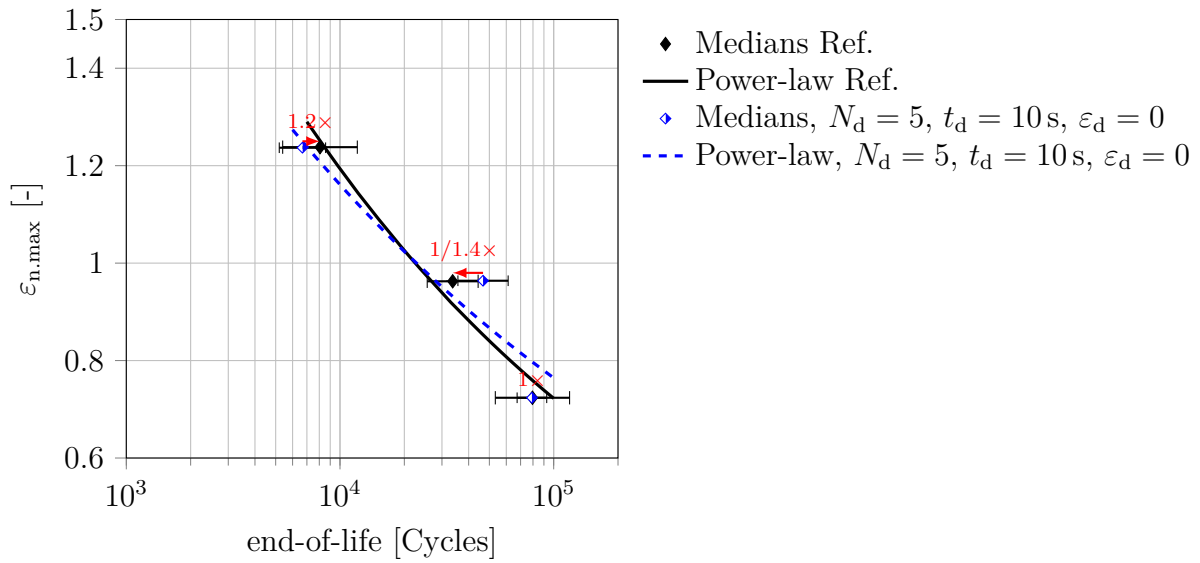
Figure 6.19: SBR 77: Figure 6.15 with a choice of relevant 3D-dumbbell data only.

6.4 Conclusions

Summing up the implication of dwell periods on the lifetime of elastomers:

- Experiments with loaded and unloaded dwell periods afford the opportunity to measure fatigue data with different stresses but almost equal strains.

- Irrespective of the 3D-dumbbell or the $\mathrm{TDS_{V2}}$, only the unfilled SBR 0 material showed a dependence on dwell periods.

- This finding disagrees with the crack growth measurements, especially for the SBR 77 material.

- The significant dependence of the SBR 0 material on the dwell period could be attributed to the effective time of loading.
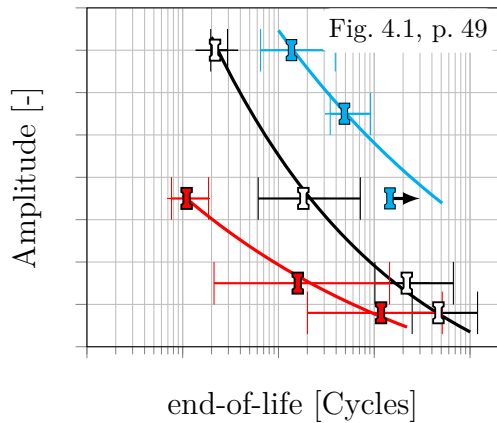
7 Summary

The present work may be divided into two segments. First, improvement of the mechanical fatigue testing method and based on this, secondly, an investigation of a possible new fatigue influencing factor. The aspects that were focused on for the improvement of fatigue testing are: the control of the fatigue test piece temperature, the determination of the local strain for displacement-controlled oscillations, and the measurement of fatigue resistance using a new test piece geometry designed to be free of initiation of failure from surface features. Chapter 5 is a hybrid between those two segments. It is dedicated to the impact of failure initiation with locus in the bulk material on the lifetime compared to surface inhomogeneity induced crack initiation. In addition, the details of the mould partition line, resulting in a flash on the test piece, are found to significantly influence the mechanical fatigue of elastomers. The present work closes with the investigation of dwell periods, in otherwise continuous sinusoidal duty cycles, and their implication on the lifetime, which is expected to show a strong lifetime-reducing effect based on crack growth examinations from literature. Except for the unfilled SBR material, this expectation is not confirmed. For the unfilled SBR material the lifetime depends significantly on the effective time of strain. The observations of this work on the significant effects of reinforcing filler on the crack growth and fatigue behaviour of SBR, and in particular its effect on time-dependent crack growth and in the influence of dwell times at zero strain on cyclic crack growth and cyclic fatigue, show that the reinforcing mechanism is not well understood. A satisfactory mechanism of reinforcement needs to account for its influence on these time-dependent effects.

In the following, the most relevant findings are summarised and complemented with corresponding figures from where these may be inferred. Bullet points with ◄-symbol may be found beside each figure.
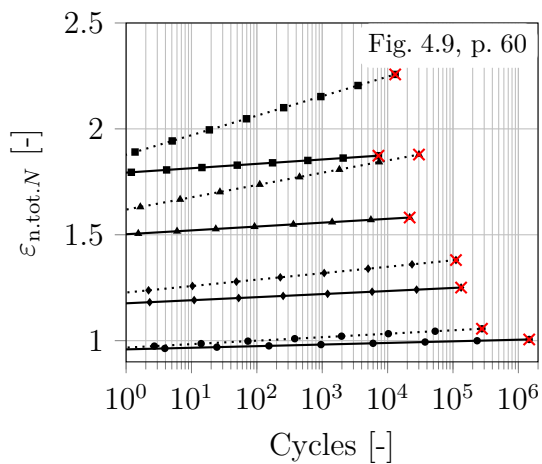
Figure	Most relevant findings are summarised
Fig. 4.1, p. 49	◄ Test piece temperature variations of some degrees influence the lifetime of the investigated elastomer significantly. • A significant reduction of the surface temperature of a test piece to a value close to ambient temperature can be achieved by forced convection. • The bulk temperature decrease is similar in magnitude to that of the surface.
Fig. 4.9, p. 60	◄ For filled rubber test pieces and engineering components with inhomogeneous strain fields but undergoing constant end-to-end displacement cycles, the local strains depend not only on the current overall displacement, but also on the number of times it has been applied. • This change of distribution of local strain during cyclic loading with constant displacement amplitude is strongly material and amplitude dependent. • If constant local stress or strain are not accessible within fatigue tests, a transfer of continuously changing strains into Wöhler curve-compliant constant equivalent strain is necessary.
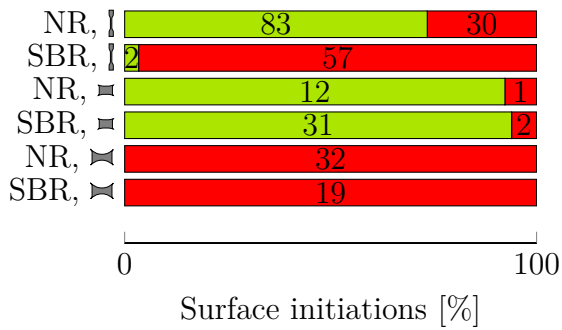
◄ The 2D-dumbbell chosen as reference test piece for the new test piece turned out to only initiate failures at the surface for the NR material due to the die-cut process.
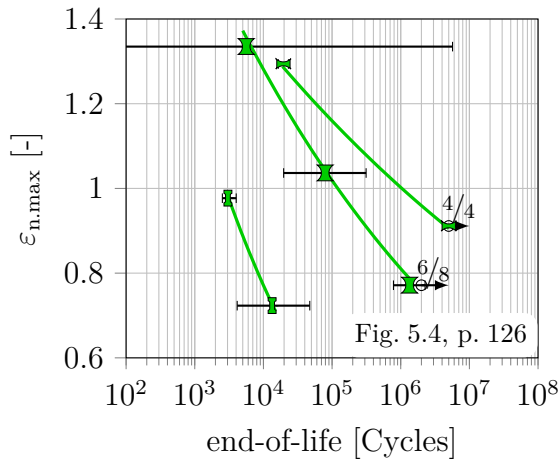
◄ The second version of the new test piece ⋈ showed the desired failure initiation behaviour with locus in the bulk material.

• This led to a significant increase in lifetime for the SBR material compared to the first version ⊨.

◄ Test pieces with propensity to crack initiation at the flash tend to have shortened lifetimes.

◄ This damage-impact depends on flash details.

• The damage by tri-axial tensile loads of significant magnitude leading to cavitation, influences the fatigue much more strongly compared to the *classic* failure initiation at inhomogeneities at the surface or within the bulk material exposed to e.g. uniaxial-dominated stress-fields.
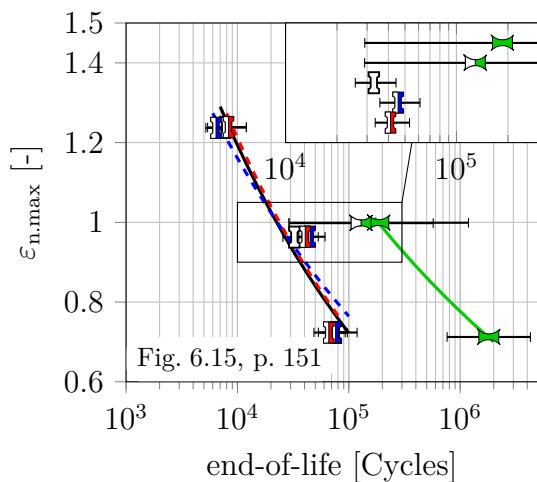
◄ Unlike seen in crack growth tests of Harbour et al. [70], repeating dwell periods do not show any impact of the lifetime of filled NR, SBR and unfilled NR.

• Only for the unfilled SBR material an effect on the fatigue behaviour is measured in case of loaded dwell periods.

• These findings suggest that insights from crack growth tests may not be simple to relate to fatigue phenomena.

Bibliography

[1] A. N. Gent. *Engineering with Rubber.* Hanser, München, 2 edition, 2001.

[2] Fritz Röthemeyer and Franz Sommer. *Kautschuk Technologie.* Hanser, München, 3 edition, 2013.

[3] J. E. Mark, B. Erman, and F. R. Eirich, Frederick. *The Science and Technology of rubber.* Elsevier, Amsterdam, 3 edition, 2005.

[4] J-B. Donnet, R. C. Bansal, and Wang M-J. *Carbon Black.* Marcel Dekker, New York, 2 edition, 1993.

[5] A. Wöhler. Über die Festigkeitsversuche mit Eisen und Stahl. *Zeitschrift für Bauwesen*, (Vol. 20):73–106., 1870.

[6] S. M. Cadwell, R. A. Merrill, C. M. Sloman, and F. L. Yost. Dynamic fatigue life of rubber. *Rubber Chemistry and Technology*, (13):304–315, 1940.

[7] P. Papadopoulos. *Introduction to Continuum Mechanics.* Department of Mechanical Engineering, University of California, Berkeley, 2008.

[8] E. Verron, J. B. Le Cam, and Laurent Cornet. A multiaxial criterion for crack nucleation in rubber. *Mechanics Research Communications*, (33):493–498, 2005.

[9] W. Becker and D. Gross. *Mechanik elastischer Koerper und Strukturen.* Springer Verlag, 2002.

[10] Gerhard Holzapfel. *NONLINEAR SOLID MECHANICS. A Continuum Approach for Engineering.* John Wiley & Sons, second print edition, 2001.

[11] G. Merziger, G. Mühlbach, D. Wille, and T. Wirth. *Formeln, Hilfen, höhere Mathematik.* Binomi Verlag, 2010.

[12] Rohan Abeyaratne. *Continuum Mechanics Volume II of lecture notes on the mechanics of elastic solids.* MIT Department of Mechanical Engineering, 2012.

[13] A.C. Ugural and S.K. Fenster. *Advanced Mechanics of Materials and Applied Elasticity.* International Series in the Physical and Chemical Engineering Sciences. Pearson Education, 2011.

[14] Ellen Arruda and Mary Boyce. A three-dimensional constitutive model of the large stretch behavior of rubber elastic materials. *Journal of the Mechanics and Physics of Solids*, 41:389–412, 02 1993.

[15] Jan Plagge, Alexander Ricker, Nils Kröger, Peter Wriggers, and Manfred Klueppel. Efficient modeling of filled rubber assuming stress-induced microscopic restructurization. *International Journal of Engineering Science*, 151:103291, 06 2020.

[16] J. Plagge and Manfred Klüppel. A physically based model of stress softening and hysteresis of filled rubber including rate-and temperature dependency. *International Journal of Plasticity*, (89):173–196, 2017.

[17] Michael Kaliske and G. Heinrich. An extended tube-model for rubber elasticity: Statistical-mechanical theory and finite element implementation. *Rubber Chemistry and Technology*, 72:602–632, 09 1999.

[18] D. S. Starnes and J. Tabor. *The Practice of Statistics*. W.H. Freeman and Company, 6 edition, 2018.

[19] Wayne Nelson. Applied life data analysis: John wiley & sons. *Wiley Series in Probability and Statistics*, 1982.

[20] Christian Müller. Zur statistischen Auswertung experimenteller Wöhlerlinien: Dissertation. *TU Clausthal*, 2015.

[21] J. Hartung, B. Elpelt, and K.-H. Klösener. *Statistik*. Oldenbourg Wissenschaftsverlag, 15 edition, 2009.

[22] E. Rossow. Eine einfache Rechenschiebernäherung an die den normal scores entsprechenden Prozentpunkte. *Zeitschrift für wirtschaftliche Fertigung.*, 59(12), 1964.

[23] Ludwig Fahrmeir, Christian Heumann, Rita Künstler, Iris Pigeot, and Gerhard Tutz. *Statistik: Der Weg zur Datenanalyse.* Springer, 8 edition, 2016.

[24] W.S. (aks *Student*) Gosset. The probable error of a mean. *Biometrika*, 6(1):1–25, 1908.

[25] Lothar Sachs and Jürgen Hedderich. *Sachs Angewandte Statistik.* Springer, 12 edition, 2006.

[26] John I. McCool. Inference on weibull percentiles and shape parameter from maximum likelihood estimates. *IEEE TRANSACTIONS ON RELIABILITY*, R-19(1), 1970.

[27] W. Weibull. *A Statistical Theory of the Strength of Materials*. Handlingar / Ingeniörsvetenskapsakademien. Generalstabens litografiska anstalts förlag, 1939.

[28] A. Benard and E. Bos-Levenbach. Het uitzetten van waarnemingen op waarschijnlijkheids-papier (the plotting of observations on probability paper). *Statistica Neerlandica*, 7:163 – 173, 09 1953.

[29] John I. McCool. Software for weibull inference. *Quality Engineering*, (23):253–264, 2011.

[30] Wayne Nelson. Accelerated testing. *A JOHN WILEY & SONS*, 1990.

[31] W. V. Mars and A. Fatemi. A literature survey on fatigue analysis approaches for rubber. *International Journal of Fatigue*, (24):949–961, 2002.

[32] W. V. Mars and A. Fatemi. Factors that affect the fatigue life of rubber: A literature survey. *Rubber Chemistry and Technology*, (77):391–412, 2004.

[33] Tee Yun Lu, Mei Loo, and Andri Andriyana. Recent advances on fatigue of rubber after the literature survey by mars and fatemi in 2002 and 2004. *International Journal of Fatigue*, 110:115–129, 05 2018.

[34] Jacopo Schieppati, Bernd Schrittesser, Alfred Wondracek, Stefan Robin, Armin Holzner, and Gerald Pinter. Impact of temperature on the fatigue and crack growth behavior of rubbers. *Procedia Structural Integrity*, 13:642–647, 2018.

[35] Jacopo Schieppati, Bernd Schrittesser, Alfred Wondracek, Stefan Robin, Armin Holzner, and Gerald Pinter. Temperature impact on the mechanical and fatigue behavior of a non-crystallizing rubber. *International Journal of Fatigue*, 144, 03 2021.

[36] A. G. James. Fatigue in elastomers. *Kautschuk und Gummi Kunststoffe*, (3):87–91, 1973.

[37] P. Charrier, T. Ramade, D. Taveau, Y. Marco, and S. Calloch. Influence of temperature on durability behavior of carbon black filled natural rubber. *Constitutive Models for Rubber VI*, pages 179–185, 2010.

[38] B. Ruellan, J.-B. Le Cam, I. Jeanneau, F. Canévet, F. Mortier, and E. Robin. Fatigue of natural rubber under different temperatures. *International Journal of Fatigue*, 124:544–557, 2019.

[39] K. Narynbek Ulu, B. Huneau, E. Verron, A.-S. Béranger, and P. Heuillet. True stress controlled fatigue life experiments for elastomers. *International Journal of Fatigue*, 104:171–182, 2017.

[40] Erhard Krempl. Cyclic creep: an interpretive literature survey. *Weld. Res. Counc. Bull.; (United States)*, 195, 06 1974.

[41] Woo-Gon Kim, Jae-Young Park, I Made Wicaksana Ekaputra, Seon-Jin Kim, and Jinsung Jang. Influence of hold time and stress ratio on cyclic creep properties under controlled tension loading cycles of grade 91 steel. *Nuclear Engineering and Technology*, 49(3):581 – 591, 2017.

[42] C. J. Derham and A. G. Thomas. Creep of rubber under repeated stressing. *Rubber Chemistry and Technology*, (50):397–402, 1977.

[43] C.K.L. Davies, D.K. De, and A. Thomas. Characterisation of the behaviour of rubber for engineering design purposes: Stress relaxation under repeated stressing. *Progress in Rubber and Plastics Technology*, 12:208–220, 01 1996.

[44] T.J. Pond and A.G. Thomas. Creep under repeated stressing. *AIChE Symposium Series*, pages 810–817, 01 1979.

[45] J.G.R. Kingston and Alan Muhr. Effects of strain crystallisation on cyclic fatigue of rubber. *6th Engineering Integrity Society International Conference on Durability and Fatigue, Queen's College, Cambridge, UK,*, pages 337–342, 03 2007.

[46] ASTM D4482-11. Standard test method for rubber property—extension cycling fatigue. *ASTM International, West Conshohocken, PA*, 2017.

[47] ISO 6943:2017. Rubber, vulcanized - Determination of tension fatigue. *International Standard*, 2017.

[48] B. J. Roberts and J. B. Benzies. The relationship between uniaxial and equibiaxial fatigue in gum and carbon black filled vulcanizates. *Proceedings of Rubbercon*, pages 1–13, 1977.

[49] F. Abraham, T. Alshuth, and S. Jerrams. The effect of minimum stress and stress amplitude on the fatigue life of non strain crystallising elastomers. *Materials and Design*, (26):239–245, 2004.

[50] F. Abraham, G. Clauß, T. Alshuth, and J. Kroll. Untersuchung und simulation des einflusses von fehlstellen auf das risswachstum und die ermüdung von elastomeren. *Elastomere und Kunstoffe*, pages 595–599, 2005.

[51] Oliver Gehrmann, Nils Hendrik Kröger, Maria Krause, and Daniel Juhre. Dissipated energy density as fatigue criterion for non-relaxing tensional loadings of non-crystallizing elastomers? *Polymer Testing*, 78:105953, 2019.

[52] A. Andriyana, N. Saintier, and E. Verron. Configurational mechanics and critical plane approach: Concept and application to fatigue failure analysis of rubberlike materials. *International Journal of Fatigue*, (32):1627–1638, 2010.

[53] G. Ayoub, M. Nait-abdelaziz, F. Zairi, and J. M. Gloaguen. Multiaxial fatigue life prediction of rubber-like materials using the continuum damage mechanics approach. *Procedia Engineering*, (2):985–993, 2010.

[54] H. Oshima, Y. Aono, and H. Noguchi. Fatigue characteristics of vulcanized natural rubber for automotive engine mounting. *Key Engineering Materials*, (353-358):178–181, 2007.

[55] Shangguan, W. B, X. Duan, and T. Liu. Prediction fatigue life of rubber mounts using stress-based damage indexes. *Journal of Materials: Design and applications*, (231):657–673, 2015.

[56] M. Flamm, T. Steinweger, and U. Weltin. Lifetime prediction of multiaxially loaded rubber springs and bushings. *Constitutive models of rubber III.*, 2003.

[57] J. B. Le Cam, E. Verron, and Bertrand Huneau. Description of fatigue damage in carbon black filled natural rubber. *Fatigue & Fracture of Engineering Materials & Structures*, 31:1031 – 1038, 12 2008.

[58] V. Le Saux, Y. Marco, S. Calloch, C. Doudard, and P. Charrier. Fast evaluation of the fatigue lifetime of rubber-like materials based on a heat build-up protocol and micro-tomography measurements. *International Journal of Fatigue*, (32):1582–1590, 2010.

[59] J.-L. Poisson, S. Meo, F. Lacroix, G. Berton, M. Hosseini, and N. Ranganathan. Comparison of fatigue criteria under proportional and non proportional multiaxial loading. *Rubber Chemistry and Technology*, (91(2)):320–338, 2018.

[60] N. Saintier, G. Cailletaud, and R. Piques. Multiaxial fatigue life prediction for a natural rubber. *International Journal of Fatigue*, (28):530–539, 2005.

[61] M. Flamm, J. Spreckels, Thomas Steinweger, and Uwe Weltin. Effects of very high loads on fatigue life of nr elastomer materials. *International Journal of Fatigue - INT J FATIGUE*, 33:1189–1198, 09 2011.

[62] W. V. Mars. Mutliaxial fatigue of rubber: Disseration. *The University of Toledo*, 2001.

[63] W. V. Mars and A. Fatemi. A novel specimen for investigating the mechanical behavior of elastomers under multiaxial loading conditions. *Society for Experimental Mechanics*, 44(2):136–146, 2004.

[64] J-B Brunac, Olivier Gérardin, and Jean-Baptiste Leblond. On the heuristic extension of haigh's diagram for the fatigue of elastomers to arbitrary loadings. *International Journal of Fatigue*, (31):859–867, 2008.

[65] E. Verron and A. Andriyana. Definition of a new predictor for multiaxial fatigue crack nucleation in rubber. *Journal of the Mechanics and Physics of Solids*, (56):417–443, 2007.

[66] T. Brüger, M. Rabkin, and U. Weltin. Hysteresis area calculated from a dynamic material model: A new damage parameter for lifetime estimations? *Constitutive Models for Rubber IV*, 2005:83–88, 2005.

[67] A.N. Gent and P.B. Lindley. Internal rupture of bonded rubber cylinders in tension. *Proceedings of The Royal Society A: Mathematical, Physical and Engineering Sciences*, 249:195–205, 01 1959.

[68] J. M. Ball and T. B. Benjamin. Discontinuous equilibrium solutions and cavitation in nonlinear elasticity. *Philosophical Transactions of the Royal Society of London. Series A Mathematical and Physical Sciences*, (306), 1982.

[69] A. Gent. Elastic instabilities in rubber. *International Journal of Non-linear Mechanics - INT J NON-LINEAR MECH*, 40:165–175, 03 2005.

[70] Ryan Harbour, Ali Fatemi, and William Mars. The effect of a dwell period on fatigue crack growth rates in filled sbr and nr. *Rubber Chemistry and Technology*, 80, 11 2007.

[71] C. Roland and J. Sobieski. Anomalous fatigue behavior in polyisoprene. *Rubber Chemistry and Technology*, 62:37, 10 1988.

[72] K. Langeheinecke, J. Jany, G. Thieleke, K. Langeheinecke, and A. Kaufmann. *Thermodynamik für Ingenieure.* Springer Vieweg, Wiesbaden, 9 edition, 2013.

[73] D. Besdo, J Ihlemann, J.G.R. Kingston, and A.H. Muhr. Modelling inelastic stress-strain phenomena and a scheme for efficient experimental characterization. *in Constitutive Models for Rubber III*, pages 309–317, 01 2003.

[74] Hamid Ahmadi, J. Kingston, and Alan Muhr. Dynamic properties of filled rubber — part i: Simple model, experimental data and simulated results. *Rubber Chemistry and Technology*, 81:1–18, 03 2008.

[75] J.G.R. Kingston and Alan Muhr. Determination of effective flaw size for fatigue life prediction. *Constitutive Models for Rubber VII - Proceedings of the 7th European Conference on Constitutive Models for Rubber, ECCMR*, pages 337–342, 01 2012.

[76] A. Lampe, Lars Kanzenbach, Jörn Ihlemann, and Alan Muhr. Characteristics of relaxation and recovery behavior of filled rubber. *Kautschuk und Gummi Kunststoffe*, 71:47–53, 10 2018.

[77] J.-L. Poisson, V. Orlando, and A.H. Muhr. Effect of strain history on crack growth of rubber using an automatic measurement technique. *Technical Meeting of Rubber Division, ACS*, 2017.

[78] Jean-Louis Poisson and Alan Muhr. Striations in natural rubber fracture surfaces. *ECCMR*, (XI):522–527, 06 2019.

[79] ISO 37:2011. Rubber, vulcanized or thermoplastic — Determination of tensile stress-strain properties. *International Standard*, 2011.

[80] Ryan J. Harbour, Ali Fatemi, and Will V. Mars. Fatigue life analysis and predictions for nr and sbr under variable amplitude and multiaxial loading conditions. *International Journal of Fatigue*, 30(7):1231 – 1247, 2008.

[81] M.A. Miner. Cumulative damage in fatigue. *J. Appl. Mech.*, 12:A159–A164, 01 1945.

[82] M. Flamm, Thomas Steinweger, and Uwe Weltin. Cumulative damage in rubber materials. *Kautschuk und Gummi Kunststoffe*, 55:665–668, 12 2002.

[83] T. Zarrin-Ghalami and A. Fatemi. Multiaxial fatigue and life prediction of elastomeric components. *International Journal of Fatigue*, 55:92–101, 10 2013.

[84] G. Ayoub, M. Naït-Abdelaziz, F. Zaïri, J. M. Gloaguen, and P. Charrier. Fatigue life prediction of rubber-like materials under multiaxial loading using a continuum damage mechanics approach: Effects of two-blocks loading and r ratio. *Mechanics of Materials*, 52:87–102, 2012.

[85] M. Flamm, Thomas Steinweger, and U. Weltin. Festigkeitshypothesen in der rechnerischen Lebensdauervorhersage von Elastomeren. *KGK Kautschuk Gummi Kunststoffe*, 56(11):582–586, 2003.

[86] J.-B Le Cam. Endommagement en fatigue des elastomeres: Dissertation. *Ecole Centrale de Nantes and Universite de Nantes*, 2005.

[87] Alan Muhr. Modeling the stress-strain behavior of rubber. *Rubber Chemistry and Technology*, 78:391–425, 07 2005.

[88] Rainer Storn and Kenneth Price. Differential evolution - a simple and efficient heuristic for global optimization over continuous spaces. *Journal of Global Optimization*, 11:341–359, 01 1997.

[89] The SciPy community. Documentation for scipy.optimize.differential_evolution.

[90] J.-B Le Cam and E. Toussaint. The mechanism of fatigue crack growth in rubbers under severe loading: the effect of stress-induced crystallization. *Macromoloecules*, 43:4708–4714, 2010.

[91] L. Munoz, L. Vanel, O. Sanseau, P. Sotta, Didier Long, L. Odoni, and L. Guy. Fatigue crack growth dynamics in filled natural rubber. *Plastics, Rubber and Composites*, 41:273–276, 09 2012.

[92] Jean-Benoit Le Cam, Bertrand Huneau, and Erwan Verron. Fatigue damage in carbon black filled natural rubber under uni- and multiaxial loading conditions. *International Journal of Fatigue*, to be published:82–94, 07 2013.

[93] Benoît Ruellan, Jean-Benoit Le Cam, Eric Robin, Isabelle Jeanneau, Frédéric Canevet, G. Mauvoisin, and Didier Loison. Fatigue crack growth in natural rubber: The role of sic investigated through post-mortem analysis of fatigue striations. *Engineering Fracture Mechanics*, 201:353–365, 07 2018.

[94] Thomas Balutch, Bertrand Huneau, Yann Marco, Pierre Charrier, and Clément Champy. Fatigue behaviour of an industrial synthetic rubber. *MATEC Web of Conferences*, 165:22004, 2018.

[95] Murakami Yukitaka and Endo Masahiro. Quantitative evaluation of fatigue strength of metals containing various small defects or cracks. *Engineering Fracture Mechanics*, 17(1):1 – 15, 1983. Special Issue: International Conference on Advanced Materials Mechanical Properties '90 (ICAMP '90).

[96] M. Ludwig. Entwicklung eines Lebensdauer-Vorhersagekonzepts für Elastomerwerkstoffe unter Berücksichtigung der Fehlstellenstatistik: Dissertation. *Universität Hannover*, 2017.

[97] T. Harris and W. Anderson. Rolling bearing analysis. *Journal of Lubrication Technology*, 89:521, 10 1967.

[98] A. Gent, P. Lindley, and A. Thomas. Cut growth and fatigue of rubbers. i. the relationship between cut growth and fatigue. *Journal of Applied Polymer Science*, 8:455 – 466, 05 1965.

[99] Christophe Fond. Cavitation criterion for rubber materials: A review of void-growth models. *Journal of Polymer Science Part B: Polymer Physics*, 39:2081 – 2096, 09 2001.

[100] ISO 3384-1:2013. Rubber, vulcanized or thermoplastic - Determination of stress relaxation in compression - Part 1: Testing at constant temperature. *International Standard*, 2013.

[101] J. J. C. Busfield, K. Tsunoda, C. K. L. Davies, and A. G. Thomas. Contributions of Time Dependent and Cyclic Crack Growth to the Crack Growth Behavior of Non Strain-Crystallizing Elastomers. *Rubber Chemistry and Technology*, 75(4):643–656, 09 2002.

[102] G. J. Lake and P. B. Lindley. Cut growth and fatigue of rubbers. ii. experiments on a noncrystallizing rubber. *Journal of Applied Polymer Science*, 8(2):707–721, 1964.

[103] G.J. Lake and P.B. Lindley. Ozone cracking, flex cracking and fatigue of rubber. *Rubber Journal*, 146:24–30, 01 1964.